University of Southampton

Faculty of Natural and Environmental Sciences

School of Chemistry

Investigations of Rate Limitation in Nanostructured Composite Electrodes and Experiments Towards a 3D Li-ion Microbattery

Phillip A Johns

A Thesis Submitted for Degree of Doctor of Philosophy

June 2011

UNIVERSITY OF SOUTHAMPTON

ABSTRACT

FACULTY OF NATURAL AND ENVIRONMENTAL SCIENCES
SCHOOL OF CHEMISTRY

Doctor of Philosophy

INVESTIGATIONS OF RATE LIMITATION IN NANOSTRUCTURED COMPOSITE ELECTRODES AND EXPERIMENTS TOWARDS A 3D LI-ION MICROBATTERY

By Phillip A Johns

The factors effecting discharge rate limitation within $LiFePO_4$ composite electrode structures have been investigated. It was found that for composite electrodes containing 'small particles' of active material solid state processes are not necessarily rate limiting. A simple model has been developed to describe the rate limitation that occurs in the composite electrode structure due to electrolyte concentration, electrode thickness and lithium ion transference number.

The conformal electrodeposition of cathode materials onto 3D current collectors has been achieved with good control of film thickness. The advantage of the 3D current collector configuration over a conventional thin film arrangement has been realised by a 250 times capacity increase for a given footprint area. It was suggested the observed rate performance of half-cell 3D microbatteries, based on a manganese dioxide cathode and a lithium foil anode, was limited by the lithium ion transport distance through the porous 3D structure.

The electrodeposition of conformal polymers layers onto 3D substrates was investigated. The use of electrodeposited, electrolyte swollen, poly(acrylonitrile) and poly(aniline) films as polymer electrolytes was demonstrated. A novel method for the determination and differentiation of electronic and ionic resistance in electrodeposited polymer layers has been developed. A 'working' cell based on consecutively electrodeposited cathode and polymer electrolyte layers and a 'soft contact' liquid anode was presented.

Acknowledgements

First and foremost I would like to thank my supervisor professor John Owen, without your help, guidance and encouragement the majority of this work would not have been possible. I would also like to than him for introducing me to electrochemistry via a fascinating final year project (as by that point the idea of a PhD in chemistry was one I had thoroughly discarded).

Secondly I would like to thank Dr Matt Robert Roberts, your help and collaboration on a significant number of projects was vital, as was you friendship. I don't think I'll ever look at red insulating tape in the same way again, nor will I underestimate the value of belts.

I would also like to thank the rest of the Owen group (Ken, Yasu, Hanna, Lacey, Pan, Gaber, Dixon, Andy, Alex) and the Southampton Electrochemistry department (both floors 6 and 7 but especially Doug, Chris, Raya, Thomas, Sosnabot, Maria, David, Rob and of course Katie) for making my time in Southampton so enjoyable.

Finally I should thank the EPSRC and EU project Superlion for the funding to enable this project to take place.

DECLARATION OF AUTHORSHIP

I, ……..,

declare that the thesis entitled

……

……

and the work presented in the thesis are both my own, and have been generated by me as the result of my own original research. I confirm that:

- this work was done wholly or mainly while in candidature for a research degree at this University;
- where any part of this thesis has previously been submitted for a degree or any other qualification at this University or any other institution, this has been clearly stated;
- where I have consulted the published work of others, this is always clearly attributed;
- where I have quoted from the work of others, the source is always given. With the exception of such quotations, this thesis is entirely my own work;
- I have acknowledged all main sources of help;
- where the thesis is based on work done by myself jointly with others, I have made clear exactly what was done by others and what I have contributed myself;
- parts of this work have been published as:

Signed: ……..

Date:……

Contents

Table of Symbols

The following tables list the various symbols (including their meanings and their units) and abbreviations used throughout this work.

Symbol	Units	Explanation
[Li]	Mol dm^{-3}	Molar demand for lithium in the charged active material per unit volume of composite electrode
$[LiX]_1$	Mol dm^{-3}	Salt concentration at the discharge front
$[LiX]_0$	Mol dm^{-3}	Salt concentration within the bulk electrolyte
[LiX]	Mol dm^{-3}	Initial salt concentration within the composite electrode
A	cm^2	Area
C	h^{-1}	Defines a discharge rate of 1 C
C_0^*	Mol dm^{-3}	Initial concentration of oxidised species
C_{MnOx}	F cm^{-2}	MnO_x psudocapacitance
D	cm^2 s^{-1}	Diffusion coefficient within the composite electrode
E	V	Potential
E_{cell}	V	Cell potential
E_{eq}	V	Equilibrium cell potential
F	C mol^{-1}	Faradays constant; 96485 Coulombs per mole
f	h	C-rate
i	A	Current
i_0	A cm^{-2}	current density at the transition between semi-infinite and finite behaviour
j	A cm^{-2}	Current density
J_{LiX}	Mol cm^{-2} s^{-1}	Flux of lithium salt within the electrolyte
L	cm	Electrode thickness
L_t	cm	Total lithium ion transport distance
m_e	g	Electrode mass

M_m	g	Molar mass
n	-	Number of electrons transferred (1 unless otherwise stated)
Ω	Ω	Resistance in Ohms
Q^0	C	Theoretical charge
Q^0_A	C or mA.h cm^{-2}	Theoretical capacity / charge normalised to footprint area
Q^0_V	C or mA.h cm^{-3}	Theoretical volumetric capacity / charge
Q_A	C or mA.h cm^{-2}	Capacity / charge per unit area
Q	C or mA.h	Capacity / charge
Q_A	C or mA.h cm^{-2}	Capacity / charge normalised to area
Q_g	C or mA.h g^{-1}	Gravimetric capacity / charge
Q_V	C or mA.h cm^{-3}	Volumetric capacity / charge
Q^{SEM}_{INF}	C or mA.h	Capacity at the transition between semi-infinite and finite behaviour
R	Ohms (Ω)	Resistance
$R_{electronic}$	Ω cm^2	Electronic resistance
R_{ionic}	Ω cm^2	Ionic resistance
T_{Li+}	-	Lithium ion transference number
T_{Li-}	-	1 – Lithium ion transference number
t_{pulse}	s	GITT current pulse duration
t_{relax}	s	GITT relaxation period duration
ΔE_{ionic}	V	Instantaneous IR drop during GITT current pulse
ΔE_{relax}	V	Change in cell potential due to application of GITT current pulse
ΔG	kJ mol^{-1}	Gibbs free energy change
λ	cm	Thickness of discharged material in the composite electrode
λ_{MAX}	cm	Thickness of discharged material in the composite electrode when the concentration of salt is equal to 0
σ	S cm^{-1}	Conductivity

Table of Symbols

τ	s	Time constant
υ	$mV\ s^{-1}$	Sweep rate

Table of Abbreviations

Abbreviation	Meaning
A.U.	Arbitrary Units
CPE	Constant Phase Element
DMC	Dimethyl Carbonate
DoD	Degree of Discharge
DSC	Differential Scanning Calorimetry
EC	Ethylene Carbonate
EDX	Energy Dispersive X-ray spectroscopy
EMD	Electrodeposited Manganese Dioxide
GITT	Galvanostatic Intermittent Titration Technique
MCMB	Mesoporous Carbon Microbeads
MEMS	Micro Electomechanical Systems
OCV	Open Circuit Voltage
PAN	Poly(acrylonitrile)
PANI	Poly(aniline)
$PANI_{eb}$	Emeraldine base form of poly(aniline)
$PANI_{es}$	Emeraldine salt form of poly(aniline)
PC	Propylene Carbonate
PE	Poly(ethylene)
PPI	Pores per Inch
PvDF-HFP	Poly(vinylidene fluoride-co-hexafluoropropene)
RVC	Reticulated Vitreous Carbon
SCE	Saturated Calomel Electrode
SEI	Solid Electrolyte Interface
SEM	Scanning Electron Microscopy
SHE	Standard Hydrogen Electrode
SMSE	Saturated Mercury Sulphate Electrode
SS	Stainless Steel
TBAP	Tetrabutyl ammonium perchlorate
TGA	Thermograimetric Analysis

Table of Abbreviations

VC	Vitreous Carbon
XRD	X-ray Diffraction

Chapter 1

General introduction

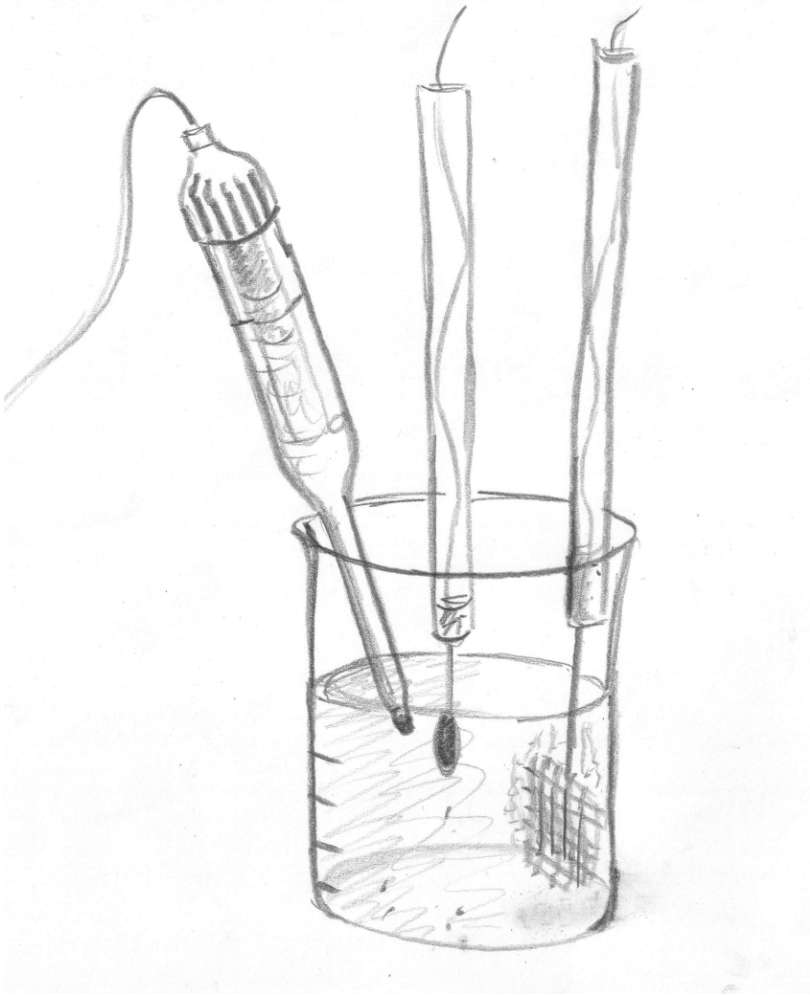

1.1. Opening Remarks

As portable sources of electrical power batteries play a major part in modern life; powering everyday objects such as torches or watches to all kinds of electronic device, such as mobile phones, laptops and even portable power tools. However, alongside providing power for electronic gadgetry, batteries are used for a multitude of other tasks. The uses of batteries contrasts from well established technology, such as the use of rechargeable lead acid batteries by the automotive industry, to rapidly emerging markets such as the numerous hybrid and electric cars currently entering production.

With increasing global emphasis on reducing CO_2 emissions leading to greater use of renewable energies the need to store this energy becomes increasingly important.

As much of the electricity produced by renewable sources, i.e. wind and solar, is on an intermittent basis the use of batteries to store this energy until needed may become an increasingly important application.

However, this work focuses on current issues at the smaller end of the energy storage scale. The pace of improvement in the power and energy performance of secondary battery technology has been far outstripped by the miniaturisation of portable electronics.

As a result there is an increasingly large amount of research being devoted to the miniaturisation of power sources, and particularly lithium-ion batteries [1-4].

1.2. Batteries

The purpose of a battery is to convert stored chemical energy directly into electrical energy by redox reaction [5-7]. The basic principles of the battery have not changed significantly since the invention of the 'voltaic pile' by Alessandro Volta in 1800. The term battery is used to describe a collection of one or more electrically connected electrochemical cells; each cell consists of two electrodes separated by an electrolyte. Figure 1.2a is an illustration of an electrochemical cell.

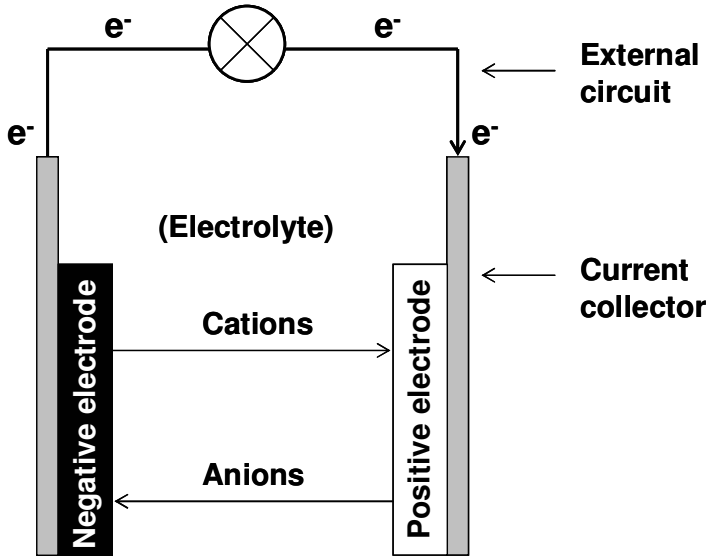

Figure 1.2a. Schematic of an electrochemical cell.

During discharge of the cell cations flow from the negative electrode (anode) to the positive electrode (cathode) through the electrolyte (ion conductive medium). During discharge the active material in the anode is oxidised, and the active material in the cathode reduced. Electrons flow through the external circuit, from the anode, toward the cathode. The difference between the electrode potentials of the anode and cathode results in the cell potential. Depending on the nature of the electrode reaction the battery can be classed as either primary (not rechargeable) or secondary (rechargeable).

In a primary battery system the oxidation of the anode and reduction of the cathode is irreversible. The zinc-air system [8-10] (used in hearing aids) is an example of a primary battery. The cathode usually consists of a porous polymer bound carbon electrode; the porosity allows atmospheric oxygen to diffuse to the reaction coordinate in a manor similar

to a fuel cell electrode. During discharge atmospheric oxygen is reduced at the cathode forming hydroxyl anions. Hydroxyl anions formed by the reduction of oxygen migrate to the zinc anode which is oxidised to $Zn(OH)_4^{2-}$ ($Zn(OH)_4^{2-}$ eventually decays to ZnO in the KOH electrolyte). The oxygen reduction and zinc oxidation gives rise to a flow of electrons through the external circuit from the anode to the cathode.

A good example of a rechargeable system is the lithium ion battery. In a typical lithium ion battery the oxidation and reduction of the anode and cathode occur in the form of intercalation of the lithium ion. As lithium batteries are the main focus of this research the lithium ion example is explained in greater detail in 1.4 and 1.5.

1.3. A Brief History of Secondary Battery Technology

The first secondary, or rechargeable, battery system was invented in 1859 by the French Physicist Gaston Planté [11]. The lead acid system basically consists of Pb and PbO_2 electrodes and (usually) a relatively concentrated (~1.8 g/cm^3) H_2SO_4 electrolyte [5, 11]. In the discharged state both electrodes are converted to $PbSO_4$, during charge the cathode (positive electrode) is transformed to PbO_2 and anode (negative electrode) to Pb. The discharge occurs with a nominal voltage of 2.1 V and achieves a specific energy of between 30-40 Wh kg^{-1} [8].

The next significant advance in secondary battery technology came in the form of nickel – cadmium batteries[12]. Invented in 1899 by Swedish scientist Waldmar Junger the nickel-cadmium system is based on Cd and Ni(OOH) electrodes and a KOH electrolyte[12]. The Cd anode and Ni(OOH) cathode become $Cd(OH_2)$ and $Ni(OH_2)$ during discharge , which occurs at a cell potential of 1.2V. The nickel – cadmium system showed significant improvements on the lead –acid system, including greater cycle life, higher specific energy (40-60 Wh kg^{-1}) and better low temperature performance.

The next step in rechargeable battery technology was the invention of the nickel metal hydride system [13-15]. Developed over two decades nickel metal hydride batteries became commercially available in the late 1980's. The nickel metal hydride system is similar to the nickel – cadmium system but with the Cd anode replaced by mixed metal alloy electrode. The cell voltage is 1.2 V, comparable to the nickel cadmium system, the specific energy is higher (60-80 Wh kg^{-1}) and the problems of toxicity associated with Cd are removed. A large downside of the nickel metal hydride system is the relatively high self discharge compared to nickel cadmium systems [16, 17]

Some recent improvements in nickel metal hydride technology have led to the developments of 'ready to use' cells with considerably less self discharge, such as the Sanyo Eneloop cell.

The most recent advance in secondary battery technology has been the creation of the rechargeable lithium-ion battery.

Research into lithium batteries began in the 1950's, lithium attracted considerable interest as an anode material because of its highly electronegative electrode potential (~ -3V *vs.* SHE) and high specific capacity (~4 Ah/g, ~7Ah/cm^3). The first commercial primary (non-rechargeable) lithium batteries were produced in the 1970's and were based on a lithium

metal anode, a non-aqueous electrolyte and a variety of cathode materials, including $(CF_x)_n$ CuO, MnO_2 and FeS [18-21].

Rechargeable lithium batteries were initially based on a lithium metal anode, a non-aqueous lithium-ion conducting electrolyte and a positive electrode able to undergo reversible reaction with lithium ions, a process is summarised by equation 1.3a.

$$x\,Li + A_zB_y \underset{\text{Charge}}{\overset{\text{Discharge}}{\rightleftharpoons}} Li_xA_zB_y \qquad \textbf{Equation 1.3a}$$

However, significant problems with passivation reactions at the surface of the lithium negative electrode, which reduced cycle life (the number of times the battery can be usefully charged and discharged), and with general safety concerns over the use of lithium metal as the anode led to the introduction of a commercial lithium ion or 'rocking chair' battery system.

The invention of the 'rocking chair' systems, which replaced the lithium metal electrode with a lithium insertion electrode, was generally accredited to Sony Energytec / Mobil energy in the early 1990's [22]. Figure 1.3a [23]compares the specific energy and energy density of a variety of secondary battery systems.

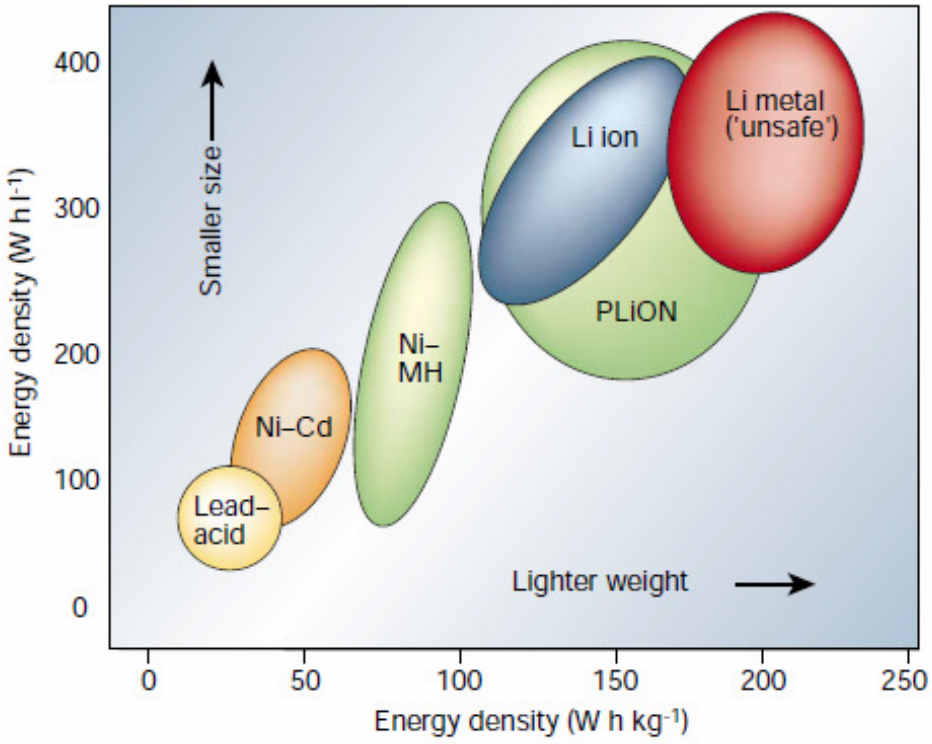

Figure 1.3a [23]. Specific energy and energy density for lead-acid, nickel cadmium, nickel metal hydride, lithium ion, lithium polymer (PLiON) and lithium metal secondary systems.

The increase in energy density between the oldest (lead-acid) and newest (lithium based) systems illustrates the drive to achieve smaller and lighter batteries to satisfy the energy requirements of ever shrinking electronic devices.

1.4. Lithium Ion Batteries

The basic operation of the 'rocking-chair' type lithium ion battery is outlined by Equation 1.4a and illustrated in Figure 1.4a. The 'rocking-chair' type battery is so called due to the movement of lithium ions from cathode to anode, and *vice-versa*.

$$Li_xC_nD_m + A_zB_y \underset{\text{Charge}}{\overset{\text{Discharge}}{\rightleftharpoons}} C_nD_m + Li_xA_zB_y \qquad \textbf{Equation 1.4a}$$

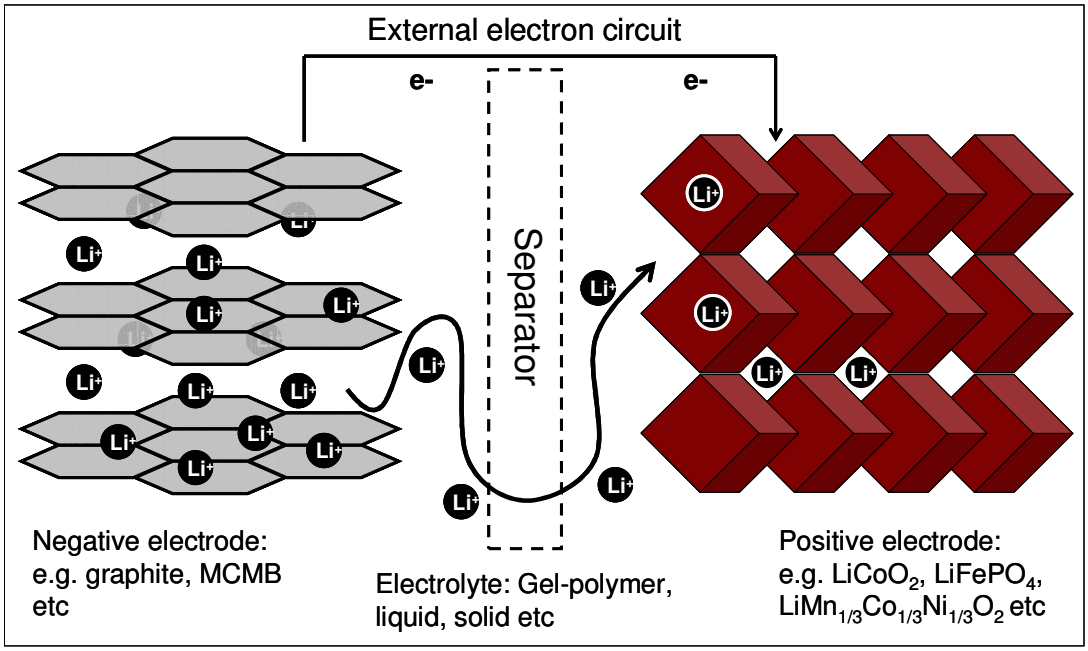

Figure 1.4a. Representation of a lithium ion battery; the black circles represent lithium ions moving from positive to negative electrode through an electrolyte and separator permeable to lithium ion migration.

The three basic components of the battery are the two lithium intercalation electrodes (cathode and anode) and the electrolyte. Generally speaking in conventional lithium ion batteries the anode consists of a graphite (or other carbon based material e.g. mesoporous carbon microbeads (MCMB)) slurry [24-27]applied to a metallic current collector foil (typically Cu foil).The composition of the slurry typically contains a small amount of binder to ensure the mechanical stability of the electrode film.

The use of graphite (and graphitic materials) as an anode material has been relatively consistent due to its potential *vs*. SHE, ~-2.5 V [24] compared to -3 V for Li, and its high

gravimetric capacity. The theoretical gravimetric capacity of graphitic carbon is 372 mA.h g^{-1}, according to a maximum stoichiometry of LiC_6 [25]; far greater than the useful capacity of most existing cathode materials. The major impetus to replace graphite as an anode material is due to adverse chemical reactions with non-aqueous electrolyte. Chemical reaction between the anode and electrolyte leads to SEI formation at the anode electrolyte interface and subsequently to an increased internal cell resistance [25].

$LiMn_2O_4$, $LiCoO_2$, $LiNiO_2$, $LiFePO_4$ and $LiMn_{1/3}Co_{1/3}Ni_{1/3}O_2$ are just a few active materials that have been used as cathode materials in lithium ion batteries [28-31]. As with the anode these materials are incorporated into an composite electrode slurry deposited onto a metallic current collector (usually Al foil).

The composition of the cathode slurry usually contains a relatively high (5-10%) percentage of conductive additive, such as acetylene black, to improve electronic conduction through the electrode and a binder to improve mechanical stability.

Unlike the anode material the electrode potentials of most cathodes is between 0-1 V *vs*. SHE, giving a cell voltage of between 3-4 V when pared with a graphite anode.

The gravimetric capacity of the cathode is typically less than for a graphite anode, with most materials exhibiting capacities within the range of 150-180 mA.h g^{-1} [23, 28-31].

The purpose of the electrolyte is two fold; to facilitate the migration / diffusion of lithium ions between the cathode and the anode whilst blocking the direct flow of electrons, ensuring electron transport occurs through the external circuit

The composition of the electrolyte varies with the type of lithium battery, i.e. lithium ion batteries use a liquid electrolyte [32, 33] and solid state batteries use a solid ceramic electrolyte. Taking the example of the lithium polymer battery the electrolyte used is typically PVdF-HFP swollen with $LiPF_6$ (or similar lithium salt) dissolved in EC:DMC (1:1) [33-35]. The use of an electrolyte contained within a polymer, a gel polymer electrolyte, overcame some safety issues related to leakage of liquid electrolyte. In a cell containing a liquid electrolyte an electronically insulating separator is required to prevent direct short circuit between cathode and anode [32, 33].

1.5. Characteristics of Electrochemical Charge and Discharge in Lithium-Ion Batteries

1.5.1. Gibbs Free Energy and Cell Potential

During charge or discharge of an electrochemical cell redox reactions occur at both the cathode (positive electrode) and anode (negative electrode). As with any chemical reaction there is a free energy change associated with the redox reactions as the 'reactant' is oxidised / reduced to form the 'product'. This free energy change is known as the Gibbs free energy (ΔG) and is related to the equilibrium cell potential by Equation 1.5.1a [36, 37].

$$\Delta G = -nFE \qquad \textbf{Equation 1.5.1a}$$

(Where ΔG denotes change in Gibbs free energy ($Jmol^{-1}$), F is faradays constant (C/mol^{-1}), n represents number of electrons and E is the equilibrium cell potential (V).

Depending on the nature of the materials within the battery the charge / discharge potential will either be constant or will vary. In the case where the charge / discharge potential of a particular material is constant, the material is said to exhibit two-phase behaviour. In other materials the potential varies throughout the charge / discharge, known as single-phase behaviour. Examples of two-phase and single-phase behaviour in lithium-ion battery materials are shown below.

The active material $LiFePO_4$ exhibits two-phase behaviour; for the majority of charge / discharge the material exists in one of two stoichiometries, $FePO_4$ (charged) and $LiFePO_4$ (discharged). Because the material only exists in the above states ΔG for the reaction is constant, and therefore the cell potential is constant (Equation 1.5.1a).The charge / discharge behaviour of $LiCoO_2$ is single-phase; rather than being in a charged or discharged state the stoichiometry varies as $Li_{1-x}CoO_2$, where $0 < x < 0.5$. As a result ΔG for the reaction varies continually, as does the cell potential (Equation 1.5.1a). The end result is a charge or discharge profile that varies between 4.3 and 3.5 V *vs.* Li [38, 39]. 1.5.4 explains one and two phase behaviour in greater detail.

1.5.2. Cell Capacity

One of the most defining features of a cell is its capacity, i.e. how much charge it can store (capacity), and in the case of a secondary battery, reversibly store.
The capacity of a battery material is normally defined by its gravimetric or specific capacity, and usually given units of mA.h g^{-1}.
The cell capacity of a given material can be estimated from its theoretical capacity; an example calculation of theoretical capacity for $LiFePO_4$ is shown below.
Equation 1.5.2 shows the discharge reaction for a $LiFePO_4$ electrode.

$$\mathbf{FePO_4 + Li^+ + e^- \rightarrow LiFePO_4} \qquad \textbf{Equation 1.5.2a}$$

During discharge 1 mole of lithium is intercalated into 1 mole of $FePO_4$ resulting in the flow of 1 mole of electrons through the external circuit. Faradays constant relates the number of electrons to the charge passed by Equation 1.5.2b.

$$Q = nF \qquad \textbf{Equation 1.5.2b}$$

(Where Q (C) denotes charge passed, n is the number of electrons and F is Faradays constant (C mol^{-1})). The theoretical capacity is obtained by dividing the charge passed by the molecular mass of the discharged product, Equation 1.5.2c.

$$Q^0 = \frac{nF}{M_M} \qquad \textbf{Equation 1.5.2c}$$

(Where Q^0 denotes theoretical capacity (C g^{-1}), n is number of electrons, F is Faradays constant (C mol^{-1}) and M_M is molecular mass.
Applying Equation 1.5.2c to the $LiFePO_4$ case gives a theoretical capacity in units of coulombs per gram (C g^{-1}). Converting the theoretical capacity from C g^{-1} to mAh.g^{-1} (a more common measure of capacity) involves a simple conversion of charge in C (A.s) to mA.h.

The theoretical capacity of a battery material may also be measured against its volume; the resulting measure being known as the volumetric capacity (mA.h cm^{-3}), a more suitable measure of capacity for applications where space is the prime consideration.

1.5.3. Rate Capability

The rate capability of a lithium-ion cell can be measured by charging / discharging at varying C-rate, the C-rate is defined by the time of charge / discharge, and therefore the charge / discharge current, according to Equations 1.5.3a and b. In order to determine the current needed at a particular C-rate, it is first necessary to calculate the capacity of the electrode (Q), as in Equation 1.5.3a.

$$Q = El_m \times Q^0 \qquad \textbf{Equation 1.5.3a}$$

(Where Q is electrode capacity (mAh), El_m denotes electrodes mass (g) (in particular it denotes mass of active material within the electrode) and Q^0 is the theoretical gravimetric capacity (mA.h g^{-1}).

Theoretically at a C rate of 1C the current applied should effect a full charge or discharge in 1 hour, and at 2C the current applied should lead to charge or discharge in 30 minutes. At C rates < 1, i.e. C / 5, the current applied should bring about a charge or discharge in 5 hours.
The current needed to achieve a particular C-rate can be calculated from Equation 1.5.3b.

$$i = f \times Q \qquad \textbf{Equation 1.5.3b}$$

(Where i denotes current (A), f is C-rate (h^{-1}), and Q is electrode capacity (mA.h))

1.5.4. One and Two Phase Behaviour.

As discussed briefly in 1.5.2 the charge or discharge mechanism of a lithium ion battery material can be described as being either one or two phase. The origin of whether a material is considered one or two phase is in the particular mechanism of charge or discharge.

In a two phase material, i.e. $LiFePO_4$, the reactants and reaction products of the charge / discharge reaction are stoichiometric (they can only be in one of two phases), as illustrated by Equation 1.5.4a.

$$\mathbf{Li_{(S)} + FePO_{4\,(S)}} \underset{\text{Charge}}{\overset{\text{Discharge}}{\rightleftharpoons}} \mathbf{LiFePO_{4\,(S)}} \qquad \textbf{Equation 1.5.4a}$$

Because the reactants and reaction products are stoichiometric, that the insertion of one lithium ion leads to the formation of one molecule of $LiFePO_4$, then the ΔG for the reaction, and therefore the equilibrium reaction potential E, are constant (Equation 1.5.1a).

In a one phase reaction the charge / discharge mechanism proceeds non-stoichiometrically. In the charge / discharge a of Li_xCoO_2 electrode (a one phase material) there is effectively a solid solution of Li ions within the CoO_2 (Equation 1.5.4b).

$$\mathbf{\delta Li_{(S)} + Li_xCoO_{2\,(S)}} \underset{\text{Charge}}{\overset{\text{Discharge}}{\rightleftharpoons}} \mathbf{Li_{x+\delta}CoO_{2\,(S)}} \qquad \textbf{Equation 1.5.4a}$$

The charge / discharge can be thought of as proceeding by an infinite number of individual reactions differing by δLi and x in Li_xCoO_2. As such each of these reactions has a different ΔG, and therefore a different E, and the charge discharge occurs over a voltage range rather than at one potential.

Chapter 2

Experimental Methods

2.1. Fabrication of Composite Electrode Pellets

In order to perform electrochemical testing and characterisation of active material powders it was necessary to incorporate them into composite electrode pellets. The composite electrode pellet comprised of three components; an active material powder, an electronically conducting medium and an inert binder. The active material powder is the electrochemically active component (providing the faradaic capacity) of the composite. An electronically conductive medium was also included in the electrode to facilitate the path of electrons from the active material particles within the composite electrode to the current collector, or vice-versa, (especially important in the case where the active material showed poor electronic conductivity). Typically this material was a type of carbon, and in the majority of this work was a type of acetylene black (Shawinigan Black 100% compressed, Chevron Philips chemical company). The final component in the composite electrode was the binder, an inert material that acted as a matrix to hold the active material and acetylene black together. Poly(tetrafluoroethylene) (PTFE) powder (type 6C-N, DuPont) was generally used as the binder in this work.

The method of preparing the composite electrode pellets involved the mixing and grinding of the three components, active material, acetylene black, and PTFE binder (typically in the weight ratios 75:20:5). The active material powder was mixed with the acetylene black using a pestle and mortar (and in some cases the mixture was subsequently ball milled). The binder was gradually ground into this mixture until it formed a thick felt like film. This film was then placed between two nickel foils and rolled to a specific thickness using a Durston 100mm rolling mill (electrode thickness was measured using a mechanical micrometer ($^{+}/_{-}$ 2 µm)).
Figure 2.1a shows an overview of the composite electrode fabrication process.
Once cut the composite electrode pellets were weighed and the thickness measured by micrometer. They were then dried under vacuum at 120 °C for 12 hours and transferred to an argon filled glove box (<0.1% H_2O,O_2; Unilab from MBraun).

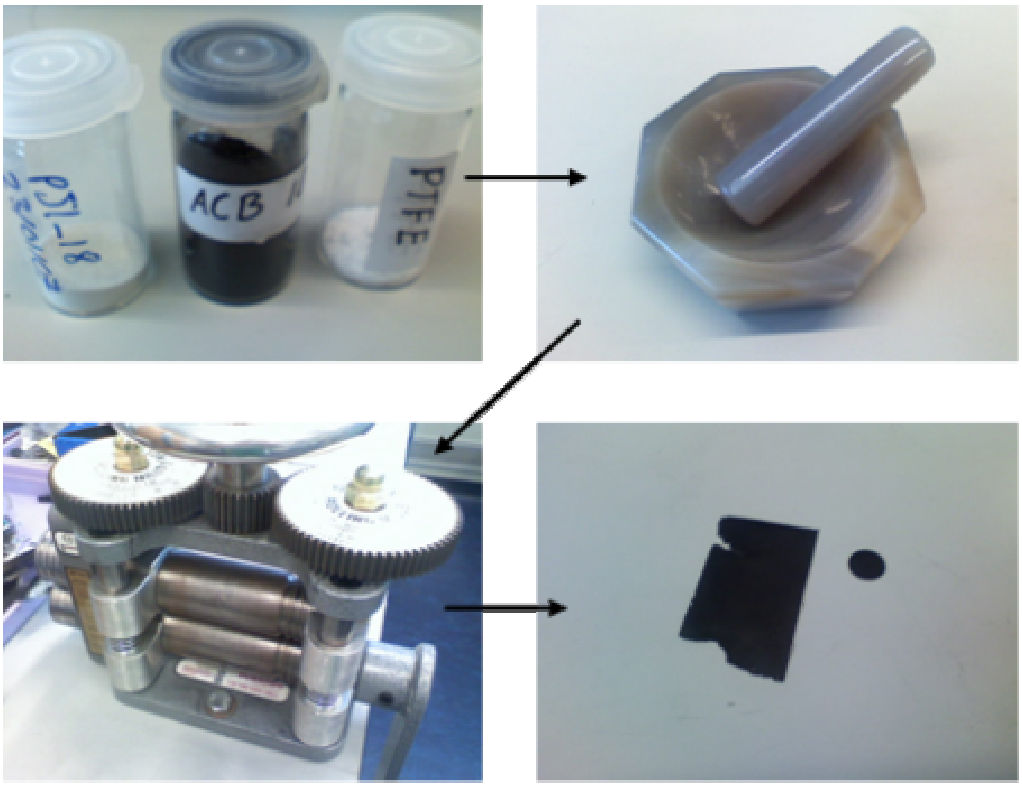

Figure 2.1a. Overview of composite electrode fabrication process, pellets were cut from the rolled composite electrode films (bottom left).

2.2. Electrochemical Cell Assembly

2.2.1 Composite Electrode Pellets

The electrochemical characterisation of composite electrode pellets was performed using stainless steel two electrode test cells, see Figure 2.2.1a.

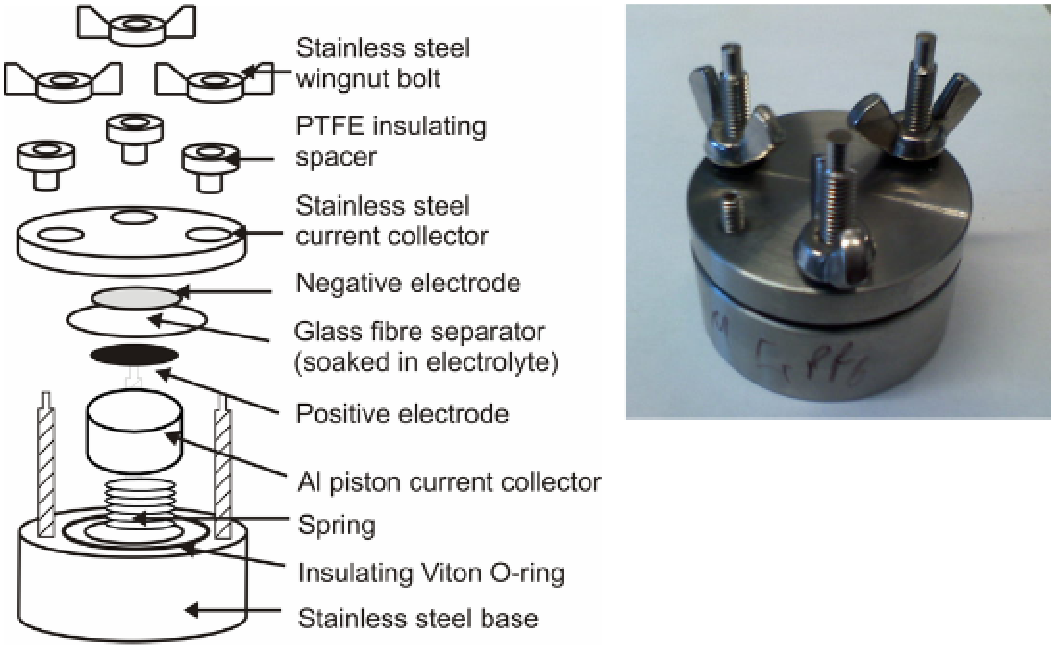

Figure 2.2.1a. Schematic of two electrode electrochemical cell (left). Image of assembled cell (right).

Cells (Figure 2.2.1a) were assembled inside an argon filled glove box, once assembled and sealed they were removed for electrochemical testing.

The two electrodes (the working electrode and a suitable counter / reference electrode) were inserted into the electrochemical cell and separated by a glass fibre separator, which in turn is soaked in a lithium battery electrolyte (unless otherwise specified 1M $LiPF_6$ in ethylene carbonate and dimethylene carbonate (EC:DMC) 1:1 by weight). The cell was sealed using a Viton® rubber O-ring (which also insulates the lid from the base). The electrodes were kept in contact with the current collectors through the force exerted by the spring (Figure 2.2.1a).

2.2.2. Electrochemical Cell Assembly (Other Electrode Formats)

The style of cell for testing unconventional electrodes (i.e. not composite pellets) was similar to the cell used in 2.2.1. However for foam type electrode testing a smaller spring, that exerted less pressure, was used to avoid crushing the electrode

2.3. Electrochemical Characterisation

2.3.1. Galvanostatic Cycling

Galvanostatic (constant current) cycling was generally performed using a VMP 2 (Bio-Logic) potentiostat / galvanostat in water jacketed compartments set to a temperature of 25°C. Experiments were controlled by either cycling between set potential limits or by limiting the time of charge and discharge.

2.3.2. AC Impedance Spectroscopy

AC impedance spectroscopy measurements were carried out using either a VMP2 (Bio-Logic) potentiostat / galvanostat or a Solatron 1250 (Solatron Analytical) frequency response analyser. Unless otherwise stated measurements were made using 10 points per decade and by taking an average of 3 measurements per frequency. The frequency range used for the majority of experiments in this work was 200,000–0.1 Hz.

2.3.3. Cyclic Voltammetry (CV)

Cyclic voltammetry measurements were performed using either a Solatron 1287 (Solatron Analytical) or VMP 2 (Bio-Logic) potentiostat / galvanostat.
The CV experiment involved sweeping the potential between two pre-designated potential limits at a constant sweep rate (ν, mV s^{-1}) for a number of cycles. The current was recorded as a function of applied potential.

2.3.4. Galvanostatic Intermittent Titration Technique (GITT)

The galvanostatic intermittent titration technique (GITT) was used in the determination and differentiation of ionic and electronic resistance in electrodeposited polymer electrolytes, Chapter 7. The GITT technique involved the application of a short current pulse, followed by a longer open circuit relaxation period. The pattern of current pulse and relaxation was repeated multiple times. In the case of a battery the current pulses effected a

small charge or discharge depending on the polarity of the current; the magnitude of which was dependant on the applied current and the duration of the pulse.

2.4. Physical Characterisation Techniques

2.4.1. SEM Characterisation

SEM characterisation was achieved using a Philips XL30 ESEM. In most cases images were recorded in high vacuum operation using the secondary electron detectors.

2.4.2. XRD Characterization

General powder XRD measurements were collected using a Bruker D5000 diffractometer. In most cases patterns were recorded between 2θ values of 10 and 70° using a $CuK_{\alpha 1}$ radiation.

XRD experiments, described in Chapter 6, used a Bruker D8 diffractometer with furnace attachment. A series of XRD patterns were recorded at intervals of 100 °C between room temperature and 1000 °C. The heating rate used was 1 °C min^{-1}, at each temperature increment the sample was left to equilibrate for 3 h before measurement. X-ray patterns were collected over 5 h between the 2θ values of 10 and 70° using a $CuK_{\alpha 1}$ radiation.

2.4.3. TGA-DSC Analysis

TGA and DSC traces were recorded using a Polymer Laboratories STA 1500 simultaneous thermogravimetric analysis system. Experiments were performed between room temperature and 800 °C at a heating rate of 1 °C min^{-1}.

Chapter 3

Thickness Effect and Rate Limitations in $LiFePO_4$ Composite Electrodes

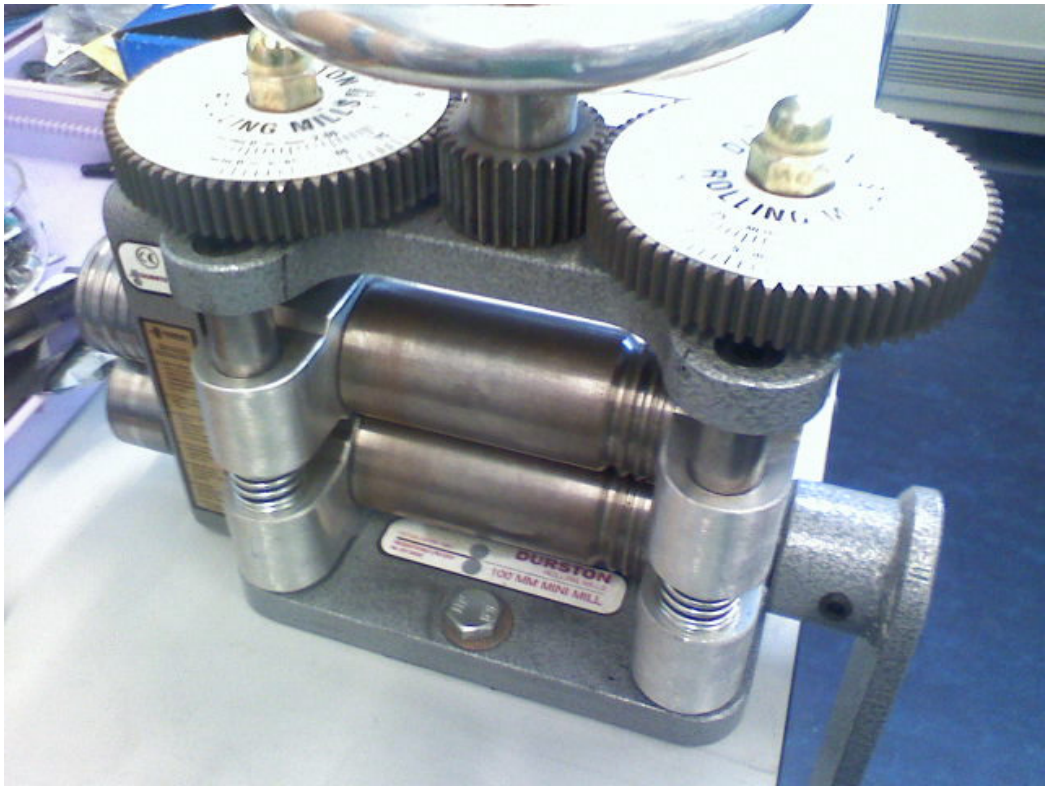

3.1. Introduction

3.1.1. $LiFePO_4$

$LiFePO_4$ was first suggested as a cathode material for lithium battery applications by the research group of Goodenough at the University of Austin at Texas in 1997 [40]. $LiFePO_4$ was touted as being a low cost, environmentally friendly and non-toxic alternative to lithium-ion battery materials of the time, e.g. $LiCoO_2$. Although the energy density of $LiFePO_4$ based cells would be lower than comparable $LiCoO_2$ cells, due to the lower discharge potential, the relatively high theoretical gravimetric capacity of $LiFePO_4$ and better cycling stability (than $LiCoO_2$) meant $LiFePO_4$ attracted considerable interest as a cathode material [40-44]. Initially performance of $LiFePO_4$ was limited by slow solid state diffusion within the $LiFePO_4$ particle and low intraparticle electronic conductivity [40, 45]. The performance of $LiFePO_4$ has since been significantly improved by carbon coating the active material [46] and by decreasing particle size [44, 47].

The rate capability of $LiFePO_4$ electrodes is a topic that has received much recent attention [48-50]. The nature of the rate limitations within composite electrodes of $LiFePO_4$ is complicated and is probably dependant on a number of factors.
Initially the slow charge / discharge kinetics of $LiFePO_4$ were attributed to the poor electronic conductivity, which resists inter-particle and intra particle electron transport [41]. Much work has concentrated on improvement of the poor electronic conductivity by coating the bulk material in an electronically conductive medium (in most cases carbon) [45, 46, 51, 52].

Gaberscek et al. suggested that high rate capability in a composite electrode is also strongly dependent on the resistance of the ionic and electronic intra particle contacts, or ‘wiring’ [53], and therefore responds to a decrease in the electrode thickness. Electron transfer between particles and the electronic conduction network has been improved with carbon coating [43, 54, 55]. Long range electron and ion transport have been improved by careful control of the composition and structure of the composite electrode [56] which supports the active material with carbon black and a binder, leaving some open porosity for admission of some electrolyte.

Work presented in this chapter suggests the presence of another rate limiting effect, salt diffusion in the composite electrode. The salt diffusion is influenced by the lithium ion transference number T_{Li+} [54].

The lithium ion transference number (T_{Li+}) is defined by the number of moles of lithium-containing species transported into the cathode by migration alone during the passage of one Coulomb of charge and is typically 0.4 for a lithium ion system [57].

Its compliment T_{Li-} ($1 - T_{Li+}$) is defined by the number of moles of lithium that cannot take part in the electrode reaction until they have reached the active particle surfaces by diffusion (rather than by migration). T_{Li-} is typically 0.6 in a lithium battery [49].

The aim of this work is to assess the significance of restricted lithium salt diffusion in composite $LiFePO_4$ electrodes, compared to the effect of solid state diffusion and $LiFePO_4$ particle size. The Sharp Discharge Front (SDF) model is presented as a simple working model for the rate limitation in composite electrodes due to salt diffusion.

3.1.2. The Sharp Discharge Front (SDF) Model

Macrocrystalline $LiFePO_4$ (grain size >100 nm), as studied in this work, has a flat discharge profile due to the co-existence of two phases during discharge. The SDF model has been developed to investigate the effect of restricted lithium salt diffusion on discharge of $LiFePO_4$ composite electrodes.

The SDF model assumes that individual $LiFePO_4$ particles are either fully charged or discharged, interfacial and solid state restrictions are absent, and therefore the electrolyte resistance is the major restriction, at least initially. Current should flow into the particles nearest the separator until they are completely discharged. Subsequently a layer of discharged material should proceed (from the separator / electrode interface towards the electrode / current collector interface) deeper into the electrode, while the potential drop to the nearest undischarged material increases, producing a linear galvanostatic discharge profile as in Figure 3.1.2a(a). In reality, discharge curves of $FePO_4$ do not resemble Figure 3.1.2a(a). Following a small increase in the IR drop, the criterion for discharge is a precipitously steep decline in potential as shown in Figure 3.1.2a(b).

The ‘‘shrinking core” [58] and other solid state models [59] explain this by saturation of the Li_{1-x} $FePO_4$ phase at the electrode/electrolyte interface. We explain the phenomenon by a lithium salt deficiency due to a non-unity transference number according to the sharp discharge front (SDF) model shown in Figure 3.1.2b.

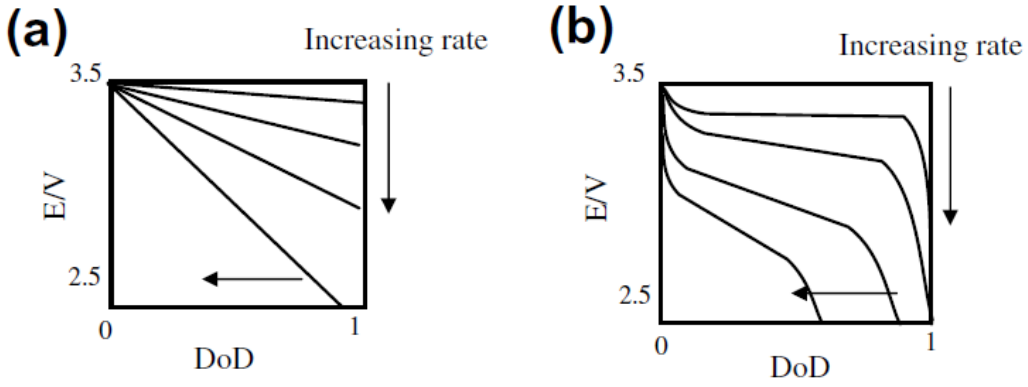

Figure 3.1.2a. Schematic plots of potential *vs*. DoD (Degree of discharge) in $FePO_4$ during galvanostatic discharges at increasing rates. As predicted by resistance limitation only (a) and as observed (b).

The SDF model incorporates the transference number (T_{Li+}) in a similar way to the simulations of West et al.[60] then Fuller et al. [61] but makes use of the following approximations.

- The existence of a sharp planar boundary between charged and discharged material perpendicular to the current direction within the composite electrode (Figure 3.1.2b)

- The initial concentration of lithium salt ([LiX]) within the composite electrode is negligible when compared to the total lithium demand during discharge.

- The concentration of lithium salt within the separator ($[LiX]_0$) is constant, it is effectively a 'bulk' concentration.

- The value of the lithium ion diffusion coefficient (D) and the lithium transference number (T_{Li+}) do not change.

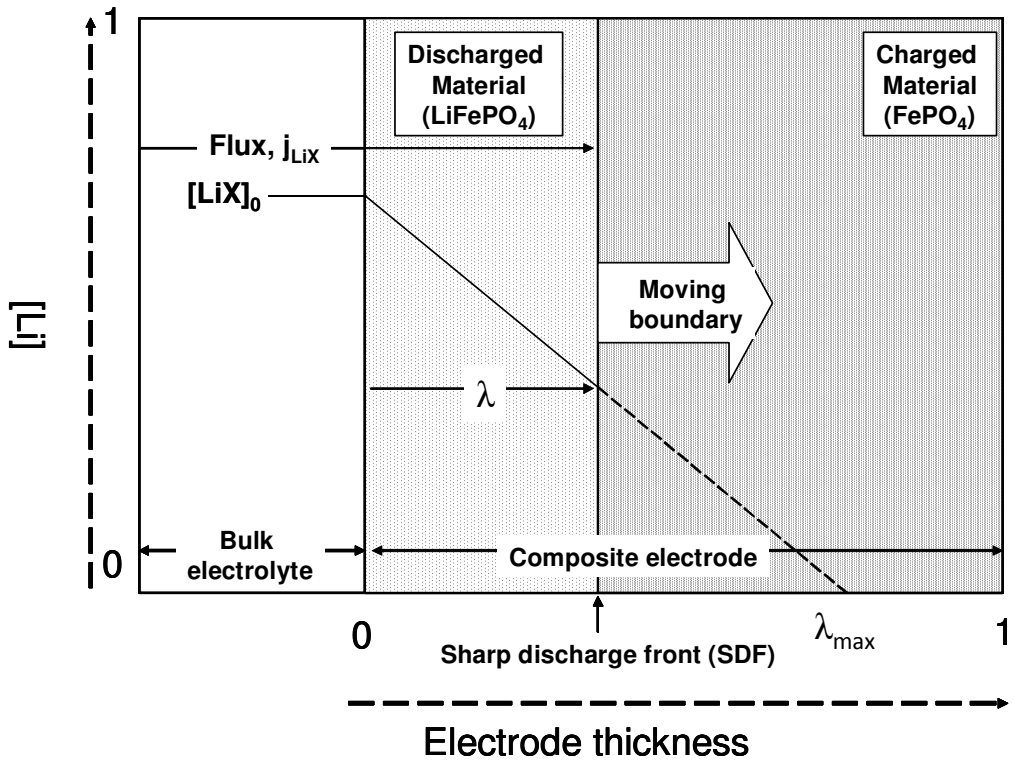

Figure 3.1.2b. SDF model showing sharp discharge front moving through depth of composite electrode structure. Where λ is the thickness of discharged material and λ_{max} is the point at which the concentration of Li salt in the composite reaches 0 i.e. premature end of discharge.

The SDF model applies under conditions where migration alone is not sufficient to ensure full charge or discharge of the cell, e.g. high rate. The SDF model, Figure 3.1.2b, makes use of the following diffusion equations.

$$J_{LiX} = \left(\frac{jT_{Li-}}{F}\right) = -D\left(\frac{d[LiX]}{dx}\right) \qquad \textbf{Equation 3.1.2a}$$

$$\left(\frac{d[LiX]}{dx}\right) = -\left(\frac{jT_{Li-}}{FD}\right) \text{ and } [LiX]_1 = [LiX]_0 + \lambda\left(\frac{d[LiX]}{dx}\right) \qquad \textbf{Equation 3.1.2b}$$

Where $[LiX]_1$ is the salt concentration at the discharge front, $[LiX]_0$ is the salt concentration in the separator, [LiX] is the initial salt concentration within the composite electrode, λ is the thickness of discharged material, j denotes current density, J is the flux of salt in the electrolyte and D is the lithium salt diffusion coefficient..

Premature discharge of the $LiFePO_4$ occurs when the concentration of lithium salt ($[LiX]_1$) in the composite electrode reaches 0, $\lambda = \lambda_{max}$.

$$\lambda_{\max} = -\frac{[LiX]_0}{\left(\frac{d[LiX]_1}{dx}\right)} = \frac{FD[LiX]_0}{(T_{Li-})j} \qquad \textbf{Equation 3.1.2c}$$

The degree of discharge (DoD) depends upon the current density j according to Equation 3.1.2d.

$$DoD = \frac{\text{charge}\,(\mathrm{Q})}{\text{theoretical charge}\,(\mathrm{Q}^0)} = \frac{\lambda_{\max}}{L} = \frac{FD[LiX]_0}{(T_{Li-})jL} \qquad \textbf{Equation 3.1.2d}$$

Where L corresponds to the thickness of the composite electrode.

The C-rate (*f*) (1.5.3) can be defined as the ratio of the current to the theoretical charge capacity, or

$$f = \frac{j}{Q_A^0} = \frac{j}{Q_V^0 L} = \frac{j}{[Li]FL}$$ **Equation 3.1.2e**

Q^0_A and Q^0_V denote theoretical charge per area and volume respectively, f corresponds to C-rate and [Li] is the molar demand for lithium in the charged active material per unit volume of composite.

The culmination of Equations 3.1.2a, b, c, d and e lead to the final equation that defines the SDF model, Equation T.1.2f.

$$DoD.f = \frac{D}{L^2} \times \frac{[LiX]_0}{(T_{Li-})[Li]}$$ **Equation 3.1.2f**

3.2. Experimental

3.2.1. Composite Electrode Fabrication

Mixtures of $LiFePO_4$, (Hydro Quebec, carbon coated or Aldrich 99.5+ % carbon coated, battery grade) acetylene black (Shawinigan Black 100% compressed, Chevron Philips chemical company) and PTFE (type 6C-N, DuPont) were fabricated into composite electrode pellets of varying thickness using the process summarised in section 2.1. Electrode thickness ranged from 40 - 200 µm in 20 µm increments.

3.2.2. Electrochemical Testing of Composite Electrodes

The varying thickness $LiFePO_4$ composite electrodes were tested electrochemically as half cells *vs*. lithium. The electrodes were assembled into half cells as described in 2.2.1. The cells containing the differing thickness electrodes were cycled galvanostatically (Chapter 2.3.1) between 4 and 2.5 V *vs*. Li at a variety of C-rates (C/10, C/5, C/2, C, 2C, 5C, 10C, 20C, 25C, 30C, 35C, 40C, 45C and 50C) in order to asses their discharge capability at higher rates. To ensure the capacities of faster rate discharges were not affected by incomplete charging due to large charging rates the rate of charge was kept constant at C/5.

3.2.3. $LiFePO_4$ 'Microelectrode Cell' Fabrication

The $LiFePO_4$ 'microelectrode' type cell was based around a narrow cavity drilled into a polyethylene (PE) housing filled with $LiFePO_4$ composite electrode material (75%, Hydro Quebec $LiFePO_4$) acetylene black (20%, Shawinigan Black 100% compressed, Chevron Philips chemical company) and PTFE binder (5%, type 6C-N, DuPont).
The cell schematic is shown in Figure 3.2.3a and Figure 3.2.3b shows an optical microscopy image of the 'microelectrode' surface and defines the dimensions of the cavity.

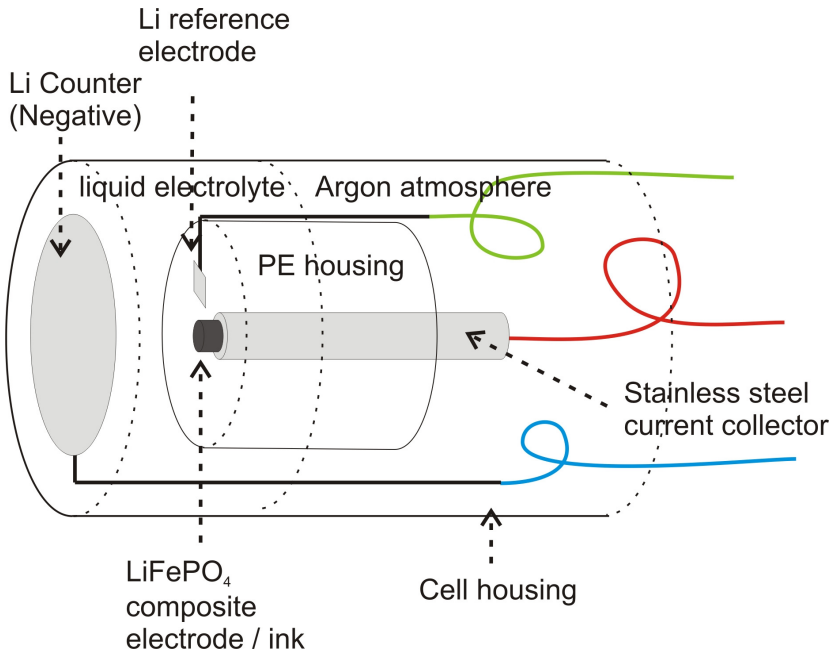

Figure 3.2.3a. Schematic of $LiFePO_4$ 'microelectrode' cell construction. The PE housing, $LiFePO_4$ 'microelectrode' and reference electrode assembly were suspended in liquid electrolyte within the argon filled cell housing. The counter electrode was positioned to maximise distance between counter and working electrodes.

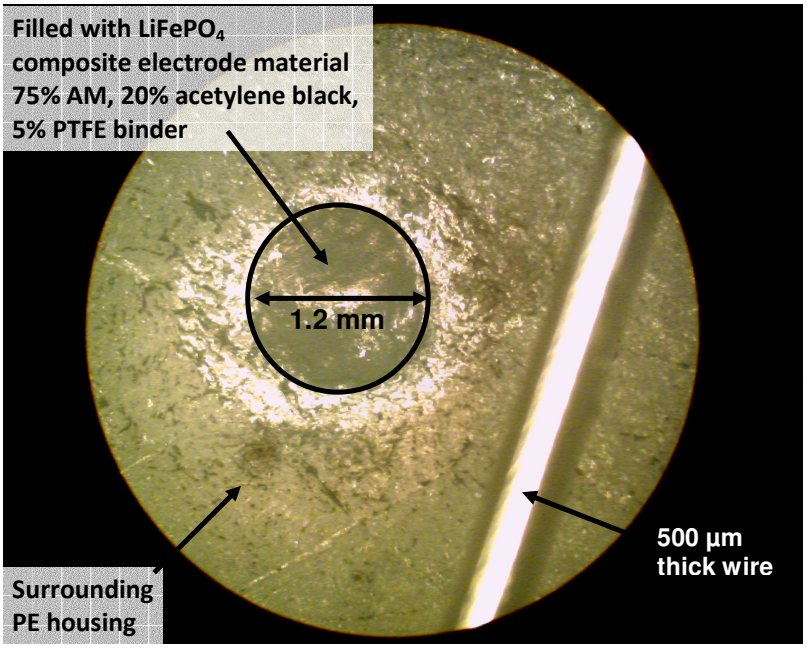

Figure 3.2.3b. Optical microscope image of $LiFePO_4$ 'microelectrode' surface highlighting cavity area.

The 'microelectrode' cavity was drilled into the polyethylene housing to a depth of ~ 0.5 mm. The diameter of the cavity was ~ 1.2 mm. $LiFePO_4$ composite electrode material was compacted into the cavity using a 1.2 mm diameter stainless steel rod in order to ensure good contact with the current collector at the rear of the cavity. The 'microelectrode', housing and reference electrode assembly was suspended in 1M $LiPF_6$ EC/DMC (1:1) electrolyte, the Li foil counter electrode was positioned as to maximise the distance between the counter and working electrodes. The reference electrode was positioned as close to the $LiFePO_4$ electrode as possible in order to minimise IR drop during charge / discharge. The 'microelectrode' / reference electrode assembly, counter electrode and electrolyte were sealed within the argon filled cell.

3.3. Results and Discussion

3.3.1. Galvanostatic Cycling Behaviour of $LiFePO_4$ Composite Electrodes

The $LiFePO_4$ | 1M $LiPF_6$ in EC:DMC (1:1) | Li cells containing the different thickness composite electrodes were cycled galvanostatically (3.2.2). The lithium insertion / extraction behaviour of the $LiFePO_4$ electrodes is illustrated in Figure 3.3.1a which shows the potential *vs*. capacity response to galvanostatic current.

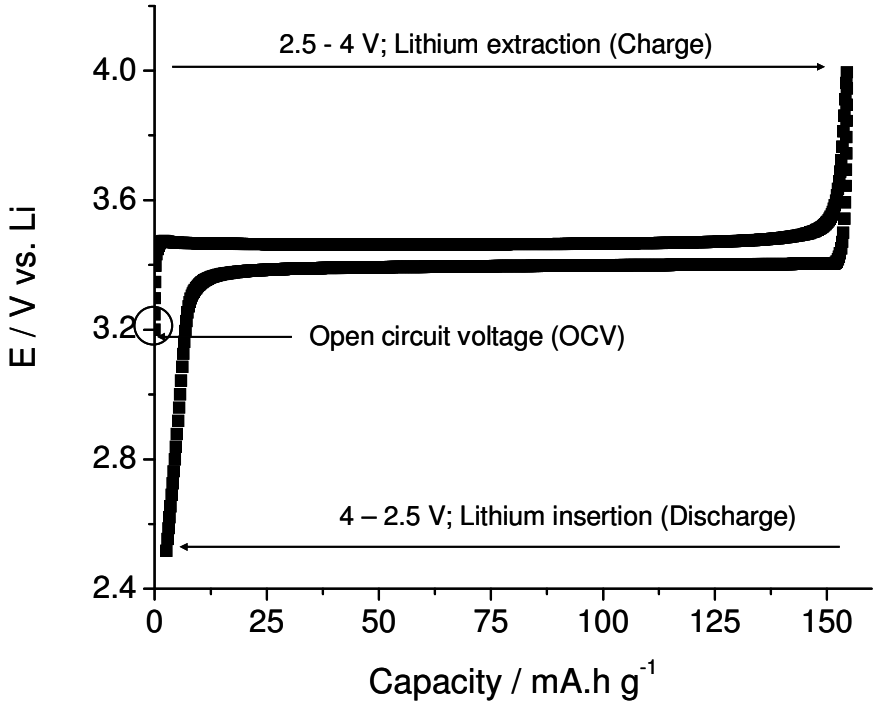

Figure 3.3.1a. Example charge and discharge curves for $LiFePO_4$ composite electrodes in $LiFePO_4$ | 1M $LiPF_6$ EC:DMC (1:1) | Li cells. This particular plot shows data for slow cycling (C/ 10) of a 100 µm thick $LiFePO_4$ electrode.

In most cases the open circuit voltage of the 'as assembled' $LiFePO_4$ cells was around 3.2 V *vs*. Li. Upon charging lithium is removed from the $LiFePO_4$ to form $FePO_4$; the example charge data shown in Figure 3.3.1a proceeds from OCV (~3.2 V *vs*. Li) to 4 V giving a gravimetric capacity of ~ 150 mA.h g^{-1} (around 20 mA.h g^{-1} less than the theoretical capacity of 169.8 mA.h g^{-1} according to the extraction of one mole of lithium per mole of $LiFePO_4$). For the majority of the charge, 10-145 $mAhg^{-1}$, the $LiFePO_4$

exhibits two phase behaviour (Chapter 1.5.4) giving rise to a plateau in potential at 3.5 V *vs*. Li.

Upon discharge lithium is inserted to the $FePO_4$ to give $LiFePO_4$, discharge proceeds at a lower potential than charge (~3.4 V *vs*. Li) though it exhibits the same two phase behaviour and shows a similar gravimetric capacity. Although the majority of the charge and discharge shows two phase behaviour there is a small portion (~5 %) that exhibits one phase characteristics [58, 62, 63].

3.3.2. Composite Electrode Thickness Effect

The effect of composite electrode thickness on discharge rate capability of $LiFePO_4$ (Hydro Quebec, particle size < 1 µm) | 1M $LiPF_6$ in EC:DMC (1:1) | Li cells was investigated using galvanostatic cycling at increasing C-rates.
Cells containing 40, 60, 80, 100, 120, 140, 160, 180 and 200 µm $LiFePO_4$ composite electrodes were fabricated and cycled galvanostatically at C/10, C/5, C/2, C, 2C, 5C, 10C, 20C, 25C, 30C, 35C, 40C, 45C and 50C for three cycles at each rate. Initially the thickness and weight of the composite electrodes was measured; the results are shown in Figure 3.3.2a.

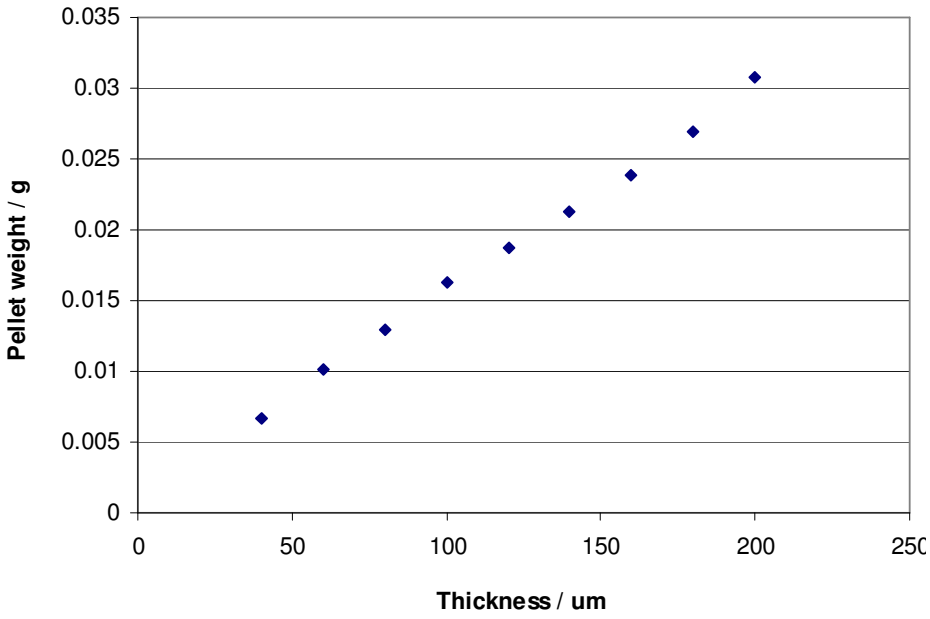

Figure 3.3.2a. Composite electrode weight as a function of thickness.

The linear relationship between the weight of the composite electrode and its thickness, shown in Figure 3.3.2a, demonstrated good control of density, and therefore mass loading, over the electrode thickness range (40-200µm).

The discharge profiles and rate capability of the $LiFePO_4$ | 1M $LiPF_6$ in EC:DMC (1:1) | Li cells containing differing thickness $LiFePO_4$ composite electrodes are summarised in Figures 3.3.2b, d, and e which show discharge at three example C-rates (0.2, 2 and 5 C).

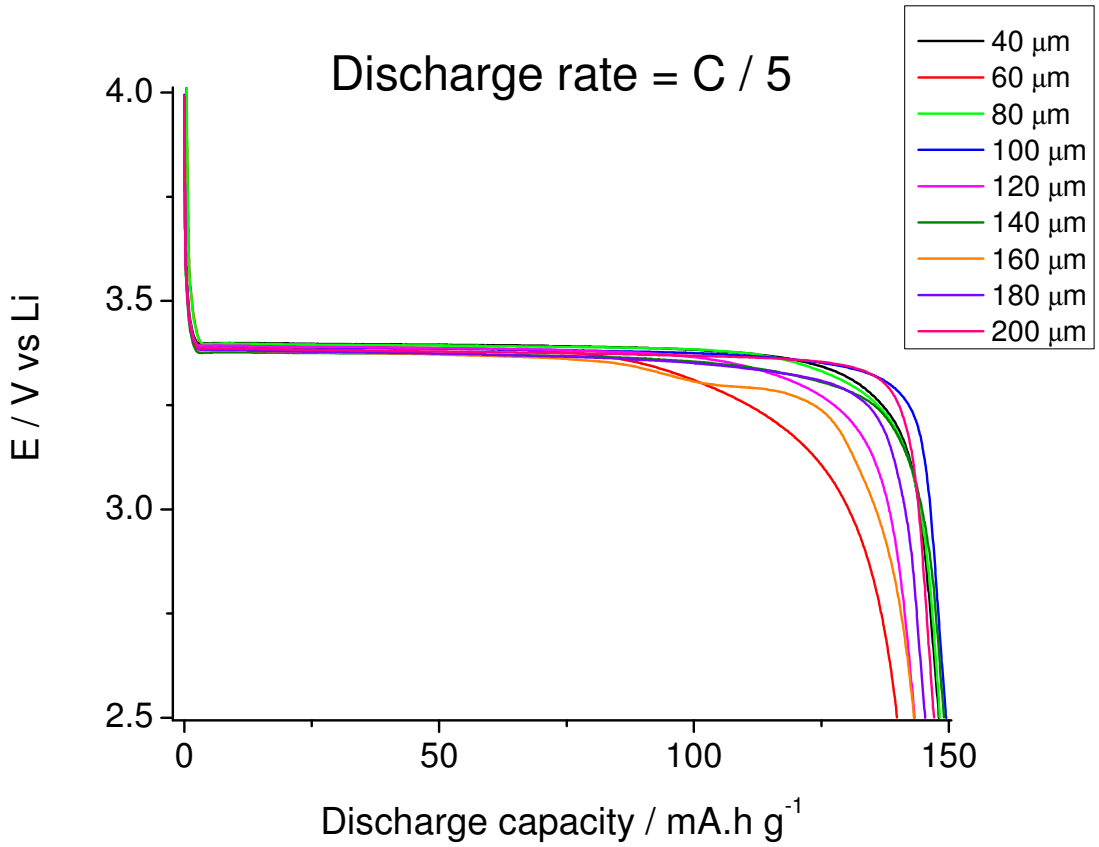

Figure 3.3.2b. Gravimetric capacity *vs*. discharge potential for 40-200 µm $LiFePO_4$ electrodes at a discharge rate of C/5.

At low rate, C / 5 and below, the performance of the $LiFePO_4$ was independent of electrode thickness. The discharge capacities seen in Figure 3.3.2b are basically the same for all electrode thicknesses; exhibiting a discharge capacity of ~ 150 mA.h g^{-1} and a discharge potential of 3.4 V *vs*. Li for all electrode thicknesses. The difference in the discharge capacity of the electrodes is shown in Figure 3.3.2c.

.

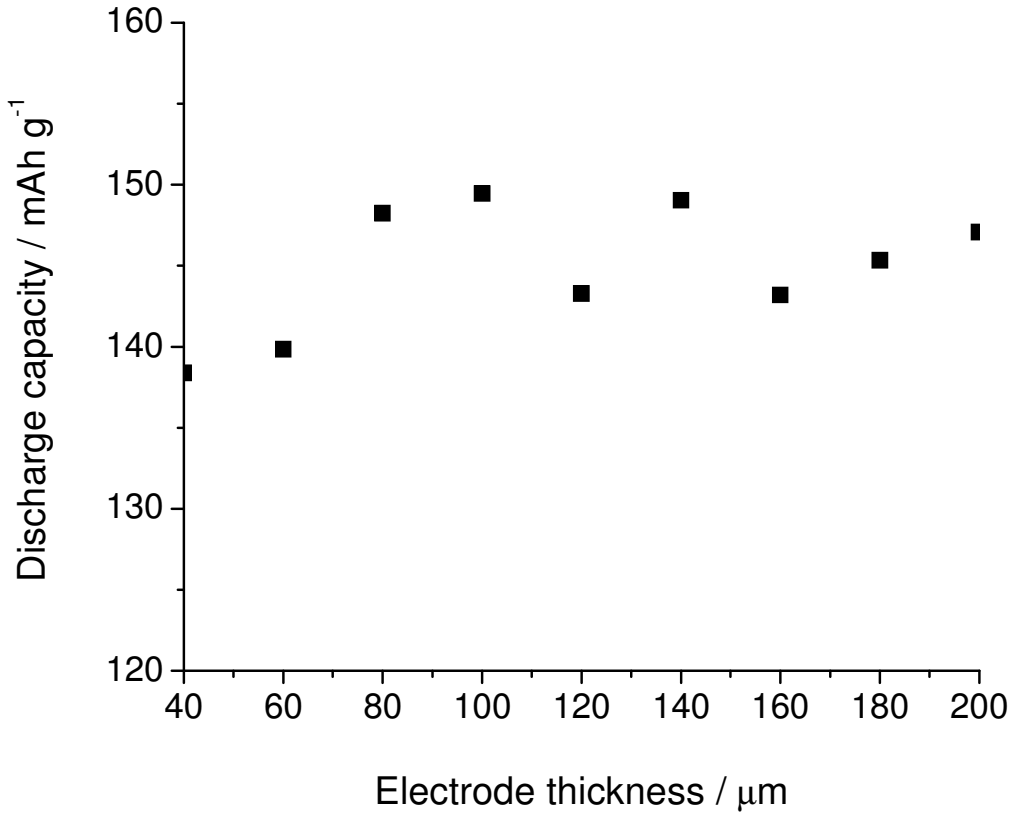

Figure 3.3.2c. Capacity *vs*. electrodes thickness in $LiFePO_4$ | 1M $LiPF_6$ in EC:DMC (1:1) | Li cells at a discharge rate of C / 5.

The difference in the discharge capacities was not dependant on electrode thickness, and there was no apparent trend to the differences in capacity (at a discharge rate of C / 5).

However, the small differences in capacity highlighted the errors present in the results. These errors were probably experimental in origin, e.g. the measurement of the active material mass in the composite electrode, or small temperature variations during charge / discharge experiments.

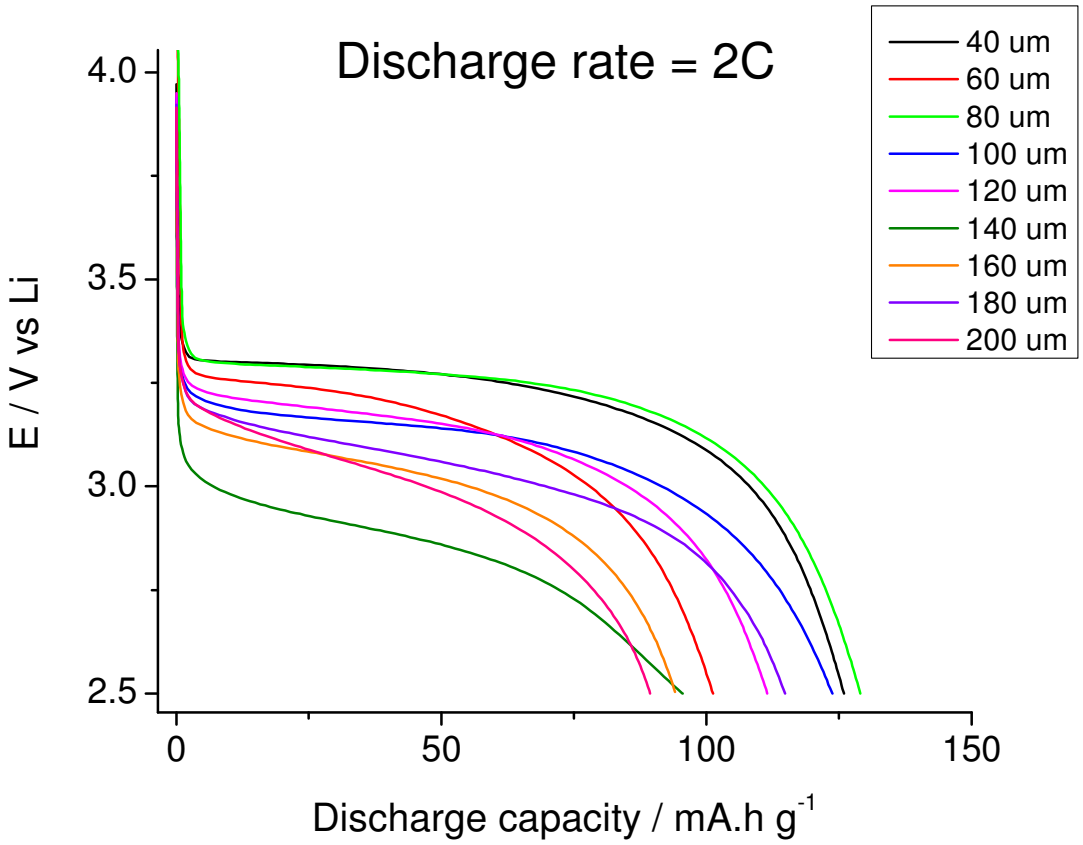

Figure 3.3.2d. Gravimetric capacity *vs*. discharge potential for 40-200 µm $LiFePO_4$ electrodes at a discharge rate of 2C.

Upon increasing the discharge rate to 2 C the effect of electrode thickness becomes apparent. The precession of decreasing capacity discharge profiles illustrated the decrease in discharged material within the composite electrode with increasing electrode thickness. All thicknesses of electrodes retained a clearly defined discharge end point, marked by a downturn in the discharge potential.

The effect of uncompensated cell resistance was clearly observed by the increase in instantaneous IR drop for the thickest electrodes at increased discharge rates, resulting in lower potential discharges with increasing electrode thickness. The effect of resistance in the composite electrode can be seen by the increasing slope of the discharge plateaux with increasing electrode thickness.

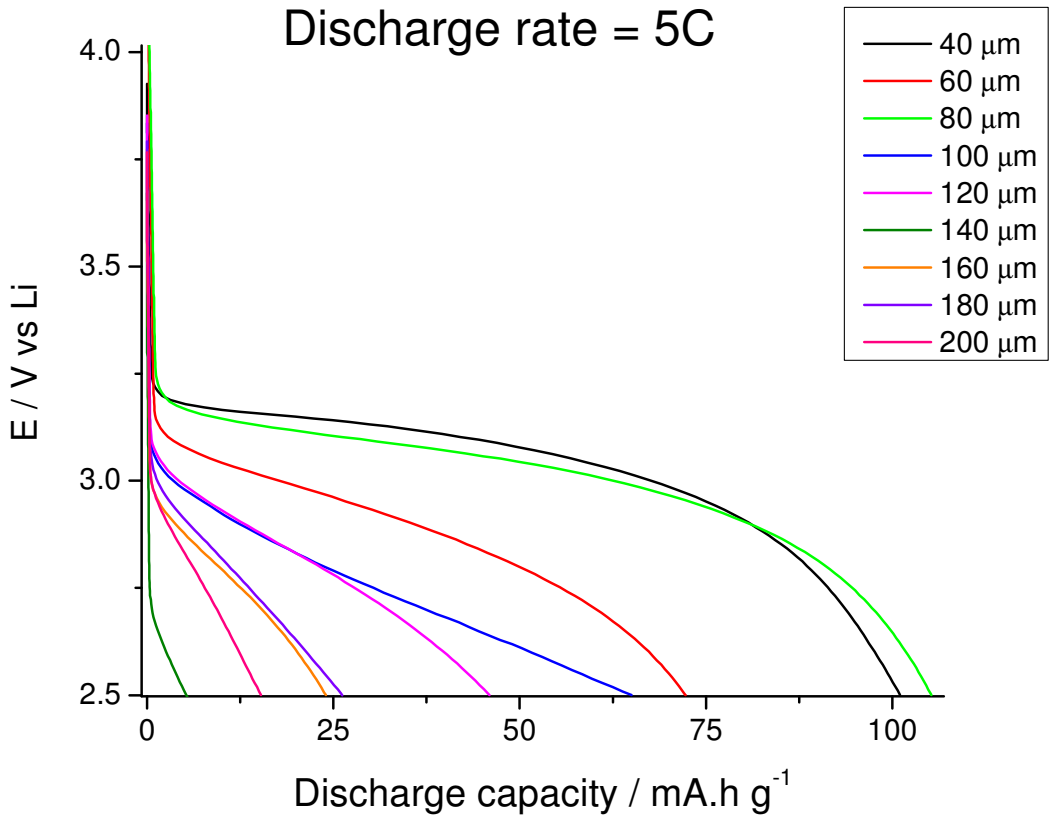

Figure 3.3.2e. Gravimetric capacity *vs*. discharge potential for 40-200 µm $LiFePO_4$ electrodes at a discharge rate of 5C.

At 5 C the effect of electrode thickness on the discharge of composite electrodes was pronounced. Whilst the thinnest electrodes retained most of their capacity the discharge of the thickest electrodes was severely curtailed. The discharge profiles seen in Figure 3.3.2e also illustrated the difficulty of accurately determining the discharge end point. The end points of the discharge profiles seen in Figure 3.3.2a were unambiguous; the maximum discharge capacity was clear and defined by a sudden downturn in potential at the end of the discharge plateaux. However at increased C-rates the effects of increased IR drop in the cell and increasing slope of the discharge plateaux, due to increasing ionic resistance in the composite, (3.1.2a) especially for the thicker composite electrodes, made determination of the maximum discharge capacity more difficult. This was demonstrated in Figure 3.3.2e by comparing the discharge profiles of the thickest (200 µm) and thinnest (40 µm) electrodes. The 40 µm electrode has reached a definitive end of discharge signified by the aforementioned downturn in potential corresponding to the saturation of the Li_1FePO_4 phase. In the case of the 200 µm electrode, the downturn in potential was not well defined, suggesting the true end of discharge was not recorded, and the

experimental potential cut off (2.5 V *vs.* Li) was at best an estimation of the minimum discharge capacity.

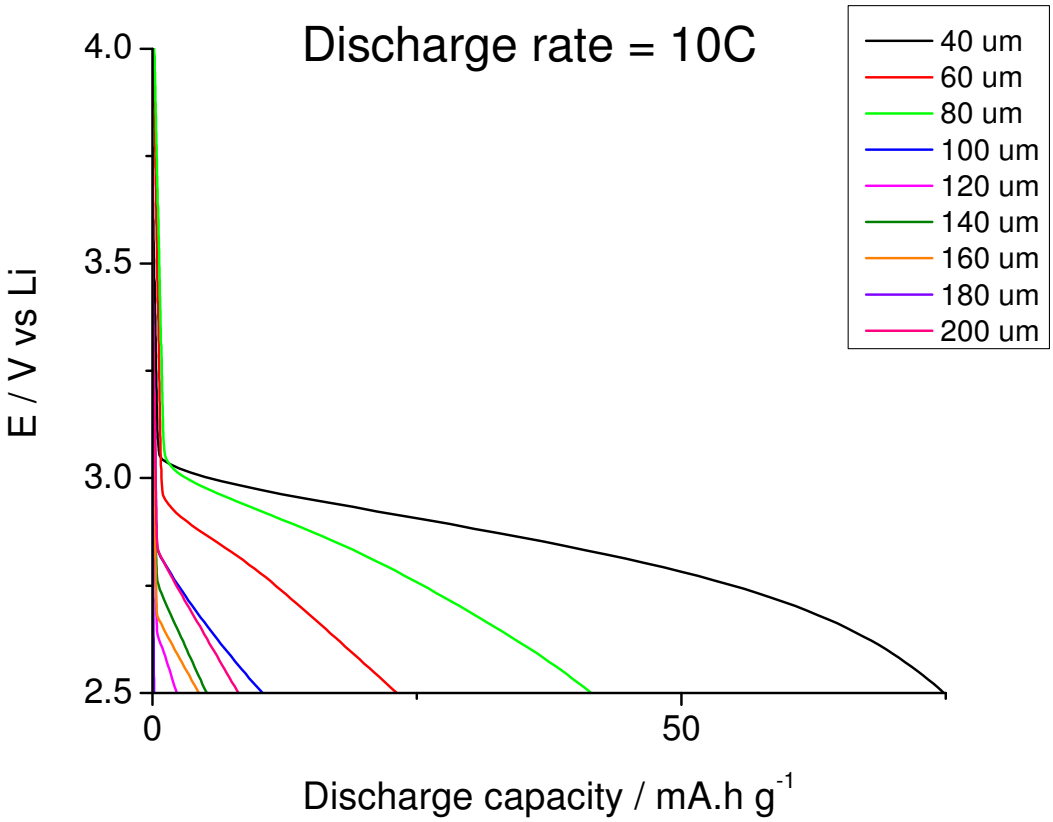

Figure 3.3.2f. Gravimetric capacity *vs*. discharge potential for 40-200 µm $LiFePO_4$ electrodes at a discharge rate of 10C.

At a discharge rate of 10 C the effects of IR drop in the cell dominated the discharge profiles, especially in the case of the thickest electrodes where the measured capacity was effectively zero. For the thickest electrodes the instantaneous IR drop was greater than 2 V, leaving less than 0.5 V for the discharge to occur before the potential cut off was reached. As the majority of the discharge profiles were prematurely cut off by the instantaneous IR drop the 10 C discharge data was excluded from the following analysis.

According to the SDF model (3.1.2) the gradients of the discharge plateaus (dE/dQ), within the two phase region, should be related to the square of the electrode thickness (L) by the following equations.

Firstly, within the conditions of the SDF mode (i.e. a salt deficiency in the composite electrode) the ionic resistance within the composite is related to the thickness of discharged material (λ), conductivity (σ) and area (A) by Equation 3.3.2a.

$$R = \frac{\lambda}{\sigma A}$$ **Equation 3.3.2a**

The ΔE for the discharge plateau can be found by applying Ohms law to equation 3.3.2a to give equation 3.3.2b.

$$\Delta E = j\frac{\lambda}{\sigma}$$ **Equation 3.3.2b**

(Where j is current normalised to electrode area, A cm^{-2}).

According to the SDF model, Figure 3.1.2b, the degree of discharge (DoD) is equal to the ratio of the thickness of discharged material (λ) and the composite electrode thickness (L). The thickness of discharged material (λ) is therefore equal to the degree of discharge multiplied by the electrode thickness, Equation 3.3.2c.

$$DoD = \frac{\lambda}{L} \quad \Rightarrow \quad \lambda = DoD.\,L$$ **Equation 3.3.2c**

Combining equations 3.3.2b and c gives equation 3.3.2d.

$$\Delta E = \frac{j.DoD.L}{\sigma}$$ **Equation 3.3.2d**

The current density (j) is related to the C-rate (f) and theoretical capacity normalised to electrode area by Equation 3.3.2e.

$$j = f.\,Q^0{}_A \quad = f.\,Q^0{}_V.\,L$$ **Equation 3.3.2e**

(Where $Q^0{}_A$ and $Q^0{}_V$ are theoretical capacity normalised to area and volume respectively)

Substituting Equation 3.3.2e into Equation 3.3.2d gives Equation 3.3.2f.

$$\Delta E = \frac{f.Q^0{}_V.DoD.L^2}{\sigma}$$ **Equation 3.3.2f**

Differentiation of Equation 3.3.2f in terms of ΔE and DoD gives Equation 3.3.2g.

$$\frac{d(\Delta E)}{d(DoD)} = \frac{f.Q^0{}_V.L^2}{\sigma}$$ **Equation 3.3.2g**

According to the above analysis, summarised in Equation 3.3.2g, a plot of d(ΔE)/d(DoD) *vs*. L^2 should give a linear relationship in the case where the SDF analysis applies, i.e. a lithium salt deficiency in the composite electrode during charge or discharge.

DoD can be expressed in terms of volumetric electrode capacity (Q_V / mA.h cm^{-3}) according to Equation 3.3.2h.

$$DoD = \frac{Q_V}{Q^0{}_V}$$ **Equation 3.3.2h**

By substitution of Equation 3.3.2h into Equation 3.3.2f we can derive Equation 3.3.2i; which describes ΔE in terms of volumetric electrode capacity rather than DoD. Equation 3.3.2i can be further modified to express gravimetric electrode capacity (Q_g / mA.h g^{-1}) using the electrode density (Equation 3.3.2j).

$$DoD = \frac{Q_V}{Q^0{}_V} \quad + \quad \Delta E = \frac{f.Q^0{}_V.DoD.L^2}{\sigma} \quad \Rightarrow$$

$$\Delta E = \frac{f.Q^0{}_V.Q_V \big/ Q^0{}_V.L^2}{\sigma} \quad \Rightarrow \quad \Delta E = \frac{f.Q_V.L^2}{\sigma}$$ **Equation 3.3.2i**

$$\Delta E = \frac{f.Q_g.L^2}{\sigma \rho}$$ **Equation 3.3.2j**

(Where ρ is electrode density / g cm^{-3})

Finally, differentiation of Equation 3.3.2j gives Equation 3.3.2k, and as with equation 3.3.2g a plot of $d(\Delta E)/d(Q_g)$ *vs*. L^2 should give a linear relationship where the SDF analysis applies.

$$\frac{d(\Delta E)}{d(Q_g)} = \frac{f.L^2}{\sigma \rho}$$ **Equation 3.3.2k**

Figure 3.3.2f shows the gradient of the discharge plateau ($d(\Delta E)/d(Q_g)$), extracted from the discharge data plotted in Figures 3.3.2b d and e, *vs*. the square of electrode thickness (L^2) for $LiFePO_4$ | 1M $LiPF_6$ in EC:DMC (1:1) | Li cells at a number of C-rates.

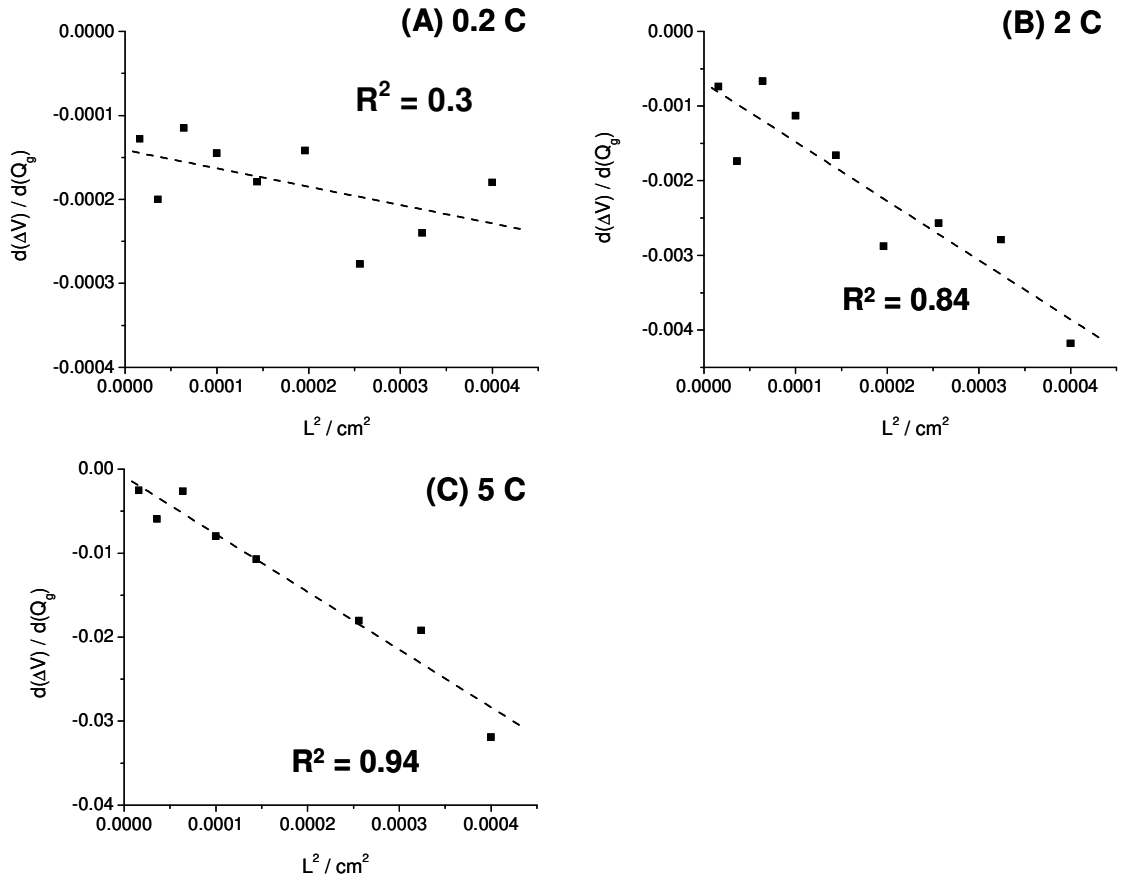

Figure 3.3.2f. Plots of d(ΔE)/ d(Q_g) *vs*. L^2 during discharge for varying thickness $LiFePO_4$ | 1M $LiPF_6$ in EC:DMC (1:1) | Li cells at 0.2 C (A), 2 C (B) and 5 C (C).

At low C-rates, i.e.0.2 C, the correlation between d(ΔE)/d(Q_g) and the square of the electrode thickness (L^2) was not obvious; with the linear fit of the data exhibiting a low R^2 value. However, the relationship predicted by Equation 3.3.2j is only valid within the conditions of the SDF model, i.e. a lithium salt deficiency in the composite electrode. At low discharge rates the concentration of lithium salt in the composite electrode ([LiX]) does not reach zero and a premature discharge is not seen.

For 2 and 5 C discharges (Figure 3.3.2f (B) and (C) respectively), where the faster rate of discharge causes a lithium salt depletion in the electrode, and therefore a premature end of discharge, the relationship between d(ΔE)/d(Q_g) and L^2 was as expected according to Equation 3.3.2j. The data in Figures 3.3.2b, d and e were the condensation of galvanostatic charge / discharge results for 40, 60, 80, 100, 120, 140, 160, 180 and 200 µm thick $LiFePO_4$ composite electrodes (in $LiFePO_4$ | 1M $LiPF_6$ in EC:DMC (1:1) | Li cells) summarised at three C-rates.

However, discharge data for each of the nine thicknesses of electrode were recorded using 14 different C-rates (C/10, C/5, C/2, C, 2C, 5C, 10C, 20C, 25C, 30C, 35C, 40C, 45C and 50C); culminating in a total of 126 discharges. This data was displayed in a single plot of discharge capacity *vs.* inverse C-rate for all thicknesses, and is shown in Figure 3.3.2g.

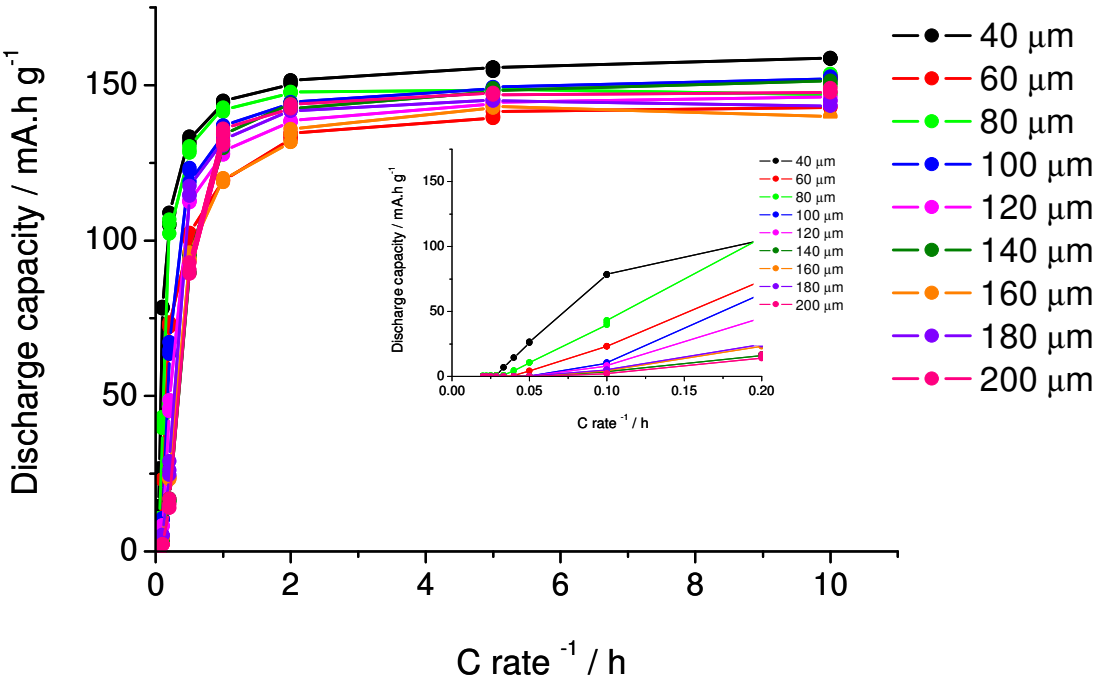

Figure 3.3.2g. Discharge capacity (mA.h g^{-1}) *vs*. inverse C-rate (h) for varying thickness $LiFePO_4$ | 1M $LiPF_6$ in EC:DMC (1:1) | Li cells. Inset shows expanded view of high C-rate region.

The origins of the discharge capacity *vs*. C-$rate^{-1}$ plot come from analysis of the discharge data; initially according to the Sand equation and then according to the SDF model analysis.

The Sand equation analysis was used to estimate the diffusion coefficient in the composite electrode and is described in 3.3.3.

3.3.3. Estimation of Lithium Ion Diffusion Within the $LiFePO_4$ Composite Electrode Using the Sand Equation Analysis

The data collected in the electrode thickness experiments for $LiFePO_4$ | 1M $LiPF_6$ in EC:DMC (1:1) | Li cells, 3.3.2, were analysed in order to estimate the lithium ion diffusion coefficient (D) within the $LiFePO_4$ composite electrodes.

Initial analysis of the data used equations based on the Sand equation [64] which describes diffusion of a redox species towards a planar electrode at a solid / liquid interface (though here it was used to describe diffusion of lithium salt into a porous electrode), D was estimated using an analysis based on the following equations.

$$\frac{i\,\tau^{1/2}}{C_o^{*}} = \frac{nF\,A\,D^{1/2}\,\pi^{1/2}}{2} \qquad \textbf{(Sand Equation)}$$

$$\frac{i\,\tau^{1/2}}{C_o^{*}} = \frac{nF\,A\,D^{1/2}\,\pi^{1/2}}{2} \quad \Rightarrow i = \quad \frac{nF\,A\,D^{1/2}\pi^{1/2}C_0^{*}}{2\,\tau^{1/2}}$$

$$\Rightarrow \quad i^2 = \quad \frac{n^2F^2A^2D\pi C_0^{*2}}{4\,\tau}$$

$$i = \quad \frac{n^2F^2A^2D\,\pi\,C_0^{*2}}{4\,i\tau} \text{ (as Q = i}\tau\text{)} \Rightarrow \quad i = \quad \frac{n^2F^2A^2D\,\pi\,C_0^{*2}}{4\,Q} \text{ (As } Q^0{}_V = FC_0^{*}$$

and n=1)

$$\Rightarrow \quad i\,Q = \quad \frac{A^2D\,\pi Q^0{}_V{}^2}{4} \quad \Rightarrow \quad j\,Q_A = \quad \frac{D\,\pi Q^0{}_V{}^2}{4} \qquad \textbf{Equation 3.3.3a}$$

Where; C_0^{*} is initial concentration of oxidised species (mol dm^{-3}), F is 96485 C mol^{-1}, A denotes area perpendicular to lithium diffusion (cm^2), τ denotes transition time (s), i is current (A), D is lithium ion diffusion coefficient ($cm^2\ s^{-1}$), Q equals charge (mA.h), $Q^0{}_V$ is theoretical volumetric capacity (mA.h cm^{-3}), Q_A is charge normalised to area (mA.h cm^{-2}), j is current normalised to area (A cm^{-2}) and n is the electron transfer number (and in the case of $LiFePO_4$, n=1)

By rearranging Equation 3.3.3a to give Equation 3.3.3b the origin of the capacity *vs.* inverse current density plot, Figures3.3.2g and 3.3.3a, used in the determination of $Q^{SEM}{}_{INF}$ / i_0 (Figure 3.3.3a) becomes apparent.

$$Q_A = \frac{D \pi Q_v^{\,2}}{4}\left(\frac{1}{j}\right) \qquad \textbf{Equation 3.3.3b}$$

Further manipulation of Equation 3.3.3a illustrates the relationship between the electrode thickness, L, the discharge capacity per area / current density ratio at the transition between finite and semi-infinite diffusion regimes (Figure 3.3.3a), $Q^{SEM}{}_{INF}$ / i_0, and the lithium ion diffusion coefficient within the composite electrode.

$$j\,Q_A = \frac{D_{Li}\,\pi\,Q^0{}_v^{\,2}}{4} \quad (\text{Where } Q^0{}_v = \frac{Q^{SEM}{}_{INF}}{L} \text{ and } j\,Q_A = i_0\,Q^{SEM}{}_{INF}) \quad \Rightarrow$$

$$i_0\,Q^{SEM}{}_{INF} = \frac{D_{Li}\,\pi\,(Q^{SEM}{}_{INF})^2}{4\,L^2} \quad \Rightarrow \quad i_0 = \frac{D\,\pi\,Q^{SEM}{}_{INF}}{4\,L^2} \quad \Rightarrow$$

$$\frac{Q^{SEM}{}_{INF}}{i_0} = \frac{4\,L^2}{\pi\,D_{Li}} \qquad \textbf{Equation 3.3.3c}$$

Where L is electrode thickness (cm) and $Q^{sem}{}_{inf}$ and i_0 denote charge (mA.h cm^{-2}) and current density (mA cm^{-2}) at the transition between semi-infinite and finite regions (Figure 3.3.3a) respectively.

Figure 3.3.3a shows an example plot of discharge capacity normalised to electrode area *vs.* inverse current density for a 40 µm $LiFePO_4$ composite electrode in a $LiFePO_4$ | 1M $LiPF_6$ in EC:DMC (1:1) | Li cell.

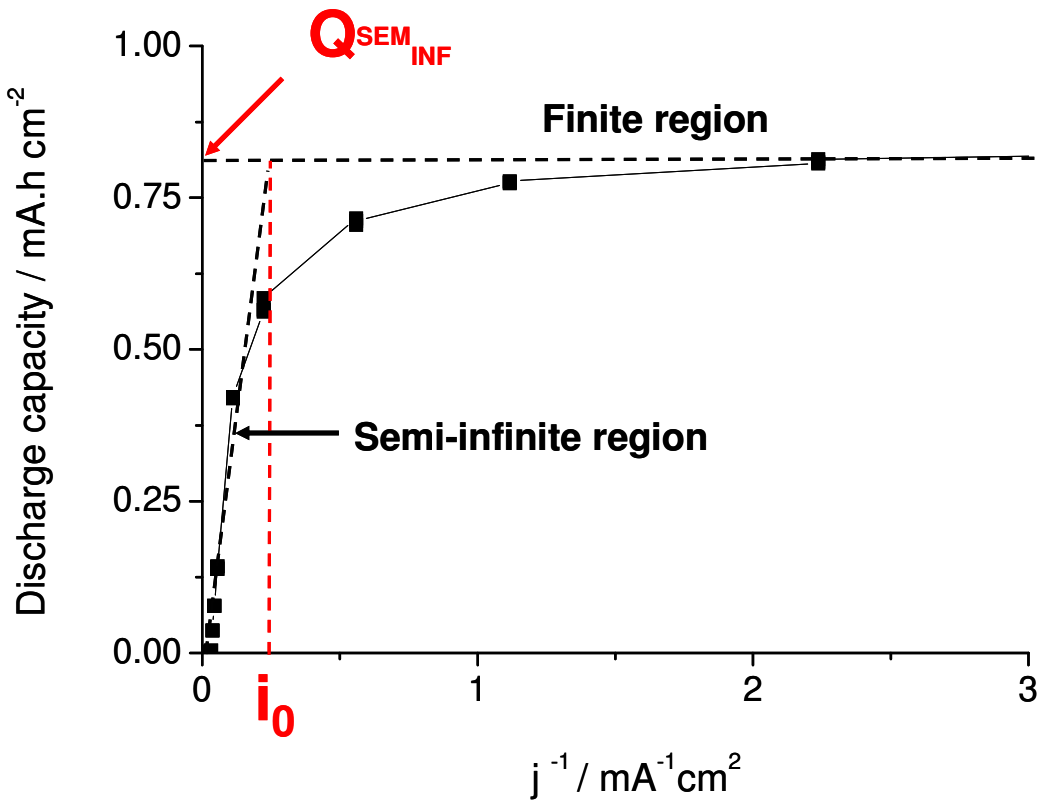

Figure 3.3.3a. Example plot showing discharge capacity *vs*. inverse current density for 40µm $LiFePO_4$ composite electrode. The current density of the transition between the semi-infinite and finite diffusion regions is denoted as i_0. The discharge capacity extrapolated from the finite region is stated as Q^{SEM}_{INF}.

The two distinct regions illustrated in Figure 3.3.3a were designated finite and semi-infinite. Within the finite region, where the current density is sufficiently low as not to affect the discharge capacity, the effect of salt diffusion within the composite electrode was negligible.

At larger discharge rates, within the semi-infinite region, the effect of salt diffusion on discharge capacity was seen by a linear decrease in discharge capacity with increasing current density (decreasing 1 / j).

The current density at the transition between semi-infinite and finite diffusion regimes, i_0, was found by extrapolation of the linear fit within the semi-infinite region.

The discharge capacity of the semi-infinite / finite transition, Q^{SEM}_{INF}, was estimated by extrapolation of the low current density, finite, region.

Figure 3.3.3b shows discharge capacity (mA.h cm^{-2}) *vs*. 1 / j ($mA^{-1}cm^2$) for all thicknesses of $LiFePO_4$ composite electrodes | 1M $LiPF_6$ in EC:DMC (1:1) | Li cells.

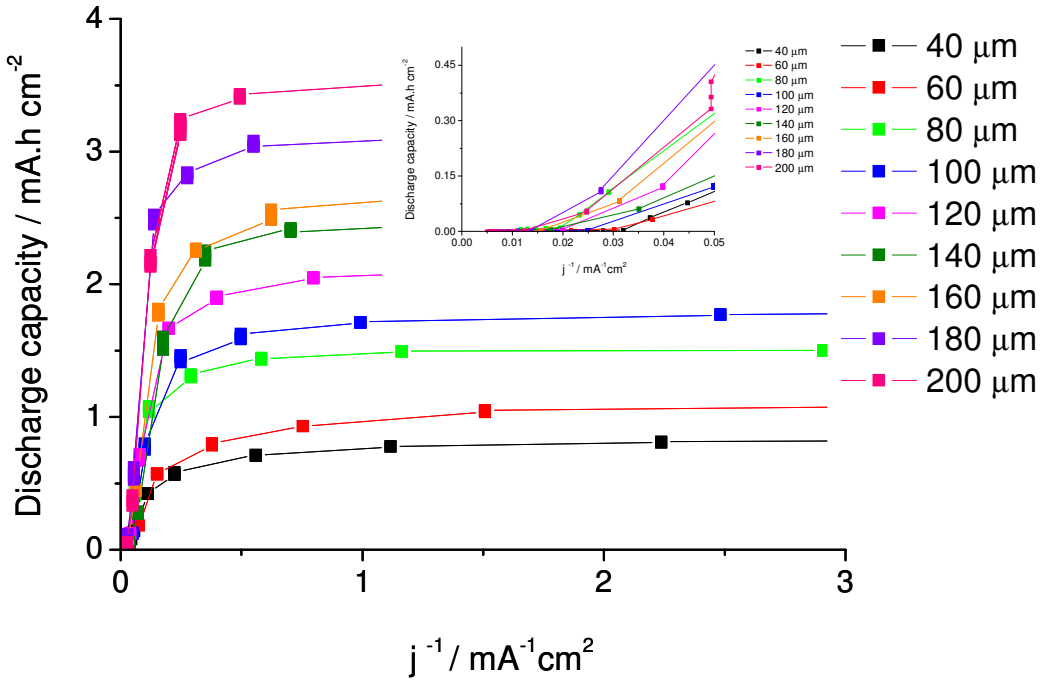

Figure 3.3.3b. Discharge capacity (mA.h cm^{-2}) plotted against inverse current density ($mA^{-1}cm^2$) for individual thicknesses of $LiFePO_4$ composite electrodes. Inset, expanded view of semi-infinite diffusion region.

In the case where discharge is limited by diffusion of the electrolyte front through the composite electrode, as described by the SDF model outlined in 3.1.2, the gradients within the semi-infinite diffusion region of Figure 3.3.3b should be equal for all electrode thicknesses.

The values of Q^{SEM}_{INF} and i_0 for each electrode thickness were estimated, as illustrated in Figure 3.3.3a, in order to estimate D within the composite electrode according to Equation 3.3.3c. The values of Q^{SEM}_{INF} and i_0 for each electrode thickness are summarised in Table 3.3.3a.

Table 3.3.3a. Q^{SEM}_{INF} and i_0 for individual thicknesses of $LiFePO_4$ composite electrodes.

Electrode Thickness (L) / µm	Q^{SEM}_{INF} / mA.h cm^{-2}	i_0^{-1} / mA^{-1} cm^2	i_0 / mA cm^{-2}	(Q^{SEM}_{INF} / i_0^{-1}) / h	L^2 / cm^2
40	0.85	0.19	5.16	0.16	0.000016
60	1.19	0.26	3.87	0.31	0.000036
80	1.55	0.34	2.97	0.52	0.000064
100	1.8	0.41	2.44	0.74	0.0001
120	2.16	0.45	2.22	0.97	0.000144
140	2.5	0.54	1.86	1.35	0.000196
160	2.7	0.58	1.73	1.56	0.000256
180	3.12	0.68	1.46	2.13	0.000324
200	3.55	0.76	1.32	2.70	0.0004

Figure 3.3.3c shows the plot of (Q^{SEM}_{INF}) / (i_0) *vs*. L^2, as described in Equation 3.3.3c, for $LiFePO_4$ composite electrode | 1M $LiPF_6$ in EC:DMC (1:1) | Li cells.

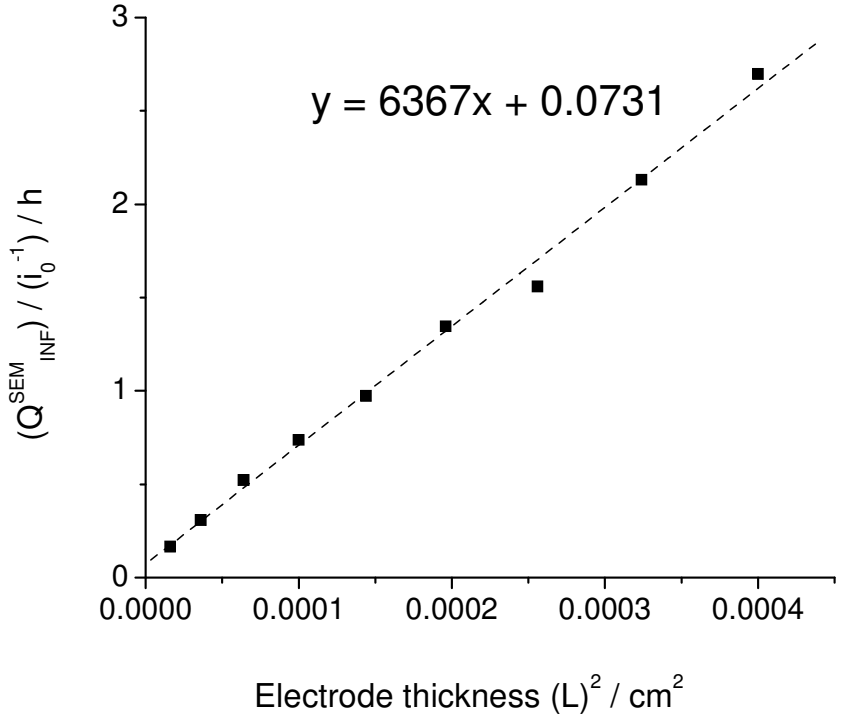

Figure 3.3.3c. Q^{SEM}_{INF} / i_0 *vs*. L^2 for varying thickness $LiFePO_4$ composite electrode | 1M $LiPF_6$ in EC:DMC (1:1) | Li cells. The lithium ion diffusion coefficient within the composite electrode (D) is equal to 4 π / the gradient.

According to equation 3.3.3c ($\frac{Q^{SEM}_{INF}}{i_0} = \frac{4L^2}{\pi D}$) and the gradient of ($Q^{SEM}_{INF}$) / ($i_0$) *vs*. L^2, Figure 3.3.3c, the lithium ion diffusion coefficient within the composite electrode, D = (4/ π) / 6367.

$D = (4 / \pi) / 6367 = 0.0002\ cm^2\ h^{-1}$

$D = 6 \times 10^{-8}\ cm^2\ s^{-1}$

Values for the lithium ion diffusion coefficient in $LiFePO_4$ have been reported to range from $10^{-14} – 10^{-16}\ cm^2 s^{-1}$ [65].The lithium ion diffusion coefficient for 1M $LiPF_6$ in non-aqueous electrolyte (PC, EC, DMC etc) has been measured as between 3-4 x $10^{-6}\ cm^2\ s^{-1}$ [66].

In a porous composite electrode (where particles size is small) we expect the diffusion of lithium, and lithium salts, to occur predominantly in the electrolyte; therefore the measured value of D should be closer to the diffusion coefficient of the electrolyte than the solid $FePO_4$.

Here the measured value of the lithium ion diffusion coefficient in the composite electrode lies somewhere between the above values, but as expected, much closer to the diffusion coefficient for 1M $LiPF_6$ in non-aqueous electrolytes.

The two orders of magnitude difference between D in the composite electrode ($6 \times 10^{-8}\ cm^2\ s^{-1}$) and the diffusion coefficient of 1M $LiPF_6$ in non-aqueous solvent ($3\text{-}4 \times 10^{-6}\ cm^2\ s^{-1}$) was most likely due to composite electrode structure.

It is suggested that the physical characteristics of the composite electrode, i.e. the porosity and tortuosity, were responsible for the two orders of magnitude increase in D, compared with in the pure electrolyte. The theory of tortuosity and porosity are complicated, especially when applied in three dimensions; however, Figure 3.3.3d shows a simplified schematic explanation of porosity and tortuosity within a composite electrode pellet.

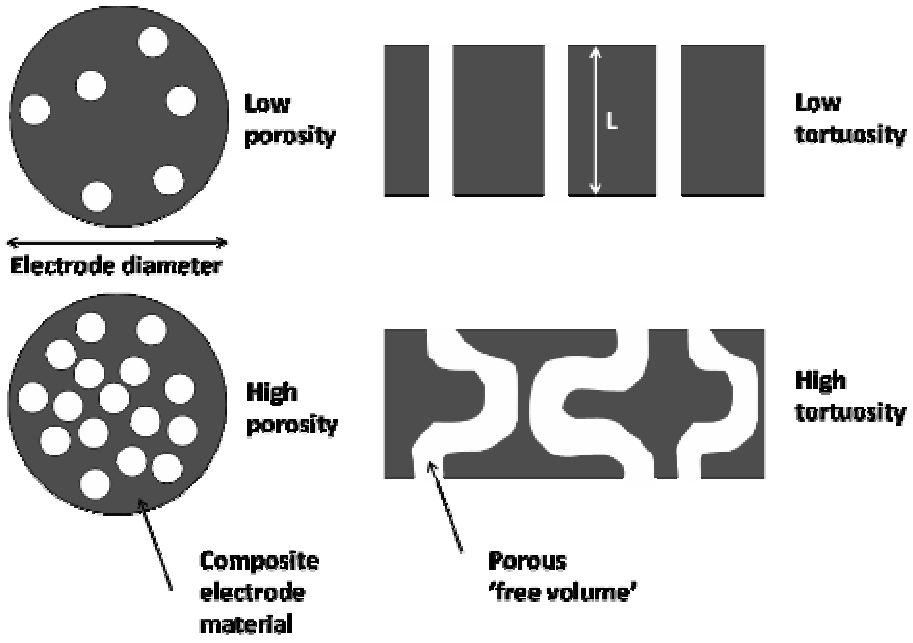

Figure 3.3.3d. Schematic representation of porosity (left) and tortuosity (right) in a composite electrode pellet. L is electrode thickness.

The composite electrode is composed of the active material (in this case $LiFePO_4$) an electronically conductive additive (acetylene black) and a binder (PTFE). The active material and acetylene black have a low tap density; and as such the composite electrode contains a certain volume of 'free space', or porosity. It is probable that this porosity percolates through the electrode, from the front, through its thickness (L) to the back. In the completed cell the porous elements of the electrode would be full of liquid electrolyte; effectively creating channels of electrolyte that run throughout the electrode thickness. The degree to which these 'channels of porosity' percolate through the electrode is referred to as the tortuosity. Figure 3.3.3d shows an example of low tortuosity, where the channels run through the thickness of the electrode with little deviation. In the high tortuosity example the porosity meanders through the electrode between areas, or agglomerations, of composite electrode material.

The difference between the measured D in the electrode and the literature values for the diffusion coefficient of the electrolyte were attributed to the restrictions of salt diffusion in the electrolyte, due to the porosity and tortuosity of the composite electrode.

3.3.4. Determination of D in the $LiFePO_4$ Composite Electrode Structure Using the SDF Analysis

The SDF model predicts the diffusion of lithium salt through the electrode thickness to be the rate limiting factor in the discharge of $LiFePO_4$ composite electrode | 1M $LiPF_6$ in EC:DMC (1:1) | Li cells. The SDF model builds on the previous analysis of salt diffusion in the composite electrode based on the Sand equation (3.3.3). The SDF model is described in detail in 3.1.2.

The effective diffusion coefficient of lithium ions within the composite electrode, D, was estimated using Equation 3.3.4a; derived from rearrangement of Equation 3.1.2f.

$$DoD.f = \frac{D}{L^2} \times \frac{[LiX]_0}{(T_{Li-})[Li]} \quad \Rightarrow \quad DoD.f = \frac{1}{L^2} \times \frac{D[LiX]_0}{(T_{Li-})[Li]} \qquad \textbf{Equation 3.3.4a}$$

The results of the galvanostatic charge / discharge experiments in varying thickness $LiFePO_4$ composite electrode | 1M $LiPF_6$ in EC:DMC (1:1) | Li cells (3.3.2) were used to produce a plot of the product of C-rate and degree of discharge (DoD) *vs*. electrode thickness (L).

The DoD (measured gravimetric discharge capacity / maximum slow cycle gravimetric capacity) for all thickness of electrode (40, 60, 80, 100, 120, 140, 160, 180 and 200 µm) was plotted as a function of C-rate *vs*. the inverse electrode thickness squared.

The SDF model was only applicable under conditions where migration alone was not sufficient to ensure full charge or discharge of the cell (Figure 3.3.2f), e.g. high discharge rate. Therefore, when plotting DoD.f *vs*. L^{-2} a 'selection' of C-rates was used. Figure 3.3.4a shows the plot of DoD.f *vs*. L^{-2} at discharge rates of 3, 5, 6 and 10 C for the varying thickness $LiFePO_4$ | 1M $LiPF_6$ in EC:DMC (1:1) | Li cells.

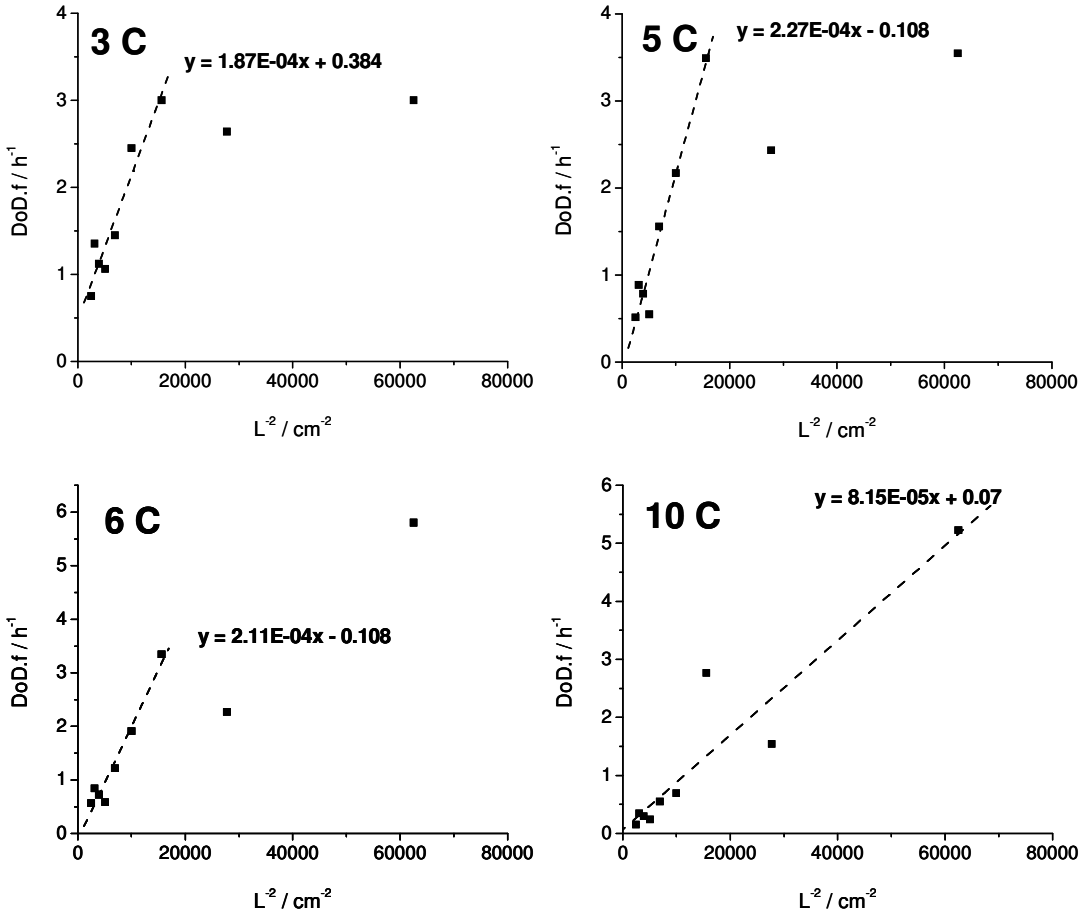

Figure 3.3.4a. DoD.f *vs*. L^{-2} for $LiFePO_4$ composite electrode | 1M $LiPF_6$ in EC:DMC (1:1) | Li cells at a 3, 5, 6 and 10 C.

For each discharge rate, Figure 3.3.4a 3, 5, 6 or 10 C, the point at which the thickness of the electrode becomes greater than the maximum depth of the discharge front (λ_{max}, Figure 3.1.2b) is marked by a linear decrease in DoD.f with L^{-2}. The one exception was for the plot at 10 C where λ_{max} was always less than the electrode thickness. This was explained by analysis of the discharge profiles at 10 C, Figure 3.3.2f, where the instantaneous IR drop pushed the majority of the discharge profile below the experimental potential cut off.

Within this linear region the value of DoD.f is dependant upon electrode thickness according to Equation 3.3.4a (according to the SDF model DoD.f should decrease linearly with L^{-2}).

D for the composite electrode was estimated according to Equation 3.3.4a. D for the composite electrode was estimated using the gradients seen in Figure 3.3.5a at 3, 5 and 6 C and therefore should be equal to the gradient / ($[liX]_0$/((T_{Li^-})[Li])).

The value of (T_{Li-}) was estimated at 0.6, based on a T_{Li+} value of 0.4[57, 67, 68], the estimated values of D are summarised in Table 3.3.4a. It should be noted that whilst the results at 5 and 10 C, Figure 3.3.5a and Table 3.3.5a, were derived from measured data points, results at 3 and 6 C were extrapolated from the linear, semi-infinite, regions of the discharge capacity *vs.* C-rate $^{-1}$ plots seen in Figure 3.3.2g

Table 3.3.4a. Diffusion coefficient of Li ions within the composite electrode with varying C-rate according to Equation 3.1.2f (where $[LiX]_0$ is bulk electrolyte concentration and [Li] is molar demand for Li during discharge of the $LiFePO_4$ composite electrode)

C rate / h^{-1}	Gradient / $cm^2\ h^{-1}$	$[LiX]_0$ / $mol.dm^{-3}$	[Li] / $mol.dm^{-3}$	(T_{Li-})	D / cm^2s^{-1}	D 1M $LiPF_6$ in PC/EC/DMC / cm^2s^{-1}
3	0.000187	1	7	0.6	2.18E-07	3-4E-06
5	0.000227	1	7	0.6	2.65E-07	3-4E-06
6	0.000211	1	7	0.6	2.46E-07	3-4E-06
AVE	0.000208	1	7	0.6	2.43E-07	3-4E-06

The calculated values of D within the composite electrodes for the three C-rates were effectively identical. The values were an order of magnitude lower than the literature value for the diffusion coefficient of 1M $LiPF_6$ in non-aqueous electrolyte, as discussed in the porosity / tortuosity section of 3.3.3. However, the values were also an order of magnitude higher than the value calculated using the Sand equation analysis, 3.3.3.

It is speculated that the reason for this order of magnitude difference is due to limitations of the sand equation analysis within the two phase region of the lithium iron phosphate discharge plateaux.

3.3.5. Effect of Particle Size on Rate Performance of $LiFePO_4$ Composite Electrode Pellets

As discussed in 3.1.1 the nature of the rate limitation within $LiFePO_4$ electrodes is dependant on several effects including: solid state limitations within the particle, as in saturation of the $Li_{1-x}FePO_4$ phase at the electrolyte / particle interface i.e. the shrinking core model [58] and the electronic and ionic wiring of the electrode [69], i.e. the effect of the electrode thickness.

In order to determine the prevalent effect in limiting the rate capability of $LiFePO_4$ composite electrodes experiments identical to those in 3.3.2 were performed on electrodes containing either large (1-5 µm) or small (<1 µm) active material particles.

Half cells were based on either nano $LiFePO_4$ (Hydro Quebec, particle size < 1 µm)| 1M $LiPF_6$ in EC:DMC (1:1) | Li or $LiFePO_4$ (Aldrich, particle size ~ 1-5µm)| 1M $LiPF_6$ in EC:DMC (1:1) | Li. A SEM comparison of the 'large particle' and 'small particle' $LiFePO_4$ is shown in Figure 3.3.5a.

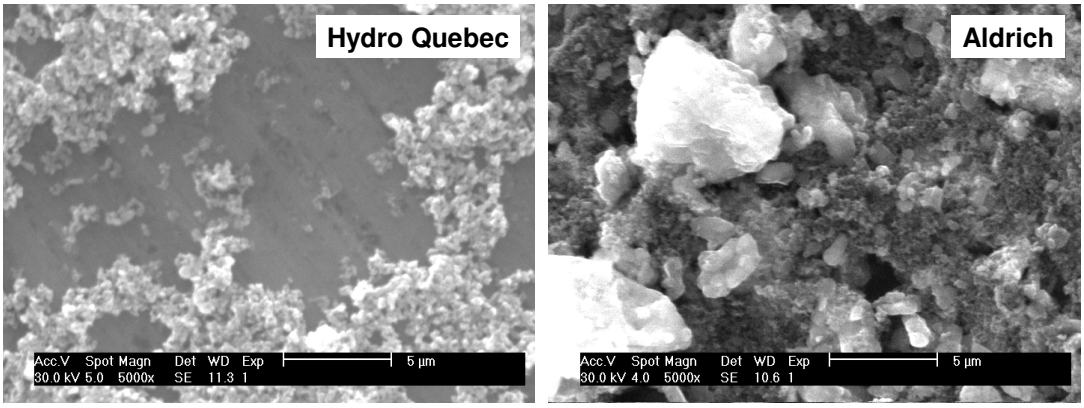

Figure 3.3.5a. Small (Hydro Quebec, < 1 µm) and large (Aldrich, 1-5 µm) $LiFePO_4$ particles. SEM images were obtained from isopropyl alcohol based dispersions of $LiFePO_4$ particles (dried at 60°C for ~1h).
Both large and small particles are carbon coated.

According to a scenario where the shrinking core model applies, the rate capability of cells containing the 'small particle' Hydro Quebec material should be significantly better than cells containing the 'large particle' Aldrich $LiFePO_4$. Conversely, if the electrode thickness effect is prevalent the rate capability will not be related to the size of the active material particles but to the thickness of the composite electrode.

As in 3.3.2 the most convenient analysis of the rate capability of discharge of $LiFePO_4$ composite electrodes is the plot of discharge capacity against inverse C-rate.

Figure 3.3.5b shows the discharge capacity *vs.* 1 / C-rate data at a variety of thicknesses for $LiFePO_4$ (Hydro Quebec, particle size < 1 µm)| 1M $LiPF_6$ in EC:DMC (1:1) | Li cells superimposed with the same data for $LiFePO_4$ (Aldrich, particle size ~ 1-5µm)| 1M $LiPF_6$ in EC:DMC (1:1) | Li cells.

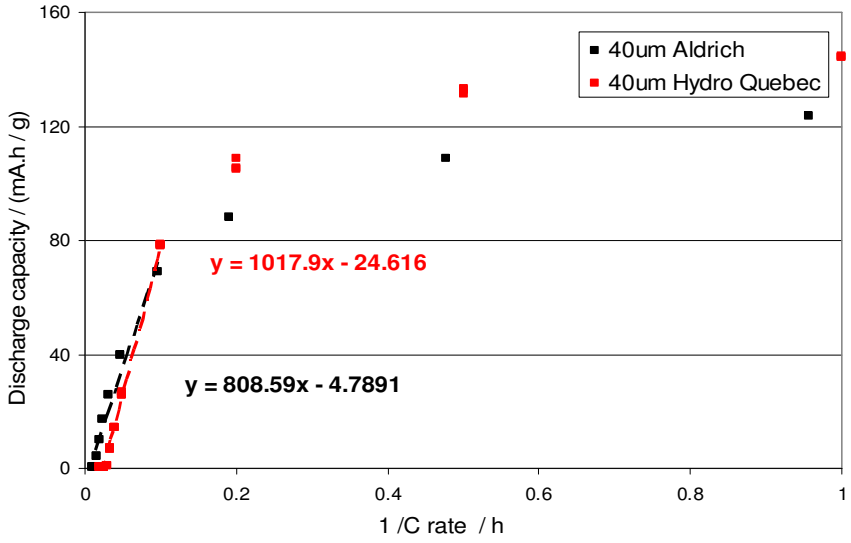

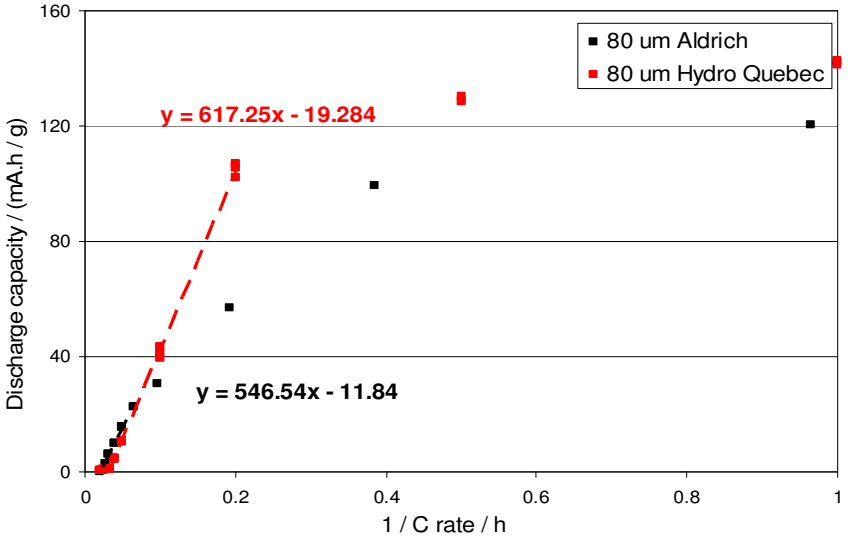

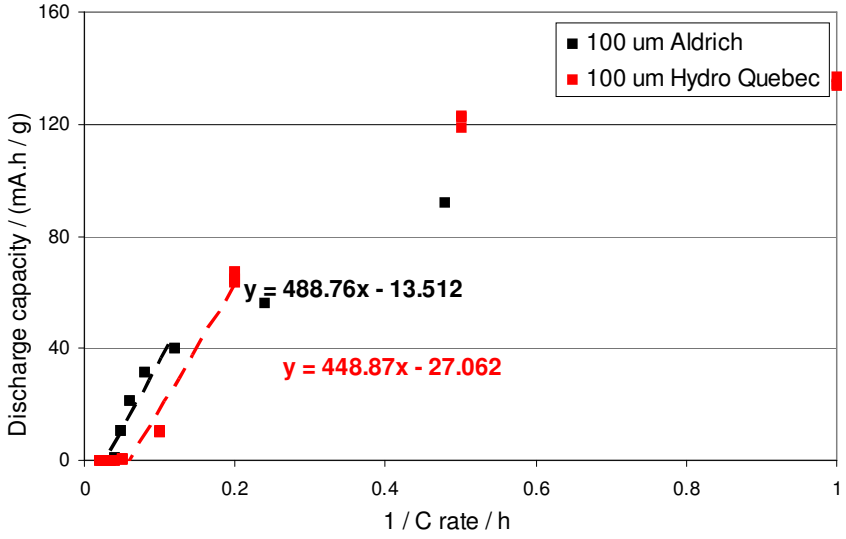
160
120
80
40
0
Discharge capacity / (mA.h / g)
0
0.2
0.4
0.6
0.8
1
1 / C rate / h
100 um Aldrich
100 um Hydro Quebec
y = 488.76x - 13.512
y = 448.87x - 27.062

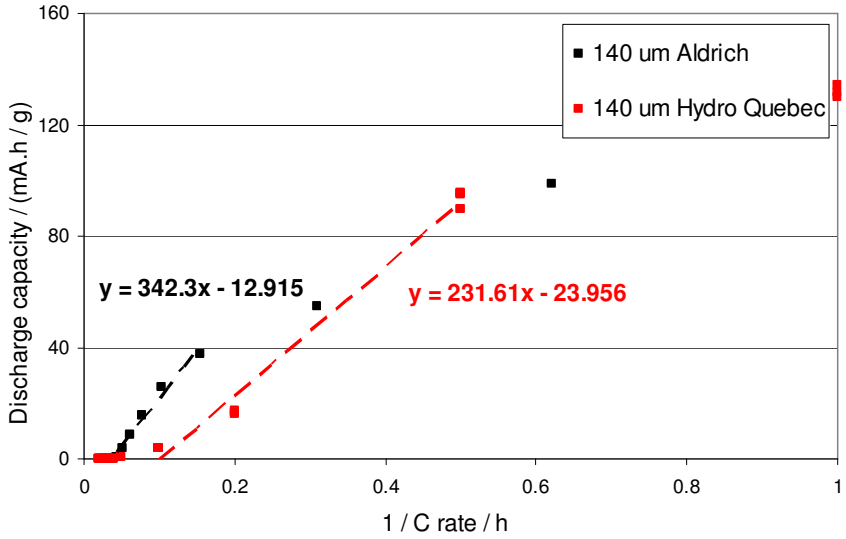
160
120
80
40
0
Discharge capacity / (mA.h / g)
0
0.2
0.4
0.6
0.8
1
1 / C rate / h
140 um Aldrich
140 um Hydro Quebec
y = 342.3x - 12.915
y = 231.61x - 23.956

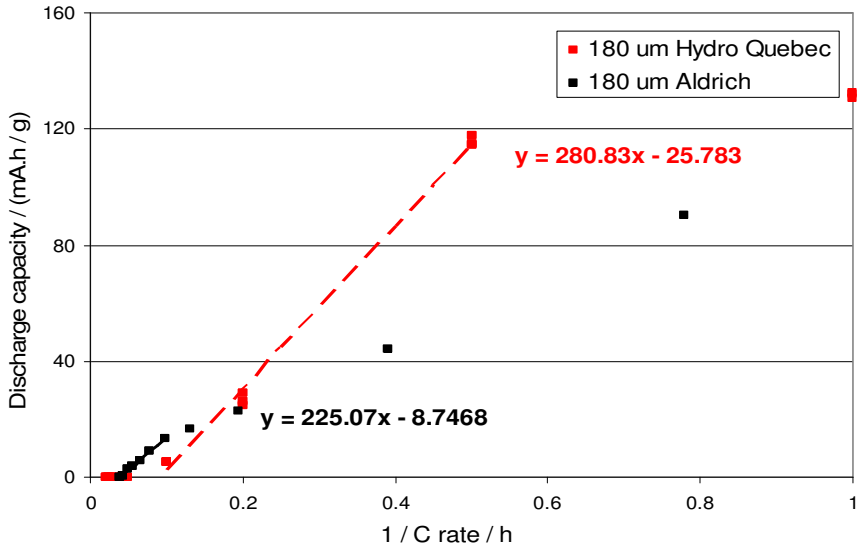

Figure 3.3.5b. Discharge capacity (mA.h g^{-1}) *vs*. C-$rate^{-1}$ for 'large particle' $LiFePO_4$ (Aldrich, particle size ~ 1-5µm)| 1M $LiPF_6$ in EC:DMC (1:1) | Li and 'small particle' $LiFePO_4$ (Hydro Quebec, particle size < 1 µm)| 1M $LiPF_6$ in EC:DMC (1:1) | Li cells.

The gradients, Table 3.3.5a, within the semi-infinite diffusion controlled regions (Figure 3.3.3a) of the plots in Figure 3.3.5b signify the rate capability of the electrode in question (a steeper gradient indicating a greater rate capability)

Table. 3.3.5a. Summary of gradients, within semi infinite region, for 'large particle' $LiFePO_4$ (Aldrich, particle size ~ 1-5µm)| 1M $LiPF_6$ in EC:DMC (1:1) | Li and 'small particle' $LiFePO_4$ (Hydro Quebec, particle size < 1 µm)| 1M $LiPF_6$ in EC:DMC (1:1) | Li cells extracted from Figure 3.3.5b.

Electrode Thickness / µm	Gradient (Aldrich)	Gradient (Hydro Quebec)
40	808.59	1017.9
80	546.54	617.25
100	488.76	448.87
140	342.3	231.61
180	225.07	280.83

According to the gradients, summarised in Table 3.3.5a, the mechanism of rate limitation within the composite electrode, i.e. shrinking core or electrode thickness, was dependant upon electrode thickness.

That was except in the thinnest electrode case, i.e. the the 40 µm composite electrodes, the rate capability here seemed to be dominated by solid state diffusion within the particle, as in the shrinking core analysis (signified by the steeper gradient seen for the 'small particle' Hydro Quebec material when compared to the 'large particle' Aldrich material). As the composite electrode thickness increased the gradients of the small and large particle $LiFePO_4$ samples converged, leading to roughly equal gradients for the large and small particle cases at thicknesses of 80 µm and above.
In the case of the shrinking core model being the dominant mechanism of rate limitation the gradients for the 'small particle' $LiFePO_4$ should be steeper than for the 'large particle' $LiFePO_4$, as in the case of the 40 µm results. However at thicknesses greater than 40 µm the particle size showed no significant effect on the gradient within the semi-infinite diffusion region. This suggested that regardless of particle size the rate limiting mechanism in composite electrodes thicker than 40 µm was the electrode thickness, i.e. the electronic and ionic diffusion within the composite electrode.

An interesting but significant effect, observed for both the 'large particle' Aldrich and 'small particle' Hydro Quebec results, was the presence of an intercept in the plot of discharge capacity *vs*. C-rate^{-1}, Figure 3.3.5b.The intercept occurred at high discharge rates (low C-rate^{-1}) and was attributed to the large instantaneous IR drop seen for the high C-rate discharges, as seen in Figure 3.3.2f. As this high rate discharge limitation was apparently independent of electrode thickness it was speculated that it could be due to the electrolyte | anode interface. This was investigated further using experiments based on a $LiFeO_4$ 'microelectrode' cell (3.3.6).

3.3.6. $LiFePO_4$ 'Microelectrode' Experiments

Analysis of the discharge capacity *vs*. inverse C-rate plots for varying thickness $LiFePO_4$ | 1M $LiPF_6$ in EC:DMC (1:1) | Li cells (both the 'large particle' Aldrich and 'small particle' Hydro Quebec results), Figure 3.3.5b, revealed an intercept corresponding to a high rate discharge limitation that was independent of electrode thickness. It was theorised that the rate limitation was due to uncompensated cell resistance, rather than electrode resistance, resulting in a large instantaneous IR drop that pushed the discharge plateaux below the negative experimental potential cut-off. In order to minimise the IR drop within the cell a $LiFePO_4$ 'microelectrode' cell was designed with the following features.

- The microelectrode cell was designed to contain a reference electrode in close proximity to the cathode (minimising uncompensated resistance in the cell).
- In the SDF model an assumption was made that the concentration of Li salt in the bulk electrolyte, $[LiX]_{0,}$ remains constant, the salt concentration gradient only builds up in the composite electrode. However for the thickest electrodes it was suggested that the volume of Li needed during discharge would effect a change in the $[LiX]_0$ adjacent to the electrode surface. The 'microelectrode' design was intended to minimise this effect, as the volume of the microelectrode would be minimal in comparison to the large volume of bulk electrolyte.
- It was also expected that interference due to the solid electrolyte interface (SEI) on the Li foil anode would be minimised by the microelectrode configuration.

The design of the $LiFePO_4$ microelectrode cell is described in 3.2.2. The $LiFePO_4$ composite 'microelectrode' had a ~1.2 mm diameter, and was ~1mm deep (L = 1mm); the volume of the 'microelectrode' cathode was therefore ~ 0.012 cm^3.
The volume of liquid electrolyte (1M $LiPF_6$ in EC:DMC (1:1)) in the cell was approximately 5 cm^3. The ratio of cathode: electrolyte volume in the microelectrode cell was therefore ~ 0.0012 :5. This was compared to the much smaller ratio of approximately 1:2.5 for the conventional cell design; based on a 100 µm thick (0.0095 cm^3) composite electrode pellet and an ~ 200 µm thick (0.023 cm^3) electrolyte soaked separator.
The presence of an SEI on the lithium electrode in conventional $LiFePO_4$ | 1M $LiPF_6$ in EC:DMC (1:1) | Li cells was confirmed using AC impedance spectroscopy.

AC impedance experiments were performed at regular intervals during cell relaxation immediately after construction in order to monitor initial SEI formation. An example relaxation / AC impedance result is shown in Figure 3.3.6a.

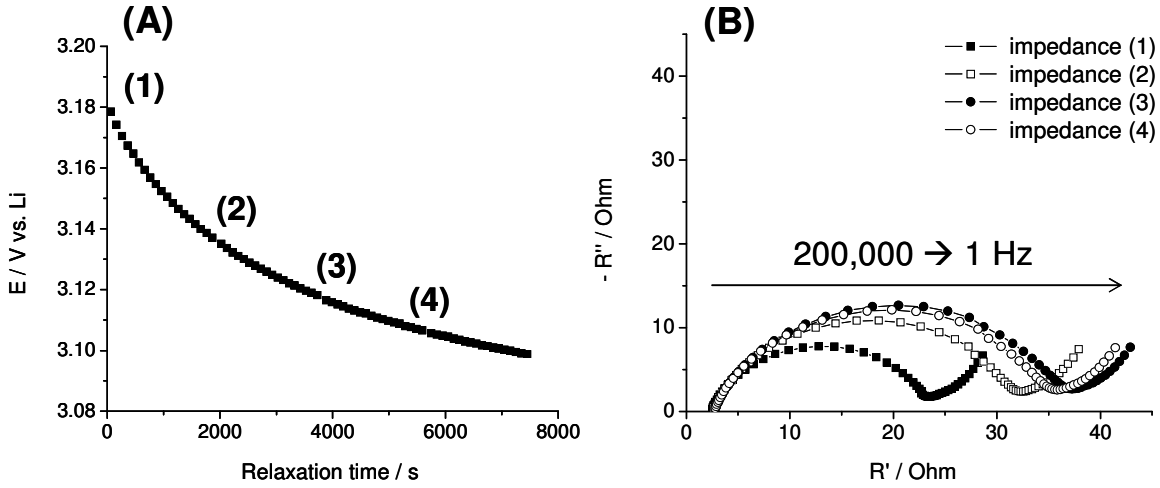

Figure 3.3.6a. (A) Example open circuit relaxation of 120 µm thickness $LiFePO_4$ composite electrode | 1M $LiPF_6$ in EC:DMC (1:1) | Li cell, numbers represent intervals during which impedance experiments were performed. (B) Example impedance plots (1-200,000 Hz) showing increasing impedance with increasing relaxation time (impedance 1, 2, 3 and 4 correspond to positions 1, 2, 3 and 4 in Figure 3.3.6a(A)).

The example AC impedance characteristics were typical for all thicknesses of $LiFePO_4$ composite electrode | 1M $LiPF_6$ in EC:DMC (1:1) | Li cells, the one exception being the shift to larger resistance values corresponding to increasing electrode thickness.

The general form of the AC impedance result was typical for a lithium-ion cell [70-72]. Initially a small uncompensated resitance was seen, probably corresponding to the resistance of the electrolyte and current collectors plus any electrical connections / instrumental impedance. The main feature is the depressed semi-circle corresponding to a combination of the Li SEI / electrolyte and $LiFePO_4$ composite / electrolyte interfaces. The final feature is the low frequency Warburg like (~ 45° phase) region describing diffusion in the $LiFePO_4$ composite.

However the most important feature seen in Figure 3.3.6a(B) was probably the relationship between increasing impedance and increasing cell relaxation time. During the initial period of relaxation (~0-1800 seconds) the increase in impedance, Figure 3.3.6a(A) 1 to 2, was 10 Ohms. However at increasing relaxation times (between ~1800-3600 and ~3600-4400 seconds) the increase in impedance, Figure 3.3.6a(A) 2 to 3 and 3 to 4, was 4 and 1 Ohm

respectively. The significance of the gradually decreasing increase in impedance becomes apparent when considering the initial SEI formation. It was suggested that the gradually decreasing increase in impedance corresponded to the formation of a self-limiting SEI layer on the anode surface. The initially large increase in impedance was attributed to SEI formation due to the reaction of lithium with the electrolyte [72-74] the passivating nature of the SEI gradually protected the Li from the electrolyte, inhibiting or slowing the growth of the SEI film and therefore offering an explanation for the decreasing impedance increase.

As previously stated the prototype $LiFePO_4$ 'microelectrode' cell was created in order to remove high discharge rate limitation due to the passivating layer (SEI) on the Li electrode. The business end of the cell was the $LiFePO_4$ composite 'microelectrode'; a 1.2 mm diameter, 1 mm deep, cavity filled with $LiFePO_4$ composite electrode material (3.2.2).

As with the conventional $LiFePO_4$ | 1M $LiPF_6$ in EC:DMC (1:1) | Li cells an AC impedance experiment was performed on the $LiFePO_4$ 'microelectrode' based cells, the AC impedance was measured over 200,000 – 1 Hz taking an average of three readings per frequency and 10 readings per decade; the AC impedance response is shown in Figure 3.3.6b.

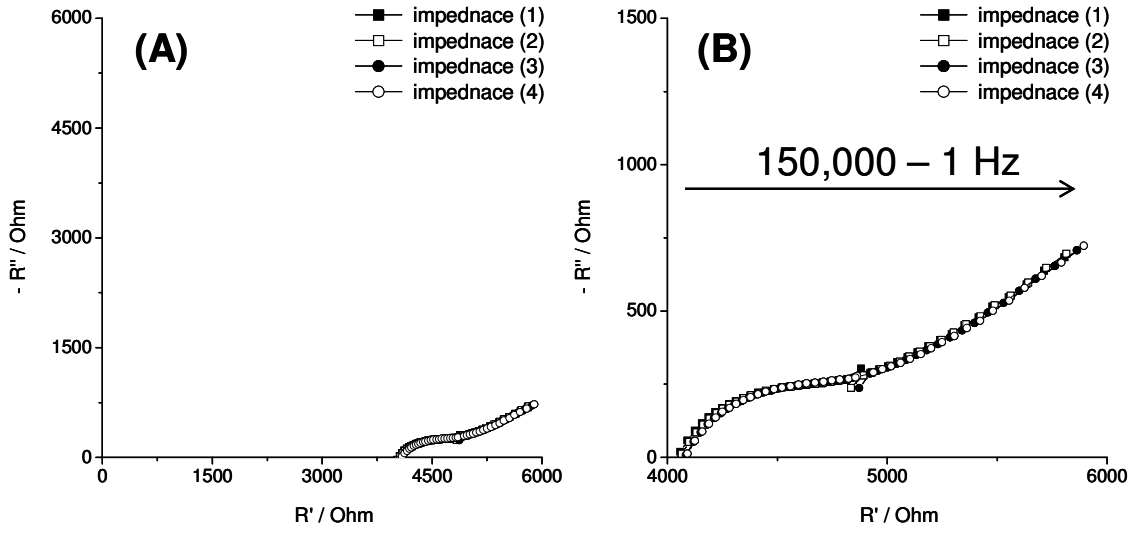

Figure 3.3.6b. (A) AC impedance (200,000 – 1 Hz*, 10 points per decade) response of the $LiFePO_4$ 'microelectrode'| 1M $LiPF_6$ in EC:DMC (1:1) | Li cell. (B) Expanded AC impedance response. The first few data points (200,000 – 150,000 Hz) have been omitted to remove high frequency artefacts.

The most notable feature of the $LiFePO_4$ 'microelectrode' cell impedance is the high uncompensated impedance (~ 4000 Ohms). The high resistance was attributed to a combination of contact resistance between the $LiFePO_4$ composite electrode and its current collector (Figure 3.2.2a) and the increased resistance due to the considerable thickness of the $LiFePO_4$ 'microelectrode'.
The considerable increase in resistance with cell relaxation, Figure 3.3.6a, was not seen in the $LiFePO_4$ 'microelectrode' based cell, though this was likely due to the much larger resistances of the $LiFePO_4$ 'microelectrode' dwarfing any Li anode resistance effects.

The $LiFePO_4$ 'microelectrode' based cell was cycled galvanostatically at discharges rates of 0.1, 0.2, 0.5, 0.75, 1, 1.5, 2, 3, 4 and 5 C, for 2 cycles at each rate, and at a constant charge rate of 0.1 C (The range of discharge rates was shifted compared to discharge rates seen in Y.3.2 to take into account the increased thickness of the electrode).
The plot of discharge potential *vs.* discharge capacity at differing C-rates is shown in Figure Y.3.6c. As in Y.3.2 the discharge capacity at each discharge rate was calculated and the discharge capacity plotted as a function of inverse C-rate (Figure 3.3.6d).

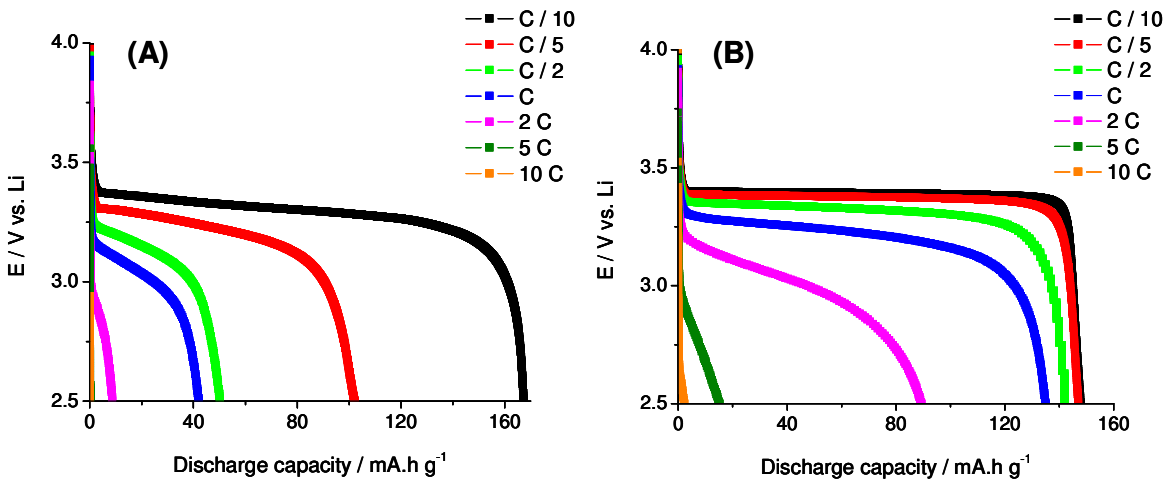

Figure 3.3.6c. (A) Discharge potential *vs.* discharge capacity for the $LiFePO_4$ 'microelectrode' | $LiPF_6$ EC:DMC 1:1 | Li foil cell at a variety of C-rates. (B) Discharge potential *vs.* discharge capacity for a 200 µm thick $LiFePO_4$ composite electrode | $LiPF_6$ EC:DMC 1:1 | Li foil cell at a variety of C-rates.

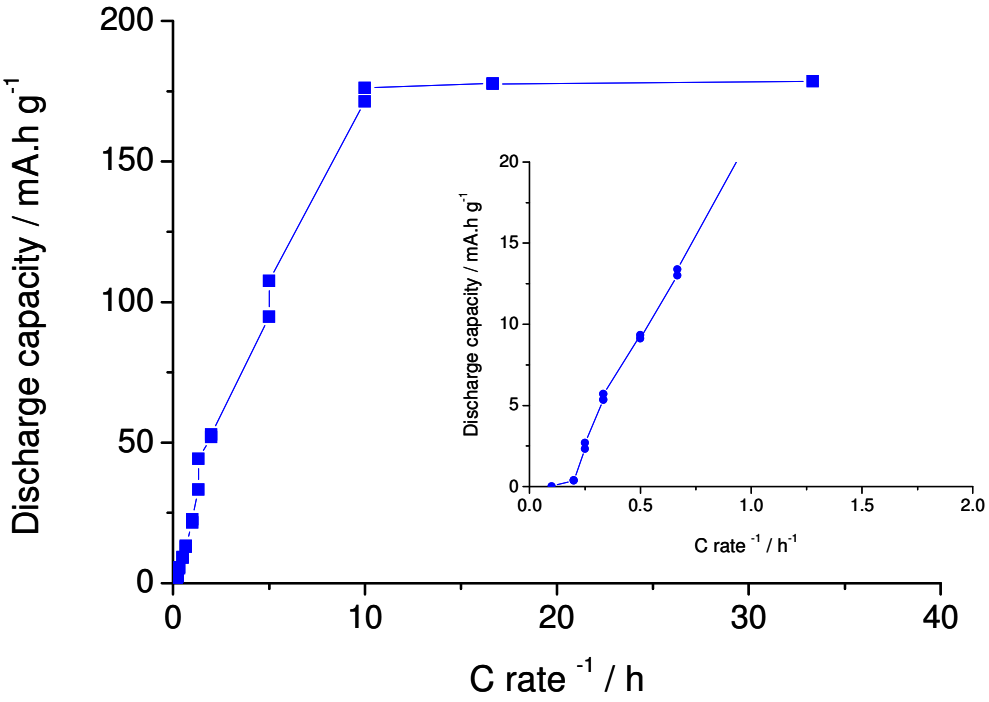

Figure 3.3.6d. Discharge capacity plotted against inverse C-rate for the $LiFePO_4$ 'microelectrode' | $LiPF_6$ EC:DMC 1:1 | Li foil cell. Inset, expanded vies of 'high-rate' region.

The increased resistance (Figure 3.3.6b) of the $LiFePO_4$ 'microelectrode' construction (~500 µm) when compared to the 'conventional' $LiFePO_4$ cells (Figure 3.3.6a), severely limited the performance during discharge at increased C-rates. This is immediately apparent when comparing the plots of discharge potential *vs*. discharge capacity for a conventional 120 µm thick $LiFePO_4$ composite electrode with that of the $LiFePO_4$ 'microelectrode' cell, Figure 3.3.6c.

The increased thickness of the electrode leads to a larger resistance which manifests itself as an increase in the gradient (in the two-phase region) of the discharge plateaux, Figure 3.3.6c(A), when compared to the cell containing the 200 µm think conventional composite electrode, Figure 3.3.6c(B).

However, the plot of discharge capacity *vs*. inverse C-rate, Figure 3.3.6d, shows a much clearer transition between the semi-infinite (where the SDF analysis applies) and finite (where the SDF analysis does not apply) regions (Figure 3.3.3a) than the same plots based on the conventional composite electrode based cells, Figure 3.3.2g. It is suggested that the greater volume of electrolyte, compared to the volume of electrode material, in the 'microelectrode' meant a more constant concentration of Li salt in the bulk electrolyte

($[LiX]_0$, Equation 3.3.4a), better fitting with the assumptions made in the SDF analysis (3.1.2).
Disappointingly the 'microelectrode' configuration did not appear to decrease the uncompensated resistance of the cell, probably due to the large increase in resistance of the thicker $LiFePO_4$ electrode. As such there is no visible decrease (if anything there is an increase) in the instantaneous IR drop of the microelectrode cell when compared to cell containing the conventional 200 µm thick electrode, Figure 3.3.6c.
As such the Y-axis intercept, also seen in Figure 3.3.5b, is still visible in Figure 3.3.6d (Inset).

A great deal of further work was conceived for the 'microelectrode' style cells. In order to drastically reduce the resistance of the $LiFePO_4$ 'microelectrode' assembly reducing the thickness of the electrode was suggested, this would be achieved through optimisation of the electrode assembly technique. A range of 'microelectrode' cells with thickness analogous to those used in the electrode thickness effect experiments, 3.3.2, would allow an analysis of the $LiFePO_4$ composite electrode diffusion coefficient, as in 3.3.3 and 3.3.4.

3.4. Conclusions

The rate limitation in $LiFePO_4$ composite electrodes in $LiFePO_4$ | 1M $LiPF_6$ in EC:DMC (1:1) | Li cells has been investigated. A simple model describing the diffusion limitations through the electrolyte phase has been presented, i.e. the Sharp Discharge Front (SDF) model (3.1.2).

A series of cells containing $LiFePO_4$ composite electrode of differing thicknesses were discharged at a variety of C-rates; as expected the rate capability showed a significant dependence on electrode thickness (3.3.2). The diffusion coefficient in the composite electrode (D) was initially estimated using the Sand equation, 3.3.3.
According to the sand equation analysis D was estimated at 6×10^{-8} cm^2 s^{-1}, somewhere between the literature values for the diffusion coefficient of $LiFePO_4$ ($10^{-14} - 10^{-16}$ cm^2s^{-1} ([65])) and $LiPF_6$ in non-aqueous electrolyte (PC/EC/DMC) ($3\text{-}4 \times 10^{-6}$ cm^2 s^{-1} [66]).
The calculated value of D was closer to the diffusion coefficient of $LiPF_6$ in non-aqueous electrolyte; this result was expected due to the nature of the rate limitation, i.e. lithium ion / salt diffusion in the electrolyte phase, rather than solid state diffusion in the $LiFePO_4$ particles (where the particle size is < 1 μm). It was suggested that the tortuosity and porosity of the composite electrode structure (Figure 3.3.3d) was the cause of the two orders of magnitude difference in diffusion coefficient for the $LiPF_6$ based electrolyte in the 'liquid' and in the composite electrolyte structure.

The same results were analysed according to the SDF model analysis (3.3.4), D was estimated at 2.4×10^{-7} cm^2 s^{-1} (averaged over C –rates where the SDF analysis was applicable). This value was an order of magnitude higher than the value calculated using the sand equation analysis, though given the approximations and errors involved in both analyses this is perhaps not unexpected. As with the sand equation analysis the estimated value of D was in-between values for the diffusion coefficient of $LiFePO_4$ and $LiPF_6$ in non-aqueous electrolyte (PC/EC/DMC), again this was attributed to the effect of the composite electrode structure.

An interesting, though somewhat qualitative, experiment involved the comparison of the effect of thickness on the rate capability of two different types of $LiFePO_4$ composite electrodes (3.3.5).

Two sets of cells were constructed each with a range of electrode thicknesses (40 – 200 µm); cells were based on either nano $LiFePO_4$ (Hydro Quebec, particle size < 1 µm)| 1M $LiPF_6$ in EC:DMC (1:1) | Li or $LiFePO_4$ (Aldrich, particle size ~ 1-5µm)| 1M $LiPF_6$ in EC:DMC (1:1) | Li.

The cells were discharged at a variety of C-rates, as in 3.3.2, the results were plotted as discharge capacity *vs*. inverse C-rate, as Figure 3.3.2g, where a steeper gradient in the semi infinite region indicates a better rate performance. For the majority of thicknesses the rate performance of the larger particle Aldrich cells was no worse than the smaller particle Hydro Quebec cells, however in the case of the thinnest electrode (40 µm) the performance of the larger particle Aldrich material cells appeared worse.

The rate performances of the two types of cell are summarised in Table 3.3.5a.

It was suggested that for thin electrodes containing large particles of active material the effect of particle size, i.e. solid state diffusion / shrinking core model, becomes increasingly significant compared to the limitation of salt diffusion in the electrolyte phase.

The $LiFePO_4$ microelectrode experiment (3.3.6) was designed to address several anomalies within the results of the rate / thickness and particle size experiments. In both cases a Y-axis intercept was noted on the discharge capacity *vs*. inverse C-rate plots corresponding to a high rate discharge limitation that was independent of electrode thickness.

It was thought that the rate limitation was due to uncompensated cell resistance, rather than electrode resistance, resulting in a large instantaneous IR drop that pushed the discharge plateaux below the negative experimental potential cut-off.

In order to minimise the IR drop within the cell a $LiFePO_4$ 'microelectrode' cell was designed (3.2.2), the key features of the 'microelectrode' cell are listed in 3.3.6.

The microelectrode design significantly improved the quality, in terms of the clarity of transition between semi-infinite and finite regions (Figure 3.3.3a), of the discharge capacity *vs*. inverse C-rate plot (Figure 3.3.6d)

However, both the AC impedance and galvanostatic discharge results (Figures 3.3.6b and c respectively) showed large uncompensated resistance, and an intercept was still visible on the capacity *vs*. inverse C-rate plot (Inset Figure 3.3.6d). The large resistance in the $LiFePO_4$ 'microelectrode' cells was attributed to the increased thickness of the $LiFePO_4$ composite electrode; it is suggested that improving the construction method to significantly reduce the thickness of the composite electrode would remove a large portion of this resistance.

The 'final' experiment in this series of experiments would be the construction of a range of 'microelectrode' cells with thickness analogous to those used in the electrode thickness effect experiments, 3.3.2.

The results of discharging these cells at different C-rates would allow an analysis of the composite electrode diffusion coefficient, as in 3.3.3 and 3.3.4, and ultimately a more accurate calculation of the diffusion coefficient within the composite electrode.

Chapter 4

3D Lithium-ion Microbatteries

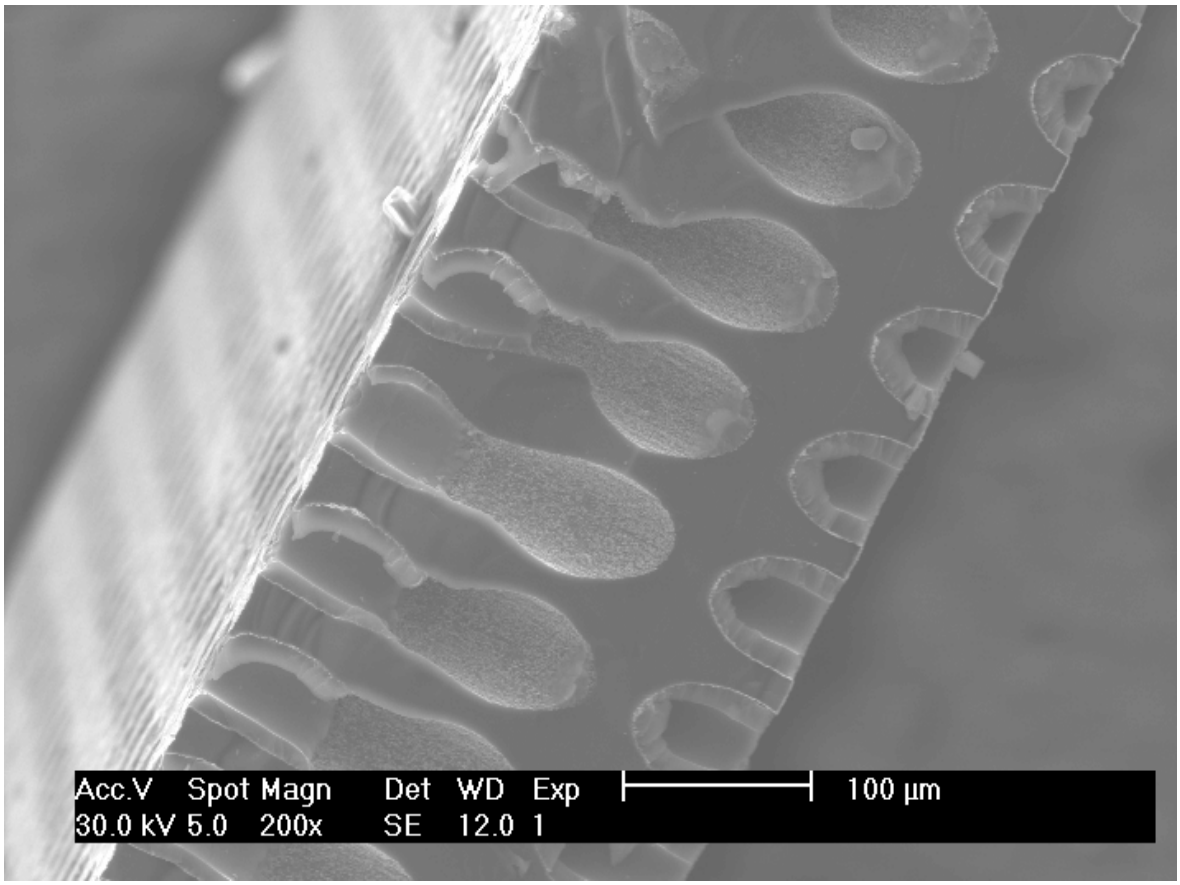

4.1. High Rate Cells

The rate capability in Li-ion cells is dependant on a number of factors, and as a general rule the larger the cell the greater the current it can supply (due to a decrease in the internal resistance with increasing internal surface area of the electrodes); the easiest way to achieve higher rate capabilities is often to use bigger cells.
However, for many applications large cells are simply not suitable; the microelectronics industry is continually downsizing its technology to produce smaller and smaller devices. These devices have a wide range of applications including; medical implants, micro sensors, self powered integrated circuits and use in microelectromechanical systems (MEMS) [18, 75-77].
The recent surge in development of MEMS is a particular driving force for the development of a reliable and versatile high rate microbattery system. The need for high rate discharge capability in small cells typically arises in applications where space is at a premium and the function of the device requires relatively large current pulses; such as in a pacemaker or radio frequency identification technologies.

Strategies to achieve fast charge and discharge rates in Li-ion cells (without simply increasing the size of battery) include keeping the electrodes thin, and the distance between them very small, thus minimising the Li ion transport distance (L) Figures 4.1a and b. This strategy has been utilised in the development of thin film cells [78-82].

The term thin film usually refers to a planar semiconductor device that is made by physical or chemical vapour deposition, and the electrode materials and electrolyte are solid ceramics or glasses. Thin film microbatteries (Figure. 4.1a) are designed for small scale applications where high storage capacities are not required. Starting with a current collector, the cell is built by depositing the layers of electrodes, electrolyte and current collectors.

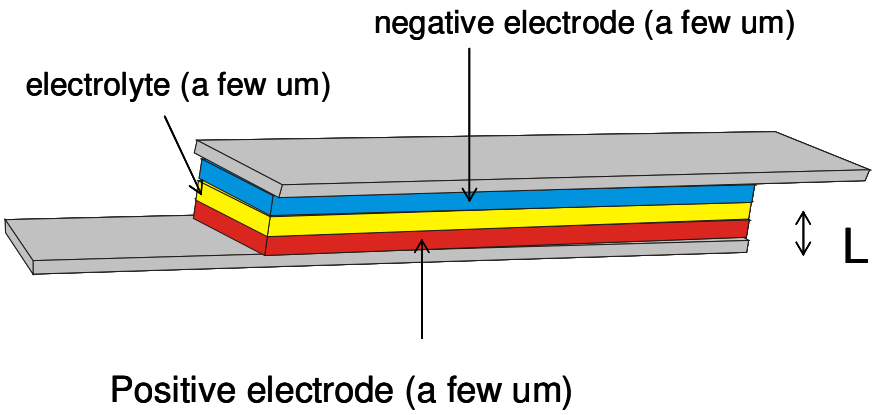

Figure 4.1a. Schematic representation of a'2D' thin film cell. Typical anode, cathode and electrolyte materials include lithium, TiS_2 and lithium phosphorus oxynitride respectively. L represents the total lithium ion transport distance between the two electrodes.

The rate capability of the thin film type cell is derived from the very short total lithium ion-transport distance (L). However, in order to keep this distance small the cathode and anode must remain as thin as possible; therefore the cell capacity (i.e. the total volume of active material in the electrodes) can only be increased by increasing the footprint area.
Increasing the footprint area affects the available capacity; capacity is usually measured according to the gravimetric (also known as specific) or volumetric capacity, mA h g^{-1} and mA h cm^{-3} respectively. However, in applications where a battery with minimal footprint area is desirable, a more appropriate measure of capacity is the amount available per unit area, i.e. mA h cm^{-2}.
The dependence of capacity on footprint area makes thin film cells unsuitable for many of the applications described previously; the need for high power batteries, with small footprint areas and greater capacities than would be available from thin film cells has led to the development of the 3D microbattery concept. The 3D microbattery retains the concepts of the thin film cell but improves upon the capacity per unit area by structuring the cell in the 3rd dimension, the 3D microbattery concept is illustrated in Figure 4.1b.

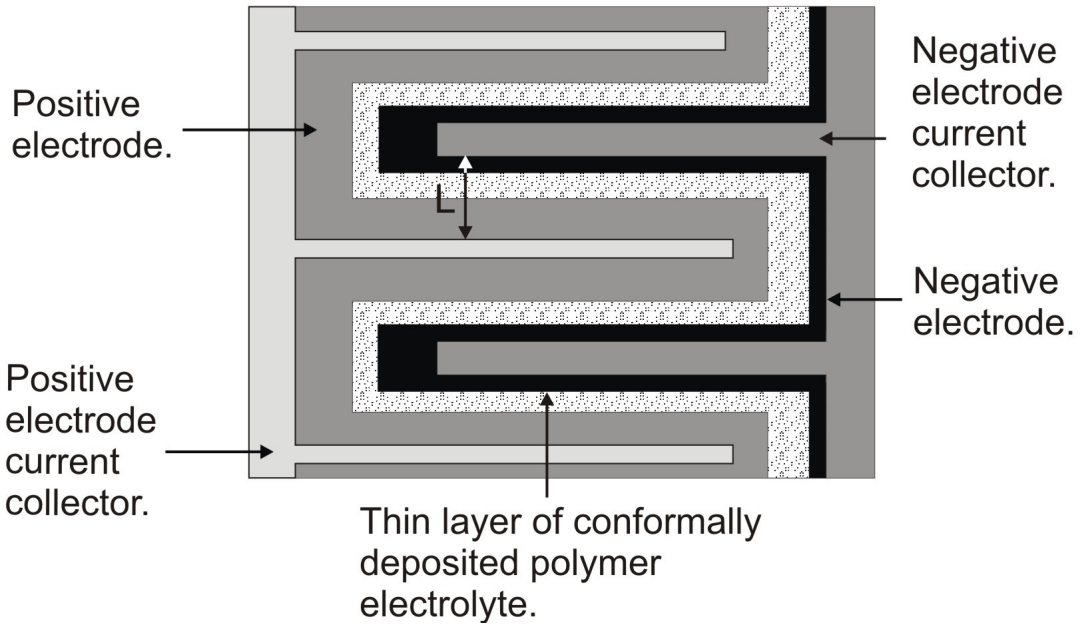

Figure 4.1b. Illustration of the cross section of a generic 3D Li-ion microbattery design.

The cross sectional illustration of the 3D microbattery concept shown in Figure 4.1b highlights the key concepts of the 3D microbattery design. As with is the case in thin film cells, the overall Li-ion transport distance (L) remains small, but the surface area of the electrodes has been greatly increased. This increased surface area means a greater amount of active material in the electrodes and therefore more capacity. The 3D Li-ion microbattery concept effectively takes a thin film cell and concertinas it up to occupy a smaller footprint area. Research into 3D Li-ion microbatteries has received much recent interest, discussed in 4.2, and has been summarised in several review papers [77, 83, 84]

There are a number of possible configurations that have been suggested for microbattery applications; these are illustrated in Figure 4.1c and discussed in greater detail in Chapter 5.

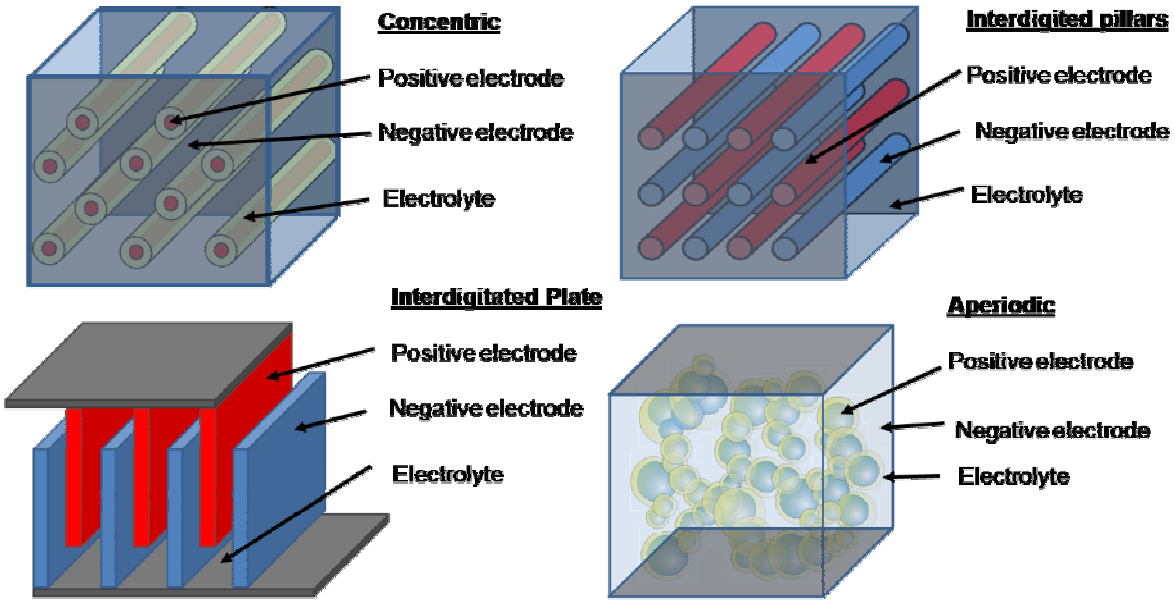

Figure 4.1c. Diagrams illustrating concentric, interdigitated pillar, interdigitated plate and aperiodic 3D lithium-ion microbattery designs.

4.2. Current Concepts in 3D Li-ion Microbattery Design

This section aims to briefly describe some of the most interesting 3D Li-ion microbattery designs currently under development. The particular designs highlighted were chosen to be representative of the range of designs being considered and demonstrate the variety of different approaches under development; as such the papers represent just a small selection of research concerning 3D microbatteries.

One of the most developed 3D microbattery designs is based around the concentric configuration, Figure 4.1c.Work carried out by Nathan et al [85] focused on the deposition of conformal battery materials on glass or silicon 'micro channel plates' (MCP, essentially silicon or glass wafers perforated by a regular array of microchannels). This work was probably the first literature example of a 'functioning full 3D' lithium ion microbattery. The structure of their 3D microbattery was based on high aspect ratio channels onto which thin films of cathode and polymer electrolyte were deposited; the remaining volume in the channel being filled with a slurry containing the anode. Fabrication involved depositing a current collector onto the silicon substrate, in this case Ni, onto which an electrodeposited cathode (molybdenum sulphide) was electroplated. The polymer electrolyte was based on PVDF and was deposited onto the molybdenum sulphide through the depth of the microchannel using what was described as 'sequential spin-coating and vacuum pulling steps'. The anode was a slurry containing mesoporous carbon microbeads (MCMB's), polymer binder and solvent (also deposited into the microchannel using sequential spin-coating and vacuum pulling steps). Once constructed the whole assembly was soaked in 1M $LiPF_6$ in EC : DEC or 1M $LiBF_4$ in EC : DEC under vacuum for 10 hours. Lithium foil placed on top of the structure provided lithium intercalation into the anode.
Figure 4.2a shows the schematic 3D microbattery construction (a) and the cross section (b).

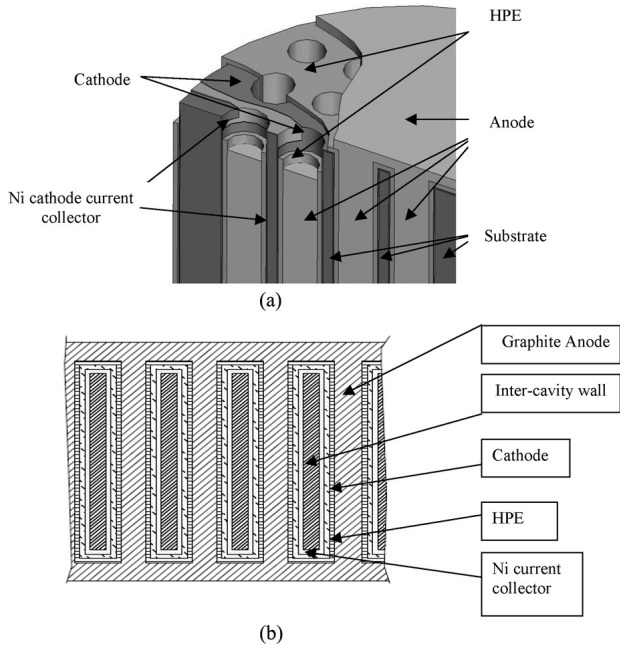

Figure 4.2a. Schematic view of the concentric 3D microbattery (a), and cross section through the microchannel plate (b).[85]

The 3D microchannel plate cell and the 2D planar equivalent were tested in parallel by galvanostatic cycling, between 2.2 and 1.3 V *vs*. lithium, in order to compare the available capacity (mA.h cm^{-2}).Figure 4.2c shows the comparative results.

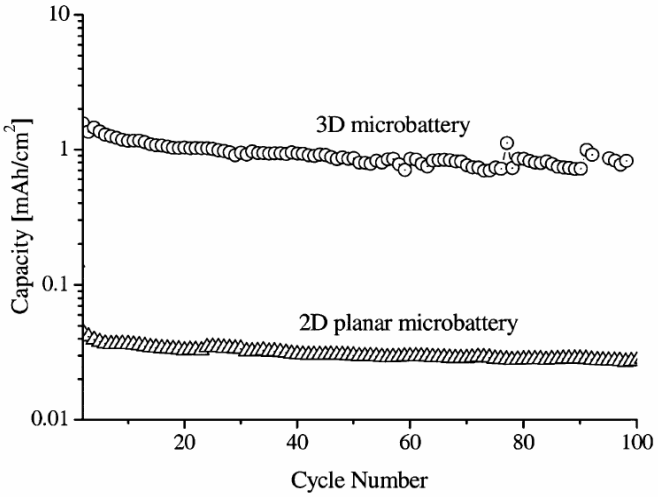

Figure 4.2c. A comparison of the capacity (mAh cm^{-2}) extracted from the 3D microchannel plate and 2D planar configurations.[85]

The results presented in Figure 4.2c clearly show the advantage of the 3D system over the 2D design. It can be seen that the 3D system had much greater capacity that the 2D system,

due to the area gain from the 3D structure (the capacity gain corresponds to the increase in surface area). Although there was some indication of the rate performance of the 3D system, the paper does not show results comparing the capacity at high rate of the 3D MCP and 2D systems. It is worth noting the authors have published several similar papers based on microchannel plate systems [75, 76, 86, 87]

An alternative silicon based system has been reported by Notten et al [88]; this differs from the previously described silicon based system in that it is based on the interdigitated plate type design, Figure 4.1c. This system was slightly unusual in its use of a solid state electrolyte. The paper demonstrated the advantage of using the solid electrolyte LiPON (lithium phosphorous oxynitride) over conventional liquid electrolytes for thin film silicon anodes. Thin film half cells based on a silicon anode (50 nm) were cycled *vs*. lithium using conventional organic lithium-ion and solid state LiPON electrolytes. The paper reports evidence of the suppression of the SEI on the silicon anode by the LiPON electrolyte leading to increased cycling stability, when compared to the organic lithium-ion electrolyte (Figure 4.2d).

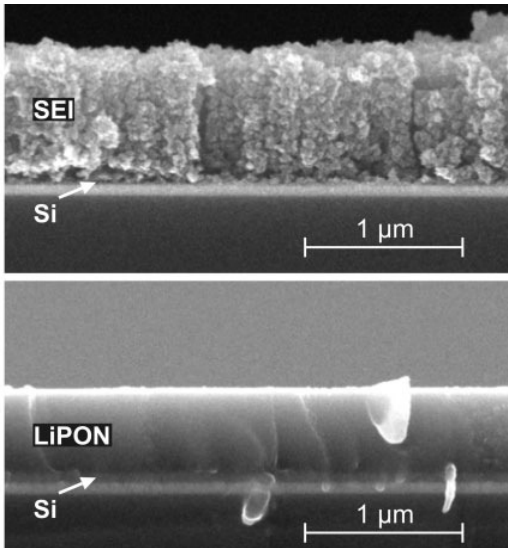

Figure 4.2d. Cross-section of the Si/liquid electrolyte interface (upper photograph) and Si/LiPON interface (lower photograph) after electrochemical cycling [88].

By using single crystalline silicon as highly ordered high surface area substrate / current collectors containing high aspect ratio pores (reactive ion etching); the authors suggested an all solid-state 3D microbattery based on a solid state electrolyte, Figure 4.2e.

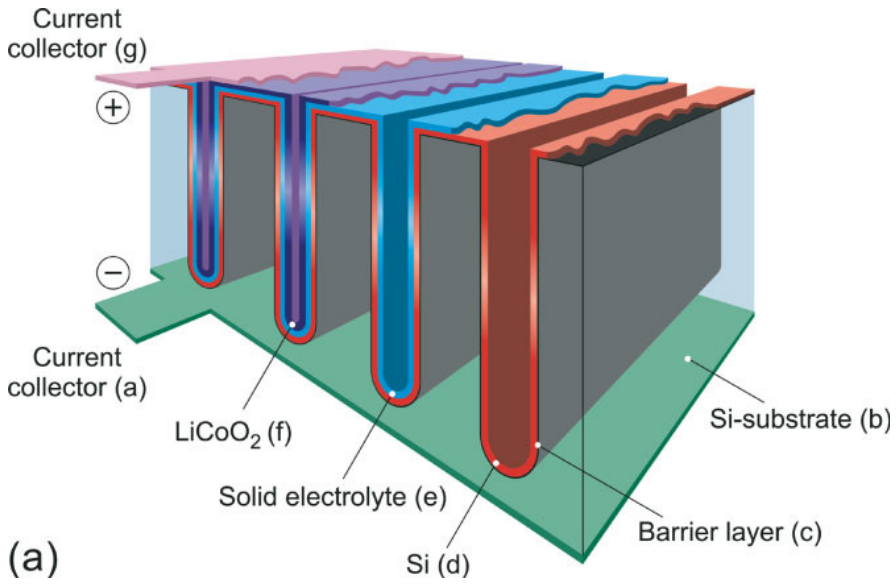

Figure 4.2e. 3-D integrated all-solid-state Li-ion battery for which surface enlargement has been accomplished by electrochemical or Reactive Ion Etching (RIE) of a silicon substrate [88].

An example of the interdigitated pillar design has been developed by Min *et al* and was based on arrays of high aspect ratio carbon / polypyrrole pillars [89]. The cathode and anode current collectors were both carbon and produced by photolithographic patterning of photoresist on silicon wafers. The carbon tracks and high aspect ratio pillars were produced from pyrolysis of the cross linked polymer based photoresist. Dodecylbenzenesulfonate doped polypyrrole (PPYDBS) was electrodeposited onto one current collector array to form a cathode; the second array of carbon pillars was used as the anode and 1M $LiClO_4$ in 1:1 EC-DMC electrolyte completed the cell. Figure 4.2f shows a completed array of carbon and PPYDBS electrodes on their individual current collectors.

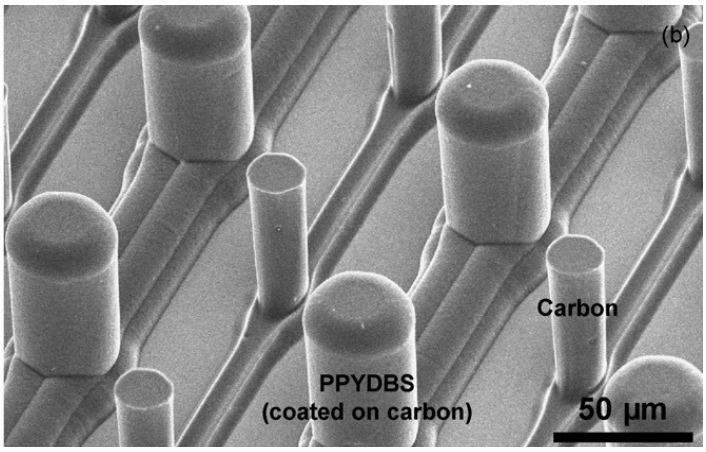

Figure 4.2f Carbon and PPYDBS electrodes on individual current collector arrays.

The authors compared the gravimetric capacity of half cells of the 3D PPYDBS electrodes to their 2D equivalents and found the 3D configuration to have slightly better performance (37.9 mAh g^{-1} at 1.15 C for the 3D and 23.4 mAh g^{-1} at 0.9 C for the 2D configuration). The increase in performance of the 3D PPYDBS electrodes was attributed to the larger active surface area and the effect of the electrolyte penetration into the entire electrode as compared to the planar front that the electrolyte makes with the 2D PPYDBS electrode. The authors also presented results of a prototype full 3D microbattery system where the PPYDBS cathode was cycled against the carbon pillar anode. However, alongside a lower than expected capacity per unit area the system was found to have problems with electronic short circuits, leading to self discharge and limited discharge capacities. The system also suffered from large internal resistances attributed to the relatively high resistance of the carbon current collector arrays. Although the microbattery demonstrated showed some serious shortcomings, the work raised some interesting questions regarding the need for a separator in this type of microbattery configuration to exclude the possibility of short circuits due to mechanical failure of the structure.

Research carried out by Kotobuki *et al*.[90] used an alternative approach to the construction of a 3D microbattery (when compared to the majority of papers). Here the microbattery was based around a 'honeycomb' structured $Li_{0.35}La_{0.55}TiO_3$ (LLT) solid electrolyte. The schematic 'honeycomb' configuration is illustrated in Figure 4.2g.

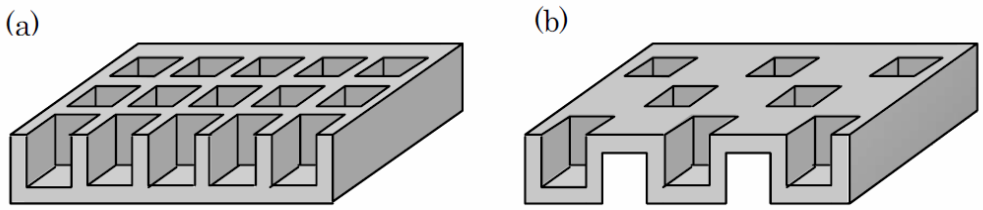

Figure 4.2g. Illustration of LLT honeycomb structures, half honeycomb structure with 400 holes on one side of LLT membrane (a) and full honeycomb structure with 200 holes on each side of LLT membrane (b). The hole size was 180 µm x 180 µm x 180 µm [90].

Sol-gel precursors of the cathode and anode materials $LiCoO_2$ and $Li_4Mn_5O_{12}$ were injected (vacuum impregnation) into opposing sides of the microstructured electrolyte, and subsequently calcined to form the full 3D microbattery, Figure 4.2h.

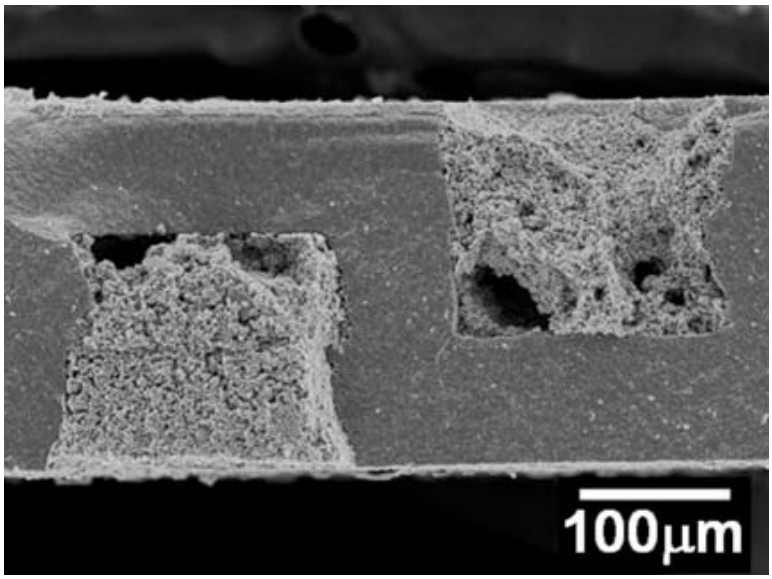

Figure 4.2h. Cross section of $LiCoO_2$ | LLT | $Li_4Mn_5O_{12}$ cell [90]

Cyclic voltammetry of the solid electrolyte / lithium half cell showed the electrolyte to be stable in the region 2.5-5 V *vs*. lithium. However the CV showed some redox activity below 2.5 V *vs*. Li, attributed to reduction of titanium in the $Li_{0.35}La_{0.55}TiO_3$. To avoid this problem $Li_4Mn_5O_{12}$ (which has a lithium insertion potential of 2.8 V *vs*. Li) was used as the anode

The sol-gel derived $LiCoO_2$ and $Li_4Mn_5O_{12}$ was cycled *vs.* lithium and characterized according to redox potential and theoretical capacity (mA.h g^{-1}), the authors reported that both cathode and anode material performed according to expectations when tested in a normal cell configuration. When tested the $LiCoO_2$ | LLT | $Li_4Mn_5O_{12}$ microstructured half cells performed notably worse than expected, 0.22 and 0.99 mA.h / g for $LiCoO_2$ and $Li_4Mn_5O_{12}$ respectively.

The full $LiCoO_2$ | LLT | $Li_4Mn_5O_{12}$ cell was successfully assembled and tested; the cell exhibited a discharge voltage of ~ 1V but, as with the cathode and anode half cells, showed a very low discharge capacity of 7.3 μA.h /cm^2, stated as only 0.1% utilization of the limiting $LiCoO_2$ electrode. The authors attributed the poor performance of the $LiCoO_2$ | LLT | $Li_4Mn_5O_{12}$ half cells and the full 3D $LiCoO_2$ | LLT | $Li_4Mn_5O_{12}$ microbattery to several factors; firstly high contact resistance between the walls of the microstructured electrolyte and the active material, and secondly size of the 'honeycomb' electrolyte. The depth of the pores in the electrolyte was 180 μm, meaning a large diffusion distance of the lithium ion from the centre of the pore to the electrolyte. The authors noted that a reduction in the size of the electrolyte pore should improve the available capacity of the system. Regardless of the poor cell performance the paper demonstrated an interesting approach to the fabrication of a Li-ion microbattery, where the cell is constructed around the electrolyte scaffold.

Another example of an interdigitated plate design was demonstrated by Dokku *et al.*[91].The proposed system used independently addressable microarrays of gold current collectors, coated in either $LiMn_2O_4$ or $Li_{4/3}Ti_{5/3}O_4$ with a gel-polymer electrolyte. Photolithography was used to pattern a SiO_2 substrate with microarrays of gold current collectors. Sol-gel precursors of $LiMn_2O_4$ and $Li_{4/3}Ti_{5/3}O_4$ were then deposited onto the current collectors, using a micro injection system, before the precursors were calcined to form the electrode materials. Thermal polymerization of methyl methacrylate in the presence of 1M $LiClO_4$ EC:DMC (1:1) formed an electrolyte film that was placed onto the microarray of $LiMn_2O_4$ and $Li_{4/3}Ti_{5/3}O_4$. Lithium foil was placed on top of the electrolyte to allow half cell characterisation of the individual electrode arrays (Figure 4.2i).

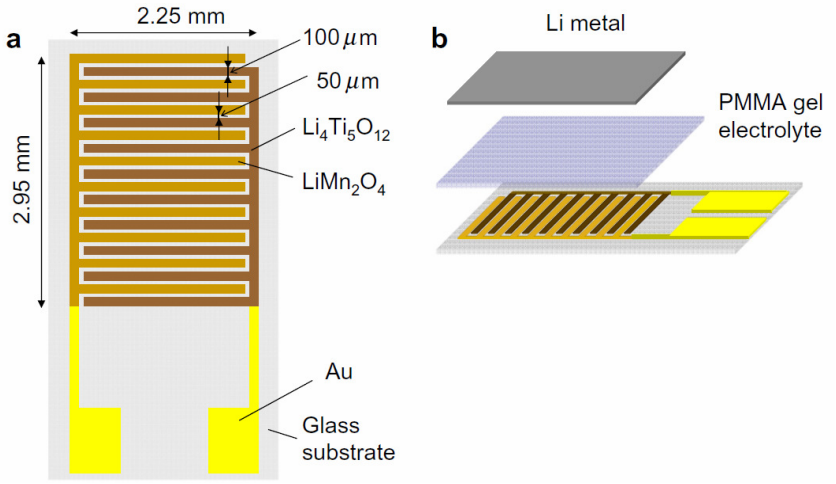

Figure 4.2i. Schematic illustrations of microarray electrodes of $LiMn_2O_4$ and $Li_{4/3}Ti_{5/3}O_4$ (a), and assembly of electrochemical cell (b) [91].

The microelectrode arrays of $LiMn_2O_4$ and $Li_{4/3}Ti_{5/3}O_4$ were characterized individually, using the lithium foil as the counter electrode. The lithium insertion / extraction behaviour is shown in Figure 4.2j, the reversibility of the CV's was used to suggest good cyclability of the electrodes.

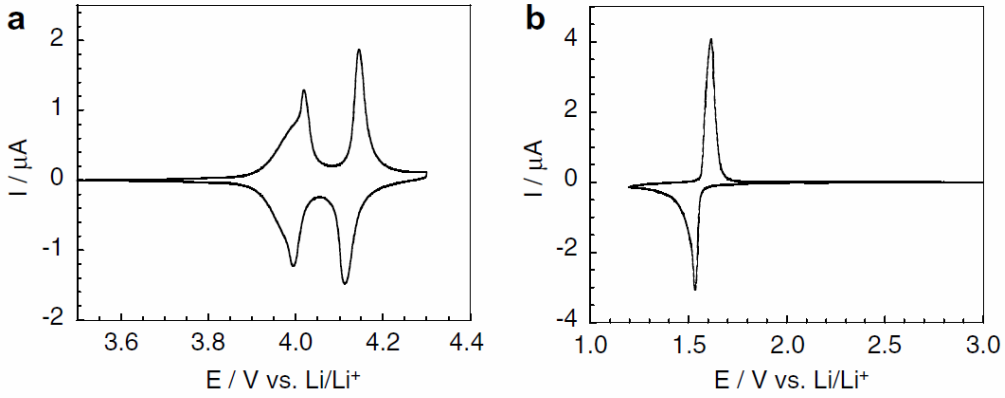

Figure 4.2j. Cyclic voltamogramms of microarray electrodes of $LiMn_2O_4$ (a) and $Li_{4/3}Ti_{5/3}O_4$ (b) [91].

Tested against each other, using an $LiMn_2O_4$ cathode and $Li4_{/3}Ti_{5/3}O_4$ anode, the microarray cell showed charge and discharge plateaus of 2.55 and 2.4V respectively, the rate performance of the cell is shown if Figure 4.2k. It is worth noting that a >50 % degree of discharge is seen at 50 C (~1 min discharge).

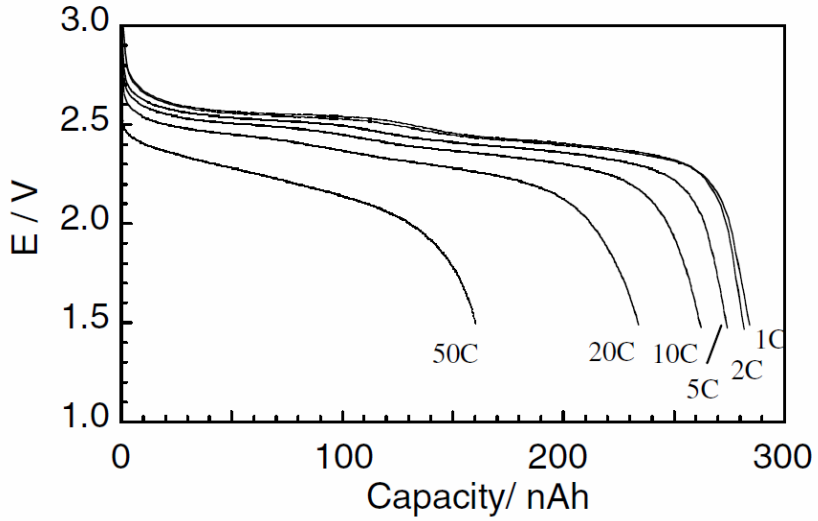

Figure 4.2.k. Discharge capacity (nAh) plotted at varying C rate for the $LiMn_2O_4$ / PMMA gel / $Li_{4/3}Ti_{5/3}O_4$ microbattery, the cell was charged at 1C for all rates [91].

The authors noted that although the system had good rate performance, which they attributed to the ionic conductivity of the polymer electrolyte and the short diffusion path of the lithium ions, the energy density compared unfavourably to thin film sputtered systems. Shortening the distance between the microelectrode arrays and increasing the thickness of the electrodes were suggested as possible methods of increasing the amount of electrode material present in the cell, therefore improving the energy density.

4.3. Conclusions

The papers described here go some way to demonstrating the wide variety of differing designs and fabrication techniques being used in the development of 3D Li-ion microbattery systems. However, despite the large variety of designs and the number of different institutions a practical and viable fully 3D Li-ion microbattery has yet to be realised. A number of hurdles remain before the 3D Li-ion microbattery can be considered as suitable for large scale production.

The approach of using etched or patterned supports, i.e. Si, for 3D microbatteries contributes a large non-electrochemically active component to the cell, reducing the volumetric and gravimetric capacity. Many designs have not fully addressed the issues of electrical connection to the cathode and anode current collector; this is especially true of some of the concentric type microchannel designs. Many of the designs based on high aspect ratio current collectors, especially when not constructed metallic current collectors, i.e. carbon based, will suffer from Ohmic losses associated with the transport of electrons through the structure.

Probably the most important challenge yet to be overcome is how to keep the cost of producing the cell low enough, especially considering the complicated and time consuming techniques proposed so far. The final issue for consideration will be devising a packaging solution without impacting too greatly on the size or energy density of the cell.

Chapter 5

3D Current Collectors and Substrates

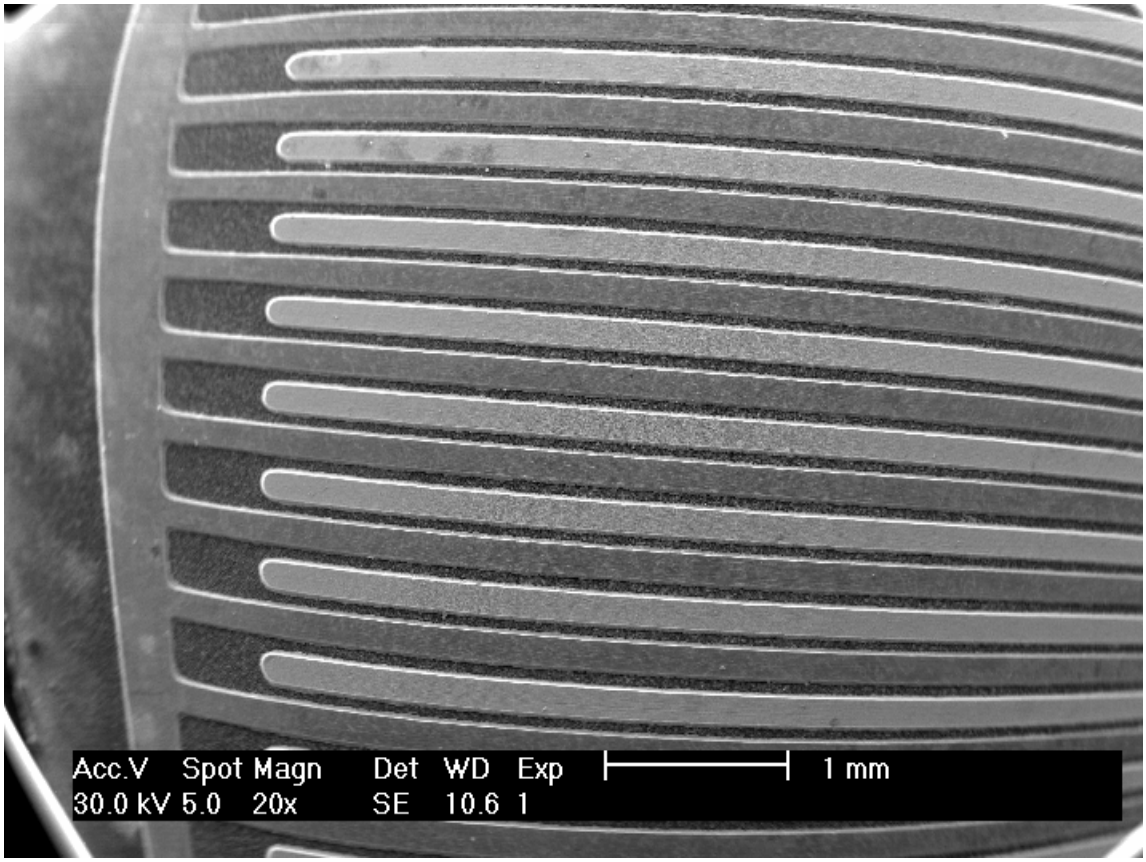

5.1. Introduction

There are a wide variety of possible configurations for the 3D lithium ion microbattery; however, common to all the designs is the need for an anode, cathode and an electrolyte. In many cases it is necessary to support either the cathode or the anode on a current collector backbone. Some of the designs that have been suggested in the literature [84] are illustrated in Figure 5.1.1.

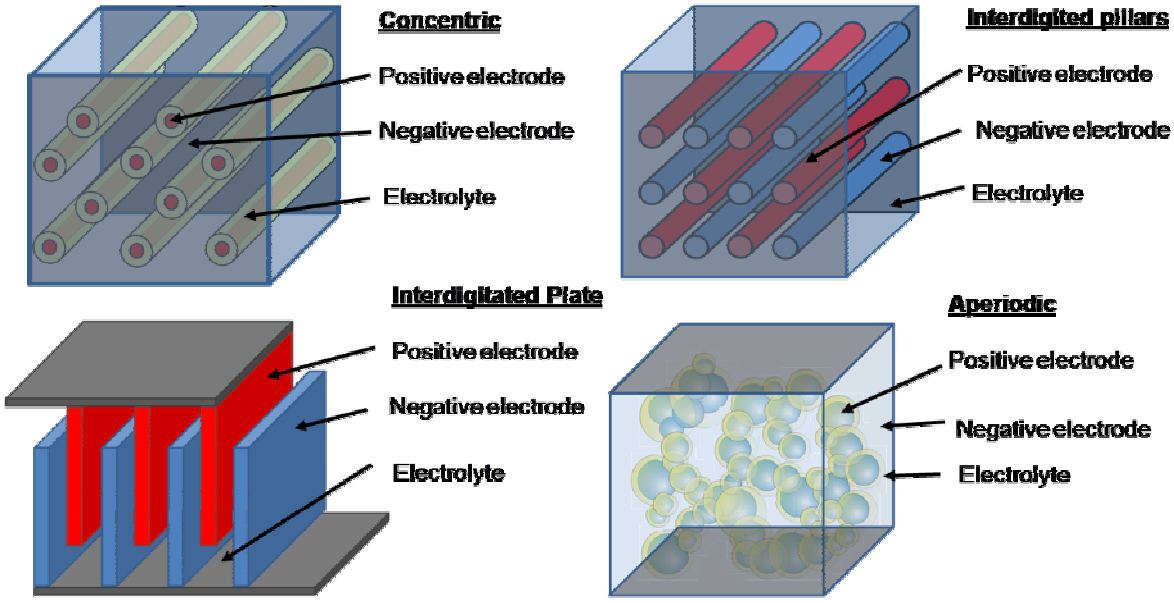

Figure 5.1a. Diagrams illustrating concentric, interdigitated pillar, interdigitated plate and aperiodic 3D lithium-ion microbattery designs.

The interdigitated pillar and interdigitated plate designs are relatively straight forward, at least in theory. The cathode and anode consist of high aspect ratio rods or plates, each connected to its own individual current collector, and separated by a space, into which an electrolyte of some sort is inserted in order to complete the cell. The cathode and anode structures can be either formed completely of the active material, as in [89, 92]; or the cathode / anode can be deposited onto a current collector support [93, 94].

The concentric type design is based is based on having an electrolyte coated electrode layer, anode or cathode, on a current collector support, with some remaining space into which the

second electrode can be inserted. Example of this kind of structure are shown by have been described extensively by Nathan *et al.*[75, 76, 85, 87].

The final type of design illustrated in Figure 5.1.1 is the aperiodic configuration; here the anode or cathode is based around an aperiodic network structure, where the first electrode coats the supporting structure (current collector) and is itself coated by the electrolyte and as in the concentric structure the second electrode fills the remaining volume. Examples of this design are less common in the literature but some research towards an aperiodic design has been reported [95].

The following experiments investigate the suitability of several 3D substrates for use in lithium ion microbattery systems. Initially carbon pillars were fabricated as the basis of a concentric type system. The process used to produce the carbon pillars was modified in order to fabricate a 'trench' like structure. The 3D carbon structures are referred to as carbon microstructure arrays. Finally, commercially available 3D foams were evaluated and used as substrates for aperiodic constructions.

5.2. Experimental

5.2.1. Fabrication of 3D Carbon Microstructure Arrays

Photolithographic patterning of photoresist films has been shown to be an effective route to the production of carbon microstructure arrays [89, 96, 97].
The basic procedure for the fabrication of the carbon microstructure arrays involved the deposition and patterning (via exposure to UV) of a photoresist layer on a carbon substrate. Once developed (removal of unwanted resist) the photoresist was pyrolised to form the carbon structures. Vitreous carbon (VC) plates (SIGRADUR® HTW, 2.5 x 2.5 x 0.1 cm) were used as the substrate for the carbon based microstructure arrays. In order to ensure sufficient wetting of the photoresist to the substrate, and to ensure the resulting bond was strong enough, the VC substrate was modified with a monolayer of amine terminated alkyl chains [98] (Figure 5.2.1.a).

A monolayer of 1-7, diaminoheptane was grafted to the VC surface by electroxidation of one amine group into an amine cation radical to form a covalent bond to the substrate surface, with the other amine facing away from the substrate into solution (Figure 5.2.1.a).

The VC substrates were polished (1 um alumina powder) and sonicated in deionised water (15 minutes) and then ethanol (15 minutes) before being dried under a stream of argon. The substrates (working electrodes) were immersed in a solution of 1-7, diaminoheptane (Sigma-Aldrich 98%) (0.02 M) and lithium perchlorate (Sigma Aldrich, ACS Reagent) (0.1 M) in Ethanol (Sigma-Aldrich, HPLC grade). The electroxidation of the amine was achieved using cyclic voltammetry 20mV s^{-1} between 0 and 1.2 V *vs.* Ag wire for 3-5 cycles using a Pt counter in the above solution. The surface modified VC electrodes were then rinsed in ethanol and deionised water, before being stored in deionised water.

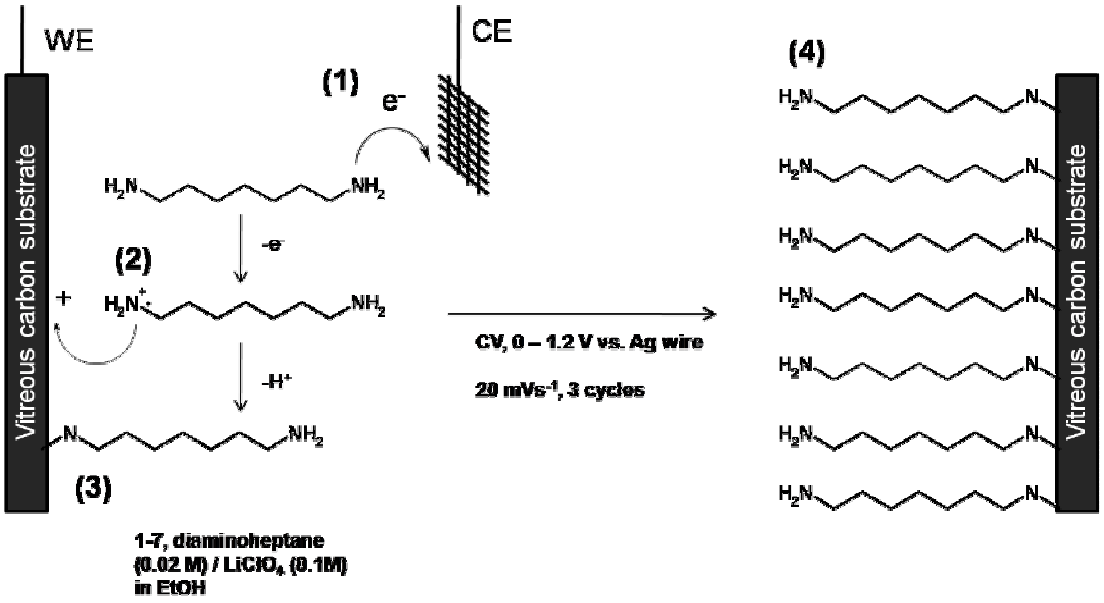

Figure 5.2.1a. Schematic representation of surface modification of VC. 1-7, diaminoheptane is electroxidised (1) to form cationic radical (2). Cationic radical bonds covalently to the VC substrate (3). The monolayer of aminoheptane molecules (4) is built up by cycling between 0 and 1.2 V *vs*. Ag wire at 20 mVs^{-1}.

The modified VC surface was characterised using the ruthenium hexamine ($Ru(NH_3)_6^{3+}$) and ferrocene carboxylic acid ($C_{11}H_{10}FeO_2$) redox couples as probes.
Modified and unmodified VC electrodes were cycled in aqueous solutions of $Ru(NH_3)_6Cl_3$ (2 mM) (Aldrich) / KCl (0.1M) (Sigma-Aldrich, 99%) and $C_{11}H_{10}FeO_2$ (1 mM) (Sigma-Aldrich, 97%) / K_2HPO_4 (0.1M) between 0.3 to -0.8 V *vs*. SCE and 0.6 to -0.3 V *vs*. SCE respectively at 100 mVs^{-1}.

The procedure for the lithographic patterning and formation of the carbon microstructures on the modified VC substrates varied depending on the particular type of structure.
The procedures for formation of carbon micropillars (25 μm high x 5 μm diameter) and trench arrays (2.5 cm x 100 μm x 20μm) are detailed below (the spinning of photoresist, patterning and development was undertaken in a cleanroom under an absence of UV light).
For the micropillar structures a 25 μm thick film of photoresist (SU8-25, Microchem) was spun onto the treated VC substrates (2.5 x 2.5 cm). Roughly 1 ml of the photoresist was pippetted onto the substrate and this was allowed to settle for ~ 5 minutes in order to aid the removal of trapped air bubbles.

This was then spin coated using the following regime; from 0 – 500 rpm at 200 rpm s^{-1} and held for 5 seconds, from 500-1000 rpm at 300 rpm s^{-1} and held for 30 seconds, from 1000-0 rpm at 200 rpm s^{-1}.
Once coated the films were heat treated at 65°C for 5 minutes and 95°C for 15 minutes. The lithographic patterning of the photoresist films was achieved using an acetate photomask with an array of 5 μm diameter spots (as the photoresist was a negative tone photoresist, i.e. exposed photoresist is polymerised with UV exposure, the mask was completely blacked out apart from the array of 5 μm spots).
The films were exposed to UV (350-400 nm, 350 mJ cm^{-2}) using the photomask (EVG 620 mask aligner) for 20 seconds, the films were then subjected to a further heat treatment, 65°C for 1 minute and 95°C for 3 minutes, in order to complete the polymerisation of the exposed sections of the film. The film was developed (i.e. the unexposed non-polymerised photoresist was removed) in proplylene glycol monometylether acetate (Sigma-Aldrich 99%) (PGMEA) with gentle agitation of the liquid for 30-60 seconds. The substrate, now containing the array of photoresist pillars, was gently rinsed in ethanol and distilled water before being dried under an indirect argon steam.

The process of converting the photoresist pillars into carbon pillars was relatively simple and involved pyrolysis of the photoresist pillars in an argon atmosphere using the following conditions (based on [93]). The substrates were loaded in a large bore (80 mm) tube furnace (Lenton) and placed under a constant flow of argon (4L min^{-1}) the temperature of the furnace was gradually increased until it reached 1000 °C.
The temperature was initially raised to 700°C at 12 °C min^{-1}, it was then raised to 900 °C at 2.2 °C min^{-1} and to 1000°C at 1.1°C min^{-1}. The temperature was held at 1000°C for 1 hour and then ramped to 900°C at 1.6°C min^{-1}, 700°C at 2.2 °C min^{-1} and to room temperature at 2.3 °C min^{-1}.

The carbon trench array structures were fabricated using a similar technique to the pillar structures, but with the following differences.
For the carbon trench structures a 100 μm layer of photoresist (SU-8 100, Microchem) was spun onto the VC substrate (0-500 rpm at 100 rpm s^{-1} held at 500 rpm for 10 seconds, 500-3000 rpm at 300 rpm s^{-1} and held at 3000 rpm for 30 seconds, 3000-0 rpm at 500 rpm s^{-1}). Due to the increased thickness of the layer the heat treatment times after spin coating were increased to 65°C for 5 minutes and 95°C for 30 minutes.

The lithographic patterning procedure was also altered, firstly a different photomask (containing a pattern of 20 μm thick lines) was used and secondly the UV exposure time was increased to 1 minute (though the wavelength and intensity of UV remained unchanged, 350 mJ cm^{-2}, 350-400 nm). Finally the post exposure heat treatment was increased to 1 minute at 65°C and 10 minutes at 95°C. The development time for the exposed substrates was increased to 1-2 minutes.

5.2.2. 3D Reticulated Vitreous Carbon Foam Substrates

A multitude of high surface area carbons have been used as battery, supercapacitor and fuel cell current collectors[99-102], in this work reticulated vitreous carbon (RVC) (80-100 ppi, 0 and 15-20 % compressed) was used as a substrate for aperiodic lithium-ion microbattery fabrications and was obtained from ERG Aerospace, California USA.

5.3. Results and Discussion

5.3.1. Carbon Microstructure Arrays

The carbon microstructure arrays were fabricated as described in 5.2.1. The fabrication process involved a substrate surface modification step, the deposition of a monolayer of 1-7, diaminoheptane. The ruthenium hexamine ($Ru(NH_3)_6^{3+}$) and ferrocene carboxylic acid ($C_{11}H_{10}FeO_2$) redox probes were used to test for the presence of a surface layer.
An example cyclic voltammogram for the surface modification of VC electrodes is shown in Figure 5.3.1a.
Figure 5.3.1b shows the results of the redox probe experiments.

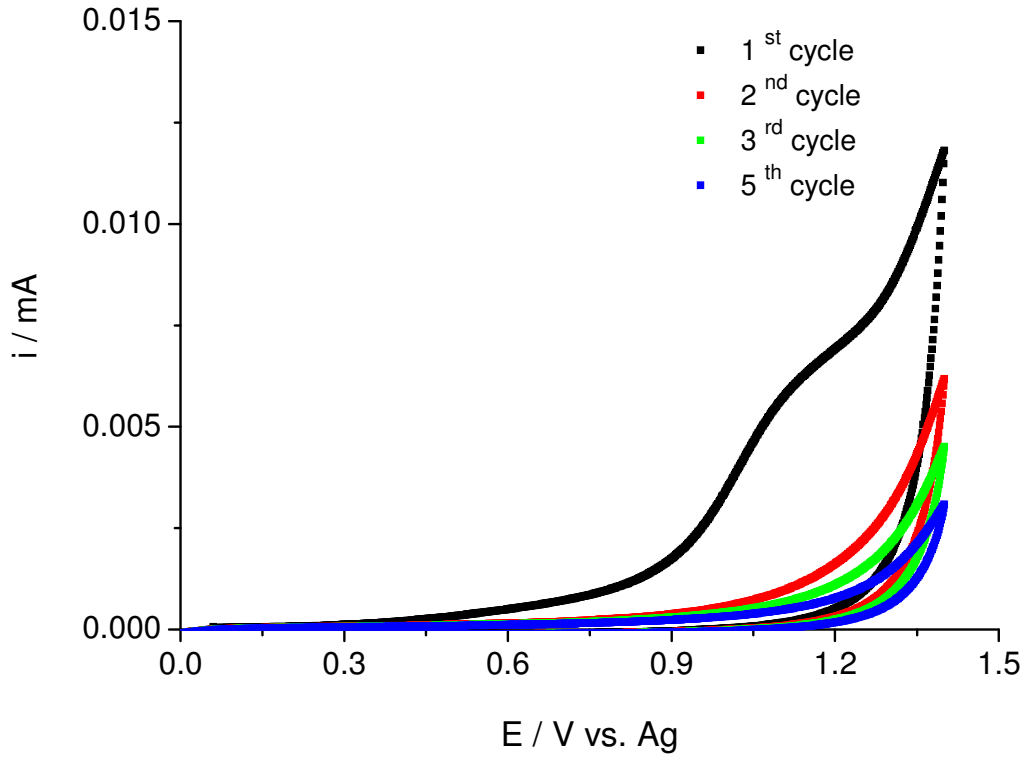

Figure 5.3.1a. Cyclic voltammetry result for surface modification of VC (3mm diameter, polished) electrode with 1,7- diaminoheptane monolayer.

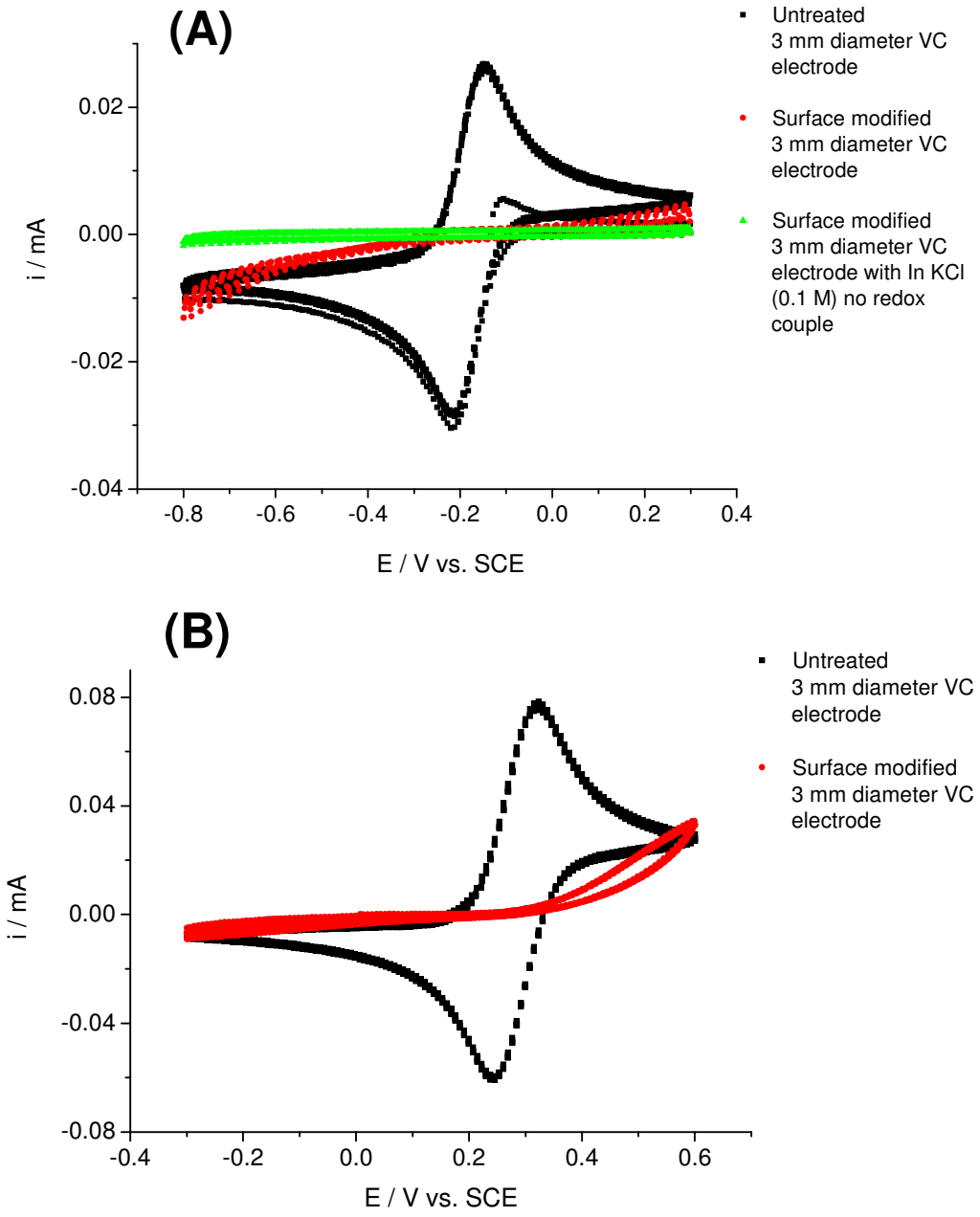

Figure 5.3.1b. (A) Cyclic voltammetry result comparing cycling of bare (black squares) and surface modified (red circles) 3mm diameter VC electrodes in aqueous 2 mM $Ru(NH_3)_6Cl_3$ / 0.1 M KCl; also shown is cycling of surface modified VC electrodes in supporting electrolyte only (0.1 M KCl, green triangles). (B) Cyclic voltammetry result comparing cycling of bare (black squares) and surface modified (red circles) 3mm diameter VC electrodes in aqueous $C_{11}H_{10}FeO_2$ (ferrocene carboxylic acid) (1 mM) / K_2HPO_4 (0.1M).

The peak visible at approximately 1.1 V *vs*. Ag (Figure 5.3.1a) during the first cycle was attributed to the electroxidation of a 1-7, diaminoheptane amine group to the cation radical [98] (Figure 5.2.1a). During subsequent cycles the peak current dropped rapidly, attributed to monolayer formation blocking further oxidation of the 1-7, diaminoheptane solution.
The results of the redox couple experiments (5.2.1), shown in Figure 5.3.1b, for surface modified and untreated 3 mm diameter VC electrodes also suggested the presence of a surface bound layer on the VC electrodes. Results for both solutions of ferrocene carboxylic acid (Figure 5.3.1b (A)) and ruthenium hexamine (Figure 5.3.1b (B)) show the disappearance of the characteristic surface redox couples in the case of the surface modified electrodes when compared to their unmodified counterparts.
However, the presence of small peaks between -0.4 and -0.8 V *vs*. SCE in the case of the ruthenium hexamine solution experiments (Figure 5.3.1b (B)) and 0.4 to 0.6 in the case of the ferrocene carboxylic acid experiments (Figure 5.3.1b (A)) suggested some defects in the surface bound layer. The lack of such peaks for cycling of the modified electrodes in a 'blank' solution containing only supporting electrolyte (Figure 5.3.1b (A)) suggested that oxidation / reduction of the surface bound layer was not the cause. It was proposed that defects in the monolayer were caused by both amine groups in the diamine molecules reacting with the electrode surface, creating a doubly surface bonded molecule.

Another, more observational piece of evidence, for the effectiveness of the surface modification was found whilst heat treating the modified VC substrates after the spin coating of the photoresist (5.2.1). The adhesion of the photoresist to the modified substrates was markedly better than to the non modified substrates; the photoresist was highly prone to de-wetting of the non-modified substrate during the various heat treatment stages.

The photolithographic patterning of the modified VC substrates and the subsequent pyrolysis to form the carbon microstructures is described in 5.2.1. Figure 5.3.1c shows SEM images of the final carbon micropillar array structures, EDX analysis (Chapter 2.4.2) confirmed the pyrolised micropillar structures to be predominantly (> 95%) carbon (Figure 5.3.1d). Figure 5.3.1e shows the structures resulting from the attempted fabrication of the carbon trench arrays.

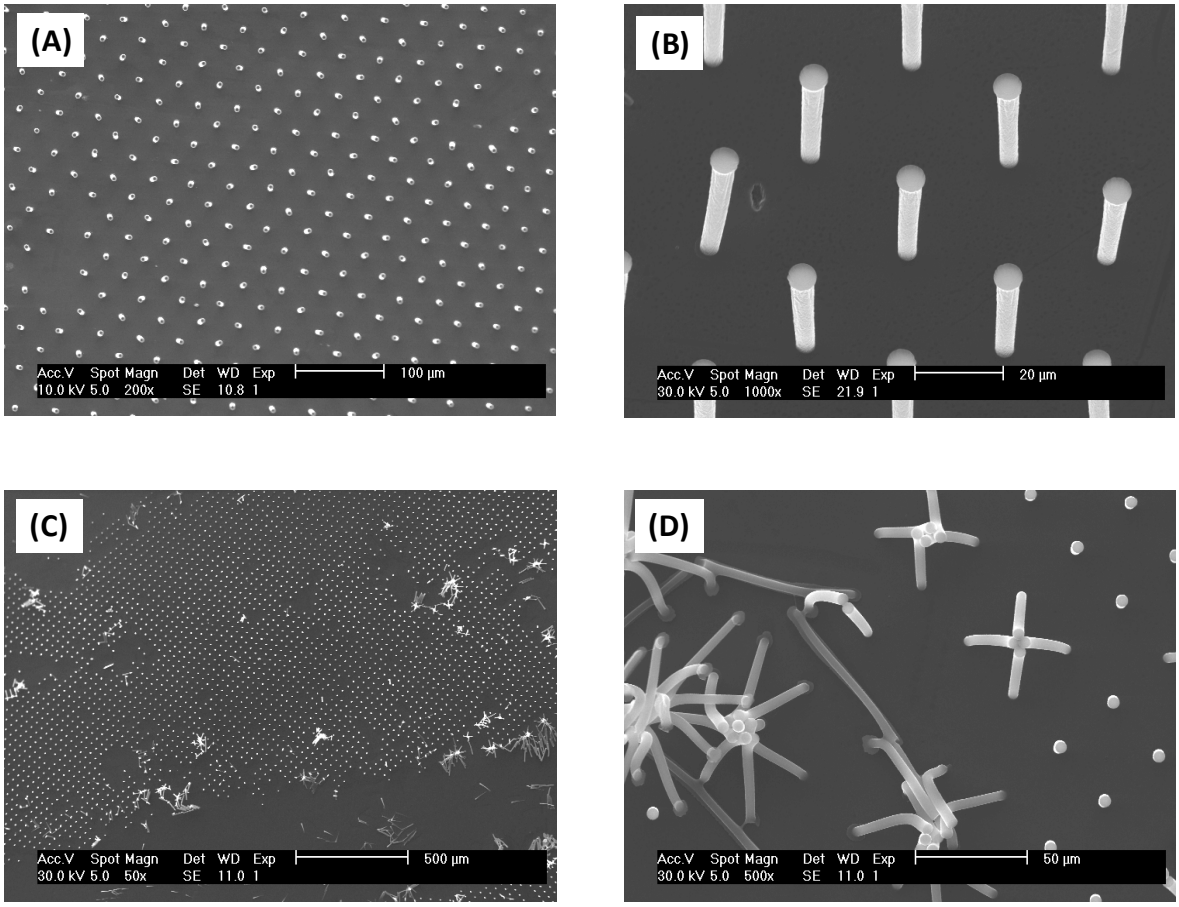

Figure 5.3.1c. SEM images of carbon micropillar arrays. Successful formation of the carbon microstructures led to arrays of high aspect ratio pillars ~ 25 µm tall with a ~5 µm diameter (A and B). However these structures were very mechanically unstable, the fabrication would often be unsuccessful (C) and successfully fabricated arrays would often contain areas of defects due to the toppling of the carbon micropillars (D).

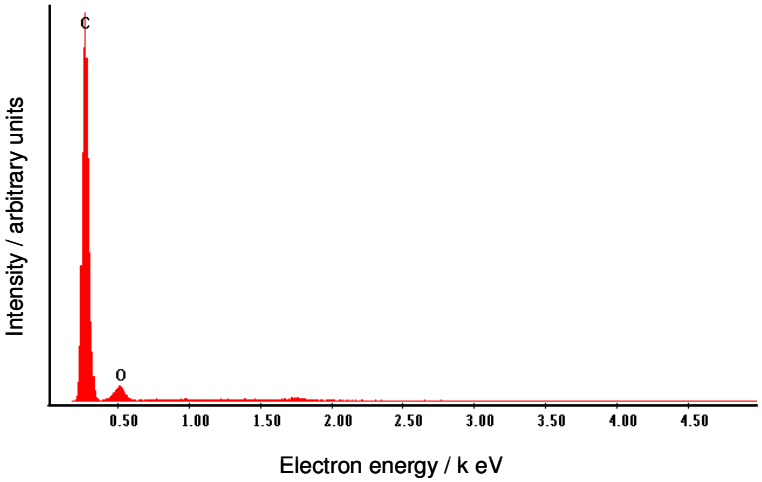

Figure 5.3.1d. EDX analysis of pyrolised micropillar arrays.

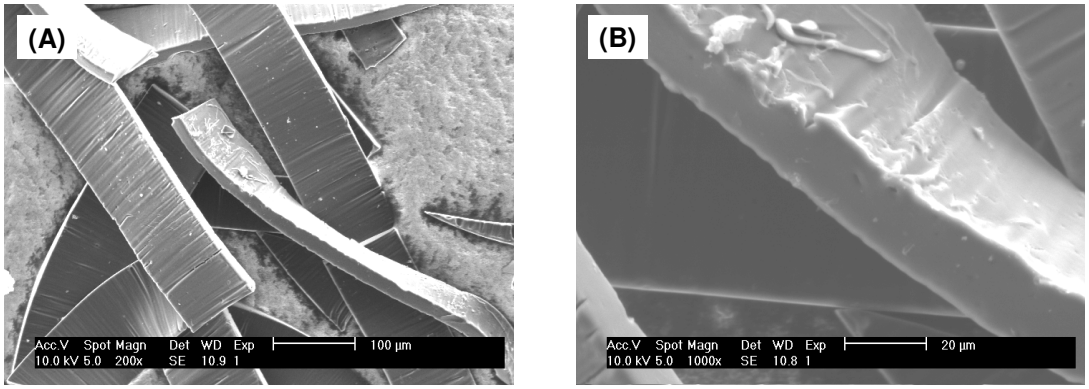

Figure 5.3.1e. (A) SEM image of failed carbon trench array structures. (B) Higher magnification SEM showing dimensions of trench cross section.

The main problem with the lithographically derived carbon microstructures was their poor mechanically durability. In the case of the micropillars it was very easy to destroy the structure and there were areas of the films where the poor mechanical strength caused defects, Figures 5.3.1c(C and D).

The main failing of the carbon trench arrays was poor adhesion between the 'walls' of the trench and the substrate (The trench structure would peel off the substrate during the development stage), although the actual dimensions of the trench structure remained intact (Figure 5.3.1e(A)). The high aspect ratio geometries (i.e. tall and thin for the micropillars and tall and long for the walls of the trench structure) were probably the cause of the poor mechanical durability / substrate adhesion of these structures; in fact, much research [93, 103] has gone into modifying the geometry of similar structures with the aim of improving their mechanical durability.

5.3.2. 3D Reticulated Vitreous Carbon Foam Substrates

The 3D RVC foams were available with a variety of porosities. The surface area of the RVC substrate was dependant on the number of pores per unit area, i.e. pores per inch (ppi).

Figure 5.3.2a is an SEM summary of the varying porosity RVC substrates; the data in Table 5.3.2a summarises the estimated area gain for the various substrate compositions (i.e. number of pores per inch). The estimation of the internal surface area of the substrate according to weight and density is detailed in Chapter 6.3.3.

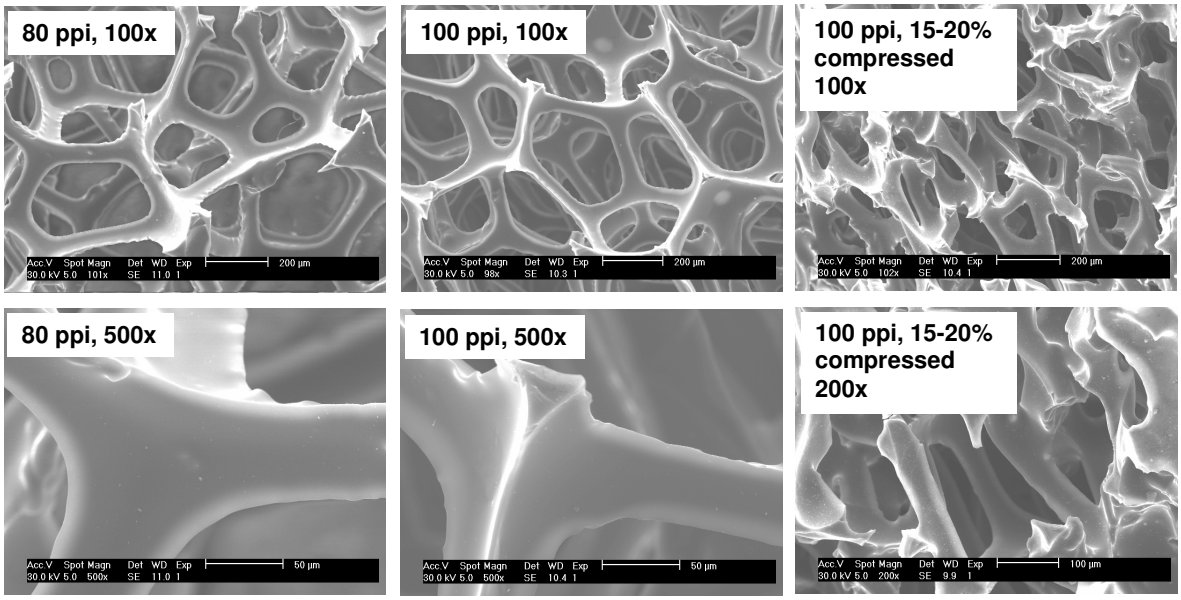

Figure 5.3.2a. SEM comparison of 80, 100 and 100 (15-20% compressed) ppi RVC foams at varying magnifications.

Table 5.3.2a. Surface area gain estimation for varying porosity RVC substrates at differing thicknesses. The area gain was estimated by comparing the internal (calculated from weight and density according to Chapter 6.3.3) and geometric areas of a 1 cm^2 piece of RVC foam

Electrode thickness / µm	Surface area gain 80 ppi	Surface area gain 100 ppi	Surface area gain 100ppi (15-20% compressed)
0.8	3	4	28
2	7.5	10	70
5	18.5	25	180
10	37	50	350

The surface area of the RVC substrates was estimated for each composition by measuring the weight of a 1 cm^2 piece of substrate of known thickness. The 'non-ideallity' of the resulting estimation of surface area gain (i.e. that the surface area gain does not relate exactly to thickness) was a result of the random nature of the 3D RVC foams.

5.4. Conclusions

Two strategies for the construction of 3D lithium ion microbatteries were investigated; the construction of cells based on either concentric / interdigitated plate or aperiodic configurations (Figure 5.1a).

The fabrication of substrates for concentric and interdigitated plate designs were based on photolithographic patterning of photoresists, as in 5.2.1. The aperiodic structures were based on commercially available reticulated vitreous carbon (RVC) foam substrates (5.2.2).

It was decided that efforts to fabricate a 3D lithium ion microbattery would be concentrated on a single configuration, and therefore a single substrate construction.

The decision on which configuration of microbattery (i.e. concentric, interdigitated or aperiodic) to use in subsequent experiments was based on the performance of the two substrate types.

In order to function effectively within the microbattery design the substrates needed to act as both current collector (cathode or anode) and as a supporting structure around which the cell could be based. These requirements were common to all three possible microbattery configurations. The effectiveness of the substrates was assessed according to the following criteria.

- The area gain for a given footprint area.
- The electronic conductivity.
- The chemical stability of the substrate with respect to the processes involved in the deposition of electrode materials.
- The electrochemical stability within the potential window of the cell operation, i.e. ~ 2 – 4.5 V *vs*. Li.

And perhaps crucially:

- The fabrication of the substrate construction should be as simple as possible and economically viable.

The surface area gain of the lithographically produced pillar substrates (5.2.1) was estimated according to a repeating pattern of micro-column pillars (25 µm x 5 µm) with a

pitch of 35 µm. The estimated area gain for the pillared structures was negligible; the 'total' surface area per cm^2 of footprint area was only 1.16 cm^2 / cm^2.
The estimated area gain for trench array structures, based on a 1 cm x 100 µm x 20 µm trench 'wall' (Figure 5.3.1e), was more significant with a total surface area of 3 cm^2 per cm^2 of footprint area. It is worth noting that the estimations of total surface area for the photolithographically produced structures did not take into account surface defects (i.e. missing or collapsed pillars, as in Figure 5.3.1c(C)). The surface area gain for the RVC substrates was estimated at between 3 and 350 cm^2 of total surface area per cm^2 of footprint area depending on foam thickness and porosity (Table 5.3.2a).

Although obtained using different methods, and of differing design, the three configurations of substrate were based on the same material, i.e. carbon (pyrolytic 'hard' carbon and vitreous carbon for the concentric / interdigitated plate and aperiodic configurations respectively).
In this respect the difference in chemical and electrochemical stability of the substrates was negligible and the difference in performance in terms of the electronic conductivity dependant on substrate morphology rather than differences in material composition.
The effect of substrate morphology with respect to electronic conductivity, particularly concerning hard carbons, has been highlighted by Bruce *et al.*[89]

The price, ease and reliability of substrate manufacture were also considered. The aperiodic RVC substrates were commercially available and therefore required very little effort to fabricate. The cost of the RVC substrates was negligible, i.e. a 100 x 100 x 1 mm piece of material cost ~ $10.
On the other hand the photolithographically produced interdigitated plate and concentric substrates required significant effort and sophisticated and expensive apparatus / facilities to produce (The total time of fabrication for the concentric substrate design, 5.2.1, was ~ 2 days).
The reliability of the fabrication of the interdigitated plate and concentric designs was poor. The ratio of success to failure for the concentric design was ~ 1:1 and the successful fabrication of the interdigitated plate configuration was not achieved (5.3.1).
In terms of materials cost the fabrication of the concentric and interdigitated plate designs was significantly more than the aperiodic RVC, though not unreasonably large, costing ~ £20 per electrode. However when the cost of fabrication, in terms of 'man-hours' and

overheads relating to the use of facilities and apparatus were taken into account the actual cost of producing these substrates was considerably larger.

After considering the three substrate configurations with respect to the required criteria it was clearly apparent the most suitable substrate for the basis of 3D Li-ion microbattery experiments was the aperiodic 3D RVC. The main factors for this decision being the much greater surface area of the RVC electrodes and the significant effort involved with, and unreliable nature of, the fabrication of the concentric and interdigitated plate designs.

Chapter 6

Electrodeposition and Electrochemical Characterisation of MnO_2 on 3D Substrates

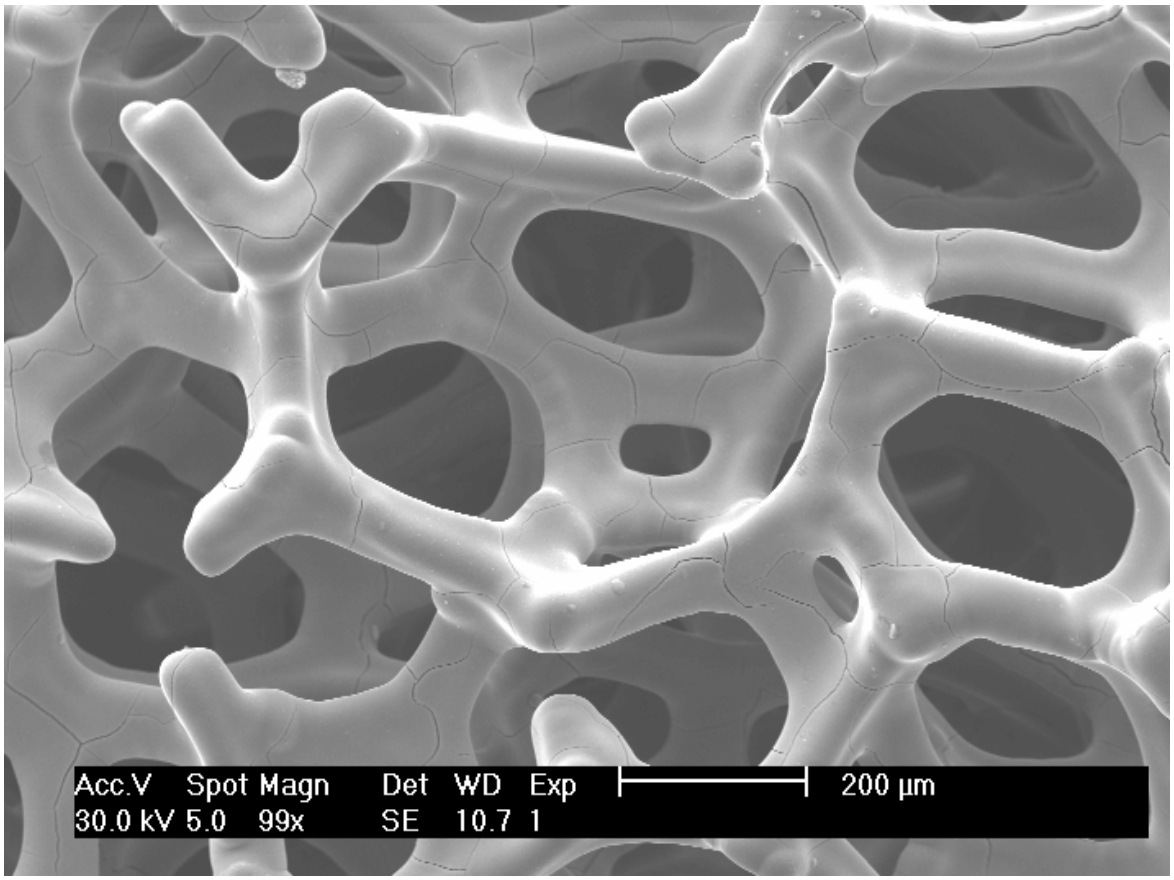

6.1. Introduction

The advantages of using reticulated vitreous carbon (RVC) foams as substrates for 3D Li-ion microbatteries were discussed in detail in the previous chapter. In summary the low cost and lack of complicated / time consuming fabrication techniques (as they are commercially available); combined with their large internal surface areas made them an ideal substrate for the basis of an aperiodic (Figure 5.1a) 3D Li-ion microbattery system. In order to fabricate the microbattery it was necessary to deposit conformal layers of cathode, electrolyte and anode around the RVC, as envisaged in an illustration of the final design, Figure 6.1a.

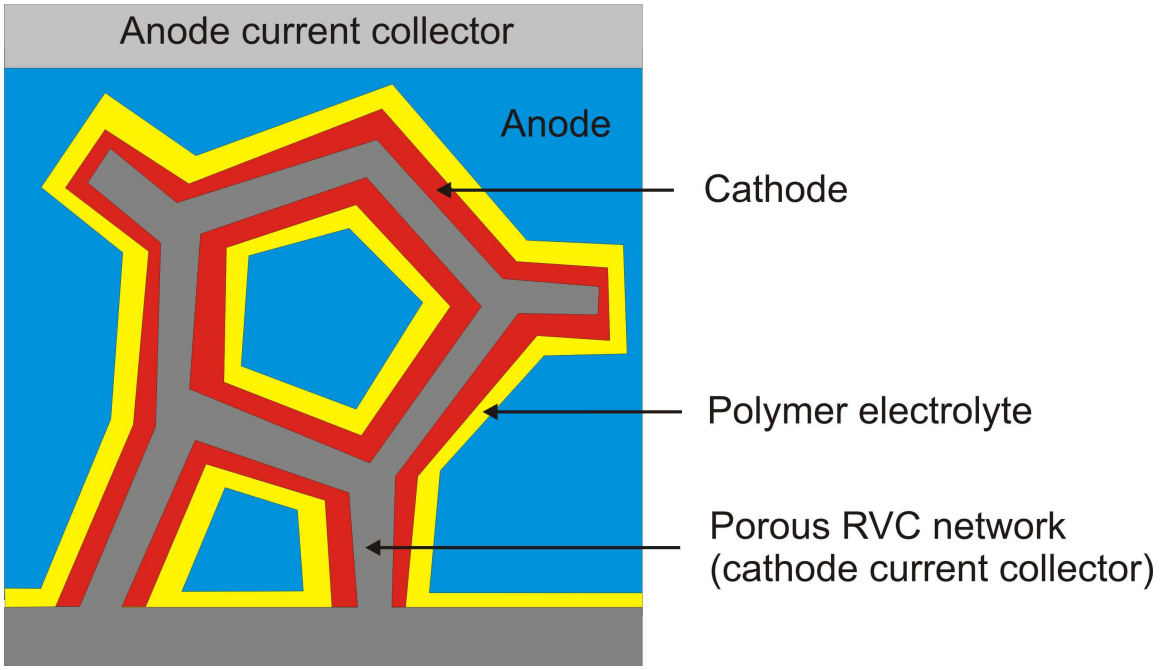

Figure 6.1a. Cross section through the envisaged aperiodic RVC based Li-ion microbattery.

Electrodeposition was used as the preferred method of depositing the first electrode layers, in this case the cathode, and the electrolyte. The advantage of using electrodeposition, over methods such as physical or chemical vapour deposition, was the ease at which highly reproducible and conformal films could be deposited into the depth of the porous structure.

The initial step in the fabrication of an aperiodic RVC based structure was deposition of the first electrode layer. MnO_2 was used as the first electrode because of the relatively simple process of electrodeposition.

Many forms of manganese oxides have been utilised in primary and secondary lithium battery systems [104-107]. Recent papers have demonstrated large capacities (~250 mA h g-1) and good cyclabilty from mesoporous β-MnO_2 in a lithium ion battery system [108, 109].

Electrolytic manganese dioxide (EMD) has been extensively used as an electrode material in both the aqueous Zn/MnO_2 and non-aqueous Li / MnO_2 systems which dominate the primary market place [5, 104, 110-112]. This material contains mainly γ-MnO_2 with some occluded water.

To successfully insert and extract lithium from this material a thermal treatment at 300-400 °C is required; this process calcines the material by removing residual water. Several reports have shown reversible lithium insertion and extraction over the range 4.5 – 2 V [104, 113, 114].

In the majority of these examples the EMD was removed from the deposition substrate, ground into a powder and made into composite electrode films with the addition of binder and conductive additive before electrochemical testing. Other work has demonstrated deposition, in-situ calcination and lithium cycling of porous EMD on planar substrates [115-117]. The aim of the experiments described in the following sections focuses on enhancing the capacity per footprint area of MnO_2 electrodes at high discharge rates using a 3D microstructure.

6.2. Experimental

6.2.1. Electrodeposition of MnO_2 (EMD)

Electrodeposited MnO_2 (EMD) was deposited from aqueous solutions of 0.3 M $MnSO_4.H_2O$ (98%+, Sigma-Aldrich) using 0.3M H_2SO_4 (>95%, Fisher) as supporting electrolyte at 98°C
($^{+}$/- 2°C). Films were deposited galvanostatically at 5 mA cm^{-2} using a large surface area Pt mesh counter electrode and a SMSE reference onto planar Ti substrates and 3D reticulated vitreous carbon substrates (ERG Aerospace, California, US). The electrodeposited films were allowed to dry at room temperature for 2-3 hours before being heat treated at 400°C in air for 5 hours (Step one to 60ºC for 1 hour, 1ºC / min ramp rate. Step 2 to 100ºC for 1 hour, 1ºC / min ramp rate. Step 3 to 400ºC for 10 hours, 1ºC / min ramp rate. Step 5 to room temperature, 1ºC / min ramp rate).

6.2.2. XRD Characterisation

The electrodeposited EMD was characterised as a powder; this involved electrodepositing the material onto large planar Ti electrodes (6.2.1), drying and finally scraping the deposit off the substrate using a scalpel. The EMD was ground to a powder using a pestle and mortar.
The XRD characterisation experiments were performed using a Bruker D8 diffractometer with a furnace attachment. A series of XRD patterns were recorded over a temperature range of 30-1000°C at 100°C intervals. A heating rate of 1°C per minute was used and the samples were left to equilibrate for 3 hours at each temperature prior to recording the XRD pattern. The XRD patterns were recorded over 5 h between the 2θ values of 10 and 70° using a $CuK\alpha_1$ radiation.

6.2.3. DSC / TGA Characterisation

The EMD (in powder form, see 6.2.2) was analysed using differential scanning calometry (DSC) and thermogravimetric analysis (TGA); see Chapter 2.4.3.

6.2.4. SEM Characterisation

Cross sectional images of EMD | RVC electrodes (Figure 3) were achieved by cutting through the electrode cross section using a sharp scalpel, SEM images were recorded according to Chapter 2.4.1.

6.2.5. Electrochemical Testing

The EMD films were tested in one of three configurations. The first technique involved testing the electrode using conventional battery testing methods, i.e. a composite electrode pellet comprised of 75% EMD (scraped off the Ti substrates and ground to a fine powder before being heat treated in air at 400°C) 20% acetylene black (sharwinigan black, 100% compressed) Chevron Phillips Chemical Company) and 5% PTFE powder (Dupont).
In the second method the EMD film was deposited directly onto planar Ti substrates. The third and final technique involved depositing the EMD onto 3D RVC substrates.
All three of the electrode configurations were tested using stainless steel two electrode cells, (Figure 6.2.5a) constructed under Argon < 0.1 ppm O_2 and H_2O) and cycled *vs.* lithium foil using 1M $LiPF_6$ EC:DMC (1:1 by weight). The various EMD electrodes were cycled galvanostatically between 4.2 and 2 V *vs.* Li/Li^+ (4.5 and 1.5 V *vs.* Li/Li^+ for the EMD | planar Ti substrates). The instrumentation and experimental set up are described in 6.3.1.

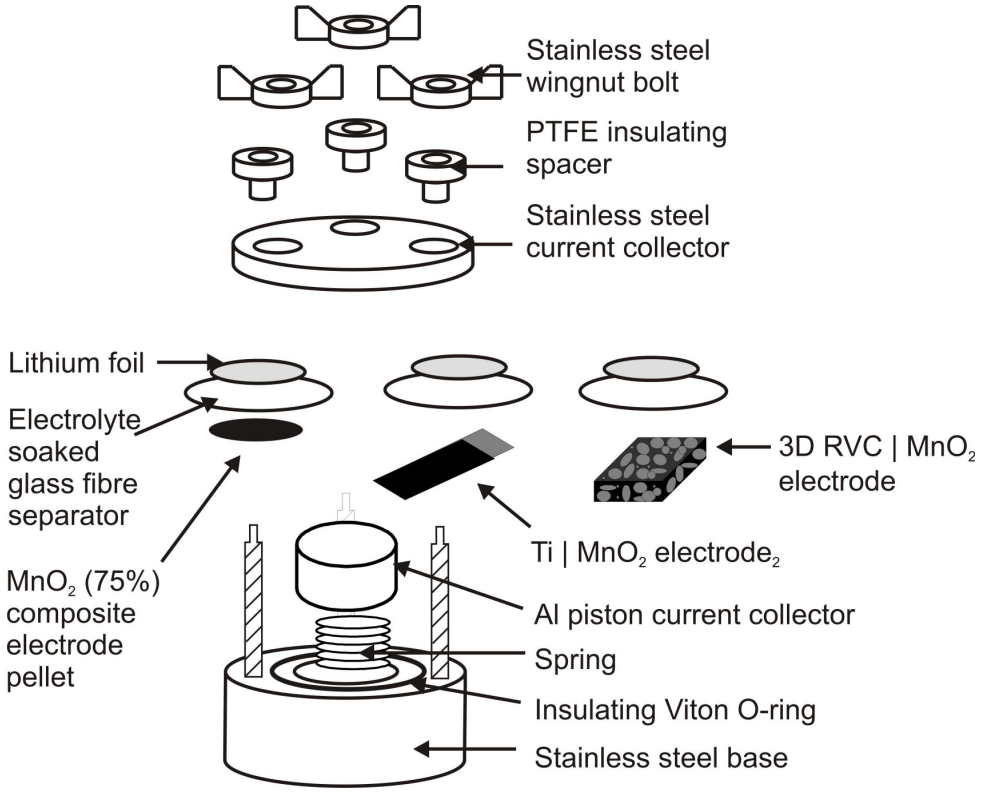

6.2.5a. Schematic of cell construction used for electrochemical testing of EMD.

6.3. Results and discussion

6.3.1. XRD, and DSC / TGA Characterisation of Electrodeposited MnO_2 (EMD)

XRD (6.2.2) was used to confirm the crystal structure of the deposited EMD both before and after heat treatment (6.2.1). Figure 6.3.1a shows the recorded XRD patterns with increasing temperature. A literature example of EMD characterised using XRD is shown in Figure 6.3.1b . The Results of the XRD experiment were supported by DSC / TGA analysis (6.2.3), Figure 6.3.1c.

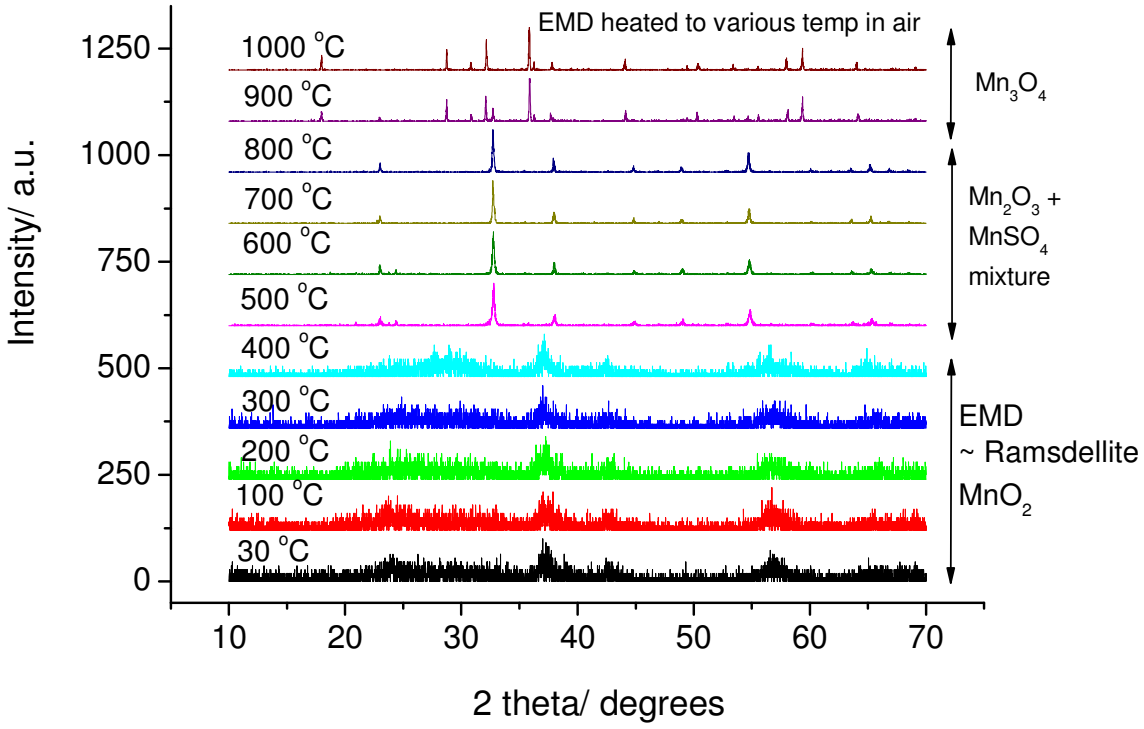

Figure 6.3.1a. XRD patterns for EMD recorded at 100°C increments between 30 and 1000°C.

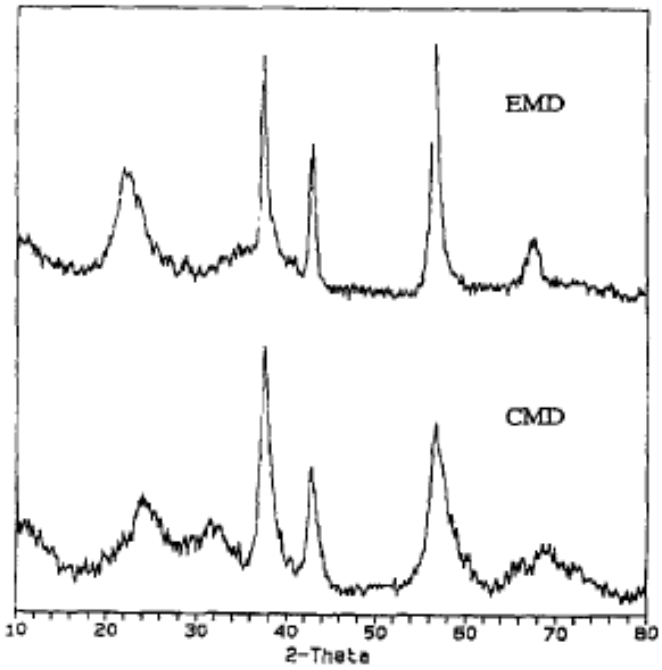

Figure 6.3.1b. X-ray diffraction pattern typical of poorly crystalline EMD (top) [104]

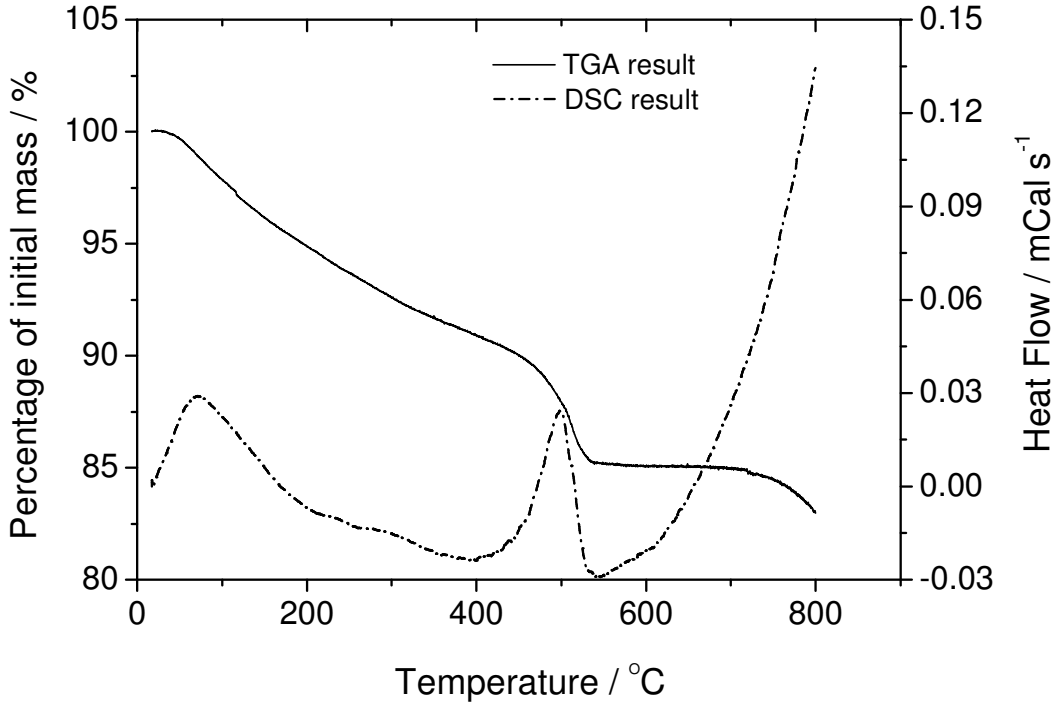

Figure 6.3.1c. DSC / TGA traces for 'as deposited' EMD.

The XRD patterns at 400°C and below were typical for that of EMD [104, 106] showing weakly defined peaks ,due to the poorly crystalline EMD layer, at 2θ values of around 25 38, 42 and 57. At temperatures above 400°C there is a phase change to the Mn_2O_3 structure with some evidence of residual $MnSO_4$ (from the deposition solution).

TGA analysis (Figure 6.3.1c) showed a significant decrease in mass between 400 and 500°C consistent with loss of oxygen due to the phase change from MnO_2 to Mn_2O_3. Although not particularly significant for this work the difference between the 500°C and 800°C patterns was attributed to a further phase change to Mn_2O_3. More importantly (see 6.3.2) in the region between 50 and 400°C there is a gradual decline in mass attributed to the removal of occluded water [118].

6.3.2. Deposition Charge *vs*. Film Thickness Calibration Experiments

A calibration experiment was required in order to accurately deposit specific thicknesses of EMD onto both planar and 3D substrates; as such the deposition charge *vs*. film thickness relationship of EMD films was investigated.

EMD was deposited onto planar Ti substrates (6.2.1) at varying deposition charges under galvanostatic conditions (5 mA cm^{-2}); using the weight of the deposited EMD and its density (4.5 g /cm^3 [5]) the thickness of the deposited layer was measured (the thickness was confirmed as within +/- 10% of the estimated value by SEM). The deposition was expected to be Faradaic according to the following reaction, Equation 6.3.2a.

$$\mathbf{Mn^{2+} + 2H_2O \longrightarrow MnO_2 + 4H^+ + 2e^-} \qquad \textbf{Equation 6.3.2.a}$$

Figure 6.3.3a shows the plot of deposition charge *vs*. estimated thickness for EMD films on planar Ti substrates.

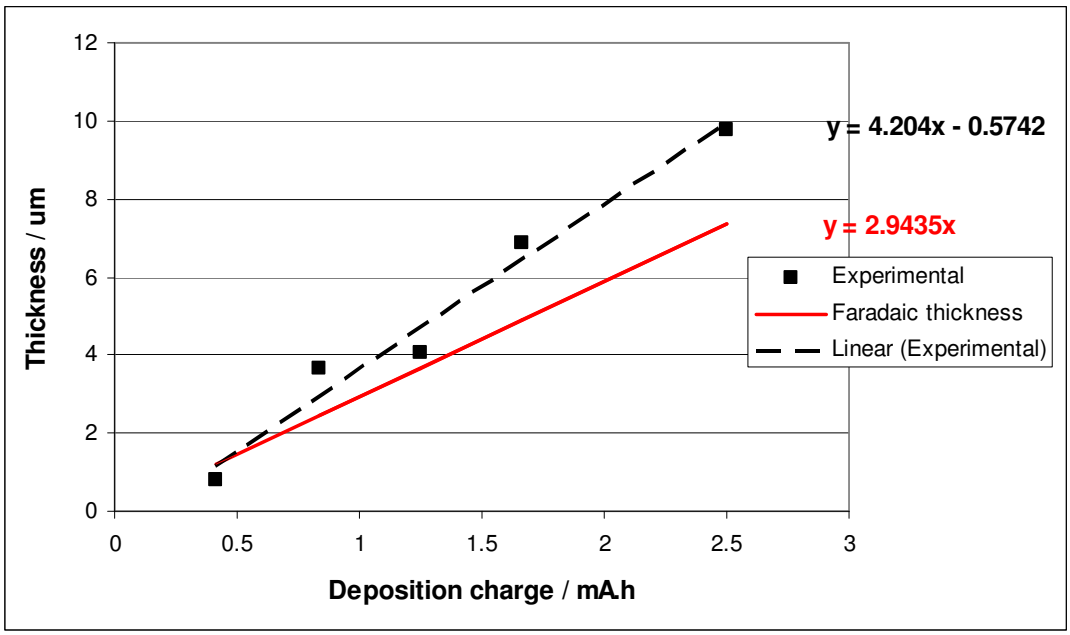

Figure 6.3.2a. Plot of deposition charge *vs*. estimated EMD film thickness and thickness according to a faradic $2e^-$ oxidation of $MnSO_4$ (Equation 6.3.2a) for 1 cm^2 films of EMD. Films were deposited using galvanostatic (5 mA cm^{-2}) current for a variety of deposition times.

The data in Figure 6.3.2a shows a linear relationship between deposition charge and film thickness over the range of deposition charges suggesting good control over film thickness in the case of the planar EMD films. Using equation 6.3.2a the Faradaic efficiency of the depositions were calculated, Table 6.3.2a, and found to be greater than 100% in almost all cases, leading to a greater than expected film thickness.

Table 6.3.2a. Faradaic efficiencies for films of EMD on planar substrates.

Deposition time / min	Deposition charge / C	Weight of Deposit / g	Estimated thickness / µm	Faradic Efficiency / %
5	1.5	0.00036	0.8	65.2
10	3	0.00164	3.6	148.6
15	4.5	0.00183	4.1	110.5
20	6	0.00309	6.9	140.0
30	9	0.0044	9.8	132.9

The discrepancy between the estimated film thickness and thickness according to the Faradaic oxidation of Mn^{2+} to Mn^{4+} (Equation 6.3.2a) was attributed to the water contained within the EMD film (see 6.3.1). As the thickness of the film was estimated using the weight of deposited EMD, and its density (4.5 g cm^{-3} [5]), the extra weight effectively

added to the estimated thickness of the film. However this did not explain the non-zero origin, i.e. the 0.14 mA.h X axis intercept, for the experimental results seen in Figure 6.3.2a, in order to explain this effect it was necessary to look at the deposition experiment, Figure 6.3.2b.

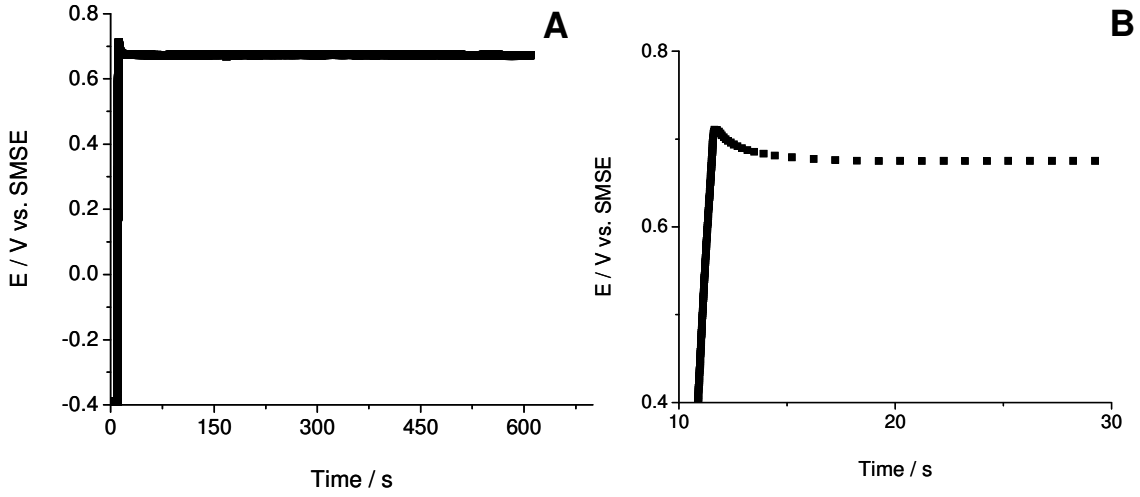

Figure 6.3.2b. (A) Example E *vs*. t trace for the galvanostatic deposition (5 mA cm^{-2}) of EMD on planar Ti substrates. (B) Expanded initial region of deposition.

The linear fit of the experimental deposition charge *vs*. deposition thickness data, shown in Figure 6.3.2a, suggested a 0.14 mA.h intercept on the charge axis. The intercept signifies for all thicknesses a certain amount of charge is passed before film deposition begins. The expanded E *vs*. t plot (Figure 6.3.2b(B)) shows an overpotential during the initial stages of deposition consistent with nucleation of EMD on the substrate surface. Re-plotting Figure 6.3.2b(B) as deposition charge *vs*. potential allows a value of 'nucleation charge' to be estimated, as in Figure 6.3.2c.

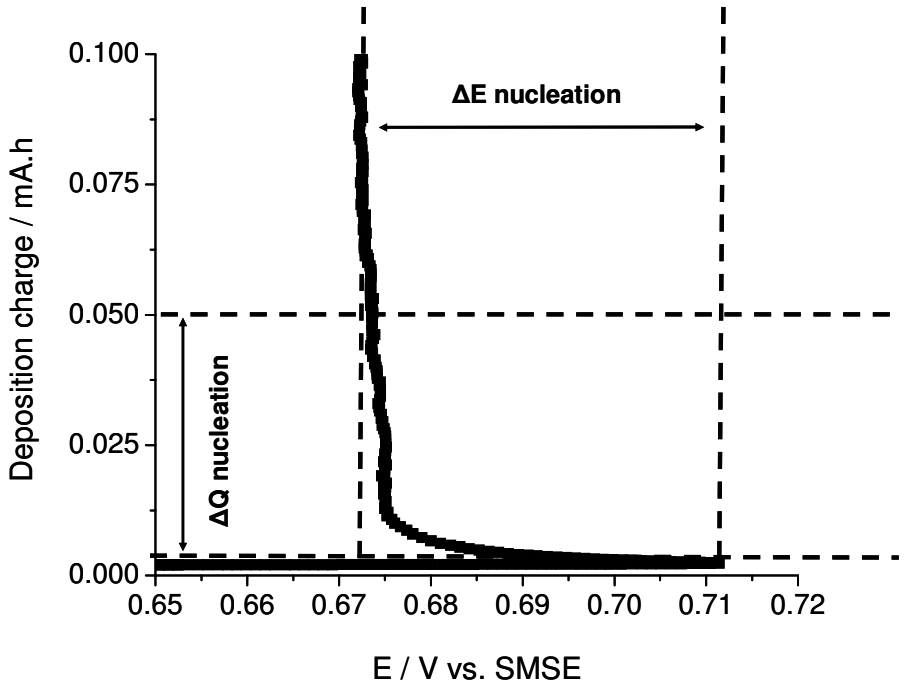

Figure 6.3.2c. Deposition charge *vs*. potential for initial region of EMD deposition on planar Ti substrate.

An estimation of the 'nucleation charge' from Figure 6.3.2c gave a value of ~ 0.05 mA.h; leaving ~ 0.9 mA.h of the estimated 0.14 mA.h 'intercept charge' unaccounted for. This apparent remaining charge may simply be due to the error in the linear fitting of the experimental data in Figure 6.3.2a.

The results of the deposition calibration experiment (Figure 6.4.2a) were used to control the thickness of the EMD film when depositing on various 3D substrates. The charge needed to deposit a specific thickness according to the calibration experiment, Figure 6.4.2a, correlated reasonably well with the deposited thickness (6.3.4) despite the small X axis intercept.

6.3.3. Estimation of the Surface Area of 3D Foam Electrodes

In order to properly control the thickness of the EMD layer it was necessary to control both the deposition charge (mA h cm^{-2}) and deposition current density (mA cm^{-2}); both of these were reliant on knowing the surface area of the substrate. This was straight forward in the case of the planar substrates but more complicated for the 3D foam electrodes.

The surface area of the foams was estimated using the average geometry of the structure and the density of the material.

Firstly the structure and cross section of the foam substrates were estimated using SEM images of the material. Figure 6.3.3a. Shows the cross section of 100 ppi RVC foam substrate coated in an EMD layer.

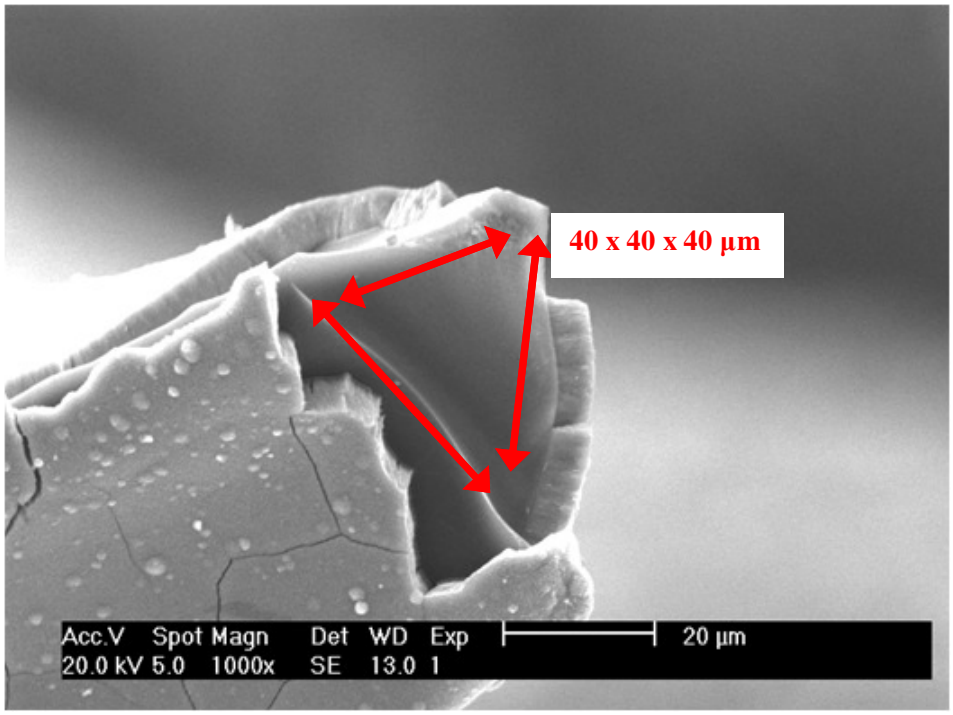

Figure 6.3.3a.Cross section of RVC foam substrate showing the triangular geometry of the structure and its dimensions (in the image the foam is coated with a ~ 5 µm film of EMD).

Using the 100 ppi RVC foam as an example, the area of the foams was estimated as follows, using the following assumptions.

That the structure of the foam consisted entirely of triangular shaped tube, 40 x 40 x 40 µm in size (Figure 6.3.3b(A)). That the manufacturers stated density for the material (1.65 g cm^{-3}) was accurate.

Dividing the density of the substrate (g cm^{-3}) by the weight (g) gave a volume (cm^3); dividing the volume by the cross sectional area ($diameter^2$ * (√ (3/4)) gave a value in cm, a length. Using this length and the geometry of the structure enabled the calculation of a surface area (Figure 6.3.3b(B))

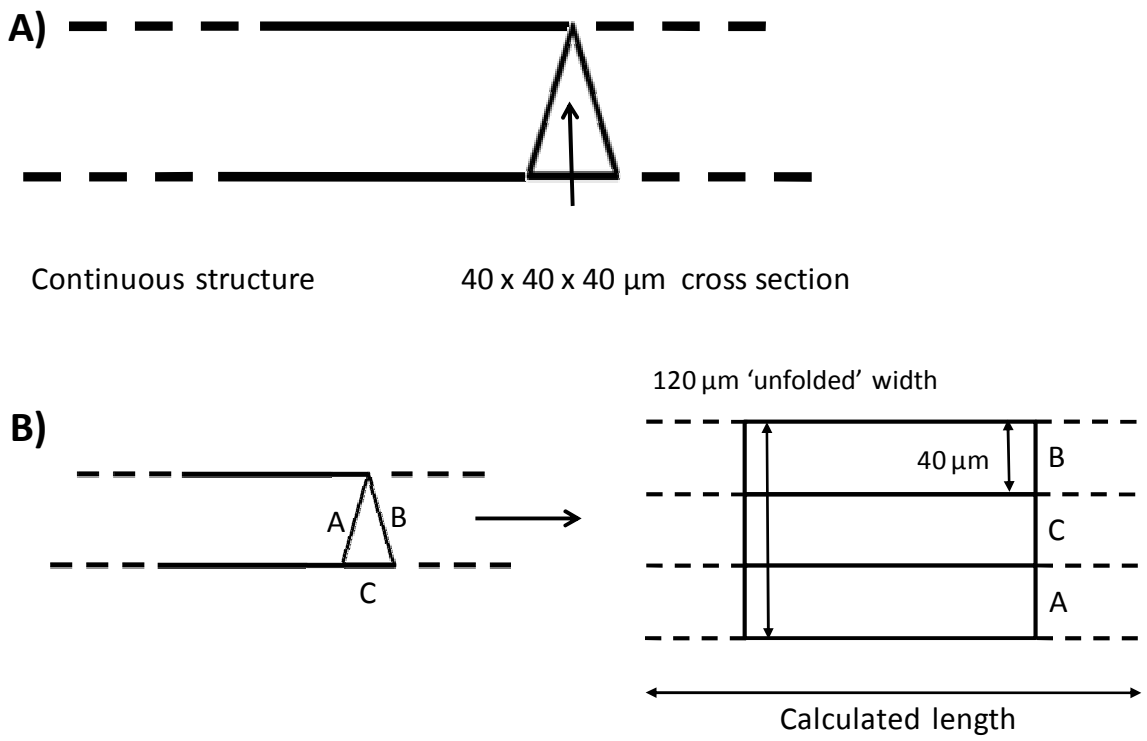

Figure 6.3.3b. A) Schematic geometric shape of 100 ppi RVC substrate; for the purpose of the calculation the structure was assumed to be a continuous triangular tube. B) For the calculation of the surface area the length estimated from the volume and cross section was multiplied by the width of the 'unfolded' structure.

6.3.4. SEM Characterisation of Electrodeposited EMD Films

EMD was electrodeposited onto RVC substrates (100 ppi 15-20% compressed) at thicknesses of 1, 5 and 10 μm as described in 6.2.1. The plot in Figure 6.3.2a was used to estimate the current and charge needed to electrodeposit the specified thicknesses. The quality of the deposition, its conformallity and how closely the deposited thickness matched the target thickness was assessed using SEM. SEM images of the different thickness EMD films on RVC substrates are shown in figure 6.3.4a.

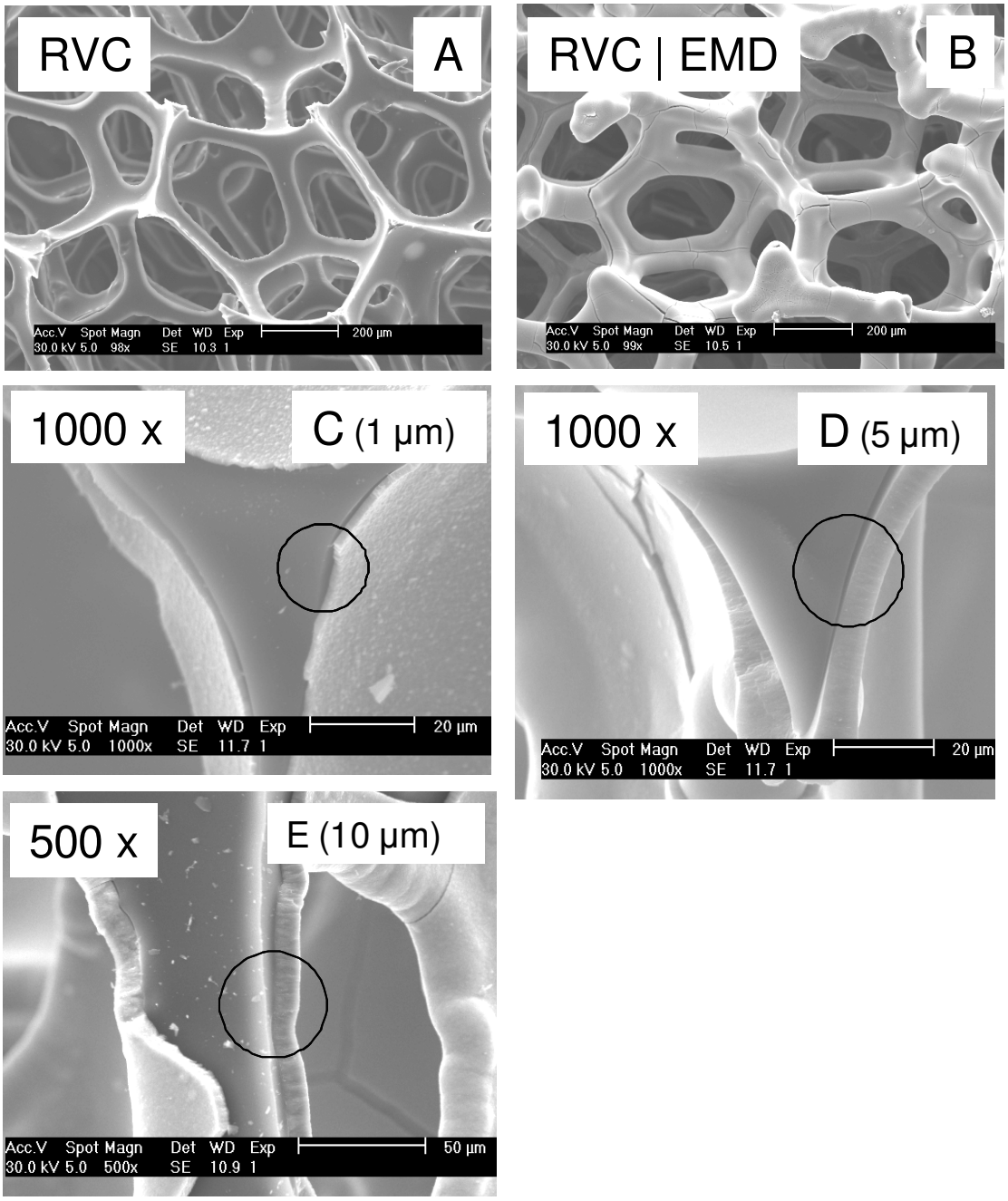

Figure 6.3.4a. SEM images of EMD films on RVC foam substrates. Blank RVC substrate and RVC | EMD electrodes are shown in A and B respectively. 1, 5 and 10 µm EMD layers are shown in C, D and E (note C and D are at magnifications of 1000 x and E is at 500 x).

The SEM images confirm the thicknesses of the film to be a good match to the target thickness, usually within +/- 10%, and the thickness of the deposited films was constant throughout the depth of the substrate structure (the substrates were pellets of RVC ~ 800 µm thick with a 4.5 mm diameter). However, for the thicker depositions of EMD the

thickness of the EMD layer tended to be slightly greater around the point of the triangular cross section (Figure 6.3.4b).

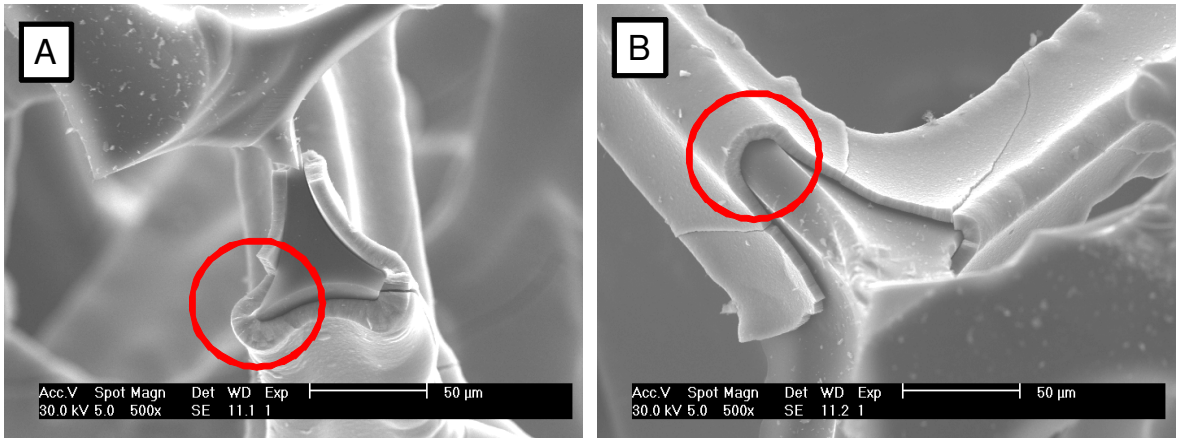

Figure 6.3.4b. Cross sections of different thickness EMD films on RVC substrates (A ~ 1µm, B ~ 5µm). (A) For thicker depositions of EMD the thickness of the deposit is greater at the point of the triangular cross section, highlighted in the red circle, than on the sides. (B) When the EMD deposit is less than ~ 5 um thick the film generally has an even thickness around the triangular cross section.

6.3.5. Electrochemical Characterisation of Electrodeposited EMD.

Initial characterisation of the EMD involved testing the material as a standard electrode, i.e. as a composite electrode pellet, to ensure the expected electrochemical behaviour.
EMD was electrodeposited onto large planar Ti substrates (6.2.1) and allowed to dry (room temperature ~ 12 hours). The EMD film was then scraped off the substrate using a scalpel and ground to a powder using a pestle and mortar. The EMD powder was fabricated into a composite electrode pellet of composition 75% EMD 20% acetylene black and 5% PTFE powder (6.2.5).
Once fabricated the composite electrode pellets were tested as lithium half cells using a 1M $LiPF_6$ EC:DMC (1:1) electrolyte (Chapter 2.3.1). The EMD composite electrode | $LiPF_6$ EC: DMC (1:1) | Li foil cell was cycled between 4.2 and 2 V *vs.* Li at C/5. The shape of the charge and discharge profiles are illustrated in Figure 6.3.5a and the capacity (mA.h g^{-1}) *vs.* cycle number result of the experiment in Figure 6.3.5b.

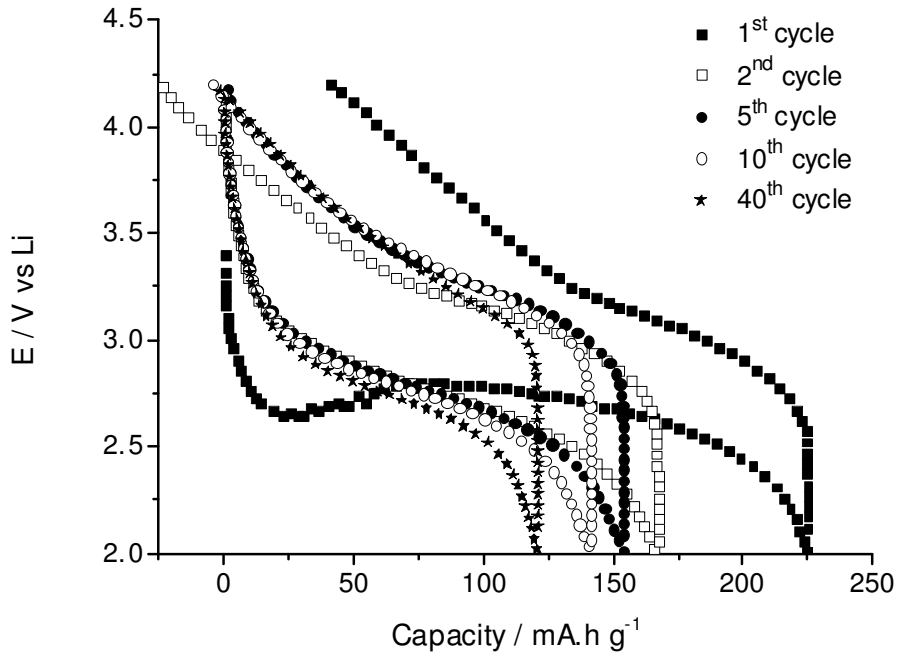

Figure 6.3.5a. Potential (E / V *vs*. Li) *vs*. Capacity (mA.h g^{-1}) plots for charge and discharge of EMD composite electrode pellets. The 1st, 2nd, 5th, 10th, and 30th cycles are displayed; the number of data points has been reduced and other cycles omitted to improve clarity of the plot.

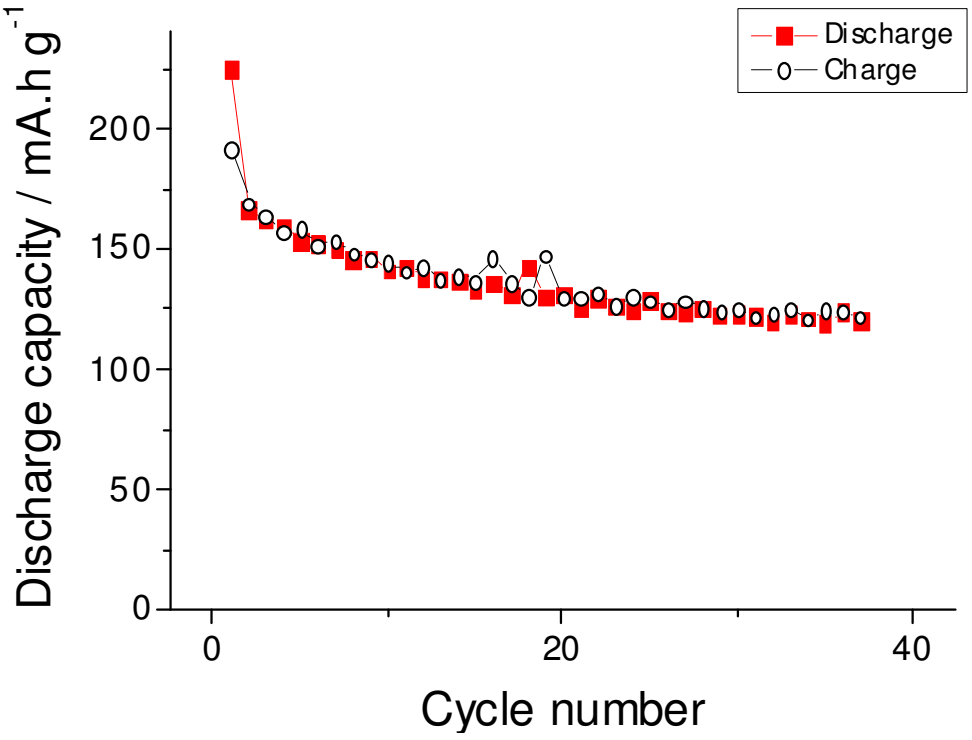

Figure 6.3.5b. Gravimetric capacity *vs.* cycle number (at C/5 according to a maximum capacity for EMD of 285 mA.h g^{-1} based on insertion of 1 mole of lithium per mole of MnO_2) for composite electrode pellets of EMD (75% EDM, 20% acetylene black, 5% PTFE powder)

The discharge occurs over the potential range ~3-2.5 V *vs.* Li ,suggesting single phase behaviour, giving a capacity of about 200 mA.h g^{-1} on first discharge. However this quickly drops to about 150 $mA.hg^{-1}$; largely due to the large first discharge irreversible capacity. After several cycles only a small decrease in available capacity is seen upon each charge discharge increment, shown in Figure 6.3.5b. The discharge capacities and profiles agree reasonably well with those found in the literature [104, 113, 114]; the first cycle irreversible capacity is commonly seen for EMD electrodes and is attributed to strain on the crystal structure (expansion / contraction of the unit cell) during initial lithium insertion / extraction [104, 110].

6.3.6. Effect of 3D structure on Footprint Capacity (mA.h cm^{-2}).

In order to asses the expected increase in footprint capacity (mA.h cm^{-2}) of the 3D electrode configuration a comparison between planar EMD and a layer of EMD deposited onto a 3D substrate was made. A 1 cm^{-2} ~ 1 μm thick layer of EMD was electrodeposited onto a planar Ti substrate (6.2.1) and assembled into a lithium half cell (6.2.5).
This was compared to an identical cell containing a 3D RVC substrate (100 ppi 15-20% compressed) (0.4 cm^2 x 2 mm) coated with 5μm layer of EMD (6.2.1). The cells were cycled galvanostatically between 4.2 and 2.0 V *vs.* Li at C / 10. Figure 6.3.6a shows capacities (mA.h cm^{-2}) for cells based on planar (2D) and RVC (3D) electrodes; included for comparison are results from EMD composite electrode experiments (6.3.5).

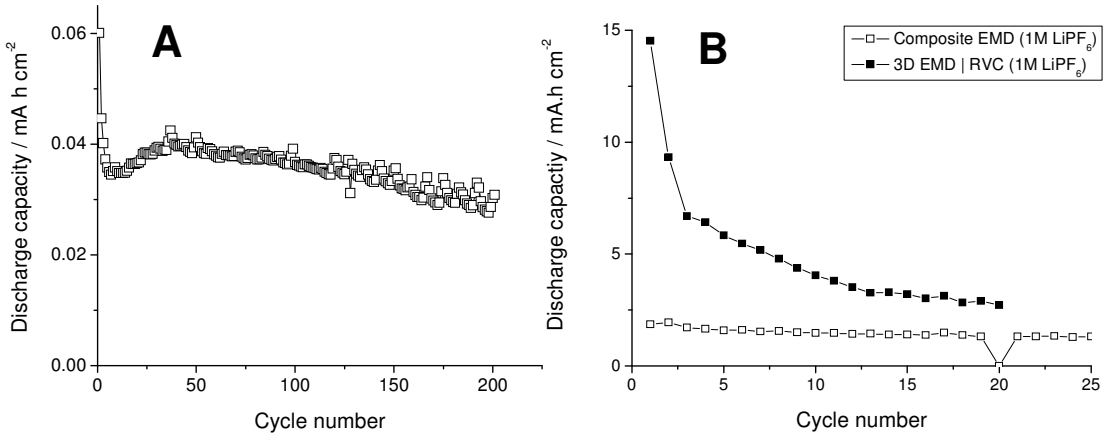

Figure 6.3.6a. Galvanostatic discharge capacity for lithium half cells containing planar EMD / Ti (A) and 3D EMD / RVC (B) electrodes. Figure 6.3.6a(B) also shows data for the planar thick film EMD composite electrode.

The charge / discharge characteristics of the 'as deposited' EMD planar (2D) and RVC (3D) electrodes showed the same features, i.e. a sloping discharge between ~3 – 2.5 V *vs.* Li, as the composite EMD electrodes.
The area specific discharge capacity (mA.h cm^{-2}) was much greater in the case of the 3D EMD | RVC and EMD composite electrodes than for the EMD | Ti thin film electrodes; this is not surprising when we consider the volume of EMD compared to the footprint area for each electrode configuration.

The electrochemical performance of the three electrode configurations, the comparable planar EMD / Ti and 3D EMD / RVC and the EMD composite electrode pellet, in terms of capacity per footprint area (mAh.cm^{-2}) is summarised in Table 6.3.6a.

Table 6.3.6a. Discharge capacity (mA.h cm^{-2}) and estimated volume (µm^3) of EMD for the three electrode configurations. *Discharge capacities included are initial discharge capacities (not including large irreversible capacity commonly seen on first discharges of EMD). ** Volume of EMD in composite electrode was adjusted to account for only 75 wt % of the pellet comprising of EMD (see 6.2.5).

Electrode configuration	Discharge capacity / mA.h cm^{-2}*	Thickness of EMD film / µm	Footprint area / cm^2	Actual area of EMD film / cm^2	Volume of EMD / µm^3	Discharge capacity mA.h/ µm^3
2D planar EMD | Ti electrode	**~ 0.04**	~ 1	1	1	1	**0.04**
3D EMD | RVC electrode	**~10**	~ 5	0.4	40	200	**0.05**
2D EMD composite electrode pellet	**~2**	70	0.95	0.95	20**	**0.1**

As expected the 3D EMD / RVC electrodes show footprint capacities (mA.h cm^{-2}) far greater than the capacities seen for the 2D planar EMD / Ti electrodes (approximately 250 times greater for the 3D configuration). However, volumetric capacities for two electrodes were similar; confirming the increase in footprint capacity was a consequence of the area gain achieved by moving from the 2D to 3D substrate. The footprint capacities of the EMD composite electrode pellets were much larger than the 2D planar EMD / Ti electrodes, due to the greater volume of material / cm^2.

It was expected that the volumetric capacity of the electrodes would be dependant on the volume of active material present; however, the volumetric capacity of the composite electrodes was roughly twice as large as that of the 'as deposited' 2D EMD / Ti or 3D EMD / RVC electrodes.

The increased volumetric capacity of the composite electrodes was attributed to the positive effect of the composite electrode formulation, i.e. the effect of the conducting (electronically) network of acetylene black.

The acetylene black additive ensured adequate electronic contact between the particles of EMD in the composite; however, in the case of the 'as deposited' electrodes the EMD was deposited as a solid film. It was suggested that a combination of the electronic resistance of the solid EMD film (when compared to that of the composite electrode) and a lower porosity, limiting electrolyte penetration, was the cause of the lower volumetric capacities in the as deposited electrodes.

6.3.7. AC Impedance Characterisation and Equivalent Circuit Analysis of Electrodeposited EMD | RVC Electrodes

EMD was electrodeposited onto RVC substrates (4.5 mm diameter x 800 μm thickness (100 ppi 15-20% compressed)) at thicknesses of 1, 5 and 10 μm (as described in 6.2.1). After drying and heat treatment the differing thickness EMD / RVC electrodes were assembled into lithium half cells (6.2.5). AC impedance spectroscopy (Chapter 2.3.2) was used to characterise the cells containing the 1,5 and 10 μm thick EMD layer | RVC electrodes.

The individual Nyquist plots for the cells, along with corresponding equivalent circuits and fit results are shown in Figure 6.3.7b. The equivalent circuits used to fit the experimental data are described below, Figure 6.3.7a.

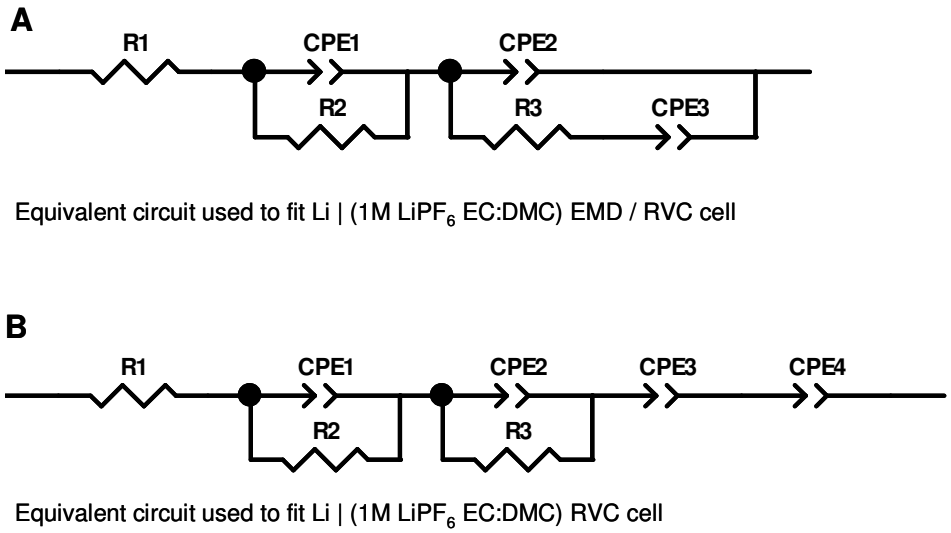

Figure 6.3.7a. Equivalent circuits used to fit the Li | (1M $LiPF_6$ EC:DMC) EMD / RVC cell (A) and the 'blank' Li | (1M $LiPF_6$ EC:DMC) RVC cell (B).

The impedance of lithium batteries can be complicated, and various different equivalent circuit models have been used to describe them [70, 105, 119]. In this work a simplified model was used to fit Li | (1M $LiPF_6$ EC:DMC) EMD / RVC cells (Figure 6.3.7a(A)). The model was based on an approximation of the various interfaces present within the cell and was modified according to the experimental response (Figure 6.3.7b, c, d and e).

The components used in the model Li | (1M $LiPF_6$ EC:DMC) EMD / RVC cell, Figure 6.3.7a(A), were representative of the following physical features.
R1 corresponded to the uncompensated cell resistance, i.e. the electrolyte resistance, the resistance of the RVC substrate, instrumental / wiring resistance etc.
CPE 1 and R2 were attributed to the lithium / electrolyte interface with CPE1 and R2 ascribed to charge transfer resistance and interfacial (double layer) capacitance respectively [120].
CPE2 and R3 were used to describe the EMD / electrolyte interface, CPE2 was used to model the EMD interfacial (double layer) capacitance and R3 the electronic / ionic resistance through the EMD. Finally the third constant phase element, CPE 3 (with the phase fixed at 0.5), was used to represent an infinite Warburg, and expressed solid state diffusion within the electrodeposited EMD.

The equivalent circuit used in the fitting of the Li | (1M $LiPF_6$ EC:DMC) RVC 'blank' cell (Figure 6.3.7e) contained an uncompensated resistance, R1, and a lithium electrolyte interface CPE1 and R2, identical to that used in the Li | (1M $LiPF_6$ EC:DMC) EMD / RVC equivalent circuit.
The nature of the second semicircle seen in the experimental data (Figure 6.3.7e) was unclear, it was suggested it was due to the reaction of the electrolyte with the carbon surface (formation of an SEI film) and the associated charge transfer resistance and interfacial capacitance.
CPE3 (phase fixed at 0.5) and CPE 4 were used to describe diffusion into the porous RVC electrode (CPE 3 was used to represent an infinite Warburg diffusion) and the total (low frequency) double layer capacitance of the RVC electrode respectively.

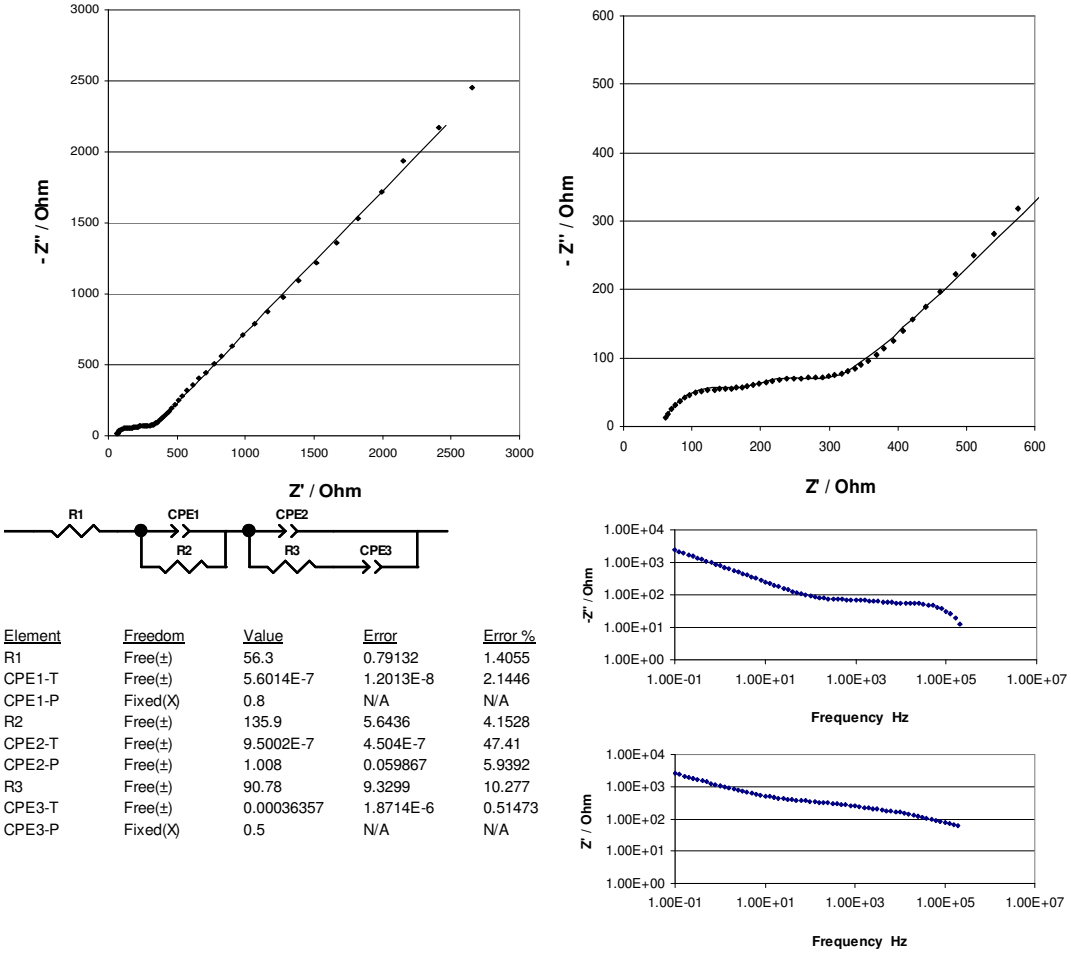

Element	Freedom	Value	Error	Error %
R1	Free(±)	56.3	0.79132	1.4055
CPE1-T	Free(±)	5.6014E-7	1.2013E-8	2.1446
CPE1-P	Fixed(X)	0.8	N/A	N/A
R2	Free(±)	135.9	5.6436	4.1528
CPE2-T	Free(±)	9.5002E-7	4.504E-7	47.41
CPE2-P	Free(±)	1.008	0.059867	5.9392
R3	Free(±)	90.78	9.3299	10.277
CPE3-T	Free(±)	0.00036357	1.8714E-6	0.51473
CPE3-P	Fixed(X)	0.5	N/A	N/A

Figure 6.3.7b. Nyquist (top) and Bode (bottom right) impedance plots, and equivalent circuit fit (bottom left) results for Li | (1M $LiPF_6$ EC:DMC) EMD / RVC cell containing 1 µm thick EMD / RVC cathode. Impedance measurements were recorded over the frequency range 200000 – 0.1 Hz; and at 10 data points per decade

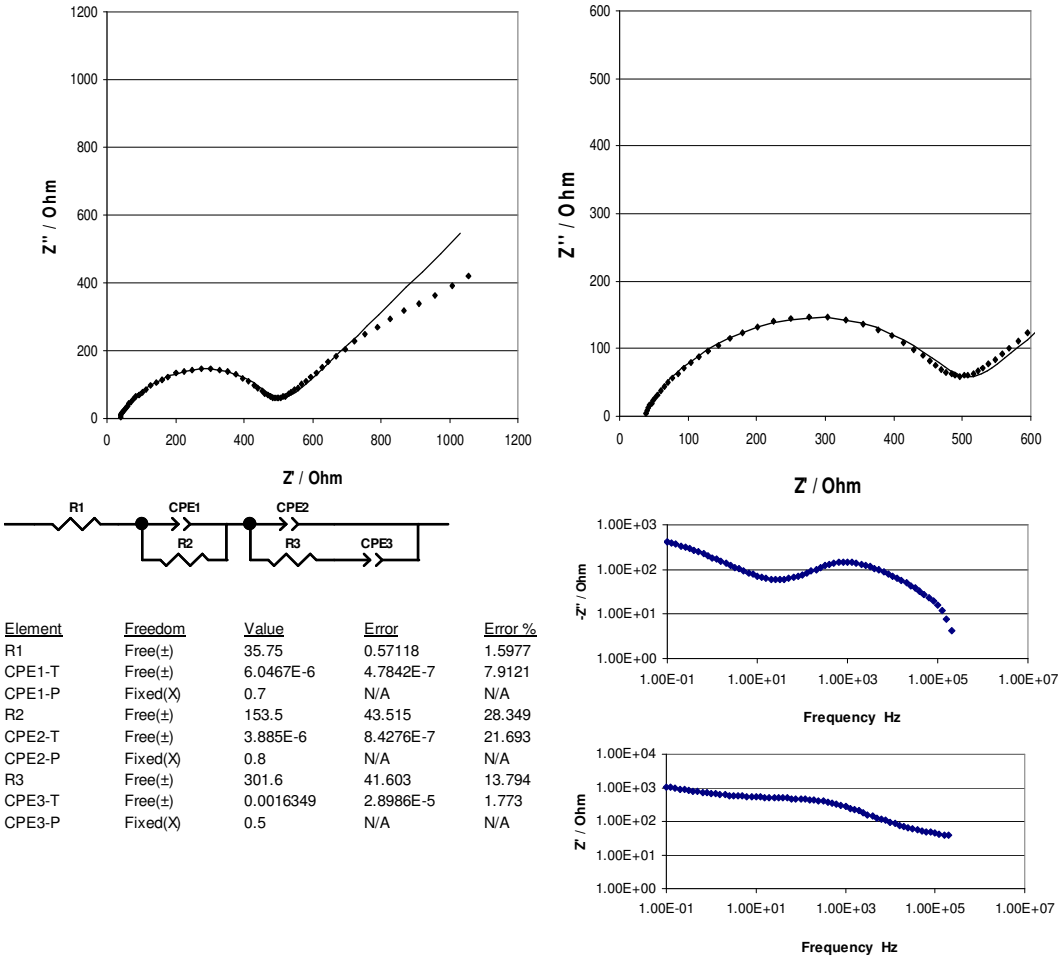

Element	Freedom	Value	Error	Error %
R1	Free(±)	35.75	0.57118	1.5977
CPE1-T	Free(±)	6.0467E-6	4.7842E-7	7.9121
CPE1-P	Fixed(X)	0.7	N/A	N/A
R2	Free(±)	153.5	43.515	28.349
CPE2-T	Free(±)	3.885E-6	8.4276E-7	21.693
CPE2-P	Fixed(X)	0.8	N/A	N/A
R3	Free(±)	301.6	41.603	13.794
CPE3-T	Free(±)	0.0016349	2.8986E-5	1.773
CPE3-P	Fixed(X)	0.5	N/A	N/A

Figure 6.3.7c. Nyquist (top) and Bode (bottom right) impedance plots, and equivalent circuit fit (bottom left) results for Li | (1M $LiPF_6$ EC:DMC) EMD / RVC cell containing 5 µm thick EMD / RVC cathode. Impedance measurements were recorded over the frequency range 200000 – 0.1 Hz; and at 10 data points per decade

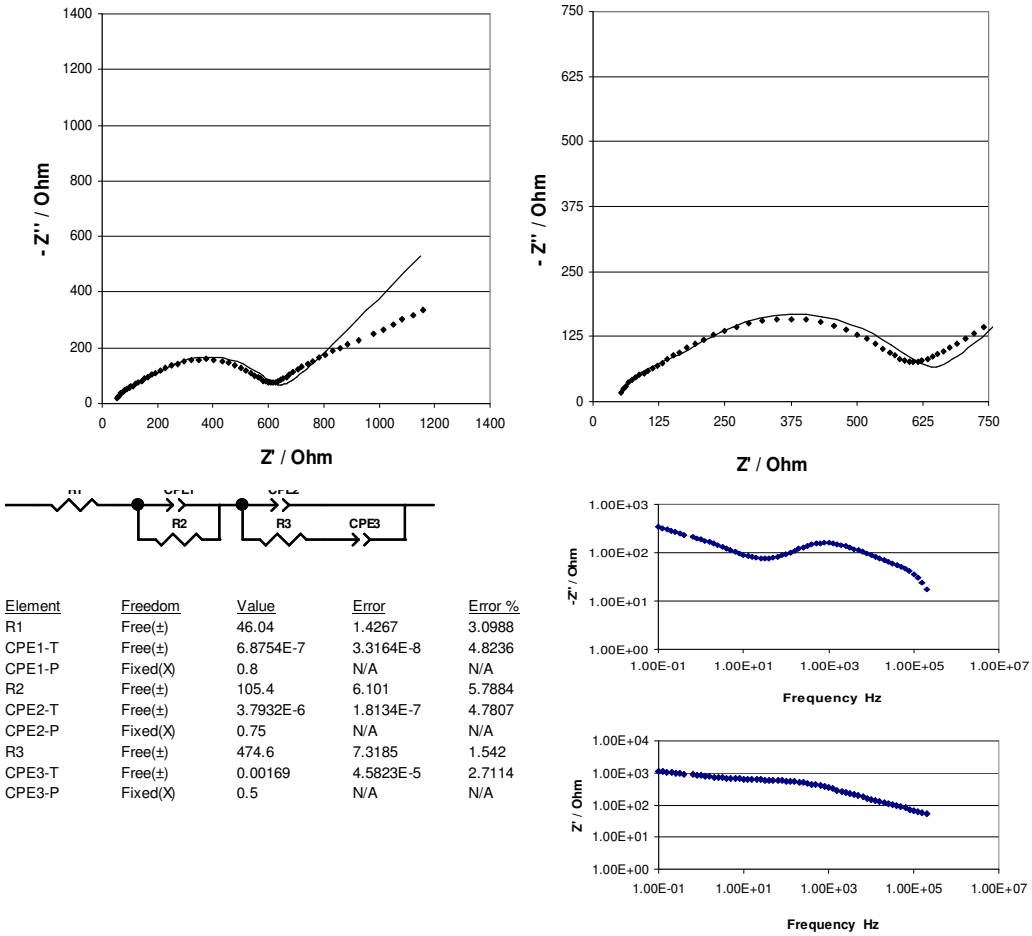

Element	Freedom	Value	Error	Error %
R1	Free(±)	46.04	1.4267	3.0988
CPE1-T	Free(±)	6.8754E-7	3.3164E-8	4.8236
CPE1-P	Fixed(X)	0.8	N/A	N/A
R2	Free(±)	105.4	6.101	5.7884
CPE2-T	Free(±)	3.7932E-6	1.8134E-7	4.7807
CPE2-P	Fixed(X)	0.75	N/A	N/A
R3	Free(±)	474.6	7.3185	1.542
CPE3-T	Free(±)	0.00169	4.5823E-5	2.7114
CPE3-P	Fixed(X)	0.5	N/A	N/A

Figure 6.3.7d. Nyquist (top) and Bode (bottom right) impedance plots, and equivalent circuit fit (bottom left) results for Li | (1M $LiPF_6$ EC:DMC) EMD / RVC cell containing 10 µm thick EMD / RVC cathode. Impedance measurements were recorded over the frequency range 200000 – 0.1 Hz; and at 10 data points per decade

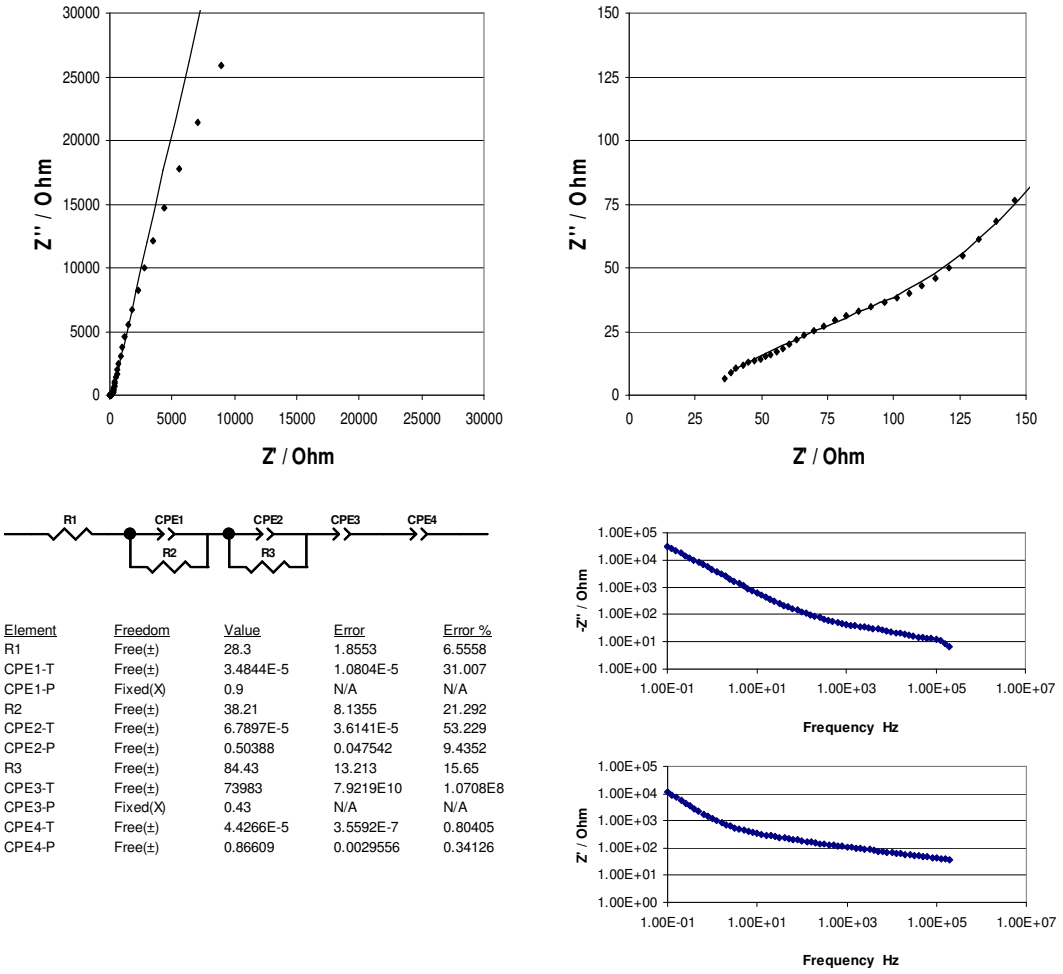

Element	Freedom	Value	Error	Error %
R1	Free(±)	28.3	1.8553	6.5558
CPE1-T	Free(±)	3.4844E-5	1.0804E-5	31.007
CPE1-P	Fixed(X)	0.9	N/A	N/A
R2	Free(±)	38.21	8.1355	21.292
CPE2-T	Free(±)	6.7897E-5	3.6141E-5	53.229
CPE2-P	Free(±)	0.50388	0.047542	9.4352
R3	Free(±)	84.43	13.213	15.65
CPE3-T	Free(±)	73983	7.9219E10	1.0708E8
CPE3-P	Fixed(X)	0.43	N/A	N/A
CPE4-T	Free(±)	4.4266E-5	3.5592E-7	0.80405
CPE4-P	Free(±)	0.86609	0.0029556	0.34126

Figure 6.3.7e. Nyquist (top) and Bode (bottom right) impedance plots, and equivalent circuit fit (bottom left) results for 'blank' Li | (1M $LiPF_6$ EC:DMC) RVC cell. Impedance measurements were recorded over the frequency range 200000 – 0.1 Hz; and at 10 data points per decade

The impedance plots in Figure 6.3.7b, c, d and e showed several characteristic features of the Li | (1M $LiPF_6$ EC:DMC) EMD / RVC cells. The high frequency semi circles were likely due to the lithium / electrolyte interface, as the resistance of the semi-circle appears to be independent of EMD layer thickness (R2, Figure 6.3.7a(A)). Similar high frequency features were seen in the impedance results for the 'blank' Li | (1M $LiPF_6$ EC:DMC) RVC cells (Figure 6.3.7e)

Although there is no noticeable increase in the uncompensated resistance (R1, Figure 6.3.7a(A)) with increasing thickness of EMD layer (as would be expected for an increasing ionic resistance through a more tortuous path of electrolyte in a thicker EMD film); the

resistance (R3, Figure 6.3.7a(A)) of the second semi circle appeared to increase with EMD thickness (Table 6.3.7a).

The increase in resistance of the second semi circles was attributed to a combination of increasing ionic and electronic resistance in the thicker EMD layers. The resistances of the various components in the equivalent circuit representations of the Li | (1M $LiPF_6$ EC:DMC) / RVC and Li | (1M $LiPF_6$ EC:DMC) EMD / RVC cells are summarised in Table 6.3.7a.

Table 6.3.7a. Summary of uncompensated cell resistance (R1) Lithium / electrolyte interface charge transfer resistance (R2) and electronic / ionic resistance through the EMD thickness (R3) for Li | (1M $LiPF_6$ EC:DMC) EMD / RVC cells.

EMD Thickness / µm	R1 / Ohm	R2 / Ohm	R3 / Ohm
RVC 'blank'	28	38	84
1	55	110	112
5	35	107	314
10	42	83	405

Figure 6.3.7f compares the Nyquist impedance plots of the varying thickness EMD / RVC electrodes with that of the porous 'blank' RVC electrode.

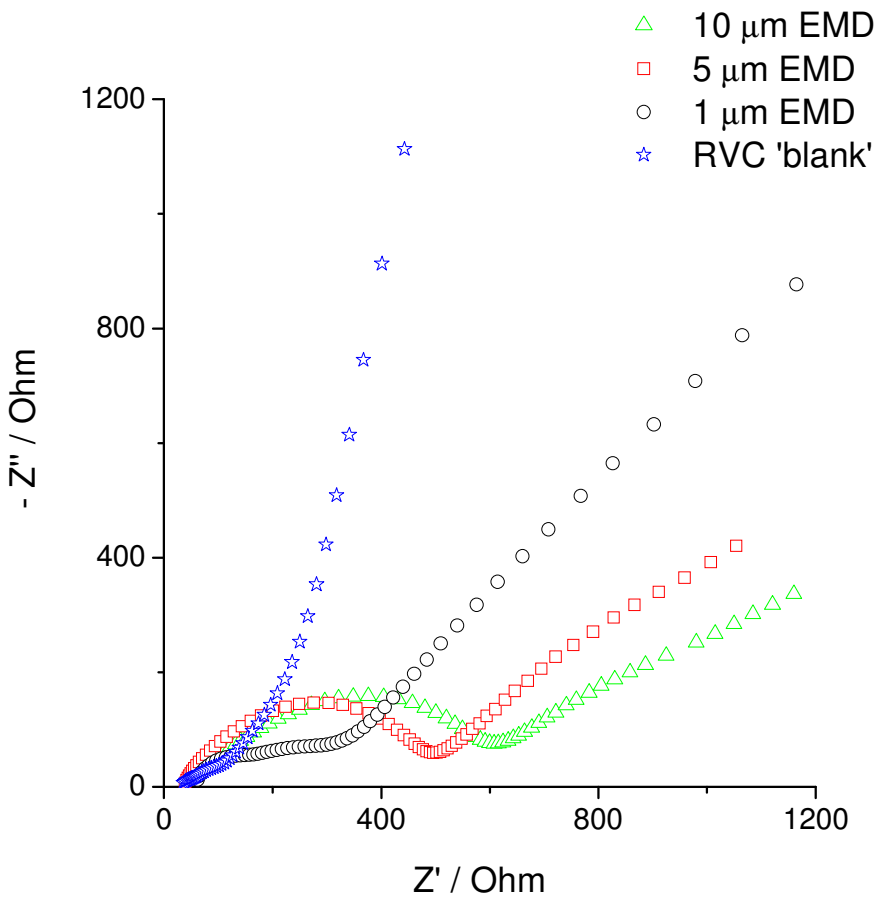

Figure 6.3.7f. Nyqist impedance plots 1, 5 and 10 µm EMD electrodes and 'blank' RVC substrate. The impedance was measured over the frequency range 200000-0.1 Hz, taking ten data points per decade.

Careful analysis of Figure 6.3.7f shows the transition between Warburg like and capacitive behaviour for the 'blank' RVC electrode; suggesting diffusion into the complete depth of the porous structure.

However, over the same frequency range this transition was not seen for electrodes coated in EMD; suggesting the presence of a rate limiting diffusive process in the EMD layer, rather than in the porous structure of the RVC substrate.

The features of the Nyquist impedance results suggest an ongoing diffusive process, i.e. an infinite Warburg diffusion where the full depth of the pore is never seen, in the EMD / RVC electrodes.

In the case where the main diffusion limiting process is in the thickness of the EMD electrode the Bode plot of capacitance *vs.* frequency should be independent of electrode thickness (as the electrode capacitance will depend on the depth of penetration into the electrode thickness, rather than the electrode thickness itself).

Figure 6.3.7g shows the AC impedance Bode plot of electrode capacitance vs. frequency for the EMD / RVC electrodes and the 'blank' RVC electrode.

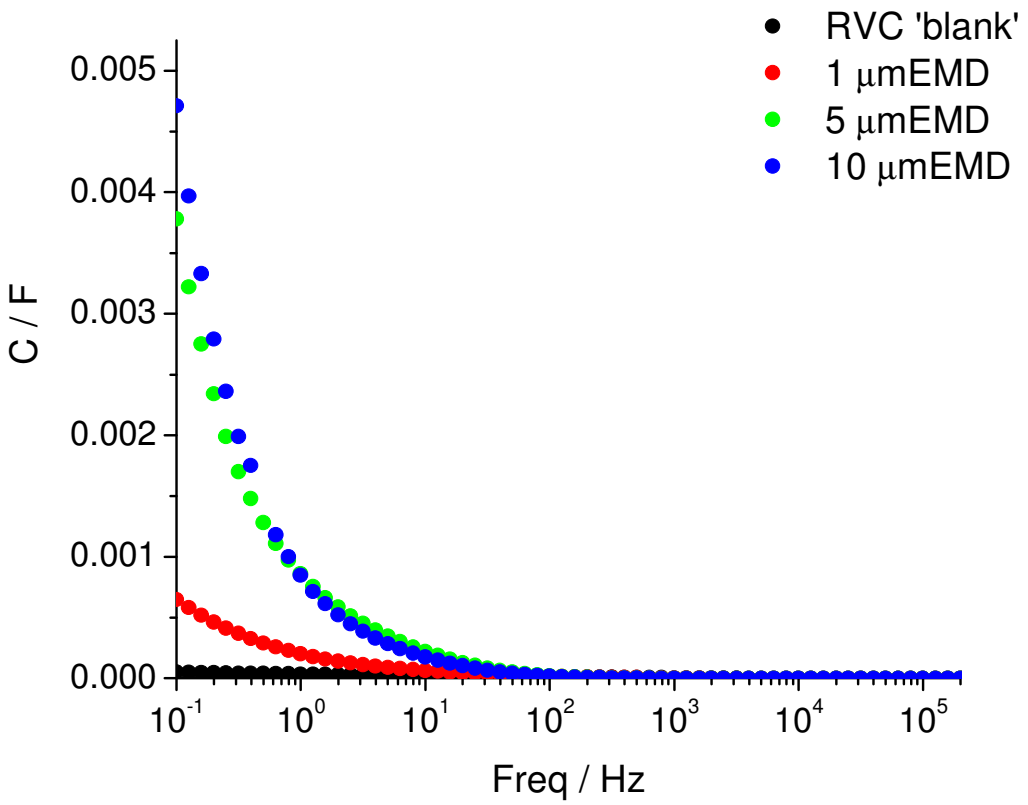

Figure 6.3.7g. Bode plot of capacitance *vs*. frequency for EMD / RVC and 'blank' RVC electrodes.

The Bode plot in Figure 6.3.7g clearly shows that the electrode capacitance was related to the thickness of the EMD layer; the capacitance is almost five times greater in the 5 µm thick electrode than in the 1 µm electrode and larger again in the 10 µm case. The capacitance of the 'blank' RVC electrode essentially zero. Table 6.3.7b compares the EMD / RVC electrode capacitance in the differing thickness EMD / RVC electrode | (1M $LiPF_6$ EC:DMC) | Li cells.

Table 6.3.7b. EMD / RVC electrode capacitance at 0.1 Hz for the three thicknesses of electrode and the RVC 'blank'

EMD thickness / um	Frequency / Hz	Electrode capacitance / F
RVC 'blank'	0.1	0.00005
1	0.1	0.00065
5	0.1	0.00378
10	0.1	0.00471

The relationship between electrode capacitance and EMD thickness suggested that the diffusion of lithium ions had reached the full thickness of the EMD layer (at least in the case of the one and 5 µm thick electrodes).

However the infinite Warburg behaviour seen in the Nyquist impedance plots, Figure 6.3.7f, suggested the presence of a third effect, solid state diffusion in the particles of EMD within the porous EMD layer. This third 'rate limiting' diffusion is illustrated in Figure 6.3.7h.

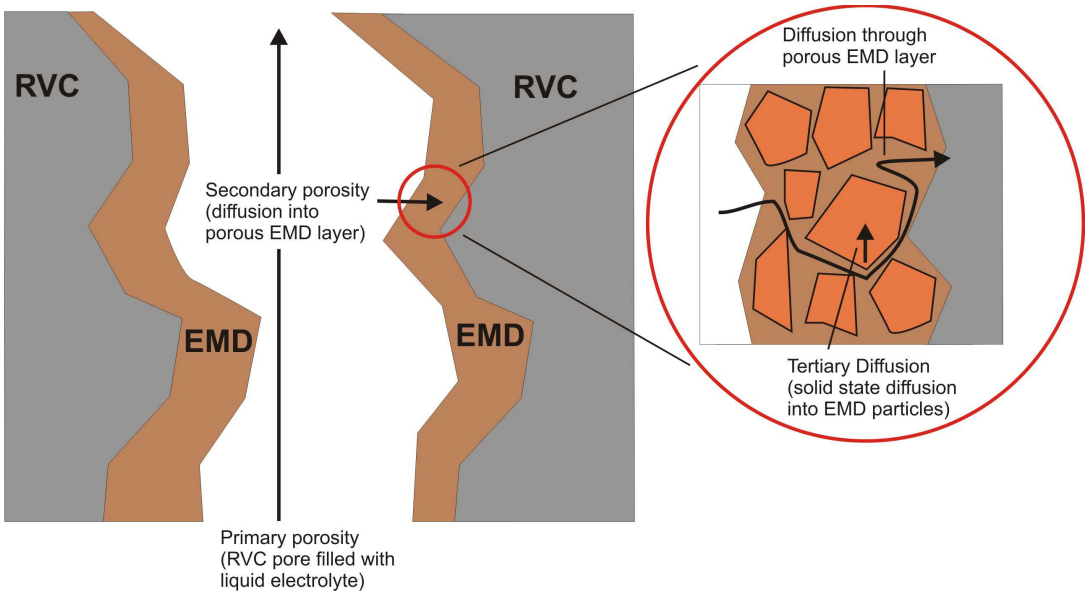

Figure 6.3.7h. Illustration of diffusion into the RVC structure (primary porosity) diffusion into the porous layer of EMD (secondary porosity) and 'rate limiting' diffusion into particles of EMD (tertiary diffusion).

As illustrated in Figure 6.3.7h the infinite Warburg diffusions seen in the Nyquist AC impedance results (Figure 6.3.7f) were attributed to solid state diffusion within the particles of EMD in the porous EMD films.

Due to the larger impedances associated with the thicker EMD electrodes (Table 6.3.7a) it was predicted that the rate performance of the Li | (1M $LiPF_6$ EC:DMC) EMD / RVC cells would diminish with increasing thickness of the EMD layer. It was also predicted that the diffusion limitation with in the solid state EMD particles may limit the rate performance of the cells.

6.3.8. Electrochemical Characterisation of Electrodeposited EMD | RVC Electrodes

The Li | (1M $LiPF_6$ EC:DMC) EMD / RVC cells were cycled galvanostatically at varying C rates (0.1, 0.2 and 0.4 C) in order to asses the effect of EMD film thickness on cyclabilty and rate capability. Initially charge and discharge cycles were performed using a discharge C-rate of 0.1 between 4.2 and 2 V *vs.* Li, this was increased to 0.2 and 0.4 C before being returned to 0.1 C for the remainder of the experiment (the charging rate was maintained at 0.1C throughout the experiment). Overall the cycling pattern consisted of 10 discharges at 0.1 C, 10 at 0.2, 10 at 0.4 before returning to 0.1 C for a further 60 discharges.
Figure 6.3.8a shows the individual discharge profiles for the differing thickness EMD / RVC cathodes at 0.1 0.2 and 0.4 C. Figure 6.3.8b shows the discharge profiles for each thickness of electrode compared to the rate of discharge.

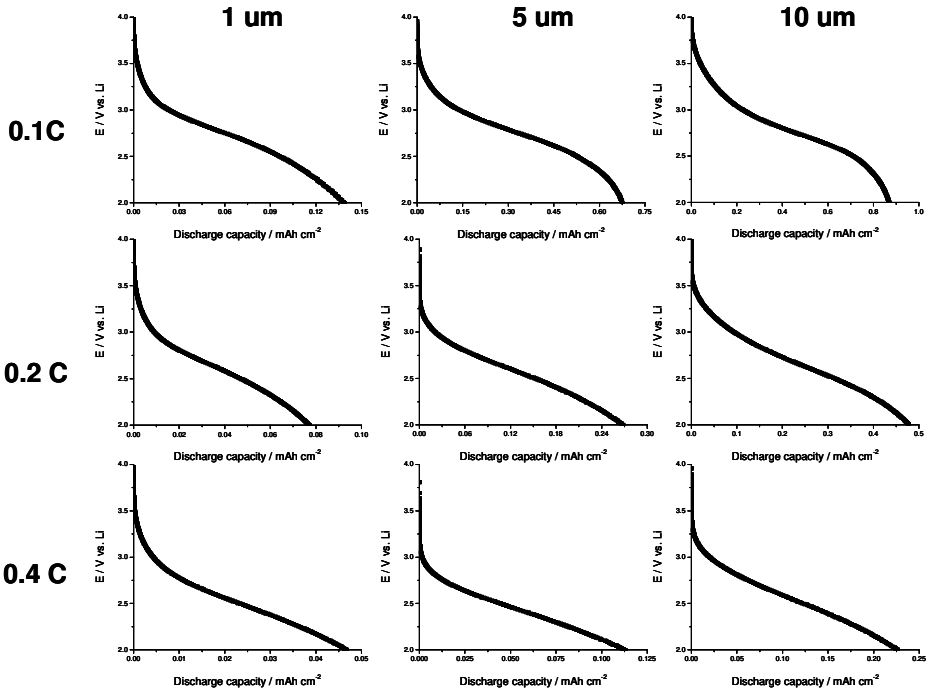

Figure 6.3.8a. Potential (*vs.* Li) *vs.* Discharge capacity at 0.1, 0.2 and 0.4 C for 1, 5 and 10 µm thick EMD / RVC cathodes in Li | (1M $LiPF_6$ EC:DMC) EMD / RVC cells (the second cycle, of 10, for each set of C-rates is shown).

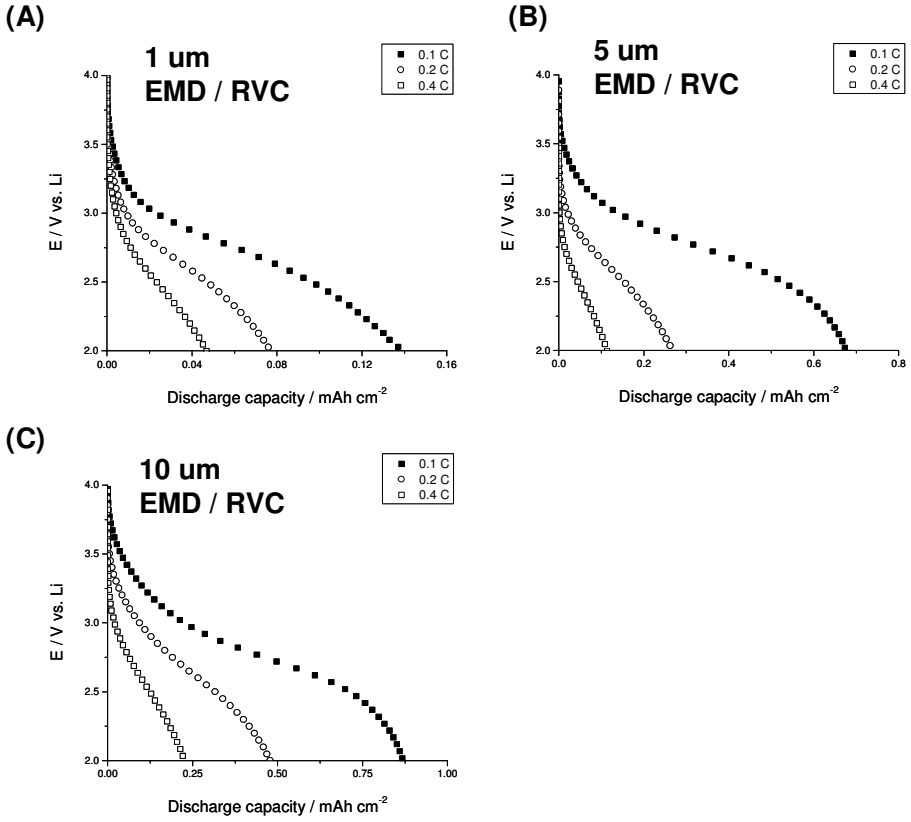

Figure 6.3.8b. Discharge profiles at 0.1, 0.2 and 0.4 C for 1 µm (A) 5 µm (B) and 10 µm (C) thick EMD cathodes in Li | (1M $LiPF_6$ EC:DMC) EMD / RVC cells.

As expected, the discharge profiles of the EMD / RVC electrodes (Figures 6.3.8a and b) show the same features as the discharge profile of the EMD composite electrode results, Figure 6.3.5a. The discharge starts at around 3 V and continues to about 2 V *vs*. Li at which point the end of discharge is marked by a downturn in potential, although this is less pronounced at higher C-rates.

The discharge capacity of the EMD / RVC electrodes decreased with increasing C-rate, however it was difficult to determine the rate performance at each thickness from Figures 6.3.8a and b alone. As such, the discharge capacity of the varying thickness EMD / RVC electrodes was plotted as a function of cycle number, including the cycling at increased C-rate, the results are shown in Figure 6.3.8c.

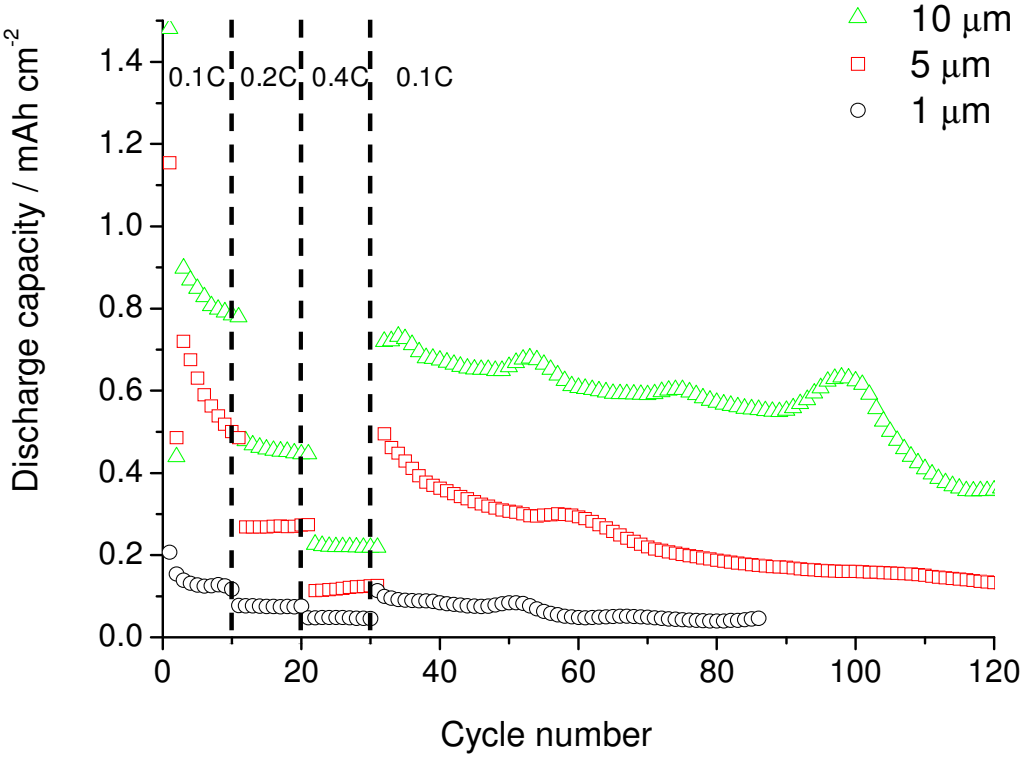

Figure 6.3.8c. Discharge capacity *vs*. cycle number for EMD (1 – 10µm) / RVC electrodes at varying C-rate.

The overall trend seen in the cycling results followed a similar pattern as the EMD composite electrode cells (Figure 6.3.5b), i.e. an initial large irreversible capacity followed by a gradual capacity fade with cycling. The effect of temperature on charge / discharge capacity was much more pronounced for the Li | (1M $LiPF_6$ EC:DMC) EMD / RVC cells than for the composite electrode pellets, visible by the periodic undulations in the charge / discharge capacity. The large amount of electrolyte in the foam based Li | (1M $LiPF_6$ EC:DMC) EMD / RVC cells was probably the reason for the greater sensitivity to temperature variation; in terms of percentage the electrolyte in the porous RVC / EMD electrode occupied a greater volume than the electrolyte soaked into the composite EMD electrode.

The cells containing electrodes with the thickest layer of EMD showed the greatest capacity at low charge / discharge rates (C / 10), this can be observed in Figure 6.3.8c by comparing results for 1 , 5 and 10 µm thicknesses. This was expected due to the simple fact that the electrodes with a thicker layer of EMD contained a greater volume of active material and therefore should have had a higher capacity.

According to the greater solid state lithium ion transport distances and of the interpretation of the impedance results (6.3.7) it was expected that the rate performance of the electrodes

containing thicker layers of EMD would be inferior to those with thinner layers (despite the higher slow cycling capacities).

A linear fit of discharge capacities was used to find the percentage capacity retention at 0.2 and 0.4 C based on a calculated initial (intercept) capacity, summarised in Figure 6.3.8d. The same technique was also used to calculate the percentage capacity at various discharge numbers.

The linear fitting procedure was used as in order to make a reasonable comparison of the rate capability of the EMD electrodes it was necessary to remove the effect of the large decrease in capacity seen between the first and second discharges (which appeared to show some dependence on EMD thickness, Table 6.3.8a). By using the linear fit of the discharge capacities it was also possible to compensate for the fluctuations in capacity due to temperature.

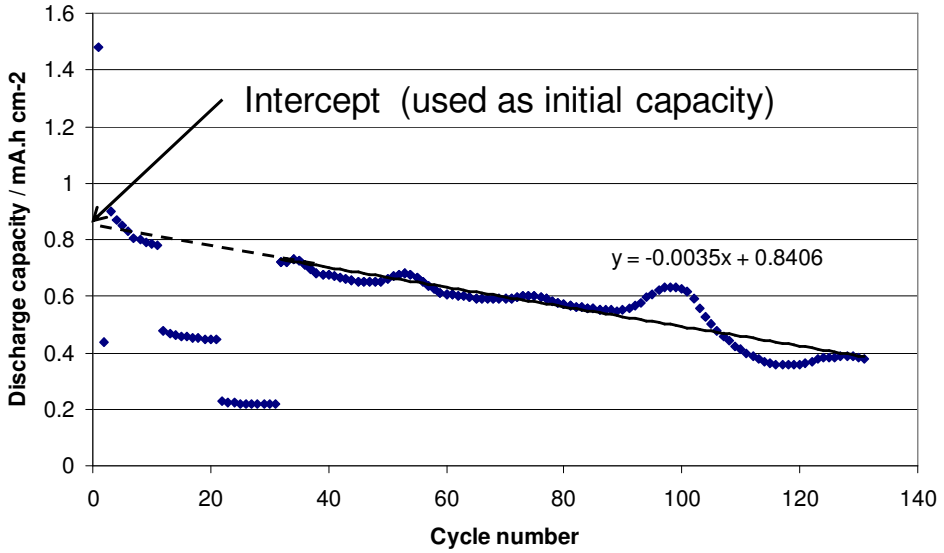

Figure 6.3.8d. Example of linear fit operation used to find initial capacity and compensate for temperature fluctuation. Initial 0.1 C and faster rate 0.2 / 0.4 C data are not used in the fit.

Table 6.3.8a. First cycle capacity loss for differing thickness EMD / RVC electrodes

Thickness / µm	Percentage discharge capacity loss between first and second cycle.
10	39.3
5	37.4
1	25.6

Table 6.3.8b compares the percentage discharge capacity retention for the differing thickness EMD electrodes at varying C rate and also shows the percentage of remaining capacity after 80 discharges.

Table 6.3.8b. Rate performance and discharge capacity (at 80 cycles) summary for differing thickness EMD / RVC electrodes. * Percentage capacity was based on a linear fit of the second 0.1C region in order to give an initial capacity (intercept) that was comparable for all thicknesses.

Thickness / μm	Percentage* capacity at 0.2 C	Percentage* capacity at 0.4 C	Percentage* capacity at cycle 80
10	54	26	33
5	58	28	52
1	57	36	73

A large drop in the discharge capacity of the EMD / RVC electrodes between the first and second cycle was expected, and had been observed in previous experiments using EMD composite electrodes (6.3.5).

The results of the galvanostatic cycling experiments suggest a dependence of initial (between first and second discharge) capacity loss on the thickness of the EMD layer in the EMD / RVC composite electrode; with the thickest electrodes losing the most capacity. (Table 6.3.8a). It was speculated that the greater mechanical stresses present in the thicker EMD layers led to a larger amount of cracking, and subsequent electronic disconnection, leading to the increased capacity losses.

The rate performance results of the EMD / RVC electrodes are summarised in Table 6.3.8b. At 0.2 C the rate performance of the different thickness EMD electrodes was comparable; the thickness appeared to have little effect on the percentage of initial capacity. However, at 0.4 C there was some indication of improved capacity retention in the 1 μm thick EMD layer compared to the 10 μm thick film, though the effect was not as pronounced as expected.

Although the difference in rate performance between the 10 and 1 μm thick EMD films was less than expected the capacity fading on cycling was much less for the thinner electrodes. This was attributed to greater cracking of the thicker EMD films with lithium extraction / insertion, leading to loss of active material by electronic disconnection from the current collector.

Although it was speculated that the thicker films cracked more than the thinner on cycling, post mortem SEM analysis of the cycled EMD / RVC electrodes found no conclusive evidence of such an effect, possibly due to the fact that much of the EMD film was hidden within the structure of the RVC foam electrode.

It was suggested the poor retention of capacity at higher (though still relatively low) rates and the seemingly minor effect of electrode thickness was due to the presence of larger 'rate limiting' effects. This rate limitation was attributed to solid state diffusion within particles of EMD in the porous EMD film.

6.4. Conclusions

The electrodeposition of electrolytic manganese dioxide (EMD), 6.2.1, onto a variety of substrates was achieved. Initially the deposition conditions and heat treatment regime were optimised to give the correct experimental conditions to deposit films in the gamma (Ramsdellite) phase [104, 106]. The XRD patterns shown in Figure 6.3.1a show peaks consistent with the EMD / Ramsdellite MnO_2 structure peaks found in the literature [104, 121-123] in the temperature range 30-400°C.

With the deposition and heat treatment conditions optimised for deposition of the correct phase of MnO_2 a series of deposition experiments were performed to create a calibration plot of deposition charge *vs*. film thickness (Figure 6.3.2a). This calibration plot was used to deposit films of EMD to a desired thickness by controlling the charge used in the deposition. When 3D substrates, such as reticulated vitreous carbons (RVC), were used the control of thickness was not affected and the films showed good conformallity to the substrate structure (Figure 6.3.4b).
Initial electrochemical characterisation of the EMD concentrated on comparing its performance to the literature performance of similar materials. The EMD was deposited onto planar titanium sheets and formed into a 'conventional' composite electrode formulation as described in 6.2.5.

The performance of the EMD was as expected showing an initial discharge capacity of ~ 220 mA.h g^{-1} (fading to ~ 150 mA.h g^{-1} after a few cycles) over the potential range 3-2.5 V *vs*. Li (Figures 6.3.5a and b) in good agreement with various literature examples of EMD / Ramsdellite [105, 106, 110, 124]. An AC impedance study was used to characterise lithium based half cells containing EMD / RVC electrodes with varying thickness EMD depositions.
The impedance results for the thicker EMD films showed an increasing resistance (Figure 6.3.7f), in comparison to the thinner films, indicative of an increase in 'solid state' ionic / electronic resistance with increasing EMD thickness.
According to an improved rate performance by minimisation of EMD thickness it was expected the rate performance of the Li | (1M $LiPF_6$ EC:DMC) EMD / RVC cells containing electrodes with the thicker coatings of EMD would be inferior to ones with the thinner layer.

Li | (1M $LiPF_6$ EC:DMC) EMD / RVC cells containing electrodes with 10, 5 and 1 μm EMD depositions were cycled galvanostatically at varying C rates and the rate performances compared.

The results are summarised in Figures 6.3.8b and c and by Table 6.3.8b but showed the thinnest (1μm) EMD electrode had only a 10% improvement in capacity retention at increased rate when compared to the thickest (10μm) electrode. The percentage capacity retention upon increasing the rate from 0.1 to 0.4 C was 36 and 26 % for the 1 μm and 10 μm electrodes respectively.

The unconvincing performance of the Li | (1M $LiPF_6$ EC:DMC) EMD / RVC cells at higher (though still relatively low) rates and smaller than anticipated electrode thickness effect was attributed to the presence of larger 'rate limiting' effect. The rate limitation in the Li | (1M $LiPF_6$ EC:DMC) EMD / RVC half cells was attributed to solid state diffusion within particles of EMD in the porous electrode film as described in 6.3.7.

Fabrication of a complete battery would require replacing the lithium foil anode with an anode that fully interpenetrates the 3D battery microstructure (Figure 4.1b).

Back filling the pores with electrode slurry would probably be the easiest method of inserting the second electrode. And some very initial experiments, not published here, suggested that incorporating an ink of negative electrode material into the RVC foam was possible. Other suggestions included electrodepositing the second electrode directly into the structure using an electronically conducting polymer electrolyte (where the electronic conductivity can be removed post deposition) or growing the second electrode into the structure using electrodeposition. However, the considerable challenge of successfully inserting the second electrode whilst maintaining electronic insulation between cathode an anode remai

Chapter 7

Electrodeposited Polymer Electrolytes; Determination and Differentiation of Electronic and Ionic Conductivity

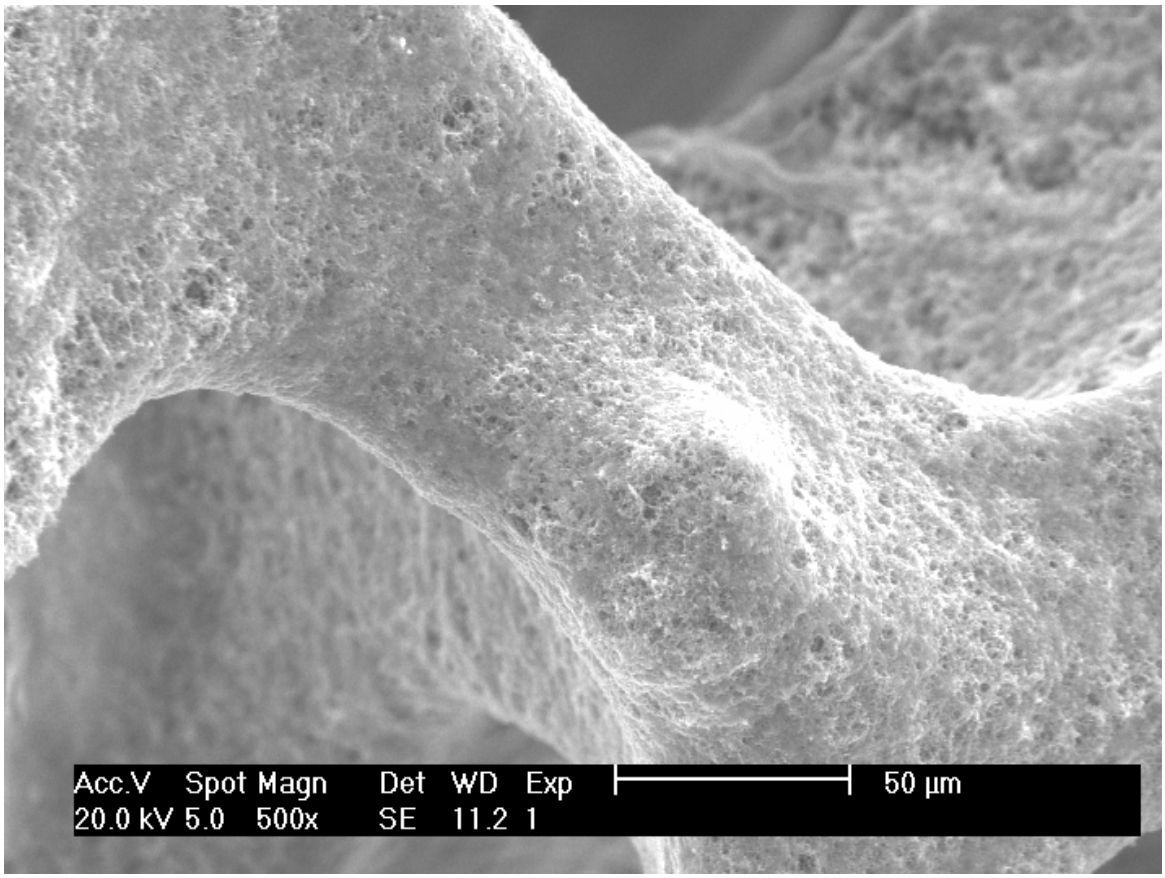

7.1. Introduction

Probably the most crucial component in the 3D Li-ion microbattery configuration (described in detail in Chapter 5) is the electrolyte. The most important properties of the electrolyte are its ability to maintain electronic isolation between the cathode and anode, especially in the case where the two electrodes are in very close proximity, whilst facilitating the transport of lithium ions.

In conventional lithium polymer batteries, such as pouch cells (commonly found in mobile phones etc), the electrolyte layer is generally formed using a gel-polymer electrolyte [125-128]. Gel-polymer electrolytes are based on a polymer film swollen with a conventional liquid electrolyte, i.e. $LiPF_6$ in EC:DMC (or similar).

A number of polymers have been proposed for use in polymer electrolytes; However, research has generally focussed on poly(ethylene oxide), poly(acrylonitrile), poly(methyl methacrylate) and poly(vinylidene fluoride), poly(vinylidene fluoride) has become the preferred polymer for industrial applications [33, 129-133]. The polymer layer is laminated to the positive and negative electrode assemblies and the whole construction can then be rolled up to form the cell, which is sealed within the cell housing.

In the case of the 3D microbattery numerous methods of incorporating the electrolyte into the cell have been developed [88, 90].The two strategies which have arguably received the most attention focus on either using a conventional liquid electrolyte, or a polymer electrolyte deposited using 'vacuum pulling' techniques.

The use of a liquid electrolyte is typically more suited to the interdigitated pillar / plate designs, (Figure 5.1a) such as those proposed by Minn *et al.* [89] where physical separation of the cathode and anode is provided by the microbattery structure. For 3D microbattery configurations where physical separation between the cathode and anode is required; i.e. the concentric and aperiodic designs (Figure 5.1a)), a 'vacuum pulling' technique (where the polymer electrolyte is drawn into a channel or pore) has been employed [75, 76, 85, 87].

This chapter describes the development of electrodeposition as an alternative technique for the incorporation of the electrolyte into the microbattery structure, and specifically focuses on the characterisation of the electrodeposited polymer layers.

The advantages of using electrodeposition to form the polymer electrolyte layer, over methods such as 'vacuum pulling' or dip coating, are briefly summarised below.

- The electrodeposited polymer electrolyte should completely coat the electrode surface, as the electrode surface is effectively the substrate of the electrodeposition.
- The problems associated with pinholes, small holes in the electrolyte layer leading to the possibility of electronic short circuits, should be minimised as the polymer should preferentially deposit on the uncoated electrode (due to the increasing resistance of the growing polymer layer.
- The electrodeposited polymer layer should fully follow the contours and features of the electrode, allowing complicated structures to be conformally coated.
- The use of electrodeposition requires little specialist equipment, and is relatively un-intensive in terms manufacturing effort.

The following experiments describe the electrodeposition of several polymer electrolytes on a variety of substrates and the development of a technique to determine, and differentiate between, their ionic and electronic resistances. Initially the electrodeposition behaviour of poly(acrylonitrile) (PAN) and poly(aniline) (PANI) on simple planar substrates was investigated, and the resultant films where characterised. Further experiments explored the deposition onto 3D, high surface area, substrates.

Spun or cast films of PAN have been extensively studied as polymer electrolyte materials [134-136]; however, in this work we focus on the properties of PAN electrodeposited directly onto the substrate / electrode surface.

The initial results for electrodeposition of poly(acrylonitrile) were used in the development of the electronic and ionic resistance determination experiment. This experiment was based on a series of electrochemical measurements performed on a cell consisting of a 'plasticized' poly(acrylonitrile) film electrodeposited onto a MnO_x cathode, and a 'soft contact' Li / Hg amalgam anode.

There has been considerable interest in the use of PANI in lithium-ion batteries, though mainly as a component in the cathode or anode [137-139]. There are very few literature examples of directly electrodeposited PANI films for lithium battery applications; there are no literature examples of electrodeposited PANI films being used as polymer electrolytes (as of April 2011).

The suitability of electrodeposited PANI as a potential polymer electrolyte was investigated using a series of AC impedance experiments.

7.2. Experimental

7.2.1. Electrodeposition of Poly(acrylonitrile) (PAN)

PAN was electrodeposited [140] onto a variety of substrates (gold, vitreous carbon and electrodeposited manganese dioxide) by cyclic voltammetry from a solution of 2 M acrylonitrile (98%+, Sigma-Aldrich) in acetonitrile (anhydrous, Sigma-Aldrich) with 0.05 M tetrabutylammonium perchlorate (TBAP) as supporting electrolyte at 50 $mV.s^{-1}$ between -0.5 and -3.5 V *vs*. Ag wire (~ +0.8 V *vs*. SHE) for 2-5 cycles.

7.2.2. Electrodeposition of Poly(aniline) PANI

PANI was electrodeposited onto a variety of substrates (planar vitreous carbon, reticulated vitreous carbon and electrodeposited manganese dioxide) by cyclic voltammetry from an aqueous solution of 0.1 M aniline (99.8%, Sigma-Aldrich) and 0.25M H_2SO_4 [141-144]. Cyclic voltammetry depositions were performed between -0.2 V and 0.75 V *vs*. SCE (0.9 V on the first cycle to nucleate the deposition and 0.75 V on subsequent cycles) at 100 $mV.s^{-1}$ for between 20-100 cycles depending on target thickness.

The electronic conductivity of PANI films was removed by switching from the conducting (emeraldine salt) to the insulating (emeraldine base) form by soaking the film in 1M LiOH (Sigma-Aldrich, 98%) for 2 hours. The films were then rinsed in de-ionised water and allowed to dry at room temperature for ~ 12 hours before being dried under vacuum, ~ 12 hours.

The electronic conductivity of the emeraldine salt ($PANI_{es}$) and emeraldine base ($PANI_{eb}$) PANI films was measured using AC-impedance, Chapter 2.3.2, according to the experimental set up illustrated in Figure 7.2.2a. The impedance measurements were recorded using an AC amplitude of 50 mV over the frequency range 200,000 to 0.1 Hz.

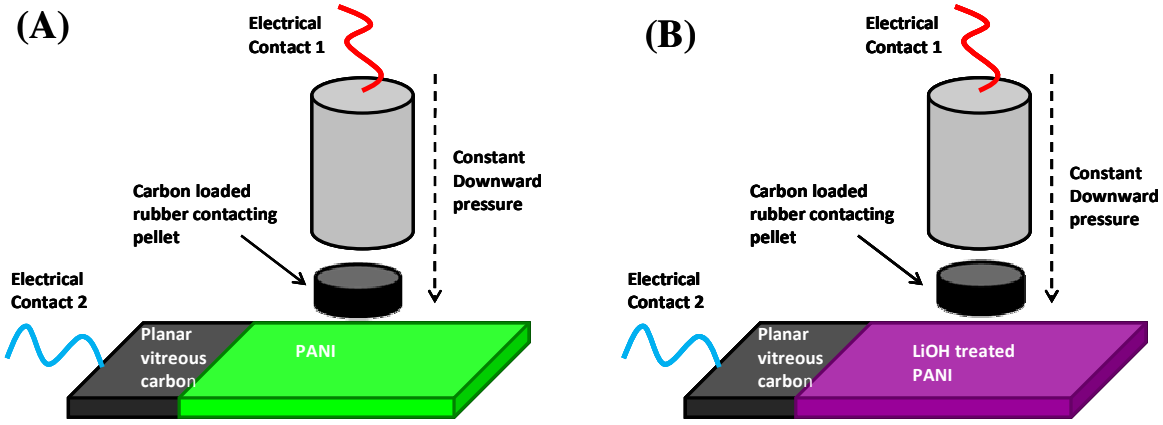

Figure 7.2.2a. Experimental set up used to measure AC impedance of electronically conducting emeraldine salt (A) and emeraldine base (B) forms of electrochemically deposited PANI film.

In order to be of interest as a polymer electrolyte it was necessary to introduce some ionic conductivity to the LiOH treated electronically insulating, emeraldine base, PANI films ($PANI_{eb}$). The $PANI_{eb}$ films were soaked in 1M $LiPF_6$ in PC battery electrolyte for 1 hour, excess electrolyte was removed by lightly dabbing the PANI film with glass fibre filter paper. The films appeared visibly swollen by the electrolyte, but crucially retained their distinctive purple colouration (indicating a lack of electronic conductivity).

The impedance of the $LiPF_6$ / PC soaked $PANI_{eb}$ film was measured using an AC amplitude of 50 mV over the frequency range 200,000 to 0.1 Hz. The soaking of the $PANI_{eb}$ films in electrolyte and the measurement of the AC impedance was performed in an Argon filled glove box.

7.2.3. Electrodeposition of Manganese Oxides

Amorphous manganese dioxides (MnO_x) were electrodeposited onto stainless steel (SS) from an aqueous solution of 0.01 M $KMnO_4$ and 0.6M KOH. The electroreduction of $KMnO_4$ was achieved using cyclic voltammetry between 0.5 and -1.5 V *vs*. Ag wire at $20mV.s^{-1}$ for 6 cycles. The MnO_x films were rinsed repeatedly in distilled water and dried under vacuum (100 °C ~12 h).
The stainless steel substrates were lightly sanded before use in order to improve the adhesion of the MnO_x to the surface. The substrates were cleaned subsequent to being sanded by sonication in ethanol /distilled (1:1) and water (15 minutes and 5 minutes respectively).

The SS / MnO_x electrodes were cycled galvanostatically as lithium half cells; the cell construction differed to that described in Chapter 2.2.1; the direct electrodeposition of cathode material on the current collector replaced the addition of a positive electrode pellet. The SS / MnO_x | 1M $LiPF_6$ EC:DMC (1:1) | Li foil cells were cycled between 1.5 and 3.5 V *vs*. Li at C / 7 for 50 cycles.
A potentiostatic top up period was employed at the end of charge (3.5 V *vs*. Li, 1 hour) and discharge (1.5 V *vs*. Li, 1 hour); in the case of premature charge or discharge the top up was used to ensure any remaining capacity in the MnO_x was inserted / extracted.

7.2.4. Electrodeposition of PAN on MnO_x

PAN was electrodeposited by cyclic voltammetry, as in 7.2.1, onto planar SS / MnO_x electrodes (7.2.3). The SS / MnO_2 | PAN electrodes were rinsed in acetonitrile and allowed to dry at room temperature for ~12 hours before being dried under vacuum at 80°C for a further 12 hours.

7.2.5. Determination of Ionic and Electronic Conductivity Within the Electrodeposited Polymer Electrolyte Using the Galvanostatic Intermittent Titration Technique (GITT)

An experiment to determine and distinguish between the electronic and ionic conductivity in polymer electrolytes was constructed. The electronic and ionic conductivity in PAN (soaked in 1M $LiPF_6$: PC, Merck) was determined for cells based on a lithium amalgam (Li / Hg) 'soft contact' liquid anode and a MnO_x cathode. The 'soft contact' (see Figure 7.2.5a) was used to reduce the chance of short circuit caused by mechanical penetration of the polymer electrolyte by the anode, and to encourage good contact between the two.
The Li / Hg liquid anode was prepared by dissolution of a small amount of lithium foil (< 5 atomic % lithium [145]) in Hg (99.9%, Aldrich) and stirring for ~ 24 hours.
PAN was electrodeposited onto MnO_x / SS (7.2.4) to form the current collector / cathode assembly; the SS / MnO_2 | PAN electrode was soaked in 1M $LiPF_6$: PC for 1 hour, excess electrolyte was removed before the assembly of the cell.
The cell was completed by the addition of the Li / Hg liquid anode. Figure 7.2.5a shows a schematic of the Li / Hg | PAN (1M $LiPF_6$: PC) | MnO_x / SS cell. The cell was assembled in an argon filled glove box (<0.1% H_2O, O_2; Unilab from MBraun) before being transferred to an argon filed plastic box (Figure 7.2.5a) (under a constant flow of argon) for electrochemical testing.

The Li / Hg | PAN (1M $LiPF_6$: PC) | MnO_x / SS cells were discharged galvanostatically to 1.5 V then charged galvanostatically to 3.5 V *vs.* Li / Hg at approximately C/30 (with 5 h relaxations after discharge / charge). The galvanostatic intermittent titration technique (GITT) experiment involved applying a charge or discharge current pulse (3.6 $\mu A\ cm^{-2}$, C/10, for 60 s) followed by an open circuit relaxation (30 min) in order to effect a small change in potential; and repeating numerous times over the desired potential range.

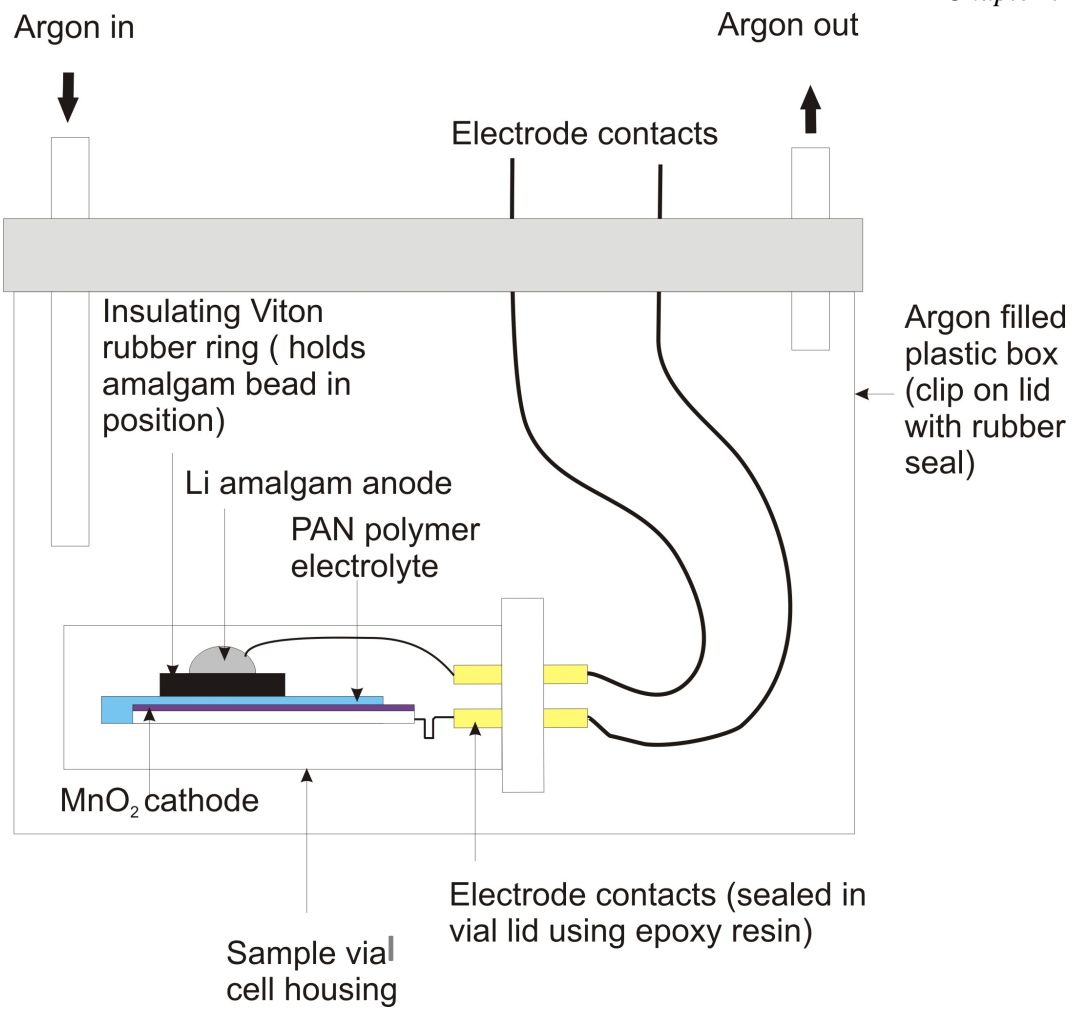

Figure 7.2.5a. Schematic representation of Li / Hg | PAN (1M $LiPF_6$: PC) | MnO_x / SS cell and surrounding argon filled chamber. A constant flow of argon through the chamber was maintained in order to reduce the chance of air leaking into the cell.

The Li / Hg | PAN (1M $LiPF_6$: PC) | MnO_x / SS cell was discharged galvanostatically to 1.5 V *vs.* Li /Hg and charged galvanostatically to 3.5 V *vs.* Li/Hg at approximately C/30 (with 5 h relaxations after discharge/charge). The GITT (Chapter 2.3.4) experiment involved applying a charge or discharge current pulse (3.6 µA cm^{-2}, C/10 for 60 s) followed by an open circuit relaxation (30 min) repeated numerous times over the desired potential range.

The results of the GITT experiments were used in the calculation of ionic and electronic conductivity of the polymer electrolyte.

The electrochemical potential of lithium amalgam (Li/Hg) *vs*. Li was measured using a Li | 1M $LiPF_6$: PC (glass fibre separator) Hg drop cell. The cell construction is shown in Figure 7.2.5b.

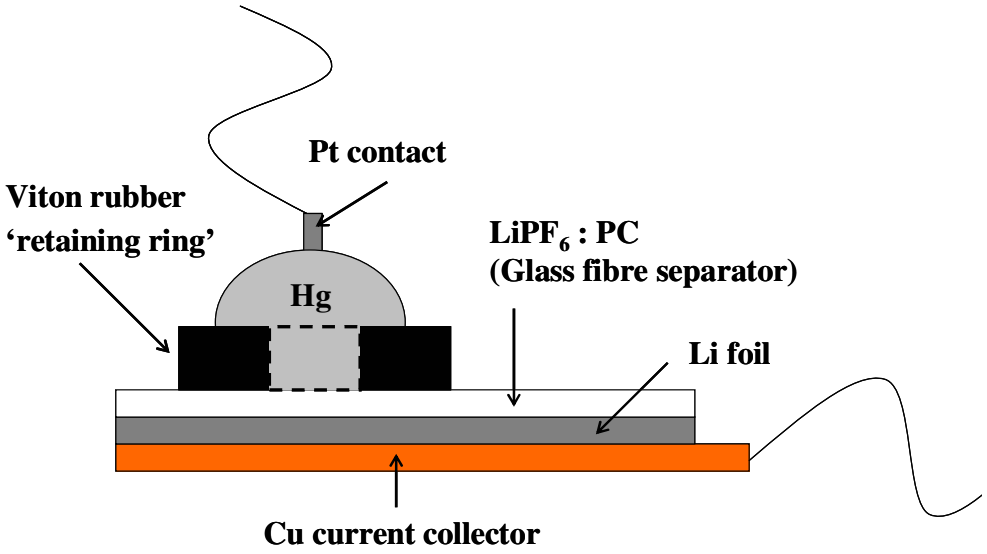

Figure 7.2.5b.Li foil | 1M $LiPF_6$: PC (glass fibre separator) Hg drop cell. Electrical connection to the Hg positive electrode is made using Pt foil.

7.3. Results and Discussion

7.3.1. Electrodeposition of Poly(acrylonitrile) (PAN)

Films of PAN were electrodeposited as described in 7.2.1. The mechanism of acrylonitrile electroreduction has been described as an 'electrographting' process initiated by cathodic electron transfer and aniline radical formation [140] . Figure 7.3.1a outlines the suggested electropolymerisation mechanism.

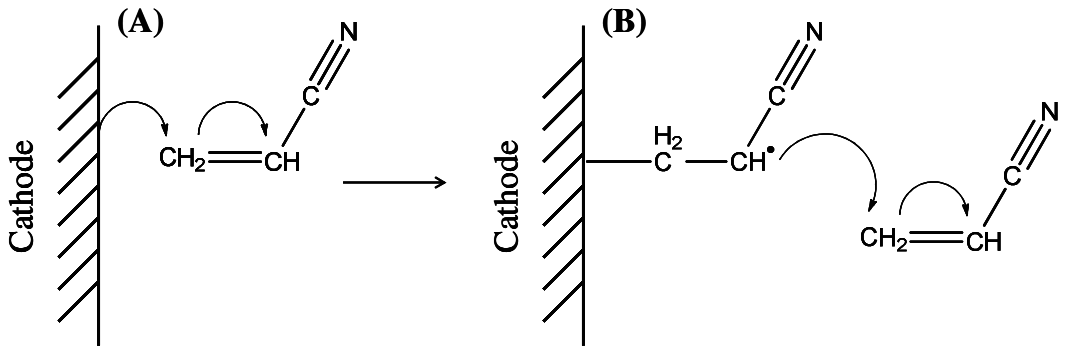

Figure 7.3.1a. Mechanism of acrylonitrile electropolymerisation as suggested by M.Mertens *et al* [140]. (A) Initiation step involving one electron reduction of acrylonitrile molecule and leading to formation of surface bound acrylonitrile radical. (B) Propagation step.

Initial experiments involved electrodeposition of PAN films on planar and 3D substrates (directly onto the substrate rather than onto a cathode or anode). Figure 7.3.1a shows a typical cyclic voltammogram for electrodeposition of PAN.

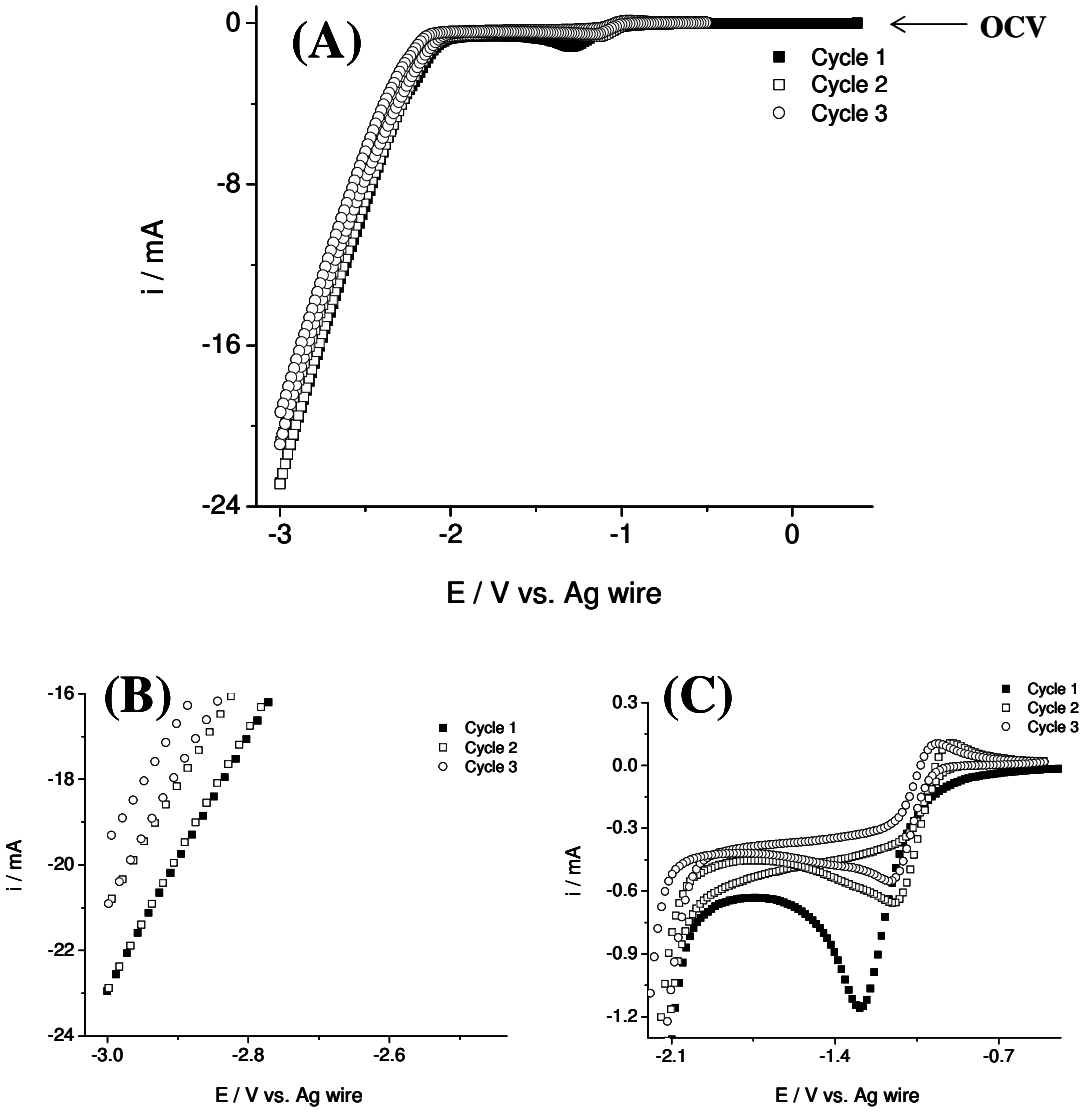

Figure 7.3.1b. Typical cyclic voltammetry for electrodeposition of PAN on a planar glassy carbon substrate. (A) Full scale voltammogram of deposition. (B) and (C) expanded views of the -3 and -1.5 V regions.

The open circuit voltage was measured as 0.38 V *vs*. Ag wire.

The voltammogram of PAN electrodeposition on vitreous carbon contained a number of features. Upon the first negative potential sweep an anodic peak was observed at ~ -1.3 V *vs*. Ag wire (Figure 7.3.1b(C)); the intensity of the peak decreased significantly on subsequent sweeps, it was suggested the peak was due to the initiation, initial radical formation, of the deposition reaction (Figure 7.3.1a).

Between -2 and -3 V *vs*. Ag wire there was a linear decrease in anodic current, the current decreased with cycle number suggesting an increase in resistance consistent with an increasing thickness deposition on the surface of the substrate.

The deposition resulted in a translucent yellow film. The presence of small pieces of translucent yellow polymer in solution after the deposition, especially when the number of deposition cycles was increased, suggested two possible effects; either the polymerisation of acrylonitrile was taking place in solution, or the mechanical stability of the PAN film was not sufficient enough to maintain a thick layer. The latter of the two explanations was considered most likely; the solution based polymer was observed accumulating directly underneath, suggesting it had fallen from, the working electrode.

Initially SEM and EDX were used to characterise the polymer deposits.
Figure 7.3.1c shows SEM and EDX data for PAN electrodeposited onto 3D Ni foam substrates.

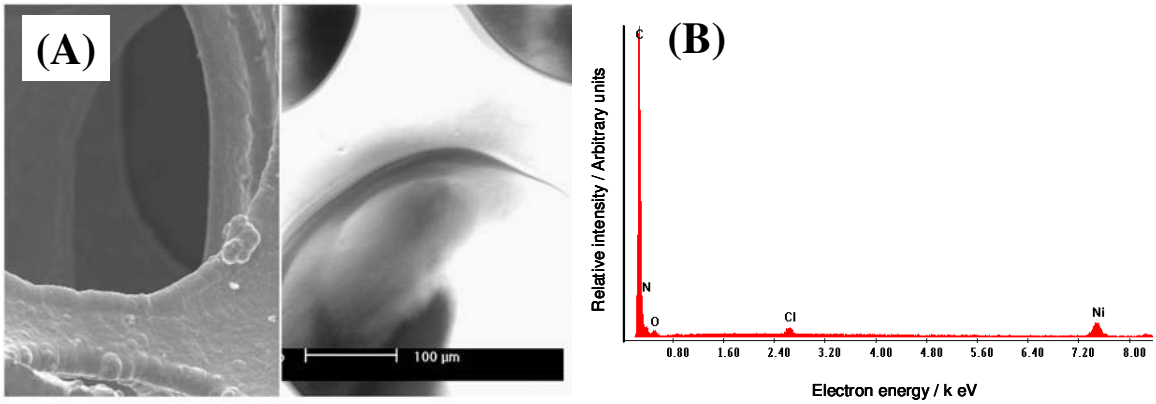

Figure 7.3.1c. (A) SEM image showing bare Ni foam (right) and Ni foam with an electrodeposited layer of PAN (left). (B) EDX spectrum of PAN coated Ni foam.

The SEM image in Figure 7.3.1c(A) shows a smooth and conformal deposition of PAN on a Ni foam electrode (the electrodeposition was carried out using the conditions stated in 7.2.2). The EDX analysis (Figure 7.3.1c(B) was taken from a spot measurement on the PAN / Ni electrode surface, the analysis showed only the expected components, i.e. carbon and nitrogen due to the PAN and a small signal from the Ni substrate (The signal due to chlorine is most likely due to the residual TBAP electrolyte salt)
The atomic ratio of the carbon nitrogen and oxygen peaks was 77:19:4; therefore the atomic percentage of nitrogen was 20(discounting the relatively small amount of oxygen). The atomic percentage of nitrogen in the electrodeposited film was in reasonably good agreement with the theoretical atomic percentage of nitrogen in PAN of 26.4 according a repeat unit of CH_2CHCN [146]. A possible explanation for the discrepancy between the

theoretical atomic percentage of nitrogen (26.4) and the measured percentage (20) was the greater carbon content in the PAN film as a consequence of the TBAP impurity.

IR spectroscopy was also used to further confirm the nature of the electrodeposited polymer. The IR spectrum showed a strong CN band at 2250 cm^{-1} as observed by Mertens et al [140].

7.3.2. Electrodeposition of Poly(aniline) (PANI)

PANI films were electrodeposited according to 7.2.2, resulting in a smooth green deposit. PANI was electrodeposited in its electronically conducting emeraldine salt form [146], due to the presence of H_2SO_4 in the deposition solution, and observed through the green colouration of the deposit.

The structure of the emeraldine salt of PANI is shown in Figure 7.3.2a.

The mechanism of the polymerisation was summarised by Mohinler et al [147] and is based on the formation of a cationic aniline radical by oxidation of aniline at the anode.

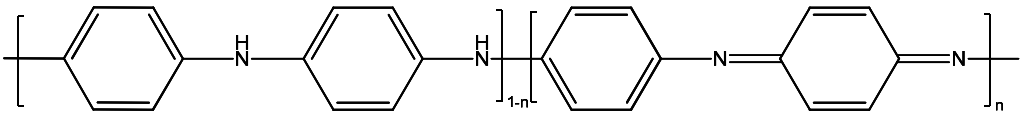

n = 1: Pernigraniline
n = 0.5: Emeraldine
n = 0: Leucoemeraldine

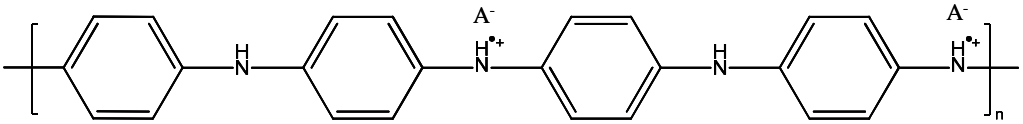

Emeraldine Salt

Figure 7.3.2a. Chemical structures of pernigraniline, emeraldine, leucoemeraldine and emeraldine salt [146]

A typical voltammogram for the deposition of PANI on vitreous carbon is shown in Figure 7.3.2b.

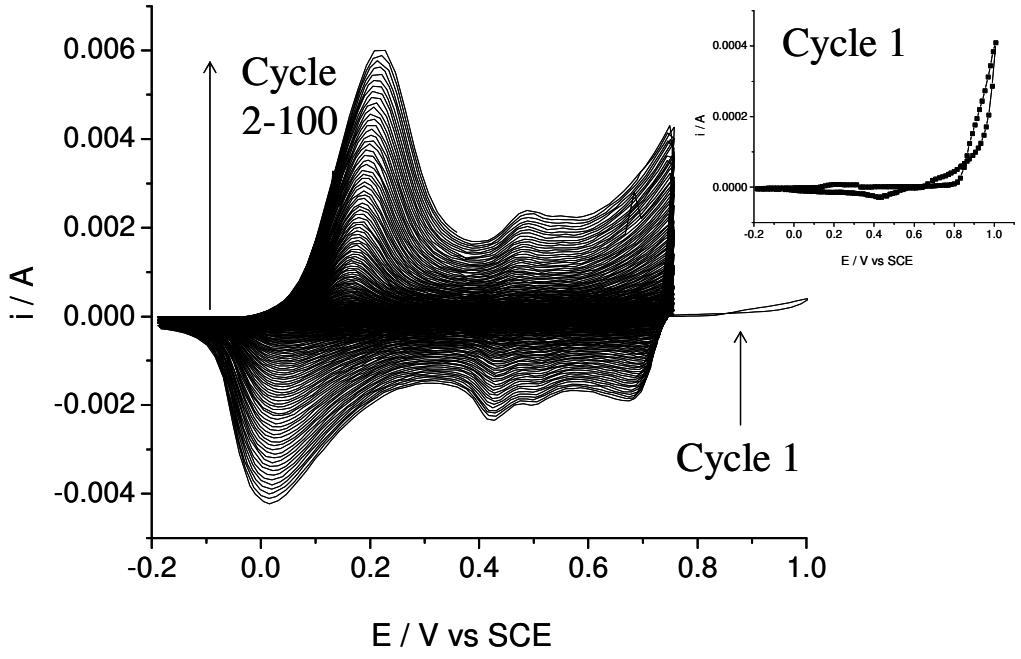

Figure 7.3.2b. Cyclic voltammogram of PANI electrodeposition on vitreous carbon rod electrode (3mm diameter). The CV deposition was performed at 100 mV s^{-1} for 100 cycles between -0.2 and 0.75 V *vs*. SCE (-0.2 and 1 V *vs*. SCE on first cycle only).

The deposition CV was complicated and showed a number of features. During the first cycle the voltammetry, Figure 7.3.2b inset, exhibited typical nucleation behaviour, visible by a decrease in nucleation overpotential upon the cathodic scan (~0.8 – 1V *vs.* SCE). The CV exhibited a number of redox peaks, at around 0.1, 0.5 and 0.7 V *vs.* SCE. The pair of peaks at 0.1 V was associated with the switching between leukoemeraldine and emeraldine (from leukoemeraldine and emeraldine on the anodic scan and from emeraldine to polyleukoemeraldine during the cathodic scan) [148] Peaks around 0.7 V *vs.* SCE were attributed to oxidation and reduction of emeraldine to pernigraniline and vice versa [148]. The pair of peaks seen at around 0.5 V *vs.* SCE has been assigned to the presence of oligomers or degradation products [149].

The relationship between increasing peak current and cycle number was evidence of an increase in deposited material and consistent with an increasing thickness of PANI film. Figure 7.3.2c shows an SEM image of PANI electrodeposited onto a reticulated vitreous carbon (RVC) electrode.

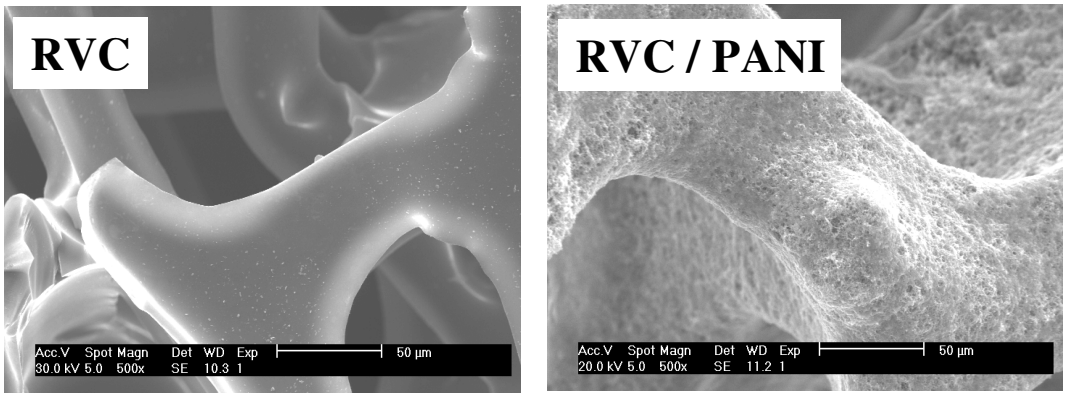

Figure 7.3.2c. Reticulated vitreous carbon (left) and electrodeposited PANI on RVC (right).

The ability to reversibly switch between electronically conducting and insulating states was one of the more interesting properties of the electrodeposited PANI films. The PANI films were electrodeposited in an electronically conducting state (emeraldine salt, $PANI_{es}$); in order to be of interest as a polymer electrolyte the material was switched to its insulating form (emeraldine base, $PANI_{eb}$) using LiOH solution (7.2.2). The $PANI_{es}$ and $PANI_{eb}$ were easily distinguished by the colour of the deposited / treated film. The as-deposited PANI films were green, indicating the PANI was in the emeraldine form; the treated PANI films were purple, indicating emeraldine base.

The electronic conductivity of the $PANI_{es}$ film was measured using AC impedance spectroscopy (Chapter 2.3.2); the same film was then treated with LiOH (7.2.2) and the AC impedance measurement repeated. The final impedance measurement was made on electronically insulating $PANI_{eb}$ films after soaking in 1M $LiPF_6$: PC battery electrolyte. The AC impedance results are shown in Figure 7.3.2d and e. The conditions of the AC impedance experiments are described in 7.2.2.

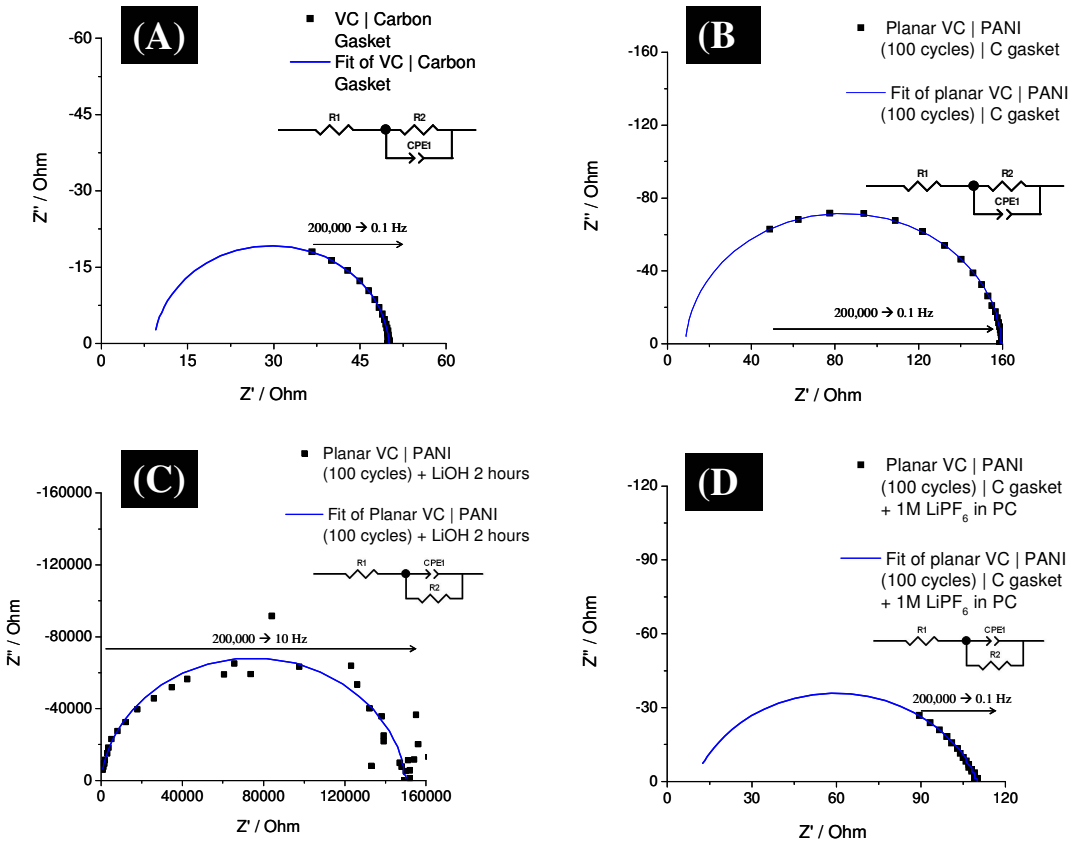

Figure 7.3.2d. (A) Nyquist AC impedance response of carbon gasket contact | VC substrate. (B) carbon gasket contact | PANI (100 cycles) | VC substrate. (C) carbon gasket contact | PANI (100 cycles) + LiOH 2 hours | VC substrate. (D) carbon gasket contact | PANI (100 cycles) + 1M $LiPF_6$ in PC | VC substrate. R1, R2 and CPE1 represent the substrate / instrumental resistance, the PANI resistance and the double layer capacitance between the C gasket contact and the PANI film (or VC substrate in the case of (A)) respectively.Large amounts of noise was observed in the low frequency data in plot (C); for reasons of clarity this data was omitted. The Impedance measurements were recorded at ten data points per decade, and using an average of three measurements per data point.

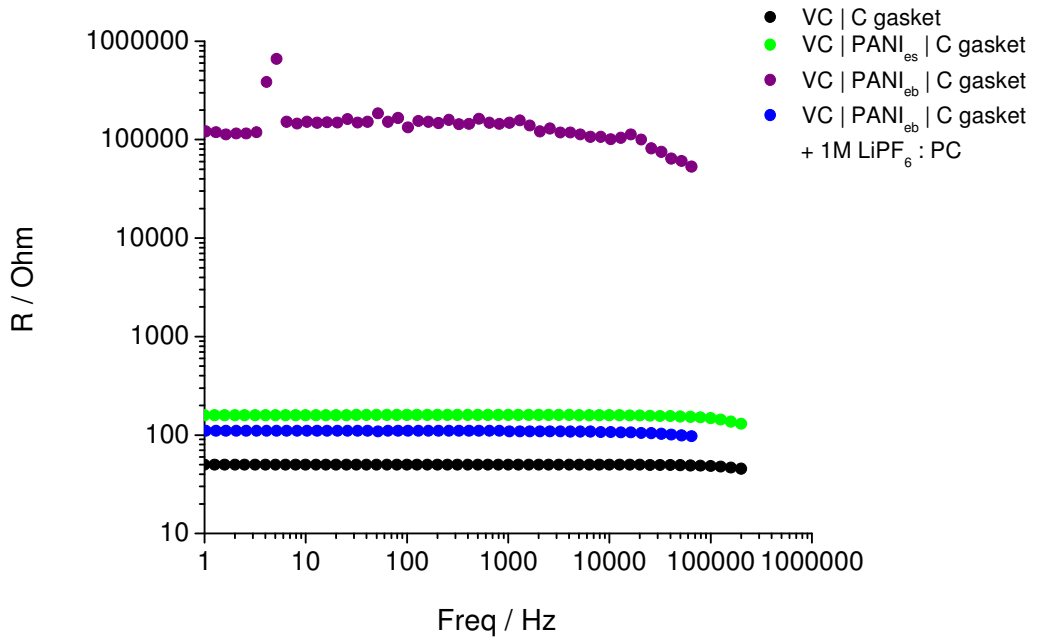

Figure 7.3.2e. Bode plot of Log Resistance / Ohm *vs*. Log frequency / Hz for the various electrodes shown in Figure 7.3.2d highlighting the differing resistances.

The experimental impedance results for the various VC | PANI | conducting carbon gasket cells were fitted to an equivalent circuit; the fit result is shown alongside the experimental results in Figure 7.2.3d (A), (B), (C) and (D).

The equivalent circuit consisted of a parallel combination of resistance (R2) and capacitance (CPE1) in series with the uncompensated resistance (R1). R1 was attributed to resistance through the substrate, plus any resistance due to the experimental set up, i.e. wires, instrumental resistance etc. R2 was asigned to the resistance through the conducting carbon gasket used to make contact between the VC | PANI electrode (or just VC electrode, Figure 7.3.2d (A)) and the top electrode contact (electrode contact 1, Figure 7.2.2a). CPE1 was used to model the double layer capacitance (C_{dl}) at the interfaces between the VC | PANI electrode (or VC, Figure 7.3.2d (A)) and the conducting carbon gasket. The model, and its application to the PANI electrodes, is illustrated by Figure 7.3.2f.

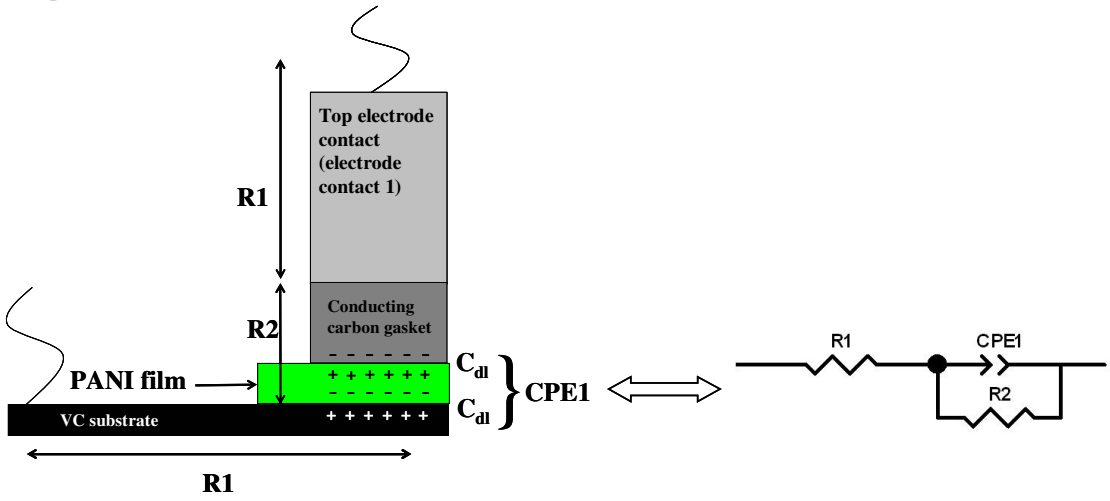

Figure 7.3.2f. Illustration of model used to fit impedance results in Figure 7.3.2d.

The experimental impedance result for the carbon gasket contact | VC electrode, Figure 7.3.2d (A), showed several prominent features. As the carbon gasket contact | VC electrode was effectively used as a control experiment it was important to determine the value of several of these features, namely R1 and R2.

The high frequency intercept was attributed to the uncompensated resistance (R1). R1 was estimated using a fit of the experimental data, as previously described, and was found to be 10 Ohms (+/- 1 Ohm); this resistance was attributed primarily to resistance through the VC substrate, and was constant for the $PANI_{es}$, $PANI_{eb}$ and electrolyte soaked $PANI_{eb}$ electrodes.

The resistance through the conducting carbon gasket, R2, was calculated by subtracting R1 from the low frequency resistance intercept. The value of R1 was calculated at 41 Ohms (+/- 1Ohm).

Figure 7.3.2d (B) shows the AC impedance result for the VC $PANI_{es}$ | conducting carbon gasket electrode. The form of the impedance is basically identical to that of the carbon gasket contact | VC electrode; the prominent difference is the increase in the value of R2 due to the resistance through the $PANI_{es}$ film. The resistance of the $PANI_{es}$ film was estimated by subtracting the resistance of the conducting carbon gasket from R2 for the electrode. The resistance value for the $PANI_{es}$ electrode is summarised in Table 7.3.2a.

Figure 7.3.2d (C) shows the impedance result for the LiOH treated VC $PANI_{eb}$ | conducting carbon electrode. As with the $PANI_{es}$ electrodes the form of the impedance plot remains unchanged from that of the carbon gasket contact | VC electrode; however R2 is significantly increased. The significant increase in R2 suggests the treatment of the $PANI_{es}$

electrodes with LiOH (7.2.2) removed a large portion of the electronic conductivity. The resistance of the resulting $PANI_{eb}$ electrodes is summarised in Table 7.3.2a.

The impedance of the electrolyte soaked $PANI_{eb}$ electrodes, Figure 7.3.2d (D), was measured in the hope that the electronic conductivity removed by the LiOH treatment would be replaced by ionic conductivity due to the electrolyte in the porous $PANI_{eb}$ film. The impedance result shows identical features to that of the previous experiments; and as expected the addition of electrolyte significantly reduced the resistance of the film, Table 7.3.2a.

Table 7.3.2a. Summary of film resistance as calculated using AC impedance for various PANI electrodes.The resistance values of the PANI films were calculated by subtracting the conducting carbon gasket resistance from the R2 value for the electrode.

Electrode	R1 / Ω	R2 / Ω	PANI resistance / Ω cm^{-2}
VC | C gasket	10 (+/- 1)	41 (+/- 1)	/
VC | $PANI_{es}$ | C gasket	9 (+/- 1)	151 (+/- 5)	**111 (+/- 6)**
VC | $PANI_{eb}$ | C gasket	100 (+/- 500)	150000 (+/- 3000)	**149900 (+/- 3500)**
VC | $PANI_{eb}$ | C gasket + 1M $liPF_6$ / PC	10 (+/- 1)	100 (+/- 5)	**60 (+/- 6)**

The resistance values highlighted in Figure 7.3.2e and summarised in Table 7.3.2a show two significant results. Firstly the large increase in resistance between the $PANI_{es}$ and $PANI_{eb}$ electrodes suggests the majority of the electronic conductivity within the film was removed. Secondly a significant amount of ionic conductivity was introduced into the porous, electronically insulating, $PANI_{eb}$ by soaking the films in 1M $LiPF_6$ / PC electrolyte. The nature of the resistance, i.e. electronic or ionic, was not easily determined using impedance alone. However, the characteristic colour change, from purple to green, involved in the transition from electronically insulating $PANI_{eb}$ to electronically conducting $PANI_{es}$ was not observed in the electrolyte soaked electrodes; suggesting the decrease in resistance was due to the ionic conductivity of the electrolyte, rather that the $PANI_{eb}$ films reverting $PANI_{es}$.

Interestingly, the resistance of the electronically conducting $PANI_{es}$ electrode was higher than the resistance of same electrode once treated with LiOH and soaked in electrolyte, $PANI_{eb}$ + 1M $LiPF_6$ / PC. It was thought that this was due to a combination of good ionic

conductivity in the electrolyte and improvement of the contact between the conducting carbon gasket and the $PANI_{eb}$ film due to the effect of being swollen with electrolyte.

The resistance values shown in Table 7.3.2a were used to estimate conductivity for each of the three types of PANI electrode, i.e. $PANI_{es}$, $PANI_{eb}$ and $PANI_{eb}$ + 1M $liPF_6$ / PC. Equation 7.2.3a was used to estimate conductivity; the conductivity results are shown in Table 7.3.2b.

$$\sigma = \frac{1}{R} \cdot \frac{L}{A}$$ **Equation 7.3.2a**

(Where σ denotes conductivity (S cm^{-1}), R is resistance (Ω), L is film thickness (cm) and A is cross sectional area (cm^2)).

Table 7.3.2b. Resistance and conductivity for $PANI_{es}$, $PANI_{eb}$ and $PANI_{eb}$ + 1M $liPF_6$ / PC based electrodes. The thickness and contact area (A) of the PANI films was estimated as 10 µm and 0.16 cm^2 for all electrodes

Electrode	PANI resistance / Ω	PANI σ / S cm^{-1}
VC| PANIes | C gasket	111	~ 6 x 10^{-5}
VC| PANIeb | C gasket	149900	~ 4 x 10^{-8}
VC| PANIeb | C gasket + 1M liPF6 /PC	60	~ 0.00011

The thickness of the PANI electrodes was measured, or approximated, as 10µm, using SEM images of the film cross section. The polymer films were not mechanically robust enough to measure using conventional methods, i.e. profilometry or with a micrometer, and too translucent to measure using optical methods. Therefore the measured thickness of the film was more an approximation than an accurate measurement. As such, the conductivity values for the $PANI_{eb}$ and $PANI_{eb}$ + 1M $LiPF_6$ films were more appropriately expressed in comparison to each other than as stand alone values.
Using the estimated values of conductivity and applying the aforementioned approximations the value of the conductivity within the $PANI_{eb}$ film was found to be ~ 2500 times smaller than in the same film swollen with electrolyte (1M $LiPF_6$: PC).

As previously stated the nature of the conductivity within the PANI based films, i.e. electronic or ionic, was not easily distinguished using the AC impedance results.

The lack of the purple to green transition expected during the transition from electronically insulating $PANI_{eb}$ to electronically conducting $PANI_{es}$ was used as the basis of the suggestion that the majority of the conductivity introduced by swelling the $PANI_{eb}$ films with electrolyte was ionic. Based on this assumption the use of 1M $LiPF_6$: PC swollen $PANI_{eb}$ films as polymer electrolytes within Li based cells was considered reasonable.

7.3.3. Electrodeposition and Characterisation of MnO_x

The cathode material MnO_x was electrodeposited onto stainless steel electrodes using cyclic voltammetry as in 7.2.3. The MnO_x was deposited by three electron electroreduction of $KMnO_4$ according to Equation 7.3.3a.

$$KMnO_4 + 2\ H_2O + 3e^- \longrightarrow MnO_2 + KOH + 3\ OH^- \qquad \textbf{Equation 7.3.3a}$$

Figure 7.3.3a shows an example cyclic voltammogram for the electrodeposition of MnO_x on stainless steel.

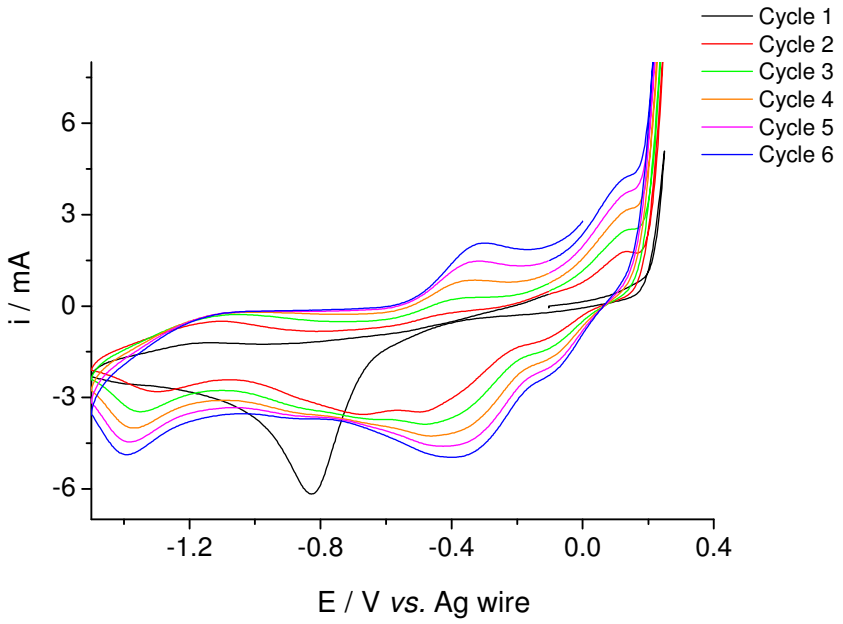

Figure 7.3.3a. Cyclic voltammogram of MnO_x deposition on stainless steel.

The first sweep of the deposition voltammogram shows one large anodic peak at ~ -0.8 V *vs.* Ag wire, in stark contrast to latter cycles. It was speculated the single large peak seen in the first cycle was the result of an 'activation' process on the surface of the stainless steel substrate, i.e. the break up of surface passivating oxide layers.

For cycles 2-6 the form of the voltammetry was constant, there were three sets of peaks observed at roughly 0.1, -0.3 and -1.2 V *vs.* Ag wire corresponding to the three electron reduction of $KMnO_4$ as in Equation 7.3.3a. The increase in charge with cycle number suggested an increasing surface area of MnO_x consistent with an increasing thickness, and therefore volume, MnO_x deposition.

The electrodeposition led to a porous dark brown film with a 'cauliflower' like structure, Figure 7.3.3b shows SEM images of a deposited MnO_x film.

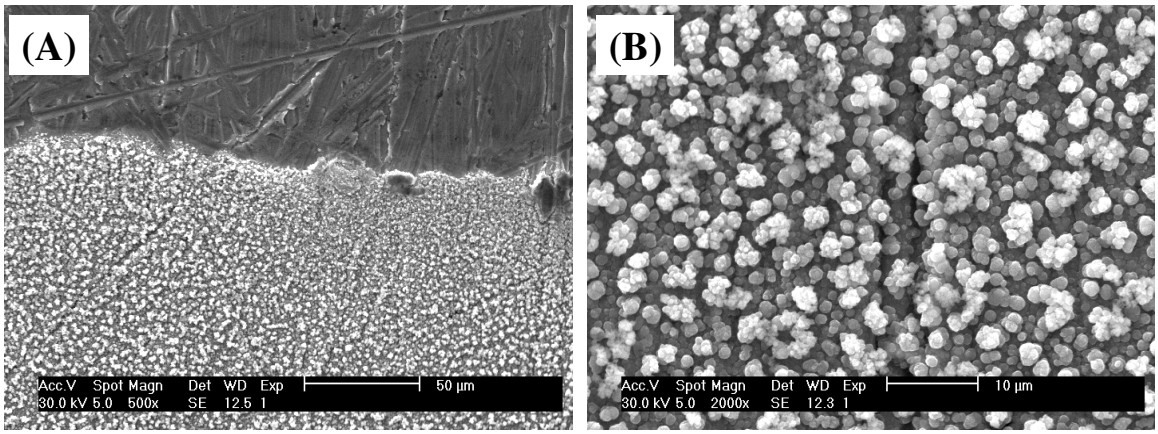

Figure 7.3.3b. SEM images of electrodeposited MnO_x films on stainless steel. (A) MnO_x (cauliflower like) and stainless steel substrate (scratched surface) at 500 x magnification. (B) MnO_x deposition at 2000 x magnification.

The composition of the deposited films was investigated using EDX and XRD spectroscopy. The XRD results suggested the MnO_x deposition were amorphous, with no obvious structural peaks. EDX spot measurements of MnO_x confirmed the presence of manganese and oxygen; the EDX results of MnO_x on a Ni substrate are summarized in Figure 7.3.3c.

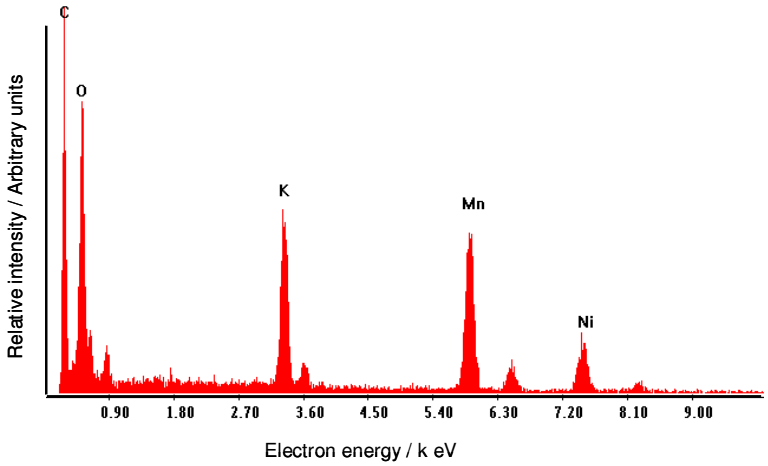

Figure 7.3.3c. EDX spectrum of electrodeposited MnO_x on a nickel substrate.

The EDX spectra for MnO_x on Ni (Ni was used as the MnO_x substrate rather than stainless steel because the electron energies of iron and manganese overlap, complicating the determination of Mn content) showed large intensity peaks for manganese and oxygen as expected. The nickel and potassium peaks were due to signals from the nickel substrate

and KOH impurities. The large carbon signal was probably due to the carbon based adhesive pad used to mount the sample.

The electrochemical performance, in terms of charge and discharge, of the SS / MnO_x electrodes was measured using a galvanostatic cycling experiment (7.2.3).

The charge and discharge profiles of the SS / MnO_x | 1M $LiPF_6$ EC:DMC (1:1) | Li foil half cells are shown in Figure 7.3.3d.

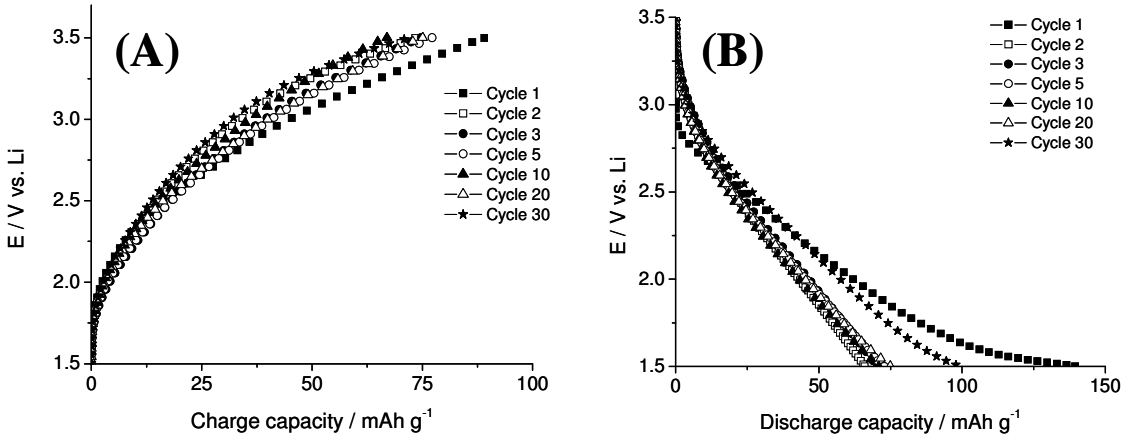

Figure 7.3.3d. Charge (A) and discharge (B) profiles of SS / MnO_x | 1M $LiPF_6$ EC:DMC (1:1) | Li foil half cells at a charge / discharge rate of C / 7. The switch between charge and discharge was preceded by a 1 hour potentiostatic top up period at 3.5 and 1.5 V *vs*. Li respectively.

During charging lithium insertion into MnO_x achieved a capacity of ~ 75 mA.h g^{-1}; conversely, upon discharge, a similar capacity was seen for lithium extraction. There was a fairly large irreversible capacity seen between first discharge and first discharge; it was suggested that a significant portion of this charge was due to extraction of potassium ions (Figure 7.3.3c) present within the MnO_x electrode (impurities from the deposition).

The effect that was not immediately obvious from Figure 7.3.3d was the dependence of charge / discharge capacity on temperature (though this effect explains the apparently anomalous result seen for the 30^{th} discharge (Figure 7.3.3d(B)). The temperature dependence effect was seen in the plot of charge / discharge capacity *vs*. cycle number, shown in Figure 7.3.3e.

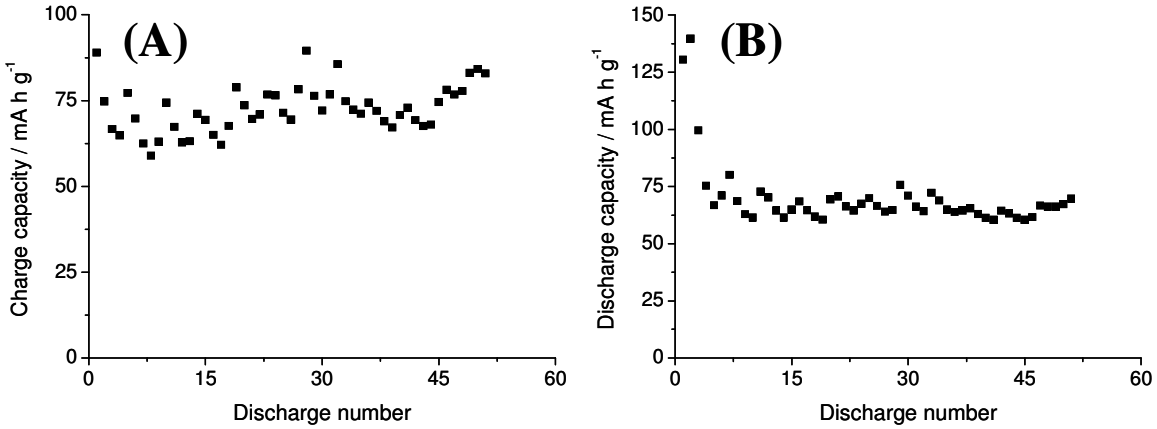

Figure 7.3.3e. Charge (A) and discharge (B) capacity *vs*. cycle number for galvanostatic cycling of SS / MnO_x | 1M $LiPF_6$ EC:DMC (1:1) | Li foil half cells at a charge / discharge rate of C / 7.

A relatively large temperature variation effect was seen leading to large fluctuations, or undulations, in charge / discharge capacity. The variation in capacity with cycle number was effectively a variation with time; with highest and lowest capacities due to a high and low in temperature (and corresponding to day or night).

Aside from the first few cycles, where a reasonably large irreversible capacity between discharge and charge was seen, the charge / discharge capacity was reasonably constant with cycle number. The observed discharge capacity, ~ 75 mA.h g^{-1}, was much less than has been seen for other types of MnO_2 ; [104, 106, 110].

The SS / MnO_x electrodes were constructed in order to asses the properties of an electrodeposited polymer electrolyte layer, 7.3.5, and as such the actual performance of the cathode in terms of charge / discharge capacity was not considered crucial.

7.3.4. Electrodeposition of PAN on Stainless Steel / MnO_x Electrodes

A PAN polymer electrolyte was electrodeposited onto SS / MnO_x electrodes according to 7.2.4. The cyclic voltammetry of the deposition is shown in Figure 7.3.4a.

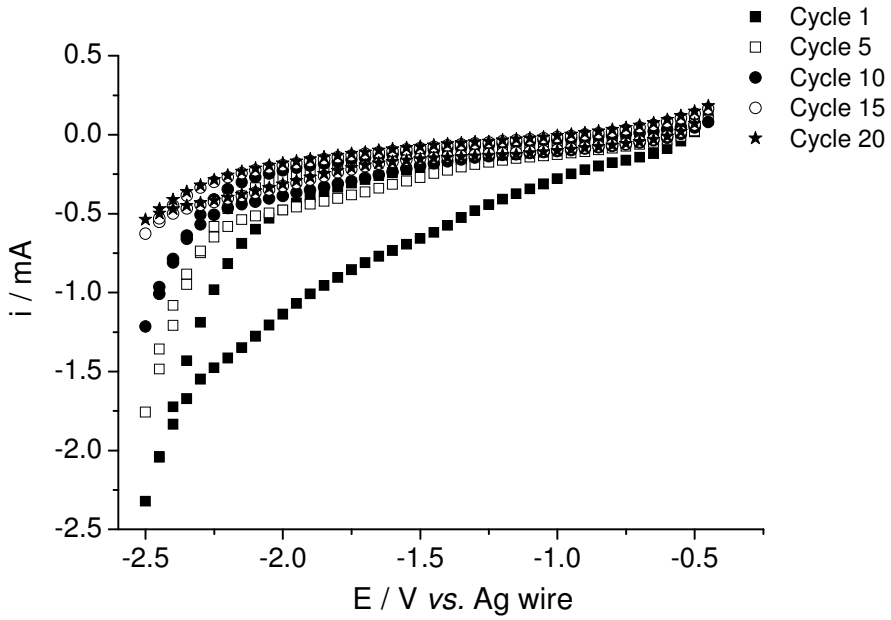

Figure 7.3.4a. Cyclic voltammetry result for 20 cycle electrodeposition of PAN on MnO_x at 50 mV s^{-1}.

The features of the cyclic voltammogram for the deposition of PAN on MnO_x were reasonably similar to the deposition on vitreous carbon (Figure 7.3.1b). As in Figure 7.3.1b(B) the effect of an increasing thickness PAN layer was observed by a decrease in limiting current with cycle number. The small 'peak' visible at ~ -1.3 V *vs*. Ag wire in the first cycle provided some evidence for an 'initiation step' (as in Figure 7.1.3b(C)) although the 'peak' was heavily masked by a large background current.

It was speculated the large background current, seen only for the first cycle, was due to the large pseudo-capacitance of the SS / MnO_x substrate; the decrease in the capacitance seen on subsequent cycles was attributed to the shielding effect of the electronically insulating electrodeposited PAN layer. The deposition produced a translucent yellow polymer on the surface of the dark brown MnO_x.

7.3.5. Determination of Ionic and Electronic Resistance Within the Electrodeposited Polymer Electrolyte

GITT (Chapter 2.3.4) was used in the determination of ionic and electronic resistance (R_i and R_e) within electrodeposited polymer electrolytes, specifically PAN.
The resistance of the polymer electrolyte was measured within the Li / Hg | PAN (1M $LiPF_6$: PC) | MnO_x / SS cell, as described in 7.2.5.
The open circuit potential of the Li / Hg | PAN (1M $LiPF_6$: PC) | MnO_x / SS cells was a stable 2.5 V *vs*. Li / Hg. The operation of the cell was summarised to the approximation outlined below. In the Li / Hg | PAN (1M $LiPF_6$: PC) | MnO_x / SS cell the electrode half reactions can be written as Equations 7.3.5a (anode) and 7.3.5b (cathode).

Anode: Li_x / Hg → $Li_{x-\delta}$ / Hg + δLi + δe^- $\quad E_{Li\ /\ Hg} = \dfrac{-\mu_{Li}(Hg)}{F}$ **Equation 7.3.5a**

Cathode: $Li_xMnO_x + \delta Li + \delta e^- \rightarrow Li_{x+\delta}MnO_x$ $\quad E_{MnOx} = \dfrac{-\mu_{Li}(MnO_x)}{F}$ **Equation 7.3.5b**

The equilibrium potential of the cell is described by Equation 7.3.5c.

$$E_{Eq} = \frac{-(\mu_{Li}(MnO_x) - \mu_{Li}(Hg))}{F} \qquad \textbf{Equation 7.3.5c}$$

The potential of the Li / Hg | PAN (1M $LiPF_6$: PC) | MnO_x / SS cell was calibrated by measuring the potential of lithium insertion into Hg; allowing the cell potential to be approximated to a value '*vs*. Li'.
The potential of Hg *vs*. Li was measured using the galvanostatic insertion of Li into Hg in a Li | 1M $LiPF_6$: PC (glass fibre separator) Hg drop cell (Figure 7.2.5b). The average potential of lithium insertion into Hg was 0.8 V *vs*. Li, starting at ~ 1 V *vs*. Li with a plateau between 0.9-0.7 V tending to 0V as the end of discharge was reached. Lithium insertion beyond ~ 5 atomic percent caused formation of solid phases of lithium amalgam (Hg_3Li, HgLi etc [145]) on the surface of the Hg drop and marked the end of discharge. Figure 7.3.5a shows the discharge curve for Li insertion into an Hg electrode.

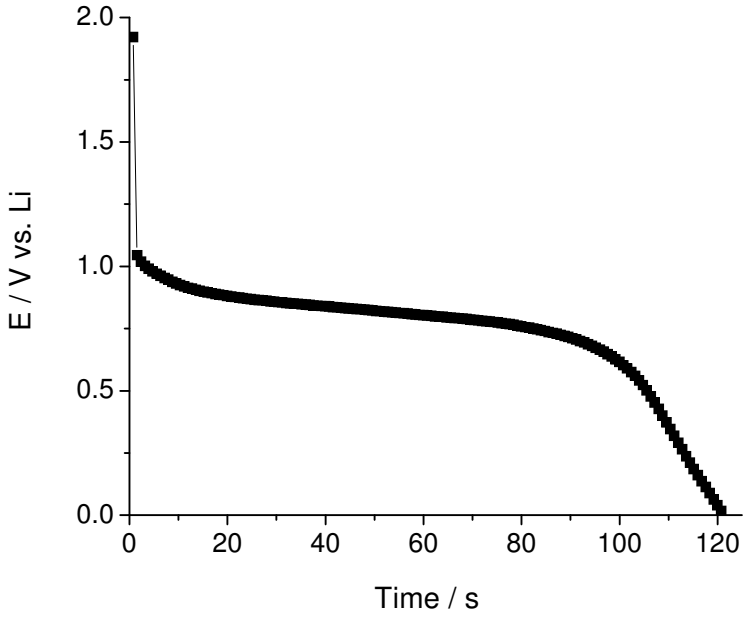

Figure 7.3.5a. Li insertion into Hg in a Li | 1M $LiPF_6$: PC (glass fibre separator) Hg drop cell. 0.1 mA discharge, approximately 0.28 cm^2 contact area (between Hg drop cathode and Li foil anode).

Based on the results of the Li insertion experiment the potential of the Li / Hg | PAN (1M $LiPF_6$: PC) | MnO_x / SS cell *vs*. Li was estimated as 0.8V positive of the potential *vs*. Li/Hg. Therefore the open circuit potential of 2.5 V *vs*. became approximately 3.2 V *vs*. lithium, within the range expected for discharge of MnO_x *vs*. lithium [104, 106, 110].
The particular design of the Li / Hg | PAN (1M $LiPF_6$: PC) | MnO_x / SS cell utilised a cathode of much lower capacity for lithium than that available from the anode. Therefore, δLi(Hg) was regarded as approximately constant, and the cell potential (E_{eq}) controlled the lithium content of the MnO_x (Equation 7.3.5c).

The Li / Hg | PAN (1M $LiPF_6$: PC) | MnO_x / SS cell was discharged and charged between 1.5 and 3.7 V *vs*. Li/Hg (~2.3 and 4.5 V *vs*. Li) at 3.6 µA cm^{-2} prior to the GITT experiment.
(The cell was discharged and allowed to relax for 5 hours, before being charged and allowed to relax for a further 5 hours before initiation of the GITT experiment). The discharge / charge result for the Li / Hg | PAN (1M $LiPF_6$: PC) | MnO_x / SS cell is shown in Figure 7.3.5b.

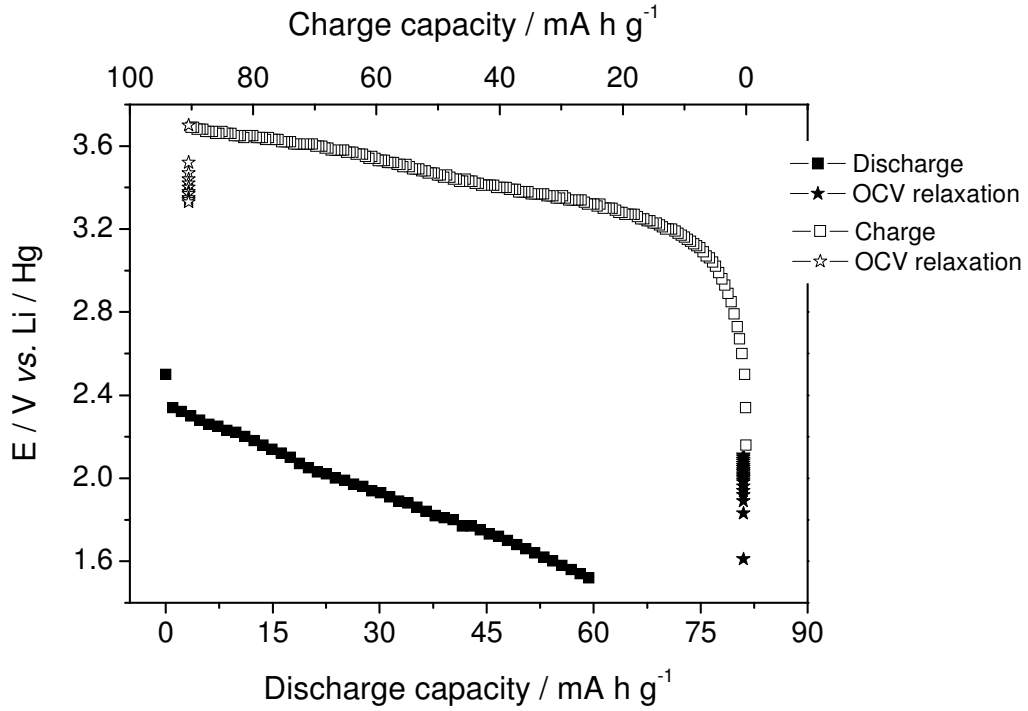

7.3.5b. Galvanostatic (3.6 µA cm^{-2}) discharge and charge of Li / Hg | PAN (1M $LiPF_6$: PC) | MnO_x / SS cell. Discharge and charge reactions were followed by open circuit periods, ⋆ and ☆ respectively, of 5 hours.

The charge / discharge characteristics of the Li / Hg | PAN (1M $LiPF_6$: PC) | MnO_x / SS cells was typical of amorphous MnO_x. The discharge occurs linearly between ~ 3 – 2.5 V *vs.* Li, resulting in a relatively low (compared to theoretical) capacity of 60 mA.h g^{-1}. Interestingly, during charge (lithium extraction) significantly more capacity is extracted than was inserted during discharge. The extra charge was attributed to extraction of K^+ present in the MnO_x film (due to the KOH electrolyte used in the deposition), Figure 7.3.3c. The general form of the charging curve shows similar features to the discharge, i.e. relatively featureless and linear between ~ 4 and 4.5 V *vs.* Li.

The GITT experiment itself involved applying a charge or discharge current pulse (3.6 µA cm^{-2}, C/10, for 60 s) followed by an open circuit relaxation (30 min) and repeating numerous times over the desired potential range. The pre-discharged and charged Li/Hg | PAN (1M $LiPF_6$: PC) | MnO_x / SS cell, Figure 7.3.5b, was discharged using GITT pulses over the potential range 3.2 – 1.5 V *vs.* Li/Hg (~4 – 2.3 V *vs.* Li).

An example GITT discharge pulse, 60s, 3.6 μA, is shown in Figure 7.3.5c(A). Figure 7.3.5c(B) shows the first five GITT discharge pulses and their subsequent relaxations.

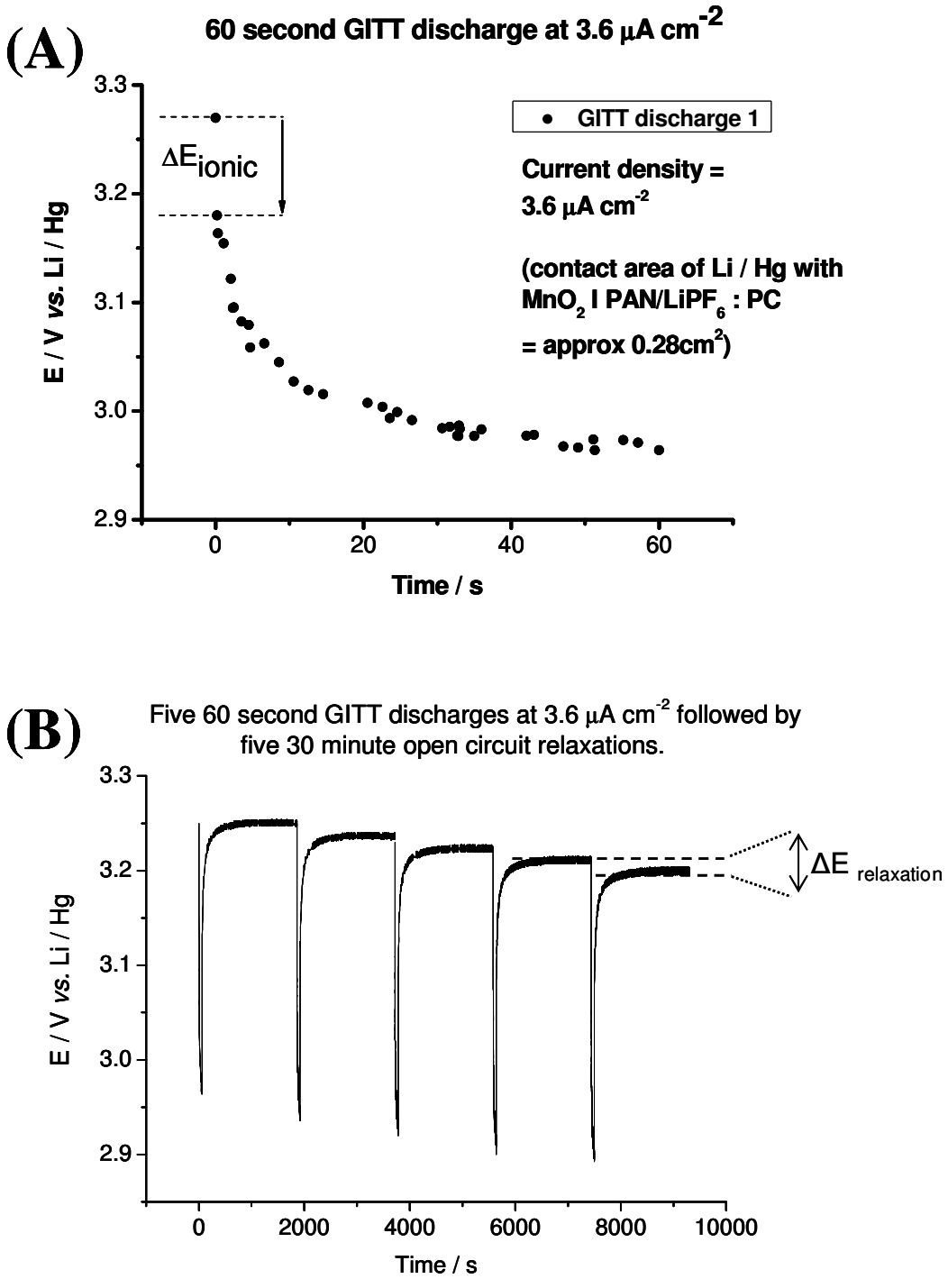

Figure 7.3.5c. (A) Potential *vs*. time during GITT pulse in Li/Hg | PAN (1M $LiPF_6$: PC) | MnO_x / SS cell. (B) Succession of GITT pulses showing potential relaxations and gradual discharge of the cell.

During the GITT current pulse, Figure 7.3.5c(A), an initial instantaneous drop in potential was observed (ΔE_{ionic}). After this instantaneous drop the potential continued to fall until a gradual linear decay was reached. At the end of the current pulse the potential recovered to its original value displaced by an amount $\Delta E_{relaxation}$ according to the charge passed during the current pulse, Figure 7.3.5c(B). Equation 7.3.5d describes how the ionic resistance within the electrolyte (R_{ionic} / cm^2) was estimated. The redox pseudocapacitance of the MnO_x, used in the estimation of the electrolyte electronic resistance ($R_{electronic}$), was obtained from Equation 7.3.5e.

$$R_{ionic} = \frac{\Delta E_{ionic}}{j} \qquad \textbf{Equation 7.3.5d}$$

Where R_{ionic} is the ionic resistance of the electrodeposited polymer electrolyte (Ω cm^{-2}), ΔE_{ionic} is the instantaneous potential change during the GITT current pulse (V) (Figure 7.3.5c(A) and j is the current pulse current density (mA cm^{-2}).

$$C_{MnO_x} = \frac{j\, t_{pulse}}{\Delta E_{relaxation}} \qquad \textbf{Equation 7.3.5e}$$

Where C_{MnOx} is the redox pseudocapacitance of the electrodeposited MnO_x layer (F cm^{-2}), t_{pulse} is the pulse time (s) and $\Delta E_{relaxation}$ (V) is the potential change due to the application of the GITT pulse after the OCV relaxation period (Figure 7.3.5c(B)).

The current leakage during the open circuit relaxation period of the GITT pulse was measured by monitoring the change in cell potential with time. The change in cell potential during this relaxation period, dE_{cell}, was interpreted to give an estimation of the electronic resistance of the polymer electrolyte according to Equation 7.3.5f.

$$R_{electronic} = \left(\frac{E_{cell}}{C_{MnO_x}}\right)\left(\frac{dE_{cell}}{dt_{relax}}\right)^{-1} \qquad \textbf{Equation 7.3.5f}$$

Where $R_{electronic}$ is the electronic resistance of the electrodeposited polymer electrolyte (Ω cm^2), E_{cell} is the cell potential (V), dE_{cell} is the change in voltage during the relaxation period (V) and t_{relax} is the time (s) of the open circuit relaxation step.

Table 7.3.5a summarises the values of ΔE_{ionic} and $\Delta E_{relaxation}$ for each of the five GITT pulses. Table 7.3.5b show the calculations, based on equations 7.3.2d, e and f and interpretation of dE_{cell} during the open circuit period, used in the estimations of R_{ionic} and $R_{electronic}$.

Table 7.3.5a. ΔE_{ionic} and $\Delta E_{relaxation}$ for the first five GITT discharge pulses, and subsequent open circuit relaxations in the Li/Hg | PAN (1M $LiPF_6$: PC) | MnO_x / SS cell.

GITT Discharge	ΔE_{ionic} / V	$\Delta E_{relaxation}$ / V
1	0.09	0.026
2	0.09	0.014
3	0.10	0.013
4	0.10	0.012
5	0.11	/
Average	0.10	0.016

Table 7.3.5b. Estimation of R_{ionic} and $R_{electronic}$ in the Li/Hg | PAN (1M $LiPF_6$: PC) | MnO_x / SS cell. The averaged values of C_{MnOx}, ΔE_{ionic} and $\Delta E_{relaxation}$, Table 7.3.2a, were used in the calculations.

dE_{ionic} / V	*	j / A cm^{-2}	=	R_{ionic} / Ω cm^2
0.098	*	3.60E-06	=	27000

(j / A cm^{-2}	*	t_{pulse} / s)	/	$\Delta E_{relaxation}$ / V	=	C_{MnOx} / F cm^{-2}
(3.60E-06	*	60)	/	0.016	=	0.013

(E_{cell} / V	/	C_{MnOx} / F cm^{-2})	*	(dE_{cell} / V	/	dt_{relax} / s)$^{-1}$	=	$R_{electronic}$ / Ω cm^2
(3.4	/	0.013)	*	(0.001	/	1800)$^{-1}$	=	4.4 x 10^8

In summary the estimated values of R_{ionic} and $R_{electronic}$ for the electrodeposited PAN (1M $LiPF_6$: PC) polymer electrolyte layer were 27000 and 4.4 x 10^8 Ω cm^2 respectivly. As with the PANI results, 7.3.2, the difficulty in measuring the thickness of a soft (plasticized with electrolyte) semi-translucent polymer with a rough surface prevented any meaningful

(repeatable) determination of thickness. As such the estimated values of R_{ionic} and $R_{electronic}$ were only compared against one another. Although R_{ionic} was estimated at 27000 Ω cm^2, a relatively large resistance, the estimated value of $R_{electronic}$ was 4.4 x 10^8 Ω / cm^2, approximately 15000 times greater than R_{ionic}.

The large difference between R_{ionic} and $R_{electronic}$ suggests that an electrodeposited PAN electrolyte plasticized with 1 M $LiPF_6$ in PC may be of interest as polymer electrolyte for Li-ion microbatteries.

7.4. Conclusions

7.4.1. Electrodeposition of Polymers

Poly(acrylonitrile) (PAN) was successfully electrodeposited from solutions of acrylonitrile using cyclic voltammetry as described in 7.2.1. A decrease in deposition current with cycle number was observed during the cyclic voltammetry deposition, Figure 7.3.1b; this was attributed to an increasing resistance associated with an increasing thickness PAN deposition.
SEM images confirmed the deposition of PAN to be conformal when coated onto 3D Nickel foam substrates, Figure 7 3.1c(A). EDX analysis of the electrodeposited PAN films suggested a composition close to that of the ideal structure.

Poly(aniline) (PANI) was electrodeposited onto 2D and 3D substrates. The PANI films were electrodeposited using cyclic voltammetry from acidic solutions of aniline, 7.2.2.
As with the PAN depositions the electrodeposition of PANI produced conformal films when electrodeposited onto 3D reticulated vitreous carbon electrodes, Figure 7.3.2c.
The ability to tailor the electronic properties of PANI films was investigated using AC impedance spectroscopy. The resistance of a PANI film was increased from roughly 100 to 150000 Ω by treatment with LiOH (7.2.2); this resistance increase was accompanied by the characteristic colour change from green to purple corresponding to a shift from electronically conducting emeraldine salt to the insulating emeraldine base form of PANI.
Plasticizing with lithium battery electrolyte reduced the resistance of the emeraldine base PANI films to below 100 Ω, Figures 7.3.2d and e. The emeraldine base PANI films remained purple when plasticized; suggesting the decrease in resistance was due to an increase in ionic, rather than electronic, conductivity.
The thickness of the electrodeposited PANI films was not easily (or reproducibly) measured, but it was estimated using SEM to allow an approximation of conductivity.
The conductivity of the un-plasticized, emeraldine base, PANI films was estimated at 4 x 10^{-8} S cm^{-1}; the conductivity of the PANI films plasticized with 1M $LiPF_6$ in PC was estimated as 0.00011 S cm^{-1}.
As discussed in 7.3.2 the thickness of the PANI films was estimated rather than measured, as such the conductivity values are more appropriately expressed in comparison to each other than as stand alone values.

When compared against one another the conductivity of the un-plasticized, electronically insulating, emeraldine base form of PANI was found to be ~ 2500 times smaller than in the same film swollen with lithium battery electrolyte (1M $LiPF_6$: PC).

Although the estimated values of conductivity, Table 7.3.2b, in the PANI films were quite small (compared to a typical conductivity for a gel polymer type lithium battery electrolyte ~ 10^{-3} S cm^{-1} [32]) the ratio of electronic: ionic conductivity was favourable.

The favourable ratio of electronic (low) to ionic (high) conductivity was the basis of the conclusion that electrolyte plasticized electronically insulating electrodeposited PANI films could be of interest as potential polymer electrolytes for 3D Li-ion microbatteries.

Although the PANI studies were interesting, much work remains; the long term chemical and electrochemical stability of the PANI films if assembled into a full cell is just one example of a variety of possible further studies.

7.4.2. Determination and Differentiation of Electronic and Ionic Resistance in Polymer Electrolyte Films

The aim of these experiments was two fold; firstly to create a process to differentiate between the individual electronic and ionic components of the total resistance in electrodeposited polymer films. The second objective was to evaluate electrodeposited poly(acrylonitrile) PAN films as polymer electrolytes.

The basis of the technique used to achieve this was the 'soft contact' liquid amalgam cell. The cell was based on an electrodeposited MnO_x cathode, coated with an electrodeposited PAN electrolyte layer (plasticized with 1M $LiPF_6$: PC) and an Li amalgam liquid anode. The electrodeposition of the MnO_x cathode and PAN electrolyte is detailed in 7.3.3 and 7.3.1 respectively. The cell construction is illustrated in Figure 7.2.5a and the properties of the 'soft contact' Li-amalgam anode described in 7.3.5.

A Galvanostatic Intermittent Titration technique (GITT) experiment was devised and used to apply a series of current pulses and open circuit relaxation to the cell; based on an analysis of the GITT results, 7.3.5, the electronic and ionic resistance in a electrolyte plasticized PAN film was estimated.

The ionic resistance of the PAN films plasticized with 1M $LiPF_6$: PC was estimated at 27000 Ω cm^2, compared to a value of 4.4 x 10^8 Ω cm^2 for the electronic resistance. As with the PANI results the electronic resistance was favourably small when compared to the ionic resistance, suggesting promise for use as a polymer electrolyte.

The process developed for the determination / differentiation of the two types of resistance would be further improved by the replacement of the Li-amalgam liquid anode with a less reactive and easier to handle soft contact liquid electrode.

Chapter 8

Conclusions and future work

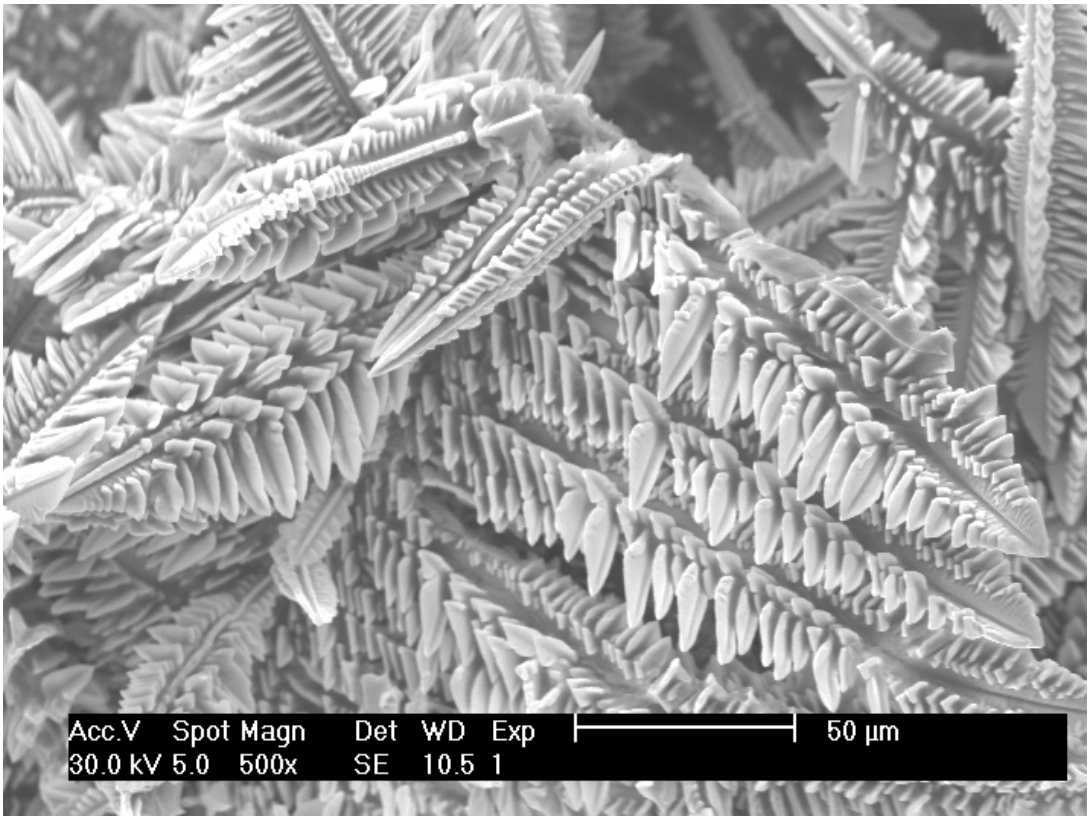

8.1. Overview

The aim of this project was two fold; initial experiments concentrated on the determination of the rate limiting mechanisms in composite electrodes for lithium-ion batteries, the second aim was the development of a high power 3D lithium-ion microbattery.

Chapter 3, "Thickness and rate limitations in $LiFePO_4$ composite electrodes", focuses on the determination of the rate limiting mechanisms in $LiFePO_4$ composite electrodes and the development of a simple model to describe the rate limiting effect of salt diffusion in the electrolyte phase.

Chapter 4, "3D Lithium-ion microbatteries" introduces the 3D lithium-ion microbattery concept and gives an overview of the current 'state of the art' research being done in the field.

Chapter 5, "3D current collectors and substrates", describes experiments concerning the development of a 3D substrate for use as the basis of a 3D microbattery.

Chapter 6, "Electrodeposition and electrochemical characterisation of MnO_2 on 3D substrates", details experiments involving the electrodeposition of cathode materials on 3D current collectors, and characterisation of the resulting structures.

The final experimental chapter, Chapter 7 "Electrodeposited polymer electrolytes; determination and differentiation of electronic and ionic resistance" looks at the electrodeposition of several polymers for use as the basis of the electrolyte layer in a 3D lithium-ion microbattery.

8.2. Thickness and Rate Limitations in $LiFePO_4$ Composite Electrodes

The rate limitation in $LiFePO_4$ composite electrodes in $LiFePO_4$ | 1M $LiPF_6$ in EC:DMC (1:1) | Li half-cells has been investigated (Chapter 3).

A simple model describing the diffusion limitations through the electrolyte phase has been presented, i.e. the Sharp Discharge Front (SDF) model (Chapter 3.1.2).

Results of galvanostatic discharge experiments for a range of electrode thicknesses (Chapter 3.2.3) showed electrode thickness to be strongly rate limiting, suggesting a rate limitation in the electrolyte phase through the composite electrode thickness rather than the active material particle (for composite electrodes containing small particle active materials < 1um).

The diffusion coefficient in the composite electrode (D) was initially estimated using the Sand equation analysis (Chapter 3.3.3).

The estimated value for D was 6 x 10^{-8} cm^2 s^{-1}, somewhere between the literature values for the diffusion coefficient of $LiFePO_4$ (10^{-14} – 10^{-16} cm^2s^{-1} [65]) and $LiPF_6$ in non-aqueous electrolyte (PC/EC/DMC) (3-4 x 10^{-6} cm^2 s^{-1} [66]). According to a rate limitation purely in the electrolyte a D of 3-4 x 10^{-6} cm^2 s^{-1} would be expected; however the measured value of 6 x 10^{-8} cm^2 s^{-1} must take into account the additional porosity and tortuosity of the composite electrode structure (Figure 3.3.3d).

Building upon the Sand equation analysis the Sharp discharge Front (SDF) model (Chapter3.3.4), which predicts a rate limitation due to salt diffusion in the electrolyte within the composite electrode matrix, is proposed. According to the SDF analysis D was estimated at 2.43 x 10-7 cm^2 s^{-1} (averaged over C –rates where the SDF analysis was applicable). The value is an order of magnitude higher than the value calculated using the sand equation analysis; the discrepancy between the two results was attributed to the errors and approximations involved in both analyses.

Galvanostatic discharge experiments on cells containing ‘large’ (1-5 µm) and ‘small’ (>1 µm) $LiFePO_4$ electrodes (Chapter 3.3.5) showed no significant improvement in rate performance in the small particle electrodes, apart from the thinnest electrode case. It was suggested that for thin electrodes (where the diffusion path in the electrolyte phase through the electrode thickness is minimised) containing large particle active materials (where the

rate limitation due to solid state diffusion is more relevant) the rate limitation is more likely to become dependant on solid state effects, i.e. the shrinking core model [57].

Final experiments focussed on the fabrication of a novel $LiFePO_4$ 'microelectrode' assembly. The 'microelectrode' experiment was designed to address several issues with the galvanostatic discharge / rate experiments (Chapter 3.3.2).
Several of the experiments (Chapter 3.3.2 and Chapter 3.3.5) involving galvanostatic discharge of $LiFePO_4$ | 1M $LiPF_6$ in EC:DMC (1:1) | Li cells had shown a high rate discharge limitation that was independent of electrode thickness. It was suggested that the high rate limitation originated from uncompensated cell resistance due to the lithium anode SEI (solid electrolyte interface). The 'microelectrode' cell was designed such that the area of the $LiFePO_4$ electrode was as small as possible in comparison to the lithium anode; therefore minimising the effect of the SEI.
Secondly the much smaller volume of the $LiFePO_4$ 'microelectrode' would ensure the concentration of lithium salt in the bulk electrolyte [LiX_0] changed as little as possible during discharge (one of the assumptions of the SDF model, Chapter 3.3.4).
The 'microelectrode' results showed a significant improvement in the transition between semi-infinite and finite regions (Figure 3.3.3a), of the discharge capacity *vs.* inverse C-rate plot (Figure 3.3.6d). However the 'microelectrode' cells showed a significant resistance, due to the much increased thickness of the $LiFePO_4$ composite electrode; as such the 'microelectrode' construction did little to remove the high rate discharge limitation.

8.3. 3D Current Collectors and Substrates

A variety of 3D substrates were considered as the basis of a 3D lithium-ion microbattery. Initial experiments focussed on the fabrication of substrates based on photolithographic patterning and pyrolysis of photoresists to form carbon based microstructure arrays. Photoresists were spin coated onto electrochemically modified vitreous carbon substrates; the substrates were subsequently patterned using photolithography and the photoresist pyrolised to reveal arrays of carbon microstructures based on either concentric or interdigitated plate (Figure 5.1a) structures (Chapter 5.2.1).
Although some 3D carbon microstructures were successfully fabricated the process was particularly unreliable and time consuming; many of the substrates contained significant defects (Figures 5.3.1c and 5.3.1e). As an alternative to photolithographic fabrication, commercially available reticulated vitreous carbons (RVC) were purchased; the 3D RVC electrodes were to form the basis of an aperiodic (Figure 5.1a) type lithium-ion microbattery.
The various types of 3D substrate were assessed according to the following criteria.

- The area gain for a given footprint area.
- Electronic conductivity.
- The chemical stability of the substrate with respect to the processes involved in the deposition of electrode materials.
- The electrochemical stability within the potential window of the cell operation, i.e. ~ 2 – 4.5 V *vs*. Li.

And perhaps crucially:

- The ease of fabrication of and economic viability

As discussed in Chapter 5 due to the difficulty (and cost) of producing consistent 3D substrates by the photolithographic technique the commercially available 3D RVC substrates were used as the current collector for 3D lithium-ion microbattery experiments.

8.4. Electrodeposition and Electrochemical Characterisation of MnO_2 on 3D Substrates

The purpose of the experiments described in Chapter 6 was to produce a prototype high power lithium-ion microbattery based on a 3D current collector. As discussed in Chapter 4, the 3D structure combines the high rate capability of 2D thin film cells whilst improving the capacity per footprint area by structuring the electrodes in the third dimension.
The electrodeposition of thin films of MnO_2 onto 3D aperiodic reticulated vitreous carbon (RVC) substrates formed the basis of the 3D lithium-ion microbattery described in this work.
Conformal films of electrolytic manganese dioxide (EMD) were successfully electrodeposited onto 3D RVC current collectors (Chapter 6.2.1).
After heat treatment, XRD analysis of the electrodeposited EMD confirmed the films to be of the EMD / Ramsdellite MnO_2 structure. A calibration plot of deposition charge *vs*. film thickness (on a substrate of known area) was created and allowed the electrodeposition of EMD layers of specific thickness on the aperiodic RVC current collectors.
Initial experiments using EMD in conventional composite electrodes confirmed the expected electrochemical performance (Chapter 6.3.5). Discharge capacities of ~ 220 mA.h g^{-1} (fading to ~ 150 mA.h g^{-1} after a few cycles) over the potential range 3-2.5 V *vs*. Li (Figures 6.3.5a and b) were recorded, in reasonable agreement with literature examples for EMD electrodes [104, 113, 114].

The expected improvement in capacity per footprint area (mA.h cm^{-2}) associated with the switch from a 2D to 3D configuration was confirmed by comparing the discharge capacity of planar Ti / EMD | $LiPF_6$ EC: DMC (1:1) | Li cells with 3D RVC/ EMD | $LiPF_6$ EC: DMC (1:1) | Li cells (Chapter 6.3.6).
The discharge capacity (mA.h cm^{-2}) of the 3D RVC / EMD electrodes was approximately 50 times greater than for the equivalent 2D Ti / EMD based cells, in reasonable agreement with the corresponding increase in surface area (roughly 40 times greater for the 3D electrode).
A series of half cells, each containing a RVC / EMD electrode with a different thickness (10, 5 and 1 µm) of EMD, was created to investigate the rate performance of the RVC / EMD composite electrodes (Chapter 6.3.8). It was expected that the rate performance of

the cells containing the thinnest EMD layers would be significantly better than that of the cells containing the thickest EMD layer.

Li | (1M $LiPF_6$ EC:DMC) EMD / RVC cells containing electrodes with 10, 5 and 1 μm EMD depositions were discharged galvanostatically at varying C-rates and the rate performances compared.

The most significant result was that capacity retention upon increased discharge rate in the thinnest (1μm) EMD electrode was only 10% better than in the thickest (10μm) electrode; coupled with the generally poor rate capability of the cells the presence of a larger rate limiting effect was suggested. The larger rate limiting effect was attributed to solid state diffusion within particles of EMD in porous EMD electrodes (Figure 6.3.7h).

The significant challenge of insertion of the second electrode in order to complete the 3D microbattery structure remains

8.5. Electrodeposited Polymer Electrolytes; Determination and Differentiation of Electronic and Ionic Conductivity

8.5.1. Electrodeposition of Polymers

Chapter 7 describes the electrodeposition of polymer layers onto 2D and 3D substrates, as potential electrolytes for use in 3D lithium-ion microbatteries. The development of a technique to determine and differentiate between the ionic and electronic resistance in electrodeposited polymer films is presented. Conformal films of poly(acrylonitrile) (PAN) and poly(aniline) (PANI) were successfully electrodeposited onto 2D and 3D substrates using cyclic voltammetry (Chapter 7.2.1 and 7.2.2 respectively).

The as deposited PANI films were electronically conducting (emeraldine salt form) (Chapter 7.3.2); the electronic conductivity was removed by deprotonating the polymer by immersion in 1M LiOH solution to form the electronically insulating emeraldine base form. AC impedance spectroscopy (Chapter 7.3.2) of the deprotonated emeraldine base films showed the resistance to be approximately 1500 times greater than in the as deposited, emeraldine salt, film.

The shift from electronically conducting emeraldine salt to electronically insulating emeraldine base was accompanied by a characteristic colour change of green to purple.

The resistance of the emeraldine base films was drastically decreased by plasticizing with lithium battery electrolyte (1M $LiPF_6$: PC); ~ 150,000 to 60 Ω or 2500 times reduction. It is speculated that this resistance is largely ionic (due to the electrolyte plasticization) based on strong purple colouration of the film.

As it was not possible to reproducibly measure the thickness of the PANI films, especially once plasticized, an estimation of film thickness was used to determine a value for electronic and ionic conductivity (Chapter 7.3.2). The conductivity of the un-plasticized, emeraldine base, PANI films was estimated at 4×10^{-8} S cm^{-1}; the conductivity of the PANI films plasticized with 1M $LiPF_6$ in PC was estimated as 0.00011 S cm^{-1}.

The relatively favourable ratio of electronic (low) to ionic (high) conductivity was the basis of the conclusion that electrolyte plasticized electronically insulating electrodeposited PANI films could be of interest as potential polymer electrolytes for 3D Li-ion microbatteries.

8.5.2. Determination and Differentiation of Electronic and Ionic Resistance in Polymer Electrolyte Films

A novel method for the determination and differentiation of electronic and ionic conductivity in electrodeposited polymer electrolytes has been developed based on a cell centred around a 'soft contact' lithium amalgam anode (Chapter 7.3.5). The cell was based on an electrodeposited MnO_x cathode (Chapter 7.3.3), coated with an electrodeposited PAN electrolyte layer plasticized with 1M $LiPF_6$: PC (Chapter 7.3.1) and an Li amalgam liquid anode.

By applying a series of galvanostatic discharge pulses and open circuit relaxations (galvanostatic intermittent titration technique (GITT)), and an appropriate analysis of the results, Chapter 7.3.5, the electronic and ionic resistance in an electrolyte plasticized PAN film was estimated.

The estimated ionic resistance of the PAN films plasticized with 1M $LiPF_6$: PC was 27000 Ω cm ^{2}, compared to a value of 4.4 x 10^8 Ω cm ^{2} for the electronic resistance. Similar difficulties were encountered when trying to measure the thickness of the plasticized PAN film as arose when measuring the thickness of the PANI films. As such, as with the PANI results, the electronic and ionic resistances were analysed in comparison to each other, rather than as stand alone values. According to the favourable ratio of ionic to electronic resistance (~ 1:16000 Ω cm^2) it is suggested that electrodeposited films of PAN (plasticized with lithium battery electrolyte) are interesting candidates for use as polymer electrolytes in lithium-ion microbatteries.

8.6. Future Work

As with the majority of things, there is always more to be done, and the work described here is no exception; the following paragraphs describe experiments that would build upon or improve existing results

8.6.1. Thickness Effect and Rate Limitations in $LiFePO_4$ Composite Electrodes

As discussed in Chapter 3 the creation of a series of 'microelectrode' style cells, over a range of thicknesses analogous to those used in Chapter 3.3.2, would allow an analysis of the diffusion coefficient within the composite electrode (D) according to Chapter 3.3.3 and 3.3.4. The improvement in the clarity of the semi-infinite (where the SDF analysis applies) to finite (where the SDF analysis does not apply) region transition seen in Figure 3.3.6d may well allow for a more accurate estimation of D

8.6.2. Electrodeposition and Electrochemical Characterisation of MnO_2 on 3D Substrates

A vast body of possible work remains possible in order to build upon the experiments detailed in Chapter 6. However the most notable challenges remain the application of a conformal and pinhole free coating polymer electrolyte on the RVC / EMD cathode, and the 'back filling' of the remaining volume within the porous structure with an anode (both of which were briefly and unsuccessfully (mostly) attempted during this work).
It was suggested that by heat treating the lithiated RVC / EMD electrodes the cycle life and discharge potential of the electrodes could be improved by converting the EMD to $LiMn_2O_4$.

8.6.3. Electrodeposition of Polymer Electrolyte Layers

Again, a large volume of possible experiments exist that could continue and improve upon the work described in Chapter 7. It would be interesting to explore the possible applications of a polymer electrolyte, based on poly(aniline), that could be switched between electronically conducting or electronically insulating; potentially allowing for the

sequential electrodeposition of all three electrode layers (anode, electrolyte and cathode) and their current collectors.

Significant improvements to the technique used to determine electronic and ionic conductivity could be made by replacing the lithium amalgam liquid anode with a similar 'soft contact' electrode that is less reactive (and most importantly easier to handle!).

References

1. A.S. Arico, P. Bruce, B. Scrosati, J.M. Tarascon, and W. Van Schalkwijk, *Nanostructured materials for advanced energy conversion and storage devices.* Nature Materials, 2005. **4**(5): p. 366-377.
2. M. Wakihara, *Recent developments in lithium ion batteries.* Materials Science & Engineering R-Reports, 2001. **33**(4): p. 109-134.
3. M.S. Whittingham, *Lithium batteries and cathode materials.* Chemical Reviews, 2004. **104**(10): p. 4271-4301.
4. J.R. Owen, *Rechargeable lithium batteries.* Chemical Society Reviews, 1997. **26**(4): p. 259-267.
5. D. Linden and T. Reddy, *Handbook of Batteries.* 2001(Second edition).
6. C.A. Vincent and B. Scrosati, *Modern Batteries: An Introduction to Electrochemical Power Sources.* 1998(Second edition).
7. J.P. Gabano, *Lithium Batteries*. 1983, Academic Press.
8. F. Beck and P. Ruetschi, *Rechargeable batteries with aqueous electrolytes.* Electrochimica Acta, 2000. **45**(15-16): p. 2467-2482.
9. S. Muller, F. Holzer, and O. Haas, *Optimized zinc electrode for the rechargeable zinc-air battery.* Journal of Applied Electrochemistry, 1998. **28**(9): p. 895-898.
10. E. Deiss, F. Holzer, and O. Haas, *Modeling of an electrically rechargeable alkaline Zn-air battery.* Electrochimica Acta, 2002. **47**(25): p. 3995-4010.
11. R.M. Dell, *Batteries - fifty years of materials development.* Solid State Ionics, 2000. **134**(1-2): p. 139-158.
12. A.K. Shukla, S. Venugopalan, and B. Hariprakash, *Nickel-based rechargeable batteries.* Journal of Power Sources, 2001. **100**(1-2): p. 125-148.
13. S.R. Ovshinsky, M.A. Fetcenko, and J. Ross, *A nickel metal hydride battery for electric vehicles.* Science, 1993. **260**(5105): p. 176-181.
14. T. Sakai, H. Miyamura, N. Kuriyama, A. Kato, K. Oguro, and H. Ishikawa, *Metal hydride anodes for nickel-hydrogen secondary battery.* Journal of the Electrochemical Society, 1990. **137**(3): p. 795-799.
15. N. Furukawa, *Development and commercialistaion of nickel metal hydride secondary batteries.* Journal of Power Sources, 1994. **51**(1-2): p. 45-59.

16. N. Cui and J.L. Luo, *An AC impedance study of self-discharge mechanism of nickel-metal hydride (Ni-MH) battery using Mg_2Ni-type hydrogen storage alloy anode.* Electrochimica Acta, 2000. **45**(24): p. 3973-3981.
17. C. Iwakura, Y. Kajiya, H. Yoneyama, T. Sakai, K. Oguro, and H. Ishikawa, *Self discharge mechanism of nickel-hydrogen batteries using hydride anodes.* Journal of the Electrochemical Society, 1989. **136**(5): p. 1351-1355.
18. R.W. Hart, H.S. White, B. Dunn, and D.R. Rolison, *3-D microbatteries.* Electrochemistry Communications, 2003. **5**(2): p. 120-123.
19. H. Arai, S. Okada, Y. Sakurai, and J. Yamaki, *Electrochemical and structural study of Li_2CuO_2, $LiCuO_2$ and $NaCuO_2$.* Solid State Ionics, 1998. **106**(1-2): p. 45-53.
20. P. Hany, R. Yazami, and A. Hamwi, *Low-temperature carbon fluoride for high power density lithium primary batteries.* Journal of Power Sources, 1997. **68**(2): p. 708-710.
21. W. Greatbatch, C.F. Holmes, E.S. Takeuchi, and S.J. Ebel, *Lithium/carbon monofluoride (Li/CFx): A new pacemaker battery.* Pace-Pacing and Clinical Electrophysiology, 1996. **19**(11): p. 1836-1840.
22. S.Y. Huang, L. Kavan, I. Exnar, and M. Gratzel, *Rocking Chair Lithium Battery Based on Nanocrystalline TiO_2 (Anatase).* Journal of the Electrochemical Society, 1995. **142**(9): p. L142-L144.
23. J.M. Tarascon and M. Armand, *Issues and challenges facing rechargeable lithium batteries.* Nature, 2001. **414**(6861): p. 359-367.
24. M. Wissler, *Graphite and carbon powders for electrochemical applications.* Journal of Power Sources, 2006. **156**(2): p. 142-150.
25. S. Flandrois and B. Simon, *Carbon materials for lithium-ion rechargeable batteries.* Carbon, 1999. **37**(2): p. 165-180.
26. R. Alcantara, F.J.F. Madrigal, P. Lavela, J.L. Tirado, J.M.J. Mateos, C.G. de Salazar, R. Stoyanova, and E. Zhecheva, *Characterisation of mesocarbon microbeads (MCMB) as active electrode material in lithium and sodium cells.* Carbon, 2000. **38**(7): p. 1031-1041.
27. S. Zhang and P.F. Shi, *Electrochemical impedance study of lithium intercalation into MCMB electrode in a gel electrolyte.* Electrochimica Acta, 2004. **49**(9-10): p. 1475-1482.
28. B.L. Ellis, K.T. Lee, and L.F. Nazar, *Positive Electrode Materials for Li-Ion and Li-Batteries.* Chemistry of Materials. **22**(3): p. 691-714.

29. R. Koksbang, J. Barker, H. Shi, and M.Y. Saidi, *Cathode materials for lithium rocking chair batteries.* Solid State Ionics, 1996. **84**(1-2): p. 1-21.
30. S. Megahed and B. Scrosati, *Lithium-ion rechargeable batteries.* Journal of Power Sources, 1994. **51**(1-2): p. 79-104.
31. J.M. Tarascon and D. Guyomard, *The $Li_{1+x}Mn_2O_4$/C rocking chair system - a review.* Electrochimica Acta, 1993. **38**(9): p. 1221-1231.
32. C. Capiglia, Y. Saito, H. Kataoka, T. Kodama, E. Quartarone, and P. Mustarelli, *Structure and transport properties of polymer gel electrolytes based on PVdF-HFP and $LiN(C_2F_5SO_2)_2$.* Solid State Ionics, 2000. **131**(3-4): p. 291-299.
33. A.M. Stephan, *Review on gel polymer electrolytes for lithium batteries.* European Polymer Journal, 2006. **42**(1): p. 21-42.
34. W.H. Meyer, *Polymer electrolytes for lithium-ion batteries.* Advanced Materials, 1998. **10**(6): p. 439.
35. J.Y. Song, Y.Y. Wang, and C.C. Wan, *Review of gel-type polymer electrolytes for lithium-ion batteries.* Journal of Power Sources, 1999. **77**(2): p. 183-197.
36. D. Pletcher, *A First Course in Electrode Processes*. 2nd Edition ed. 2009: RSC Publishing.
37. M. Winter and R.J. Brodd, *What are batteries, fuel cells, and supercapacitors?* Chemical Reviews, 2004. **104**(10): p. 4245-4269.
38. T. Ohzuku, A. Ueda, M. Nagayama, Y. Iwakoshi, and H. Komori, *Comparitive study of $LiCoO_2$, $LiNi_{1/2}Co_{1/2}O_2$ AND $LiNiO_2$ for 4 volt secondary lithium cells.* Electrochimica Acta, 1993. **38**(9): p. 1159-1167.
39. J.J. Auborn and Y.L. Barberio, *Lithium intercalation cells without metallic lithium - MoO_2/$LiCoO_2$ AND WO_2/$LiCoO_2$.* Journal of the Electrochemical Society, 1987. **134**(3): p. 638-641.
40. A.K. Padhi, K.S. Nanjundaswamy, and J.B. Goodenough, *Phospho-olivines as positive-electrode materials for rechargeable lithium batteries.* Journal of the Electrochemical Society, 1997. **144**(4): p. 1188-1194.
41. S.Y. Chung, J.T. Bloking, and Y.M. Chiang, *Electronically conductive phospho-olivines as lithium storage electrodes.* Nature Materials, 2002. **1**(2): p. 123-128.
42. P.S. Herle, B. Ellis, N. Coombs, and L.F. Nazar, *Nano-network electronic conduction in iron and nickel olivine phosphates.* Nature Materials, 2004. **3**(3): p. 147-152.

43. H. Huang, S.C. Yin, and L.F. Nazar, *Approaching theoretical capacity of $LiFePO_4$ at room temperature at high rates.* Electrochemical and Solid State Letters, 2001. **4**(10): p. A170-A172.
44. A. Yamada, S.C. Chung, and K. Hinokuma, *Optimized $LiFePO_4$ for lithium battery cathodes.* Journal of the Electrochemical Society, 2001. **148**(3): p. A224-A229.
45. Z.H. Chen and J.R. Dahn, *Reducing carbon in $LiFePO_4$/C composite electrodes to maximize specific energy, volumetric energy, and tap density.* Journal of the Electrochemical Society, 2002. **149**(9): p. A1184-A1189.
46. N. Ravet, Y. Chouinard, J.F. Magnan, S. Besner, M. Gauthier, and M. Armand, *Electroactivity of natural and synthetic triphylite.* Journal of Power Sources, 2001. **97-8**: p. 503-507.
47. M. Gaberscek, R. Dominko, and J. Jamnik, *Is small particle size more important than carbon coating? An example study on $LiFePO_4$ cathodes.* Electrochemistry Communications, 2007. **9**(12): p. 2778-2783.
48. G. Ceder and B. Kang, *Response to "unsupported claims of ultrafast charging of Li-ion batteries".* Journal of Power Sources, 2009. **194**(2): p. 1024-1028.
49. B. Kang and G. Ceder, *Battery materials for ultrafast charging and discharging.* Nature, 2009. **458**(7235): p. 190-193.
50. K. Zaghib, J.B. Goodenough, A. Mauger, and C. Julien, *Unsupported claims of ultrafast charging of $LiFePO_4$ Li-ion batteries.* Journal of Power Sources, 2009. **194**(2): p. 1021-1023.
51. R. Dominko, M. Gaberscek, J. Drofenik, M. Bele, and J. Jamnik, *Influence of carbon black distribution on performance of oxide cathodes for Li ion batteries.* Electrochimica Acta, 2003. **48**(24): p. 3709-3716.
52. R. Dominko, M. Gaberscek, J. Drofenik, M. Bele, S. Pejovnik, and J. Jamnik, *The role of carbon black distribution in cathodes for Li ion batteries.* Journal of Power Sources, 2003. **119**: p. 770-773.
53. M. Gaberscek, M. Kuzma, and J. Jamnik, *Electrochemical kinetics of porous, carbon-decorated $LiFePO_4$ cathodes: separation of wiring effects from solid state diffusion.* Physical Chemistry Chemical Physics, 2007. **9**(15): p. 1815-1820.
54. M.R. Roberts, A.D. Spong, G. Vitins, and J.R. Owen, *High throughput screening of the effect of carbon coating in $LiFePO_4$ electrodes.* Journal of the Electrochemical Society, 2007. **154**(10): p. A921-A928.

55. J.D. Wilcox, M.M. Doeff, M. Marcinek, and R. Kostecki, *Factors influencing the quality of carbon coatings on $LiFePO_4$.* Journal of the Electrochemical Society, 2007. **154**(5): p. A389-A395.

56. D. Guy, B. Lestriez, R. Bouchet, V. Gaudefroy, and D. Guyomard, *Tailoring the binder of composite electrode for battery performance optimization.* Electrochemical and Solid State Letters, 2005. **8**(1): p. A17-A21.

57. S. Stewart and J. Newman, *Measuring the salt activity coefficient in lithium-battery electrolytes.* Journal of the Electrochemical Society, 2008. **155**(6): p. A458-A463.

58. V. Srinivasan and J. Newman, *Discharge model for the lithium iron-phosphate electrode.* Journal of the Electrochemical Society, 2004. **151**(10): p. A1517-A1529.

59. G.Y. Chen, X.Y. Song, and T.J. Richardson, *Electron microscopy study of the $LiFePO_4$ to $FePO_4$ phase transition.* Electrochemical and Solid State Letters, 2006. **9**(6): p. A295-A298.

60. K. West, T. Jacobsen, and S. Atlung, *Modeling of porous electrodes with liquid electrolyte.* Journal of the Electrochemical Society, 1982. **129**(7): p. 1480-1485.

61. M. Doyle, T.F. Fuller, and J. Newman, *The importance of the lithium ion transference number in lithium polymer cells.* Electrochimica Acta, 1994. **39**(13): p. 2073-2081.

62. C. Delacourt, P. Poizot, J.M. Tarascon, and C. Masquelier, *The existence of a temperature-driven solid solution in Li_xFePO_4 for $0 <= x <= 1$.* Nature Materials, 2005. **4**(3): p. 254-260.

63. A. Yamada, H. Koizumi, N. Sonoyama, and R. Kanno, *Phase change in $LixFePO_4$.* Electrochemical and Solid State Letters, 2005. **8**(8): p. A409-A413.

64. A.J. Bard and L.R. Faulkner, *Electrochemical methods Fundamentals and Applications.* Vol. Second Edition. 2001: John Wiley and Sons.

65. P.P. Prosini, M. Lisi, D. Zane, and M. Pasquali, *Determination of the chemical diffusion coefficient of lithium in LiFePO4.* Solid State Ionics, 2002. **148**(1-2): p. 45-51.

66. L.O. Valoen and J.N. Reimers, *Transport properties of $LiPF_6$-based Li-ion battery electrolytes.* Journal of the Electrochemical Society, 2005. **152**(5): p. A882-A891.

67. J.S. Zhao, L. Wang, X.M. He, C.R. Wan, and C.Y. Jiang, *Determination of lithium-ion transference numbers in $LiPF_6$-PC solutions based on electrochemical polarization and NMR measurements.* Journal of the Electrochemical Society, 2008. **155**(4): p. A292-A296.

68. Y. Aihara, T. Bando, H. Nakagawa, H. Yoshida, K. Hayamizu, E. Akiba, and W.S. Price, *Ion transport properties of six lithium salts dissolved in gamma-butyrolactone studied by self-diffusion and ionic conductivity measurements.* Journal of the Electrochemical Society, 2004. **151**(1): p. A119-A122.

69. M. Gaberscek and J. Jamnik, *Impact of electrochemical wiring topology on the kinetics of insertion electrodes.* Solid State Ionics, 2006. **177**(26-32): p. 2647-2651.

70. D. Aurbach, B. Markovsky, A. Shechter, Y. EinEli, and H. Cohen, *A comparative study of synthetic graphite and Li electrodes in electrolyte solutions based on ethylene carbonate dimethyl carbonate mixtures.* Journal of the Electrochemical Society, 1996. **143**(12): p. 3809-3820.

71. M. Takahashi, S. Tobishima, K. Takei, and Y. Sakurai, *Reaction behavior of $LiFePO_4$ as a cathode material for rechargeable lithium batteries.* Solid State Ionics, 2002. **148**(3-4): p. 283-289.

72. J. Vetter, P. Novak, M.R. Wagner, C. Veit, K.C. Moller, J.O. Besenhard, M. Winter, M. Wohlfahrt-Mehrens, C. Vogler, and A. Hammouche, *Ageing mechanisms in lithium-ion batteries.* Journal of Power Sources, 2005. **147**(1-2): p. 269-281.

73. S.S. Zhang, *A review on electrolyte additives for lithium-ion batteries.* Journal of Power Sources, 2006. **162**(2): p. 1379-1394.

74. K. Edstrom, T. Gustafsson, and J.O. Thomas, *The cathode-electrolyte interface in the Li-ion battery.* Electrochimica Acta, 2004. **50**(2-3): p. 397-403.

75. D. Golodnitsky, M. Nathan, V. Yufit, E. Strauss, K. Freedman, L. Burstein, A. Gladkich, and E. Peled, *Progress in three-dimensional (3D) Li-ion microbatteries.* Solid State Ionics, 2006. **177**(26-32): p. 2811-2819.

76. D. Golodnitsky, V. Yufit, M. Nathan, I. Shechtman, T. Ripenbein, E. Strauss, S. Menkin, and E. Peled, *Advanced materials for the 3D microbattery.* Journal of Power Sources, 2006. **153**(2): p. 281-287.

77. M. Roberts, P. Johns, J. Owen, D. Brandell, K. Edstrom, G.E. Enany, C. Guery, D. Golodnitsky, M. Lacey, C. Lecoeur, H. Mazor, E. Peled, E. Perre, Manikoth, Shaijumon, P. Simon, and P.-L. Taberna, *3D lithium ion batteries—from fundamentals to fabrication* J. Mater. Chem., 2011. **21**: p. 9876-9890.

78. L. Baggetto, N.A.M. Verhaegh, R.A.H. Niessen, F. Roozeboom, J.C. Jumas, and P.H.L. Notten, *Tin Nitride Thin Films as Negative Electrode Material for Lithium-Ion Solid-State Batteries.* Journal of the Electrochemical Society. **157**(3): p. A340-A347.

79. S.D. Jones and J.R. Akridge, *Development and performance of a rechargable thin-film solid-state microbattery.* Journal of Power Sources, 1995. **54**(1): p. 63-67.

80. V. Palomares, I.R. de Larramendi, J. Alonso, M. Bengoechea, A. Goni, O. Miguel, and T. Rojo, *$LiFePO_4$ thin films grown by pulsed laser deposition: Effect of the substrate on the film structure and morphology.* Applied Surface Science. **256**(8): p. 2563-2568.

81. J. Song, M.Z. Cai, Q.F. Dong, M.S. Zheng, Q.H. Wu, and S.T. Wu, *Structural and electrochemical characterization of SnOx thin films for Li-ion microbattery.* Electrochimica Acta, 2009. **54**(10): p. 2748-2753.

82. X.J. Zhu, Z.P. Guo, G.D. Du, P. Zhang, and H.K. Liu, *$LiCoO_2$ cathode thin film fabricated by RF sputtering for lithium ion microbatteries.* Surface & Coatings Technology, 2009. **204**(11): p. 1710-1714.

83. J.W. Long, B. Dunn, D.R. Rolison, and H.S. White, *Three-dimensional battery architectures.* Chemical Reviews, 2004. **104**(10): p. 4463-4492.

84. D.R. Rolison, R.W. Long, J.C. Lytle, A.E. Fischer, C.P. Rhodes, T.M. McEvoy, M.E. Bourga, and A.M. Lubers, *Multifunctional 3D nanoarchitectures for energy storage and conversion.* Chemical Society Reviews, 2009. **38**(1): p. 226-252.

85. M. Nathan, D. Golodnitsky, V. Yufit, E. Strauss, T. Ripenbein, I. Shechtman, S. Menkin, and E. Peled, *Three-dimensional thin-film Li-ion microbatteries for autonomous MEMS.* Journal of Microelectromechanical Systems, 2005. **14**(5): p. 879-885.

86. T. Ripenbein, D. Golodnitsky, M. Nathan, and E. Peled, *Electroless nickel current collector for 3D-microbatteries.* Journal of Applied Electrochemistry. **40**(2): p. 435-444.

87. M. Nathan, D. Golodnitsky, V. Yufit, E. Strauss, T. Ripenbein, I. Shechtman, S. Menkin, and E. Peled, *Recent advances in three dimensional thin film microbatteries*, in *Solid State Ionics-2004*, P. Knauth, et al., Editors. 2005. p. 367-372.

88. P.H.L. Notten, F. Roozeboom, R.A.H. Niessen, and L. Baggetto, *3-D integrated all-solid-state rechargeable batteries.* Advanced Materials, 2007. **19**(24): p. 4564-4567.

89. H.S. Min, B.Y. Park, L. Taherabadi, C.L. Wang, Y. Yeh, R. Zaouk, M.J. Madou, and B. Dunn, *Fabrication and properties of a carbon/polypyrrole three-dimensional microbattery.* Journal of Power Sources, 2008. **178**(2): p. 795-800.

90. M. Kotobuki, T. Sugiura, J. Sugaya, H. Munakata, and K. Kanamura, *Fabrication of Lithium-ion Microarray Battery by Electrophoresis.* Electrochemistry. **78**(4): p. 273-275.

91. K. Dokko, J. Sugaya, H. Nakano, T. Yasukawa, T. Matsue, and K. Kanamura, *Sol-gel fabrication of lithium-ion microarray battery.* Electrochemistry Communications, 2007. **9**(5): p. 857-862.

92. F. Chamran, Y. Yeh, H.S. Min, B. Dunn, and C.J. Kim, *Fabrication of high-aspect-ratio electrode arrays for three-dimensional microbatteries.* Journal of Microelectromechanical Systems, 2007. **16**(4): p. 844-852.

93. G.T. Teixidor, R.B. Zaouk, B.Y. Park, and M.J. Madou, *Fabrication and characterization of three-dimensional carbon electrodes for lithium-ion batteries.* Journal of Power Sources, 2008. **183**(2): p. 730-740.

94. S.K. Cheah, E. Perre, M. Rooth, M. Fondell, A. Harsta, L. Nyholm, M. Boman, T. Gustafsson, J. Lu, P. Simon, and K. Edstrom, *Self-Supported Three-Dimensional Nanoelectrodes for Microbattery Applications.* Nano Letters, 2009. **9**(9): p. 3230-3233.

95. P. Johns, M. Roberts, and J. Owen, *Conformal electrodeposition of manganese dioxide onto reticulated vitreous carbon for 3D microbattery applications* J. Mater. Chem, 2011(21): p. 10153-10159.

96. M. Madou, A. Lal, G. Schmidt, X. Song, K. Kinoshita, M. Fendorf, A. Zettl, and R. White, *Carbon micromachining (C-MEMS)*, in *Proceedings of the Symposium on Chemical and Biological Sensors and Analytical Electrochemical Methods*, A.J. Ricco, et al., Editors. 1997, Electrochemical Society Inc: Pennington. p. 61-69.

97. C.L. Wang, L. Taherabadi, G.Y. Jia, M. Madou, Y.T. Yeh, and B. Dunn, *C-MEMS for the manufacture of 3D microbatteries.* Electrochemical and Solid State Letters, 2004. **7**(11): p. A435-A438.

98. J. Liu and S. Dong, *Grafting of diaminoalkane on glassy carbon surface and its functionalization.* Electrochemistry Communications, 2000. **2**(10): p. 707-712.

99. L.B. Hu, J.W. Choi, Y. Yang, S. Jeong, F. La Mantia, L.F. Cui, and Y. Cui, *Highly conductive paper for energy-storage devices.* Proceedings of the National Academy of Sciences of the United States of America, 2009. **106**(51): p. 21490-21494.

100. T. Hottinen, I. Himanen, and P. Lund, *Effect of cathode structure on planar free-breathing PEMFC.* Journal of Power Sources, 2004. **138**(1-2): p. 205-210.

101. A. Burke, *Ultracapacitors: why, how, and where is the technology.* Journal of Power Sources, 2000. **91**(1): p. 37-50.

102. T. Kudo, Y. Ikeda, T. Watanabe, M. Hibino, M. Miyayama, H. Abe, and K. Kajita, *Amorphous V_2O_5/ carbon composites as electrochemical supercapacitor electrodes.* Solid State Ionics, 2002. **152**: p. 833-841.

103. C.L. Wang, G.Y. Jia, L.H. Taherabadi, and M.J. Madou, *A novel method for the fabrication of high-aspect ratio C-MEMS structures.* Journal of Microelectromechanical Systems, 2005. **14**(2): p. 348-358.

104. M.M. Thackeray, *Manganese oxides for lithium batteries.* Progress in Solid State Chemistry, 1997. **25**(1-2): p. 1-71.

105. J. Barker, R. Koksbang, and M.Y. Saidi, *Lithium insertion in manganese oxides: A model lithium ion system.* Solid State Ionics, 1995. **82**(3-4): p. 143-151.

106. Y. Chabre and J. Pannetier, *Structural and electrochemical properties of the proton gamma-MnO_2 system.* Progress in Solid State Chemistry, 1995. **23**(1): p. 1-130.

107. B.B. Owens, S. Passerini, and W.H. Smyrl, *Lithium ion insertion in porous metal oxides.* Electrochimica Acta, 1999. **45**(1-2): p. 215-224.

108. J.Y. Luo, J.J. Zhang, and Y.Y. Xia, *Highly electrochemical reaction of lithium in the ordered mesoporosus beta-MnO_2.* Chemistry of Materials, 2006. **18**(23): p. 5618-5623.

109. F. Jiao and P.G. Bruce, *Mesoporous crystalline beta-MnO_2- a reversible positive electrode for rechargeable lithium batteries.* Advanced Materials, 2007. **19**(5): p. 657-+.

110. T. Ohzuku, M. Kitagawa, and T. Hirai, *Electrochemistry of manganese-dioxide in lithium non-aqueous cell .1. X-ray diffreactional study on the reduction of electrolytic manganese-dioxide.* Journal of the Electrochemical Society, 1989. **136**(11): p. 3169-3174.

111. B.D. Desai, J.B. Fernandes, and V.N.K. Dalal, *Manganese dioxide - a review of battery chemical .2. Solid-state and electrochemical properties of manganese dioxides.* Journal of Power Sources, 1985. **16**(1): p. 1-43.

112. J.B. Fernandes, B.D. Desai, and V.N.K. Dalal, *Manganese dioxide - a review of a battery chemical .1. chemical synthesis and X-ray-diffraction studies of manganese dioxides.* Journal of Power Sources, 1985. **15**(4): p. 209-237.

113. J.C. Nardi, *Charaterization of the Li/MnO_2 multistep discharge.* Journal of the Electrochemical Society, 1985. **132**(8): p. 1787-1791.

114. W. Bowden, T. Bofinger, F. Zhang, N. Iltchev, R. Sirotina, Y. Paik, H. Chen, C. Grey, and S. Hackney, *New manganese dioxides for lithium batteries.* Journal of Power Sources, 2007. **165**(2): p. 609-615.

115. W.H. Ho and S.K. Yen, *Characterization of electrolytic manganese oxide coating on pt for lithium battery applications.* Journal of the Electrochemical Society, 2005. **152**(3): p. A506-A510.

116. C.P. Rhodes, J.W. Long, M.S. Doescher, B.M. Dening, and D.R. Rolison, *Charge insertion into hybrid nanoarchitectures: mesoporous manganese oxide coated with ultrathin poly(phenylene oxide).* Journal of Non-Crystalline Solids, 2004. **350**: p. 73-79.

117. W.C. West, N.V. Myung, J.F. Whitacre, and B.V. Ratnakumar, *Electrodeposited amorphous manganese oxide nanowire arrays for high energy and power density electrodes.* Journal of Power Sources, 2004. **126**(1-2): p. 203-206.

118. H. Ikeda and S. Narukawa, *Behaviour of various cathode materials for non-aqueous lithium cells.* Journal of Power Sources, 1983. **9**(3-4): p. 329-334.

119. J. Barker and R. Koksbang, *The interfacial impedance variation of V_6O_{13} composite electrodes during lithium insertion and extraction.* Electrochimica Acta, 1995. **40**(6): p. 673-679.

120. Olsen, II, J. Barker, and R. Koksbang, *Impedance measurements on the lithium-polymer electrolyte interface.* Solid State Ionics, 1996. **83**(1-2): p. 125-133.

121. L.A.H. MacLean and F.L. Tye, *Chemical hydrogen insertion into gamma-manganese dioxide exhibiting low microtwinning.* Journal of Materials Chemistry, 1997. **7**(6): p. 1029-1035.

122. E. Levi, E. Zinigrad, H. Teller, M.D. Levi, D. Aurbach, E. Mengeritsky, E. Elster, E. Granot, P. Dan, and H. Yamin, *Structural, and electrochemical studies of 3V $LixMnO_2$ cathodes for rechargeable Li batteries*, in *Proceedings of the Symposium on Batteries for Portable Applications and Electric Vehicles*, C.F. Holmes and A.R. Landgrebe, Editors. 1997, Electrochemical Society Inc: Pennington. p. 963-973.

123. S. Sarciaux, A.L. La Salle, A. Verbaere, Y. Piffard, and D. Guyomard, *gamma-MnO_2 for Li batteries Part I. gamma-MnO_2: Relationships between synthesis conditions, material characteristics and performances in lithium batteries.* Journal of Power Sources, 1999. **81**: p. 656-660.

124. F.Y. Cheng, J.Z. Zhao, W. Song, C.S. Li, H. Ma, J. Chen, and P.W. Shen, *Facile controlled synthesis of MnO_2 nanostructures of novel shapes and their application in batteries.* Inorganic Chemistry, 2006. **45**(5): p. 2038-2044.

125. B. Scrosati, *Recent advances in lithium ion battery materials.* Electrochimica Acta, 2000. **45**(15-16): p. 2461-2466.

126. J.M. Tarascon, A.S. Gozdz, C. Schmutz, F. Shokoohi, and P.C. Warren, *Performance of Bellcore's plastic rechargeable Li-ion batteries.* Solid State Ionics, 1996. **86-8**: p. 49-54.

127. T. Osaka, *Lithium Ion Batteries on the Upswing.* Interface, 1999. **8**(3): p. 9.

128. M. Salomon and B. Scrosati, *Lithium batteries: Present trends and prospects.* Gazzetta Chimica Italiana, 1996. **126**(7): p. 415-427.

129. A.M. Christie, S.J. Lilley, E. Staunton, Y.G. Andreev, and P.G. Bruce, *Increasing the conductivity of crystalline polymer electrolytes.* Nature, 2005. **433**(7021): p. 50-53.

130. F. Croce, G.B. Appetecchi, L. Persi, and B. Scrosati, *Nanocomposite polymer electrolytes for lithium batteries.* Nature, 1998. **394**(6692): p. 456-458.

131. C. Capiglia, Y. Saito, H. Kataoka, T. Kodama, E. Quartarone, and P. Mustarelli, *Structure and transport properties of polymer gel electrolytes based on PVdF-HFP and LiN(C2F5SO2)(2).* Solid State Ionics, 2000. **131**(3-4): p. 291-299.

132. J.K. Lee, Y.J. Lee, W.S. Chae, and Y.M. Sung, *Enhanced ionic conductivity in PEO-$LiClO_4$ hybrid electrolytes by structural modification.* Journal of Electroceramics, 2006. **17**(2-4): p. 941-944.

133. C.P. Rhodes, J.W. Long, and D.R. Rolison, *Direct electrodeposition of nanoscale solid polymer electrolytes via electropolymerization of sulfonated phenols.* Electrochemical and Solid State Letters, 2005. **8**(11): p. A579-A584.

134. D. Peramunage, D.M. Pasquariello, and K.M. Abraham, *polyacrylonitrile based electrolytes with ternary solvent mixtures as plastsizers.* Journal of the Electrochemical Society, 1995. **142**(6): p. 1789-1798.

135. S. Slane and M. Salomon, *Composite gel electrolyte for rechargeable lithium batteries.* Journal of Power Sources, 1995. **55**(1): p. 7-10.

136. B.Y. Huang, Z.X. Wang, L.Q. Chen, R.J. Xue, and F.S. Wang, *The mechanism of lithium ion transport in polyacrylonitrile-based polymer electrolytes.* Solid State Ionics, 1996. **91**(3-4): p. 279-284.

137. F. Leroux, B.E. Koene, and L.F. Nazar, *Electrochemical lithium intercalation into a polyaniline/V_2O_5 nanocomposite.* Journal of the Electrochemical Society, 1996. **143**(9): p. L181-L183.

138. Y.H. Huang and J.B. Goodenough, *High-Rate $LiFePO_4$ Lithium Rechargeable Battery Promoted by Electrochemically Active Polymers.* Chemistry of Materials, 2008. **20**(23): p. 7237-7241.

139. H. Zhang, G.P. Cao, Z.Y. Wang, Y.S. Yang, Z.J. Shi, and Z.N. Gu, *High-Rate Lithium-Ion Battery Cathodes Using Nanostructured Polyaniline/Carbon Nanotube Array Composites.* Electrochemical and Solid State Letters, 2008. **11**(12): p. A223-A225.

140. M. Mertens, C. Calberg, L. Martinot, and R. Jerome, *The electroreduction of acrylonitrile: A new insight into the mechanism.* Macromolecules, 1996. **29**(14): p. 4910-4918.

141. G. Zotti, S. Cattarin, and N. Comisso, *Electrodeposition of polythiophene, polypryrole and polyaniline by the cyclic potential sweep method.* Journal of Electroanalytical Chemistry, 1987. **235**(1-2): p. 259-273.

142. A.F. Diaz and J.A. Logan, *Electroactive polyaniline films.* Journal of Electroanalytical Chemistry, 1980. **111**(1): p. 111-114.

143. P.N. Bartlett and E.N.K. Wallace, *The oxidation of ascorbate at poly(aniline)-poly(vinylsulfonate) composite coated electrodes.* Physical Chemistry Chemical Physics, 2001. **3**(8): p. 1491-1496.

144. R. Murugesan and E. Subramanian, *Effect of organic dopants on electrodeposition and characteristics of polyaniline under the varying influence of H_2SO_4 and $HClO_4$ electrolyte media.* Materials Chemistry and Physics, 2003. **80**(3): p. 731-739.

145. H.J. Deiseroth, *Alkali metal amalgams, a group of unusual alloys.* Progress in Solid State Chemistry, 1997. **25**(1-2): p. 73-123.

146. J.E. Mark, *Polymer Data handbook.* 1999: Oxford University Press.

147. D.M. Mohilner, R.N. Adams, and W.J. Argersinger, *Investigation of the Kinetics and Mechanism of the Anodic Oxidation of Aniline in Aqueous Sulfuric Acid Solution at a Platinum Electrode.* Journal of the American Chemical Society, 1962. **84**(19): p. 3618-3622.

148. A. Frydrychewicz, S.Y. Vassiliev, G.A. Tsirlina, and K. Jackowska, *Reticulated vitreous carbon-polyaniline-palladium composite electrodes.* Electrochimica Acta, 2005. **50**(9): p. 1885-1893.

149. T. Kobayashi, H. Yoneyama, and H. Tamura, *Electrochemical reactions concerned with electrochromism of polyaniline film-coated electrodes.* Journal of Electroanalytical Chemistry, 1984. **177**(1-2): p. 281-291.